

Radial-capped mesoporous silica nanoparticles for multiple drug delivery

Gabriel Martínez Edo

<http://hdl.handle.net/10803/669168>

ADVERTIMENT. L'accés als continguts d'aquesta tesi doctoral i la seva utilització ha de respectar els drets de la persona autora. Pot ser utilitzada per a consulta o estudi personal, així com en activitats o materials d'investigació i docència en els termes establerts a l'art. 32 del Text Refós de la Llei de Propietat Intel·lectual (RDL 1/1996). Per altres utilitzacions es requereix l'autorització prèvia i expressa de la persona autora. En qualsevol cas, en la utilització dels seus continguts caldrà indicar de forma clara el nom i cognoms de la persona autora i el títol de la tesi doctoral. No s'autoritza la seva reproducció o altres formes d'explotació efectuades amb finalitats de lucre ni la seva comunicació pública des d'un lloc aliè al servei TDX. Tampoc s'autoritza la presentació del seu contingut en una finestra o marc aliè a TDX (framing). Aquesta reserva de drets afecta tant als continguts de la tesi com als seus resums i índexs.

ADVERTENCIA. El acceso a los contenidos de esta tesis doctoral y su utilización debe respetar los derechos de la persona autora. Puede ser utilizada para consulta o estudio personal, así como en actividades o materiales de investigación y docencia en los términos establecidos en el art. 32 del Texto Refundido de la Ley de Propiedad Intelectual (RDL 1/1996). Para otros usos se requiere la autorización previa y expresa de la persona autora. En cualquier caso, en la utilización de sus contenidos se deberá indicar de forma clara el nombre y apellidos de la persona autora y el título de la tesis doctoral. No se autoriza su reproducción u otras formas de explotación efectuadas con fines lucrativos ni su comunicación pública desde un sitio ajeno al servicio TDR. Tampoco se autoriza la presentación de su contenido en una ventana o marco ajeno a TDR (framing). Esta reserva de derechos afecta tanto al contenido de la tesis como a sus resúmenes e índices.

WARNING. The access to the contents of this doctoral thesis and its use must respect the rights of the author. It can be used for reference or private study, as well as research and learning activities or materials in the terms established by the 32nd article of the Spanish Consolidated Copyright Act (RDL 1/1996). Express and previous authorization of the author is required for any other uses. In any case, when using its content, full name of the author and title of the thesis must be clearly indicated. Reproduction or other forms of for profit use or public communication from outside TDX service is not allowed. Presentation of its content in a window or frame external to TDX (framing) is not authorized either. These rights affect both the content of the thesis and its abstracts and indexes.

DOCTORAL THESIS

Title	Radial-capped mesoporous silica nanoparticles for multiple drug delivery.
Presented by	Gabriel Martínez Edo
Centre	IQS School of Engineering
Department	Química Orgànica i Farmacèutica
Directed by	Dr. David Sánchez García

A la meva família

La realitat és una representació, i
la representació és la realitat. El
més important és acceptar la
representació tal com és.

La mort del comanador (2017)

Agraïments

En primer lloc m'agradaria agrair al Dr. David Sánchez per haver confiat en mi durant aquests anys. Moltes gràcies David per haver-me guiat pel camí de la tesi doctoral. Camí que tot i requerir de molt d'esforç i dedicació he gaudit gràcies als teus consells. M'has ensenyat a ser perseverant i no defallir davant de les adversitats per tal d'arribar a la meta, i he de dir, que al final hem recollit els fruits de la feina ben feta. També et voldria donar les gràcies pels bons moments viscuts fora de la laboratori, on he après que de tant en tant és necessari descansar de la feina i gaudir de la bona gastronomia i dels postres amb molta nata.

Per altra banda, agrair a la Dra. Maria Llinàs tota l'ajuda que em va brindar als inicis de la tesi doctoral. Moltes gràcies Maria per tota la teva feina i per haver-me ensenyat el camí a recórrer, sense els teus primers passos aquest projecte no hauria estat possible.

Tampoc em puc oblidar de tots aquells estudiants que han participat activament en aquesta tesi doctoral. Moltes gràcies Anna, Jana, Pau H i Raquel per la vostra dedicació a l'hora de fer la feina. Amb vosaltres no només he après la importància de dirigir projectes, sinó també saber transmetre d'una forma entenedora la ciència. Agrair també al futur doctor Teixidó Jr. per haver desenvolupat un mètode eficient per tal de netejar les nanopartícules. Sense ell, estic convençut que encara estaria davant de la microcentrifuga.

Un agraïment molt especial al "professor" Iris, moltes gràcies per la teva obstinació i perseverança davant de la feina, que ens ha permès tirar endavant quan les coses no acabaven de sortir. També et voldria donar les gràcies per la teva companyia en les llargues tardes al laboratori, on no només parlàvem de ciència, sinó també de la vida i de la textura dels "pastelitos".

Agrair també a tots els membres del laboratori de Química Supramolecular per haver-me acompanyat durant aquesta etapa. Moltes gràcies Albert pels esmorzars a les 7:30 h del matí i les converses sobre series. Moltes gràcies Oriol, Marta i Carlos per tots els moments i pica-pica que hem viscut plegats. També agrair a l'Andrea la seva visió crítica i les seves educades formes a l'hora de parlar de compres, de fotografia, de viatges i de qualsevol cosa en general.

Agraeixo al laboratori de Bioquímica I i II, i Biomaterials per obrir-me sempre totes les portes i deixar-me utilitzar els seus equips. En especial, donar les gràcies a la Irene Porcar i a la Dra. Anna Cascante per ensenyar-me a treballar en el món dels cultius cel·lulars. També voldria agrair a la Dra. Cristina Fornaguera la seva ajuda en la preparació/visionat de mostres pels experiments de

microscòpia confocal, gràcies per la teva bona disposició i per atendre tots els meus dubtes. També agraeixo a la Dra. Marta Guerra per desvelar-me els secrets del citòmetre i tota la seva dedicació amb els futurs experiments en ratolins que estan a tocar. Sobretot voldria agrair al Dr. Salvador Borros per haver posat a la meva disposició tots els recursos disponibles per tal de tirar endavant aquest projecte. Gràcies Salvador per creure en aquest projecte i per les teves aportacions, aquesta tesi no seria la mateixa sense els teus consells.

Agradecer también al Profesor Tomas Torres de la Universidad Autonoma de Madrid su buena disposición al facilitarnos la ftalocianina. I would like to thank Professor Denis K. P. Ng from Hong Kong University for the collaboration with the future PDT experiments.

Agrair als meus pares tot el seu suport i comprensió durant tots aquests anys de tesi doctoral, sense vosaltres aquesta etapa no hauria estat possible. Muchas gracias papa por enseñarme a usar el programa de dibujo de nanopartículas, sin tu interés las figuras de la tesis no habrían sido las mismas. Sobretot agrair a la Laura totes les seves paraules d'ànims quan em veia ofuscat per la feina, gràcies a tu aquesta etapa s'ha fet molt més planera.

Finalment, voldria agrair al IQS per aquests 10 anys que he passat en aquesta institució. Quan vaig entrar per primer cop al 2009 per començar la carrera de química no m'imaginaria que sortiria com a doctor. A més, també voldria agrair al IQS haver-me concedit la beca salari que m'ha permès dur a terme aquesta tesi doctoral.

Summary

In this PhD dissertation, a pH-responsive multiple drug delivery system (DDS) based on mesoporous silica nanoparticles (MSN) with a radial-capping of its pores has been developed. This is a new concept that relies on the functionalization of the particle surface with PEG chains substituted with a drug at its end to preserve the inner cargo of the MSN.

First, the concept of radial-capping has been studied to assess the practical usefulness of such capping method. Thus, different types of charged PEGs, namely quaternary amines and neutral PEGs, have been introduced upon an MSN in order to study its capping ability. As a proof of concept, the dye safranin was loaded into the nanoparticles pores, which were subsequently capped with PEGs chains. Then, the release of safranin was assessed under physiological conditions (pH 7.4). The results obtained demonstrated that PEG chains possessing positive charge provides a more efficient capping than the neutral PEGs of the same length.

Using this approach, a drug delivery system (DDS) based on the radial capping for the delivery of camptothecin (CPT) and topotecan (TPT) has been studied. CPT or TPT has been loaded within the pores of an MSN, and subsequently sealed with a PEG chain decorated with doxorubicin (DOX) at its end (DOX-PEG moiety). The system is stable under physiological conditions (pH 7.4) which confirms the effectiveness of the radial capping. On the other hand, under acidic pH, a burst release of drugs takes place. Furthermore, the *in vitro* cytotoxicity test has demonstrated that this DDS can effectively deliver CPT and DOX to HeLa cells achieving a better synergistic effect than the combination of TPT and DOX.

With the aim to improve the loading of CPT to enhance the synergistic effect with the latter system (DOX-PEG moiety), a prodrug of CPT has been synthesised. To do so, a cleavable reductive short PEG chain has been bonded to CPT. An increase of loading of 30% has been achieved in comparison with the unmodified drug. The stability of the radial-capping methodology has been tested as mentioned above. Under physiological conditions, the release of drugs is negligible. The cytotoxicity activity of the system has been tested in two different cell lines: HeLa and HepG2 cells. The results showed a better synergistic effect of this new synthesised system towards HepG2 cells.

In order to further improve the selectivity of the system towards HepG2 cells, the MSN were decorated with glycyrrhetic acid (GA) ligand over the DOX-PEG moiety. Uptake studies have shown that this new system preferably accumulates in HepG2 cells in comparison to HeLa cells. Finally, a tri-deliver system of drugs has been developed with the aim to try to overcome the multiple drug-resistant (MDR) effect by the combination of chemotherapeutic drugs (DOX and

CPT) with a phototherapeutic agent (phthalocyanine). In this regard, a new CPT conjugate with a phthalocyanine has been synthesised and loaded within the pores of an MSN. Then, the system has been sealed with the DOX-PEG moiety. The uptake studies have demonstrated the proper endocytosis of the system inside HeLa cells and the subsequent delivery of the three drugs in the cytoplasm and nucleus. Furthermore, the synergistic effect of DOX and CPT has been assessed *in vitro*.

Resumen

En la presente tesis doctoral, se ha desarrollado un sistema de liberación de fármacos sensible a pH basado en nanopartículas mesoporosas de sílice (MSN). Los poros de la nanopartícula están radialmente obstruidos mediante la funcionalización de cadenas de PEG, sustituidas con un fármaco en uno de sus extremos. El objetivo de esta nueva metodología es la de preservar la carga interna de estas MSN.

En primer lugar, se ha estudiado el concepto de obstrucción radial para evaluar la utilidad práctica de este método. Por esta razón, diferentes tipos de cadenas de PEG con carga, a saber, aminas cuaternarias y PEG neutrales, se han funcionalizado sobre la MSN para estudiar su capacidad de obstrucción. Como prueba de concepto, se ha estudiado la liberación de safranina en medio fisiológico (pH 7.4). Los resultados obtenidos han demostrado que las cadenas de PEG que contienen una carga positiva obstruyen mejor los poros que las cadenas de PEG neutrales de la misma longitud.

Utilizando esta aproximación, se ha diseñado un sistema de liberación de fármacos para la vehiculización de camptotecina (CPT) y topotecán (TPT). En primer lugar, uno de los anteriores fármacos se ha adsorbido dentro de los poros de la MSN. Posteriormente, los poros se han sellado mediante una cadena de PEG que contiene doxorrubicina (DOX) en uno de sus extremos (DOX-PEG). La estabilidad de dicho sistema en condiciones fisiológicas prueba la eficacia de la obstrucción radial. Por otro lado, en condiciones ácidas, se produce una liberación descontrolada de los fármacos. Asimismo, los experimentos de citotoxicidad *in vitro* han demostrado que el sistema puede liberar CPT y DOX en las células cancerígenas HeLa, logrando un mayor efecto sinérgico que la combinación de TPT y DOX.

También se ha sintetizado un profármaco de la CPT con el objetivo de aumentar su carga en una MSN y mejorar así su efecto sinérgico con la DOX. Para llevarlo a cabo, se ha unido una cadena escindible de PEG a la CPT. Empleando esta estrategia se ha conseguido cargar un 30% más de CPT en el interior de las MSN. El sistema muestra una gran estabilidad en condiciones fisiológicas, ya que se observa una liberación negligible de los fármacos. Además, se ha evaluado la citotoxicidad del sistema en dos líneas celulares diferentes: HeLa y HepG2. Los resultados obtenidos demuestran que el nuevo profármaco sintetizado en combinación con DOX, resulta en un mayor efecto sinérgico en las células HepG2.

Por otro lado, la selectividad de las MSN hacia las células HepG2 se ha mejorado mediante la introducción del ligando ácido glicirretínico (GA) sobre el grupo DOX-PEG. Para llevarlo a cabo, se ha empleado la misma aproximación radial establecida para los otros sistemas. Los estudios

de internalización celular han demostrado que este nuevo sistema es capaz de discriminar entre las células HeLa y HepG2, acumulándose preferentemente en estas últimas.

Finalmente, se ha evaluado un sistema de administración triple de medicamentos con el objetivo de superar el efecto de resistencia de los tumores a múltiples fármacos. Esta acción se puede emprender mediante la combinación de medicamentos quimioterapéuticos, DOX y CPT, con un agente fototerapéutico (ftalocianina). Por esta razón, se ha sintetizado un nuevo conjugado de la CPT con una ftalocianina. Dicho conjugado se ha cargado dentro de los poros de la MSN y posteriormente se han sellado con el grupo DOX-PEG. Los experimentos de internalización celular han demostrado la endocitosis de este sistema en las células HeLa y la posterior liberación de los fármacos. Asimismo, se ha evaluado *in vitro* el efecto sinérgico entre la DOX y la CPT.

Resum

En la present tesi doctoral, s'ha desenvolupat un sistema d'alliberament de fàrmacs sensible a pH basat en nanopartícules mesoporoses de sílice (MSN). Els porus de la nanopartícula estan radialment obstruïts mitjançant la funcionalització de cadenes de PEG, substituïdes amb un fàrmac en un dels seus extrems. L'objectiu d'aquesta nova metodologia és la de preservar la càrrega interna d'aquestes MSN.

En primer lloc, s'ha estudiat el concepte d'obstrucció radial per avaluar la utilitat pràctica d'aquest mètode. Per aquesta raó, diferents tipus de cadenes de PEG amb càrrega, a saber, amines quaternàries i PEG neutrals, s'han funcionalitzat sobre la MSN per estudiar la seva capacitat d'obstrucció. Com a prova de concepte, s'ha estudiat l'alliberament de safranina en medi fisiològic (pH 7.4). Els resultats obtinguts han demostrat que les cadenes de PEG que contenen una càrrega positiva obstrueixen millor els porus que les cadenes de PEG neutres de la mateixa longitud.

Utilitzant aquesta aproximació, s'ha dissenyat un sistema d'alliberament de fàrmacs per a la vehiculització de camptotecina (CPT) i topotecan (TPT). En primer lloc, un dels anteriors fàrmacs s'ha adsorbit dins dels porus de la MSN. Posteriorment, els porus s'han segellat mitjançant una cadena de PEG que conté doxorubicina (DOX) en un dels seus extrems (DOX-PEG). L'estabilitat d'aquest sistema en condicions fisiològiques prova l'eficàcia de l'obstrucció radial. D'altra banda, en condicions àcides, es produeix un alliberament descontrolat dels fàrmacs. Així mateix, els experiments de citotoxicitat *in vitro* han demostrat que el sistema pot alliberar CPT i DOX en les cèl·lules cancerígenes HeLa, aconseguint un major efecte sinèrgic que la combinació de TPT i DOX.

També s'ha sintetitzat un profàrmac de la CPT amb l'objectiu d'augmentar la seva càrrega en una MSN i millorar així el seu efecte sinèrgic amb la DOX. Per dur-ho a terme, s'ha unit una cadena de PEG escindible a la CPT. Emprant aquesta estratègia s'ha aconseguit carregar un 30% més de CPT a l'interior de les MSN. El sistema mostra una gran estabilitat en condicions fisiològiques, ja que s'observa un alliberament negligible dels fàrmacs. A més, s'ha avaluat la citotoxicitat de sistema en dues línies cel·lulars diferents: HeLa i HepG2. Els resultats obtinguts demostren que el nou profàrmac sintetitzat amb combinació amb la DOX té un major efecte sinèrgic en les cèl·lules HepG2.

D'altra banda, la selectivitat de les MSN cap a les cèl·lules HepG2 s'ha millorat mitjançant la funcionalització sobre el grup DOX-PEG amb el lligant àcid glicirretínic (GA). Per fer-ho, s'ha emprat la mateixa aproximació radial establerta pels altres sistemes. Els estudis d'internalització

cel·lular han demostrat que aquest nou sistema és capaç de discriminar entre cèl·lules HeLa i HepG2, acumulant-se preferentment en aquestes últimes.

Finalment, s'ha avaluat un sistema d'administració triple de medicaments amb l'objectiu de superar l'efecte de resistència dels tumors a múltiples fàrmacs. Aquesta acció es pot emprendre mitjançant la combinació d'agents quimioterapèutics, DOX i CPT, amb un agent fototerapèutic (ftalocianina). Referent a això, s'ha sintetitzat un nou conjugat de la CPT amb una ftalocianina. Aquest conjugat s'ha carregat dins dels porus de la MSN i posteriorment s'han segellat amb el grup DOX-PEG. Els experiments d'internalització cel·lular han demostrat l'endocitosi d'aquest sistema en les cèl·lules HeLa i el posterior alliberament dels fàrmacs. Així mateix, s'ha avaluat *in vitro* l'efecte sinèrgic entre la DOX i la CPT.

List of figures

Figure 1. Classification of chemotherapeutics drugs.....	36
Figure 2. a) Camptothecin (4) and b) Doxorubicin (1).	37
Figure 3. a) Topotecan (5) and b) Doxorubicin (1).	37
Figure 4. a) Doxorubicin (1) and b) cis-platin (2).....	38
Figure 5. Size scale.	40
Figure 6. Nanostructural representation of organic (a) and inorganic (b) for the transport and release of drugs [58]	41
Figure 7. Structures of mesoporous materials: MCM-41, (2D-hexagonal, space group p6mm); MCM-48 (3D-cubic, space group Ia3d); and MCM-50 (lamellar, space group p2). Reprinted with permission from [66]. Copyright 2014 Wiley-VCH Verlag GMBH & Co. KGAA, Weinheim.....	42
Figure 8. Schematic representation of MSNs channels.	43
Figure 9. Mechanism of silica condensation.....	43
Figure 10. Preparation of MSN scheme [74].....	44
Figure 11. Regioselective di-functionalization of MCM-41 [74].	45
Figure 12. Nano gate triggered release by stimuli.....	46
Figure 13. Relevant strategies for controlled release systems.	49
Figure 14. Simulation of MSN pore outlets functionalized with a) hexadecyl groups and b) protonated triamine $[-C_4H_8NH_2C_3H_6NH_2C_3H_6NH_2C_3H_7]^{3+}$ b). Reprinted with permission from [115]. Copyright 2012 American Chemical Society.	49
Figure 15. a) passive targeting and b) active targeting. Reprinted with permission from [117]. Copyright 2010 Elsevier.....	50
Figure 16. Ligands for active tumour targeting.....	51
Figure 17. MSN representation following a radial-capping approximation.	54
Figure 18. MSN functionalized with DOX-PEG moiety.....	59
Figure 19. a) MSN capped with quaternary amines PEG chains and b) MSN capped with neutral PEG chains.	60
Figure 20. PEGs chains: a) 2,5,8,11-tetraoxatridecan-13-amine (9), b) 2-(2-(2-(2-aminoethoxy)ethoxy)ethoxy)-N,N,N-trimethylethanaminium (10).....	60
Figure 21. Regioselective synthesis of $MSN-(NH_2)_i-(NCS)_o$	61
Figure 22. Loading of $MSN-(NH_2)_i-(NCS)_o$ with safranin and functionalization with PEGs: 9 and 10	62
Figure 23. FTIR spectra of $MSN-(NH_2)_i(NCS)_o(CTAB)$, $MSN-(NH_2)_i(NCS)_o$ and $MSN-(NH_2)_i(R)_o$	62

Figure 24. Zeta potential distribution of MSN-(NH ₂) _i (N ⁺) _{long} and MSN-(NH ₂) _i (OMe) _{long} . Data represented as mean ± SD (n=3).	63
Figure 25. Release profile of Safranin: Aminated nanoparticles (MSN-(NH ₂) _i (Safranin) _o), aminated nanoparticles functionalized with PEG 9 (MSN-NH ₂) _i (OMe) _{long} (Safranin)), aminated nanoparticles functionalized with PEG 10 (MSN-(NH ₂) _i (N ⁺) _{long} (Safranin)). Data represented as mean ± SD (n=3).	63
Figure 26. a) MSN capped with PEG/quaternary amines and b) MSN capped with DOX-PEG moiety.	64
Figure 27. MSN for the codelivery of DOX (1) and CPT (4).	66
Figure 28. CPT (4) structure and equilibrium between the active lactone form and the inactive carboxylate form.	66
Figure 29. Dual DDS scheme.	67
Figure 30. Synthesis of MSN-(NH ₂) _i (CHO) _o .	68
Figure 31. Transmission electron microscopy (TEM) micrographs of (a) MSN-(NH ₂), (b) MSN-(NH ₂) _i (CHO) _o and (c) CPT@MSN-hyd-PEG-hyd-DOX [149].	68
Figure 32. Schematic synthesis of 3,6,9,12,15-pentaoxaheptadecanedihydrazide (14).	69
Figure 33. a) CPT (4), b) TPT (5) and DOX (1) release profile of CPT@MSN-hyd-PEG-hyd-DOX and TPT@MSN-hyd-PEG-hyd-DOX at different pH values under stirring at 100 rpm and t=37 °C. Data represented as mean ± SD (n=3).	70
Figure 34. CLSM images of the uptake of CPT@MSN-hyd-PEG-hyd-DOX scale bar 20 μm. a) corresponds to fluorescein diacetate (FDA) fluorescence, b) CPT (4) fluorescence, c) DOX (1) fluorescence and d) DOX (1) and CPT (4) merged images [149].	72
Figure 35. Flow cytometry analysis of the internalization of DOX (1) into HeLa cells using CPT@MSN-hyd-PEG-hyd-DOX. Data represented as mean ± SD (n=3).	72
Figure 36. DOX (1) release kinetics in HeLa cells. Data represented as mean ± SD (n=3) [149].	73
Figure 37. IncuCyte® images of CPT@MSN-hyd-PEG-hyd-DOX scale bar 400 μm. a), b) and c) corresponds to the bright field at 0 h, 25 h and 50 h, respectively. d), e) and f) corresponds to the red field at 0 h, 25 h and 50 h, respectively [149].	73
Figure 38. a) TEM images of HeLa cells incubated for 4 h with 50 μg·mL ⁻¹ of CPT@MSN-hyd-PEG-hyd-DOX b) a cluster of nanoparticles that have escaped from the endosome c) internalization of the nanoparticles [149].	74
Figure 39. Cell viability of HeLa cells incubated with a) TPT@MSN-hyd-PEG-hyd, CPT@MSN-hyd-PEG-hyd, MSN-hyd-PEG-hyd-DOX, TPT@MSN-hyd-PEG-hyd-DOX and CPT@MSN-hyd-PEG-hyd-DOX and b) MSN-(NH ₂) and MSN-(NH ₂) _i (CHO) _o for 72 h. Data represented as mean ± SD (n=3), *p<.05 and **p<.01. The concentration of free DOX (1) is the released drug at pH 5.5.	75

Figure 40. Cytotoxicity effect of a), b) and c) of TPT@MSN-hyd-PEG-hyd-DOX and MSN-hyd-PEG-hyd-DOX; d), e) and f) of CPT@MSN-hyd-PEG-hyd-DOX and MSN-hyd-PEG-hyd-DOX. Data represented as mean \pm SD (n=3), *p<.05 and **p<.01.....	77
Figure 41. Cleavage of CPT-PEG (22) with GSH.....	81
Figure 42. Retrosynthetic analysis of CPT-PEG (22).....	82
Figure 43. The synthetic pathway followed to obtain molecule PEG-SH (24).....	82
Figure 44. ¹ H-NMR comparison between PEG (28) and PEG-SH (24).....	83
Figure 45. Synthesis of CPT-PYR (34).....	84
Figure 46. Synthesis of CPT-PEG (22).....	84
Figure 47. ¹ H-NMR comparison between a) CPT-PYR (34) and b) CPT-PEG (22).....	85
Figure 48. ESI-FIA-TOF spectrum of CPT-PEG (22).....	85
Figure 49. Cleavage study of CPT-PEG (22) with GSH 10 mM in for 1 h.....	86
Figure 50. The shape of the absorption spectrum of CPT (4) and CPT-PEG (22) in CHCl ₃ /MeOH 4:1.....	87
Figure 51. Preparation of the DDS with CPT-PEG (22).....	88
Figure 52. CPT-PEG (22) release profile of CPT-PEG@MSN-hyd-PEG-hyd-DOX at different pH values under stirring at 100 rpm and at t=37 °C. Data represented as mean \pm SD (n=3).....	88
Figure 53. Cell viability of a) HeLa cells and b) HepG2 incubated with MSN-hyd-PEG-hyd-DOX, CPT@MSN-hyd-PEG-hyd-DOX and CPT-PEG@MSN-hyd-PEG-hyd-DOX for 72 h. Data represented as mean \pm SD (n=3), *p<.05, **p<.01 and *** p<0.0001. The concentration of free DOX (1) is the released drug at pH 5.5 for HeLa cells and pH 6.5 for HepG2 cells.....	90
Figure 54. Schematic representation of MSN functionalized with GA.....	93
Figure 55. CPT-PEG@MSN-hyd-PEG-hyd-DOX system.....	93
Figure 56. Dynamic interaction between DOX (1) and benzaldehyde (35) via pH-sensitive benzoic-imine bond.....	94
Figure 57. DDS with GA targeting (CPT-PEG@MSN-hyd-PEG-hyd-DOX-PEG-GA).....	94
Figure 58. MSN uptake by passive and active targeting.....	95
Figure 59. Retrosynthetic analysis of PEG 37	96
Figure 60. Schematic synthesis of benz-PEG (42).....	97
Figure 61. ¹ H-NMR comparison between PEG 41 a) and PEG 42 b).....	97
Figure 62. GA with carboxylic acid (44).....	98
Figure 63. Synthesis of benz-PEG-GA (45).....	98
Figure 64. ¹ H-RMN comparison between (44) and (45).....	99
Figure 65. ESI-FIA-TOF-spectrum of benz-PEG-GA (47).....	100
Figure 66. Synthesis of the DDS with GA targeting.....	100

Figure 67. Functionalization of CPT-PEG@MSN-hyd-PEG-hyd-DOX with PEG (42) and (45)....	101
Figure 68. Zeta potential distribution of CP-PEG@MSN-hyd-PEG-hyd-DOX, CPT-PEG@MSN-hyd-PEG-hyd-DOX-PEG-OH and CPT-PEG@MSN-hyd-PEG-hyd-DOX-PEG-GA. Data represented as mean \pm SD (n=3). Data measurements pH 5.5.....	101
Figure 69. Flow cytometry analysis of HepG2 cells a) and HeLa cells b) that were incubated with CPT-PEG@MSN-hyd-PEG-hyd-DOX, CPT-PEG@MSN-hyd-PEG-hyd-DOX-PEG-GA, CPT-PEG@MSN-hyd-PEG-hyd-DOX-PEG-OH for 4 h at 100 $\mu\text{g}\cdot\text{mL}^{-1}$. Data represented as mean \pm SD (n=3).....	103
Figure 70. CLSM images of HepG2 cells incubated with CPT-PEG@MSN-hyd-PEG-hyd-DOX a), CPT-PEG@MSN-hyd-PEG-hyd-DOX-PEG-GA b) and CPT-PEG@MSN-hyd-PEG-hyd-DOX-PEG-OH d) at 37 $^{\circ}\text{C}$ for 4 h at 100 $\mu\text{g}\cdot\text{mL}^{-1}$. Scale bar 20 μm . Blue: dapi, red: DOX.....	104
Figure 71. Kinetics of CPT-PEG@MSN-hyd-PEG-hyd-DOX and CPT-PEG@MSN-hyd-PEG-hyd-DOX-PEG-GA by Flow Cytometry of HepG2 cells at 1, 4, 10 and 24 h at 100 $\mu\text{g}\cdot\text{mL}^{-1}$. Data represented as mean \pm SD (n=3).....	104
Figure 72. CLSM images of the uptake of CPT-PEG@MSN-hyd-PEG-hyd-DOX and CPT-PEG@MSN-hyd-PEG-hyd-DOX-PEG-GA (100 $\mu\text{g}\cdot\text{mL}^{-1}$) at 37 $^{\circ}\text{C}$ for 1 h at 100 $\mu\text{g}\cdot\text{mL}^{-1}$. Scale bar 20 μm . Blue: dapi, red: DOX, green: RAB7.....	105
Figure 73. CLSM images of the uptake for 10 h of CPT-PEG@MSN-hyd-PEG-hyd-DOX and CPT-PEG@MSN-hyd-PEG-hyd-DOX-PEG-GA (100 $\mu\text{g}\cdot\text{mL}^{-1}$) at 37 $^{\circ}\text{C}$ for 10 h at 100 $\mu\text{g}\cdot\text{mL}^{-1}$. Scale bar 20 μm . Blue: dapi, red: DOX, green: RAB7.....	106
Figure 74. Cell viability of HepG2 cells incubated with CPT-PEG@MSN-hyd-PEG-hyd-DOX-PEG-OH, CPT-PEG@MSN-hyd-PEG-hyd-DOX-PEG-GA and CPT-PEG@MSN-hyd-PEG-hyd-DOX for 72 h. Data represented as mean \pm SD (n=3).	107
Figure 75. PDT factors.....	109
Figure 76. Schematic illustration of photodynamic therapy [229].	110
Figure 77. Molecular structure of zinc carboxyphthalocyanine (TT1).	111
Figure 78. a) MSN carrying a combination of two therapies; b) Schematic illustration of the structural compounds of the conjugate.....	111
Figure 79. TT1-PEG-CPT conjugate (47). Key bonds to the synthesis of 47 are remarked by red circles.....	112
Figure 80. Retrosynthetic analysis of compound 47	113
Figure 81. Synthetic route for the obtention of CPT-COOH (50).	114
Figure 82. $^1\text{H-NMR}$ spectra comparison between compounds 49 a) and 50 b).	115
Figure 83. Synthesis of compound 53	115
Figure 84. $^1\text{H-NMR}$ spectra of compound 53	116

Figure 85. ESI-FIA-TOF spectrum of 53	117
Figure 86. Synthesis of compound 47	118
Figure 87. ¹ H-NMR spectrum in CDCl ₃ of TT1-PEG-CPT (47).	119
Figure 88. ESI-FIA-TOF spectrum of 47	120
Figure 89. Disulphide bridge cleavage monitored by tlc 7:3 Dioxane:Cy. Spot of CPT (4) circled in orange.	121
Figure 90. Construction of the DDS loaded with TT1-PEG-CPT (47).	122
Figure 91. Shape of absorption spectrum of TT1-PEG-CPT (47) in MeOH.	123
Figure 92. Absorption spectrum shape of TT1-PEG-CPT (47) in acetate buffer (0.1M NaAcO/0.1M AcOH) pH 4.	124
Figure 93. a) TT1-PEG-CPT (47) release profile at pH 4, pH 5.5 and pH 7.4 values under stirring at 100 rpm and t=37 °C b) Absorption supernatants of TT1-PEG-CPT (47) in CHCl ₃ from pH 4 and c) DOX (1) release at pH 4, pH 5.5 and pH 7.4 values under stirring at 100 rpm and t=37 °C.	125
Figure 94. Flow cytometry analysis of HeLa cells that were incubated with TT1-PEG-CPT-PEG@MSN-hyd-PEG-hyd-DOX for 4 h at 100 µg·mL ⁻¹	126
Figure 95. CLSM of the uptake of TT1-PEG-CPT@MSN-hyd-PEG-hyd-DOX at 37 °C for 4 h at 100 µg·mL ⁻¹ . Scale bar 20 µm. Blue: dapi; red: DOX; green: RAB 7.	126
Figure 96. CLSM of the uptake of TT1-PEG-CPT@MSN-hyd-PEG-hyd-DOX at 37°C for 4 h at 100 µg·mL ⁻¹ . Scale bar 20 µm. Blue: CPT; red: DOX; green: RAB 7; purple: Pcs.	127
Figure 97. Cell viability of HeLa cells incubated with TT1-PEG-CPT@MSN-hyd-PEG-hyd-DOX, MSN-hyd-PEG-hyd-DOX and TT1-PEG-CPT@MSN-hyd-PEG-hyd for 72 h. Data represented as mean ±SD (n=3), *p<.05 and **p<.01. The concentration of free DOX is the released drug at pH 5.5.	128

List of Tables

Table 1. Types of gate and stimulus.....	47
Table 2. List of the approved antibodies for cancer therapy.....	52
Table 3. MSN-(NH ₂) _i (CHO) _o size and ζ potential (pH 5.5).	68
Table 4. IC ₅₀ values of camptothecin (4), topotecan (5) and irinotecan (21) at 24 h in HeLa cells ([184]–[186]).	80
Table 5. IC ₅₀ and CI values of CPT-PEG@MSN-DOX (CPT-PEG@MSN-hyd-PEG-hyd-DOX) and CPT@MSN-DOX (CPT@MSN-hyd-PEG-hyd-DOX) in HeLa and HepG2 cells at 72 h.....	89
Table 6. Effect of the pH of the cell on CPT (4) release from CPT-PEG (22).	91
Table 7. Values of Q band in nm and loading in % of solvents used to load TT1-PEG-CPT (47).	123

List of abbreviations

ABS: Absorption

ACN: Acetonitrile

AcOEt: Ethyl acetate

Benz-PEG: 4-(2-(2-(2-(2-hydroxyethoxy)ethoxy)ethoxy)ethoxy)benzaldehyde

Benz-PEG-GA: 10-((1-(4-formylphenoxy)-13-oxo-3,6,9,12-tetraoxahexadecan-16-oyl)oxy)-2,4a,6a,6b,9,9,12a-heptamethyl-13-oxo-1,2,3,4,4a,5,6,6a,6b,7,8,8a,9,10,11,12,12a,12b,13,14b-icosahydricene-2-carboxylic acid

CI: Combination index

CLSM: Confocal Laser Scanning Microscopy

Cis-Pt: *cis*-platin

CPT: Camptothecin

CPT-PEG: (S)-4-ethyl-3,14-dioxo-3,4,12,14-tetrahydro-1*H*-pyrano[3',4':6,7]indolizino[1,2-*b*]quinoline-4-yl 2,5,8,11-tetraoxa-14,15-dithiaheptadecan-17-yl carbonate

CPT-PYR: (S)-4-ethyl-3,14-dioxo-3,4,12,14-tetrahydro-1*H*-pyrano[3',4':6,7]indolizino[1,2-*b*]quinolin-4-yl (2-(pyridin-2-yl)disulfanyl)ethyl carbonate

CPT@MSN-hyd-PEG-hyd: Loaded CPT MSNs with hydrazinePEG chain functionalized at the external surface

CPT@MSN-hyd-PEG-hyd-DOX: Loaded CPT MSNs with DOX-hydrazinePEG chain functionalized at the external surface

CPT-PEG@MSN-hyd-PEG-hyd-DOX: Loaded CPT-PEG MSNs with DOX-hydrazinePEG chain functionalized at the external surface

CPT-PEG@MSN-hyd-PEG-hyd-DOX-PEG-GA: Loaded CPT-PEG MSNs with GA-PEG-DOX-hydrazinePEG chain functionalized at the external surface

CPT-PEG@MSN-hyd-PEG-hyd-DOX-PEG-OH: Loaded CPT-PEG MSNs with OH-PEG-DOX-hydrazinePEG chain functionalized at the external surface and PEG-OH

CTAB: Cetyltrimethylammonium bromide

Cy: Cyclohexane

DCC: N,N'-Dicyclohexylcarbodiimide

DCM: Dichloromethane

DDS: Drug Delivery System

DOX: Doxorubicin

DMAP: 4-dimethylaminopyridine

DMF: Dimethylamine formamide

DMSO: Dimethyl sulfoxide

EM: Emission (Fluorescence)

EMA: European Medicines Agency

EtOH: Ethanol

FA: Folic acid

FDA: Food Drug Administration

GA: Glycyrrhetic acid

GSH: Glutathione

HA: Hyaluronic acid

HOBt: N-hydroxybenzotriazole ester

IC₅₀: Half Maximal Inhibitory Concentration

MCM: Mobil Composition of Matter

MeOH: Methanol

MSN: Mesoporous Silica Nanoparticles

MSN-hyd-PEG-hyd-DOX: DOX-hydrazine linker functionalized at the external surface of a MSN- $(\text{NH}_2)_i(\text{CHO})_o$

MSN-NH₂: Aminated silica nanoparticle

MSN-(NH₂)_i(Acet)_o: Inner amino MSNs with acetal moieties at the external surface.
Regioselective bifunctionalized amino-acetal MSNs

MSN-(NH₂)_i(Acet)_oCTAB: Inner amino MSNs with acetal moieties at the external surface in the presence of CTAB

MSN-NH₂ CTAB: Amino MSNs in the presence of CTAB

MSN-(NH₂)_i(CHO)_o: Inner amino MSNs with outer aldehyde moieties. Regioselective bifunctionalized amino-aldehyde MSNs

MSN-(NH₂)_i(NCS)_o: Inner amino MSNs with outer isothiocyanate moieties. Regioselective bifunctionalized amino-isothiocyanate MSNs

MSN-(NH₂)_i(N⁺)_{long}: Inner amino MSNs functionalized with 2-(2-(2-(2-aminoethoxy)ethoxy)ethoxy)-*N,N,N*-trimethylethanaminium

MSN-(NH₂)_i(OMe)_{long}: Inner amino MSNs functionalized with 2,5,8,11-tetraoxatridecan-13-amine

MSN-(NH₂)_i(R)_o: Inner amino MSNs functionalized with 2,5,8,11-tetraoxatridecan-13-amine /2-(2-(2-(2-aminoethoxy)ethoxy)ethoxy)-*N,N,N*-trimethylethanaminium

MSN-(NH₂)_i(NCS)_o (Safranin): Loaded Safranin in MSN-(NH₂)_i(NCS)_o

MSN-(NH₂)_i(OMe)_o (Safranin): Loaded Safranin in MSN-(NH₂)_i(OMe)_o

MSN-(NH₂)_i(N⁺)_o (Safranin): Loaded Safranin in MSN-(NH₂)_i(N⁺)_o

MSN-(NH₂)_i(NCS)_o (CTAB): Inner amino MSNs with outer isothiocyanate moieties in the presence of CTAB.

NCS: Isothiocyanate

NHS: *N*-Hydroxysuccinimide

NP: Nanoparticles

NSLC: Non-small cell lung cancer

P: Phosphorescence

Pc: Phthalocyanine

PDT: Photodynamic therapy

PEGs: Polyethylene glycol

PEG-SH: 2,5,8,11-tetraoxatridecane-13-thiol

PS: Photosensitizer

PTX: Paclitaxel

ROS: Reactive Oxygen Species

RT: Radiotherapy

SCC: Squamous cell carcinoma

TEM: Transmission electron microscopy

TEOS: Tetraethyl orthosilicate

TOP1: Topoisomerase 1

TOP2: Topoisomerase 2

TPT: Topotecan

TPT@MSN-hyd-PEG-hyd: Loaded TPT MSNs with hydrazonePEG chain functionalized at the external surface

TPT@MSN-hyd-PEG-hyd-DOX: Loaded TPT MSNs with DOX-hydrazonePEG chain functionalized at the external surface

TT1: Zinc carboxyphthalocyanine

TT1-PEG-CPT@MSN-hyd-PEG-hyd: Loaded TT1-PEG-CPT MSNs with hydrazonePEG chain functionalized at the external surface

TT1-PEG-CPT@MSN-hyd-PEG-hyd-DOX: Loaded TT1-PEG-CPT MSNs with DOX-hydrazonePEG chain functionalized at the external surface

Index: Table of contents

Chapter 1. Introduction	33
1.1. Cancer and chemotherapy	33
1.1.1. Cancer therapies	33
1.1.2. Types of chemotherapeutics agents	34
1.1.3. Combined therapies	38
1.1.4. Limitations of the current therapies and outlook	39
1.2. Drug Delivery Systems	39
1.3. Nanoparticles	40
1.4. Mesoporous Silica Nanoparticles	42
1.4.1. Synthesis of Mesoporous Silica Nanoparticles	43
1.4.2. MSN as drug delivery systems	45
1.4.2.1. Design of an MSN as theranostic nanoplatform	46
1.4.2.2. Limitations and outlook of MSN as a theranostic agents	52
1.5. Aims of the thesis	53
Chapter 2. Results and discussion	59
2.1. Radial-capping of MSN with PEG chains	59
2.1.1. Introduction	59
2.1.2. MSN capped with PEGs chains	60
2.1.3. Conclusions and Outlook	64
2.2. Preparation of an MSN for dual DOX/CPT and DOX/TPT pH triggered delivery	65
2.2.1. Introduction	65
2.2.2. Preparation of MSN-(NH ₂) _i (CHO) _o	67
2.2.3. Loading and release of the MSN	69
2.2.3.1. CPT / TPT and DOX loading	69
2.2.3.2. Controlled drug release	70
2.2.4. Intracellular uptake	71
2.2.5. Cytotoxicity	75
2.2.6. Conclusions and Outlook	77
2.3. Synthesis of a prodrug of CPT and study its synergistic effect with DOX	79
2.3.1. Introduction	79
2.3.2. Design of a Prodrug of CPT	80
2.3.2.1. Synthesis of PEG-SH (24)	82
2.3.2.2. Synthesis of CPT-PYR (34)	83
2.3.2.3. Synthesis of CPT-PEG (22)	84

2.3.2.4.	Cleavage of CPT-PEG (22) with GSH	86
2.3.3.	Loading of CPT-PEG (22)	87
2.3.4.	Construction of CPT-PEG@MSN-hyd-PEG-hyd-DOX.....	87
2.3.4.1.	Controlled drug release	88
2.3.5.	Cytotoxicity	89
2.3.6.	Conclusions and Outlook.....	91
2.4.	Glycyrrhetic acid-functionalized MSN for the co-delivery of DOX/CPT-PEG for targeting HepG2 cells	92
2.4.1.	Introduction	92
2.4.2.	Synthesis of the target ligand.....	93
2.4.2.1.	Synthesis of the targeting linker	96
2.4.2.2.	Synthesis of benz-PEG (42).....	96
2.4.2.3.	Synthesis of GA anhydride (44).....	98
2.4.2.4.	Synthesis of benz-PEG-GA (45).....	98
2.4.3.	Construction of the system	100
2.4.4.	Cellular uptake and intracellular distribution	102
2.4.5.	Cytotoxicity	107
2.4.6.	Conclusions and Outlook.....	107
2.5.	Delivery of chemotherapeutic drugs and a PDT drug based on an MSN.....	109
2.5.1.	Introduction	109
2.5.2.	Design of TT1-PEG-CPT conjugate (47).....	112
2.5.2.1.	Synthesis of TT1-PEG-CPT (47)	113
2.5.2.2.	Cleavage of TT1-PEG-CPT (47)	120
2.5.3.	Construction of the DDS	122
2.5.3.1.	Loading of the TT1-PEG-CPT (49) into MSN-(NH ₂) _i (CHO) _o	122
2.5.3.2.	Release of TT1-PEG-CPT (47)	124
2.5.4.	Cellular uptake and intracellular distribution	125
2.5.5.	Cytotoxicity	128
2.5.6.	Conclusions and Outlook.....	129
Chapter 3.	Experimental Part.....	133
3.1.	Instrumentation.....	133
3.2.	Protocols	134
3.3.	Synthetic part of chapter 2.1.	135
3.3.1.	Synthesis of Amino MSNs with CTAB (MSN-NH ₂ (CTAB)) [139]	135
3.3.2.	Synthesis of isothiocyanate MSNs ((MSN)-(NH ₂) _i (NCS) _o [139]	135
3.3.3.	Synthesis of tetra(ethylene glycol) methyl ether tosylate (28) [250]	136
3.3.4.	Synthesis of 1-Azido-2-[2-[2-[2-(methoxyethoxy)ethoxy]ethoxy]	136
3.3.5.	Synthesis of triethylene glycol 2-aminoethyl methyl ether (9) [252]	137

3.3.6.	Safranin loading in MSN-(NH ₂) _i -(NCS).....	137
3.3.7.	Functionalization of Safranin loaded MSN-(NH ₂) _i -(NCS) _o with (9) (MSN-(NH ₂) _i (OMe) _{long}	138
3.3.8.	Synthesis of tetraethylene glycol monotosylate (41) [253].....	138
3.3.9.	Synthesis of 2-(2-(2-(2-azidoethoxy)ethoxy)ethoxy)ethan-1-ol (59) [254].....	139
3.3.10.	Synthesis of 2-(2-(2-(2-azidoethoxy)ethoxy)ethoxy)ethyl 4-methylbenzenesulfonate (60) [255].....	139
3.3.11.	Synthesis of 2-(2-(2-(2-aminoethoxy)ethoxy)ethoxy)ethyl 4-methylbenzenesulfonate (61) [256].....	140
3.3.12.	Synthesis of 2,2-dimethyl-4-oxo-3,8,11,14-tetraoxa-5-azahexadecan-16-yl 4-methylbenzenesulfonate (62) [257].....	140
3.3.13.	Synthesis of tert-butyl-(2-(2-(2-(2-azidoethoxy) ethoxy) ethoxy) ethyl) carbamate (63) [258].....	141
3.3.14.	Synthesis of tert-butyl (2-(2-(2-(2-aminoethoxy)ethoxy)ethoxy)ethyl)carbamate (64) [258].....	141
3.3.15.	Synthesis of N,N,N,2,2-pentamethyl-4-oxo-3,8,11,14-tetraoxa-5-azahexadecan-16-aminium (65) [259].....	142
3.3.16.	Synthesis of 2-(2-(2-(2-aminoethoxy)ethoxy)ethoxy)-N,N,N-trimethylethan-1-aminium (10).....	142
3.3.17.	Functionalization of Safranin loaded MSN-(NH ₂) _i -(NCS) _o with (10) (MSN-(NH ₂) _i (N ⁺) _{long}	143
3.3.18.	Release experiments [139].....	143
3.4.	Synthetic part of chapter 2.2.	144
3.4.1.	Synthesis of 2-isothiocyanate-1,1-dimethoxyethane (15) [149].....	144
3.4.2.	Synthesis of bifunctionalized amino-aldehyde (MSN-(NH ₂) _i (CHO) _o) [149].....	144
3.4.3.	Synthesis of diethyl 3,6,9,12,15-pentaoxaheptadecanedioate (19) [149].....	145
3.4.4.	Synthesis of dimethyl 3, 6, 9, 12, 15 pentaoxaheptadecanedihydrazide (14) [149].....	145
3.4.5.	Dual CPT@MSN-hyd-PEG-hyd-DOX [149].....	146
3.4.6.	Dual TPT@MSN-hyd-PEG-hyd-DOX [149].....	147
3.4.7.	Synthesis of MSN-hyd-PEG-hyd-DOX [149].....	148
3.4.8.	Synthesis of CPT@MSN-hyd-PEG-hyd.....	149
3.4.9.	Synthesis of TPT@MSN-hyd-PEG-hyd.....	150
3.4.10.	Release experiments of CPT@MSN-(NH ₂) _i (PEG-DOX) _o and TPT@MSN-(NH ₂) _i (PEG-DOX) _o [149].....	150
3.4.11.	<i>In vitro</i> cytotoxicity [149].....	151
3.4.12.	Confocal microscopy for cellular internalization [149].....	151
3.4.13.	Bio-TEM [149].....	151
3.4.14.	Flow cytometry [149].....	152
3.4.15.	IncuCyte® S3 live-cell analysis [149].....	152
3.5.	Synthetic part of chapter 2.3.	153

3.5.1.	Synthesis of 2,5,8,11-tetraoxatridecane-13-thiol (24) [260]	153
3.5.2.	Synthesis of 2-(Pyridyl-disulfanyl)ethanol (33) [261]	153
3.5.3.	Synthesis of Camptothecin-(4-pyridyldisulfanyl)ethyl carbonate (CPT-PYR) (34) [261]	154
3.5.4.	Synthesis of (S)-4-ethyl-3,14-dioxo-3,4,12,14-tetrahydro-1H-pyrano[3',4':6,7]indolizino[1,2-b]quinolin-4-yl (2,5,8,11-tetraoxa-14,15-dithiaheptadecan-17-yl) carbonate (CPT-PEG) (22)	155
3.5.5.	Dual CPT-PEG@MSN-hyd-PEG-hyd-DOX [149]	156
3.5.6.	Release experiments of CPT-PEG@MSN-hyd-PEG-hyd-DOX [149]	157
3.5.7.	<i>In vitro</i> cytotoxicity [149]	157
3.6.	Synthetic part of chapter 2.4.	158
3.6.1.	Synthesis of 4-(2-(2-(2-(2-hydroxyethoxy) ethoxy) ethoxy) ethoxy) benzaldehyde (benz-PEG) (42) [262]	158
3.6.2.	Synthesis of 10-((3-carboxypropanoyl)oxy)-2,4a,6a,6b,9,9,12a-heptamethyl-13-oxo-1,2,3,4,4a,5,6,6a,6b,7,8,8a,9,10,11,12,12a,12b,13,14b-icosahydricene-2-carboxylic acid (44) [127]	159
3.6.3.	Synthesis of 10-((1-(4-formylphenoxy)-13-oxo-3,6,9,12-tetraoxahexadecan-16-oyl)oxy)-2,4a,6a,6b,9,9,12a-heptamethyl-13-oxo-1,2,3,4,4a,5,6,6a,6b,7,8,8a,9,10,11,12,12a,12b,13,14b-icosahydricene-2-carboxylic acid (benz-PEG-GA) (45) [116]	160
3.6.4.	Dual conjugate CPT-PEG@MSN-hyd-PEG-hyd-DOX-PEG-OH and CPT-PEG@MSN-hyd-PEG-hyd-DOX-PEG-GA [208]	161
3.6.5.	<i>In vitro</i> cytotoxicity [149]	161
3.6.6.	Flow cytometry [149]	162
3.6.7.	Confocal microscopy for cellular internalization [149]	162
3.7.	Synthetic part of chapter 2.5.	163
3.7.1.	Synthesis of (S)-4-ethyl-3,14-dioxo-3,4,12,14-tetrahydro-1H-pyrano[3',4':6,7]indolizino[1,2-b]quinolin-4-yl (2-((2-hydroxyethyl)disulfanyl)ethyl) carbonate (49) [239]	163
3.7.2.	Synthesis of (S)-4-(2-((2-(((4-ethyl-3,14-dioxo-3,4,12,14-tetrahydro-1H-pyrano[3',4':6,7]indolizino[1,2-b]quinolin-4-yl) oxy) carbonyl) oxy) ethyl) disulfanyl) ethoxy)-4-oxobutanoic acid (50) [239]	164
3.7.3.	Synthesis of TT1-PEG-NHBOC (56)	165
3.7.4.	Synthesis of TT1-PEG-NH ₂ (54)	165
3.7.5.	Synthesis of TT1-PEG-CPT (47)	166
3.7.6.	Dual conjugate TT1-PEG-CPT@MSN-hyd-PEG-hyd-DOX	167
3.7.7.	Synthesis of TT1-PEG-CPT@MSN-hyd-PEG-hyd	168
3.7.7.	Release experiments of TT1-PEG-CPT@MSN-hyd-PEG-hyd-DOX [149]	168
3.7.8.	<i>In vitro</i> cytotoxicity	169
3.7.9.	Flow cytometry	169
3.7.10.	Confocal microscopy for cellular internalization [149]	169
Chapter 4.	Conclusions	173

Chapter 5. Bibliography..... 179

Chapter 1. Introduction

Chapter 1. Introduction

1.1. Cancer and chemotherapy

Cancer is a term used for diseases in which affected cells divide without control and have the potential ability to invade or spread to other parts of the body [1]. Despite the great effort made during these last two decades to understand cancer at a molecular level, still, there is not an adequate treatment for such illness [2],[3]. Due to the heterogeneity of the disease, which encompasses more than 200 affections [4], different approaches are being used to overcome cancer.

1.1.1. Cancer therapies

The treatments for cancer mainly depends on the type and stage of the tumour. For breast cancer, 49% of the patients undergo radiation, although 34% receive aggressive surgery (mastectomy). Those patients diagnosed with the metastatic disease most often are treated with chemotherapy or radiation alone (56%). On the other hand, immunotherapy is usually applied together with other therapies such as chemotherapy and radiation. Nevertheless, 12% of patients diagnosed with non-small cell lung cancer (NSLC) are treated only with immunotherapy [5].

Surgery and radiotherapy work through various ways to remove localized cancer cells. Surgery is not only employed for the total or partial elimination of cancer by resection, but it is also a fundamental tool for diagnosis and staging of tumours, as biopsies are usually required. On the other hand, radiation diminishes the tumoral mass using ionizing radiation which works by damaging the DNA of cancerous tissue [6].

Although the use of immunotherapy has been explored for many years, it was only in the late 80s that it has been used to fight cancer. This therapy focuses on eliminating cancer indirectly by harnessing the power of the host's immune system. There are two different approaches to do so. The first one entails the stimulation of the immune system to work harder/smarter to attack cancer cells. The second, by the administration of human-made immune systems components to restore/improve its response against cancer cells [7], [8].

However, chemotherapy is the most frequently used approach to overcome cancer. Only in 2016, 1.6 billion of chemotherapeutic agents have been delivered to treat this terrible disease [9]. These anti-neoplastic drugs have been administrated to fight several types of cancer such as breast cancer, colon cancer, rectal cancer, colorectal cancer, non-Hodgkin lymphoma, lung

cancer, testicular cancer, bladder cancer and uterine cancer. The use of this therapy, again, depends on the stage of the disease and occasionally, it is administrated in combination with other therapies [10], [11]. The therapeutic principle of chemotherapy is the administration of one or more cytotoxic anti-neoplastic drugs which kills cells that divide rapidly, a critical feature of most cancer cells [12]. Nevertheless, its application encounters many issues, especially the development of chemoresistance and lack of selectivity through affected tissues [13].

1.1.2. Types of chemotherapeutics agents

Chemotherapy, unlike radiation or surgery, which target specific areas, acts throughout the body by systemic administration. Therefore, its frequent application not only affects the unhealthy cells but the healthy ones as well, like those of the skin, hair, intestines and bone marrow [14].

The objective of this therapy is to cure the patient by effectively destroying the cancerous cells by the administration of chemical drugs. However, in some cases, it may only be able to control the disease from spreading through the body and slow down the growth of tumours. Finally, if the chemotherapeutic drug cannot either eliminate or control the cancer progression, it is administered to shrink tumours that cause pain [14].

There are more than 100 chemotherapeutic agents that can be sorted out according to their mechanism of action (Figure 1) [15]:

- Antitumor antibiotics: induce tumour cell death by DNA intercalation and the generation of free radicals. As an example of such kind of drugs that acts following this mechanism of action is doxorubicin (DOX) (**1**). This drug is a very potent chemotherapeutic agent approved by the food drug administration (FDA) which belong to the family of anthracyclines [16]. This group of compounds is characterized by its tetracyclic structure, which has the ability to intercalate with the DNA bases pairs, with an anthraquinone backbone connected to a sugar moiety by a glycosidic linkage [16].
- Alkylating agents: the primary mechanism of action of these drugs is the covalent binding of an alkyl group to form an adduct with the guanine base of DNA. These types of drugs work in all phases of the cell cycle. Thus, its administration permits the treatment of many kinds of cancers. *Cis*-platin (*cis*-Pt) (**2**) is a well-known example of alkylating agents and it is widely used to treat a vast range of diseases due to its cytotoxicity [17].

- Antimetabolites: encompasses drugs that interfere with cellular metabolic processes that are important for the synthesis of purines and pyrimidines. For instance, fluoropyrimidine-based anti-cancer drugs, such as 5-fluorouracil (**3**) inhibit thymidylate synthase suppressing DNA replication [18].
- Topoisomerase inhibitors: these drugs aim to interfere with enzymes called topoisomerases, which help to separate the strands of DNA for their replication. These inhibitors can be classified into two different categories:
 - o Inhibitors of topoisomerase 1 (TOP1): camptothecin (CPT) (**4**) and its derivatives such as topotecan (TPT) (**5**) are considered to be among the most promising anticancer drugs of the 21st century [19]. Both anticancer agents act as DNA topoisomerase 1 inhibitors to form a ternary cleavable complex between this enzyme and DNA, thus, leading to DNA breakage and cell death [20]. Regrettably, the therapeutic use of CPT (**4**) is extremely limited due to its poor water solubility and toxic side effects [20].
 - o Inhibitors of topoisomerase 2 (TOP2): Etoposide (**6**) is a topoisomerase 2 inhibitor that derives from a toxin found in the American Mayapple. It was approved for cancer therapy in 1983 by FDA. Research studies have demonstrated that etoposide (**6**) targets DNA topoisomerase 2 activities, thus leading to the production of DNA breaks [21]. Similarly, DOX (**1**) apart of its function as an antitumor antibiotic, also inhibits the progression of the TOP2 enzyme, enhancing the DNA-damaging efficiency [22].
- Corticosteroids: natural hormones and hormone-like drugs that are useful in the treatment of a wide range of cancers. These substances were discovered in the early 1950s after chemical modifications of natural steroids such as cortisol [23]. For instance, fluorination at the 9-alpha position of the steroids produced dexamethasone (**7**) [23]. The therapeutic function of this corticosteroid is to decrease the swelling around tumors, thanks to its anti-inflammatory properties [24].
- Mitotic inhibitors: the primary mechanism of action for these drugs is the induction of cellular arrest during mitosis through targeting of the microtubule cytoskeleton [25]. A well-known drug administrated with this purpose is the taxane Paclitaxel (PTX) (**8**). The

pharmaceutical formulation of this drug (Taxol®), is well-known for improving the overall survival rate and progression-free survival of patients [26].

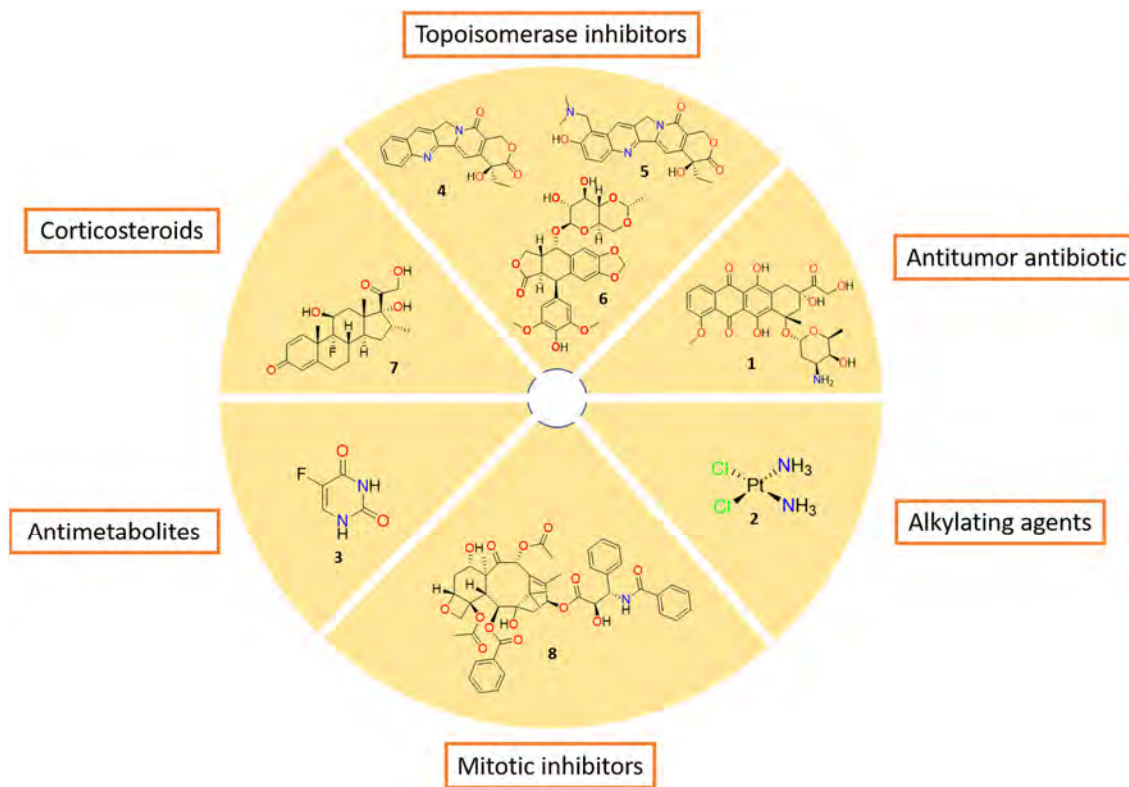


Figure 1. Classification of chemotherapeutics drugs.

Although the wide range of chemotherapeutic agents, the administration of a single drug is not usually enough to accomplish the complete remission of the tumour. For this reason, a combination of chemotherapeutic agents has been introduced as an alternative for treating metastatic cancers. The general principle of combined chemotherapy is the application of drugs with independent mechanisms of action and to deliver multiple drugs at their maximum tolerated dose as early as possible in the disease [27]. In certain instances, this combination can lead to the so call synergistic effect. This effect can be ascribed to the interaction between two or more drugs that causes the total effect of the drugs to be greater than the sum of the individual effects of each drug [28].

An excellent example of this therapy is the inhibition of TOP1 and TOP2 enzymes [29]. In this regard, the combination of CPT (**4**) with DOX (**1**) has been described to overcome the difficulties for the treatment of glioblastoma cancer [30]. Both chemotherapeutic agents are DNA-damaging drugs that result in the unwinding of DNA for transcription by inhibiting the progression of the TOP1 (CPT) (**4**) and the TOP2 (DOX) (**1**) (Figure 2) [29].

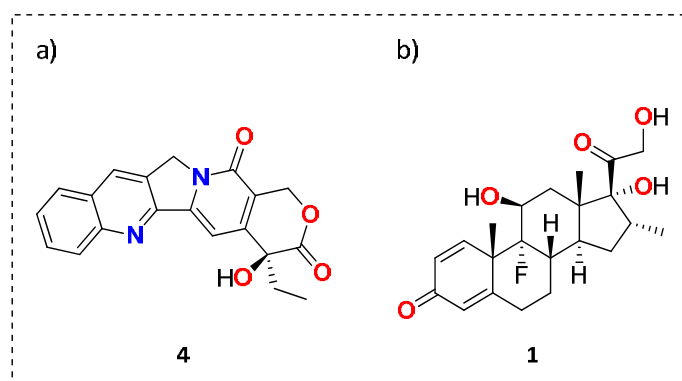


Figure 2. a) Camptothecin (4) and b) Doxorubicin (1).

DOX (1) has also been administrated with TPT (5), a CPT (4) analogue, for the treatment of ovarian cancer (Figure 3). As has been said before, TPT (5) targets DNA-TOP1 while DOX (1) stabilize TOP2, preventing the DNA double helix from being released; thus, the replication process is stopped. *In vitro* and *in vivo* results show that the cytotoxicity of the treatment is time-dependent and the synergy is achieved when the tumour cells are exposed to both drugs under a long period of time [31].

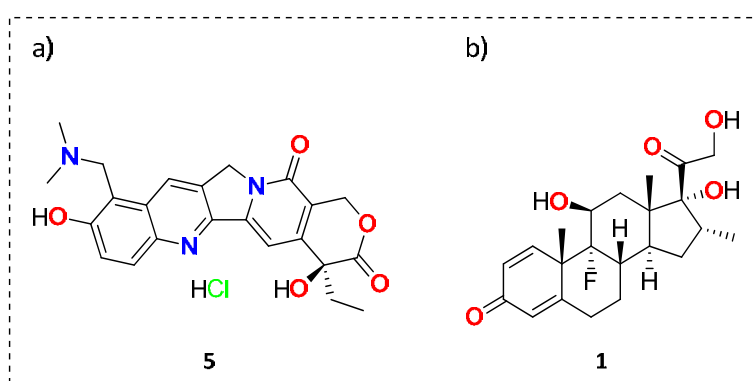


Figure 3. a) Topotecan (5) and b) Doxorubicin (1).

Another example of drugs used for combined chemotherapy is given by *cis*-Pt (2) and DOX (1) (Figure 4), which are commonly administrated to fight advanced basal cell carcinoma or squamous cell carcinoma (SCC) of the skin [32]. The therapeutic efficacy of *cis*-Pt (2) is enhanced thanks to the combination with DOX (1). This drug not only exhibits an anti-cancer effect by intercalating duplex DNA and inhibiting the activity of TOP2 but also has the capacity to inhibit the self-repair of *cis*-Pt-damaged DNA by TOP2; thus the efficacy of *cis*-platin is improved [33].

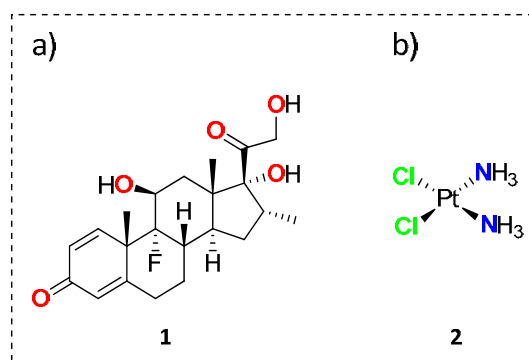


Figure 4. a) Doxorubicin (1) and b) *cis*-platin (2).

Unfortunately, in many instances, the combination of chemotherapeutic agents is not effective due to tumour drug resistance. Therefore, to overcome these resistances, the combination of therapies has been studied.

1.1.3. Combined therapies

The complexity of cancer prompts the researchers to explore new treatment approaches. Therefore, the combination of therapies has arisen as an alternative to battle this terrible disease. An appropriate choice of therapies might achieve efficacy with lower doses or less toxic drugs. Besides, it can chemosensitize cells, making an additional compound more potent or even obtain additive or synergistic effect between two therapies [34].

By way of illustration, surgery has often been combined with chemotherapeutic agents for fighting localized SCC of the thoracic esophagus [35]. Frequently, very aggressive surgery is applied in order to overcome this cancer. Besides, as the invasiveness of this procedure approaches the limit of tolerability for patients, more aggressive surgery is precluded. For this reason, it is necessary to introduce a multimodality treatment to improve the impact of this cancer. In this regard, the administration of *cis*-Pt (2) or fluorouracil (3) after the surgical treatment has shown a definite relapse of the disease in comparison with untreated patients. However, a rational answer about how the synergistic effect between these two therapies work is not completely known [35].

Another approach is the combination of radiotherapy with chemotherapeutic agents in patients with locally advanced cervical cancer [36]. It has been demonstrated that a radiotherapy treatment together with *cis*-Pt (2) improved the rates of survival and progression among women affected by this type of cancer. It is hypothesized that *cis*-Pt (2) enhances the effect of radiation by inhibiting DNA repair and by sensitizing hypoxic cells to radiation [36].

The combination of radiotherapy with immunotherapy has been used to fight NSCLC [37]. Even though radiotherapy is usually combined with chemotherapy achieving good results, patients

often develop metastases, suggesting an ongoing need to improve systemic disease control in early stages [37]. Radiotherapy can mediate what is known as the abscopal effect, a phenomenon in which tumour regression occurs in nonirradiated lesions. This effect has been applied to treat patients with immunotherapy drugs after a radiotherapy treatment because they will be more responsive to them [38]. Nevertheless, the amount of radiation necessary to trigger the immunologic response of cancer cells mediated by drugs must be properly studied for each patient [38].

A different approach is the implementation of photodynamic therapy (PDT) combined with chemotherapeutic drugs or X-ray irradiation [39], [40]. PDT is based on the generation of cytotoxic singlet oxygen ($^1\text{O}_2$) and other reactive oxygen species (ROS) such as hydrogen peroxide and hydroxyl radical under photo-irradiation of a photosensitizer (PS). Typical PS are phenothiazine dyes, phthalocyanine dyes, chlorophyll platform, porphyrins, xanthenes and monoterpene [41]. After chemotherapeutic treatment, the cell may be more sensitive to $^1\text{O}_2$; thus, complete inhibition of DNA repair would be achieved, causing cell death.

1.1.4. Limitations of the current therapies and outlook

As has been seen so far, chemotherapy is the most widely used approach to fight cancer either with combination with different drugs or combined with other therapies. Nevertheless, the systemic administration of antineoplastic agents throughout the body can produce chemoresistance to cancerous cells and the development of several side effects [42]. Besides, the major part of these agents shows insufficient dosage to the affected tissues or high insolubility in aqueous solvents. These drawbacks hamper the bioavailability of the drugs, thus higher amounts of these toxic agents are usually administrated [42]. Although solutions have been presented, such as the derivatisation of drugs, which improves solubility and targeting, unsatisfactory results are usually obtained [43], [44].

As a fitting solution, the integration between nanotechnology and medicine to treat any disease at the nanoscale level has attracted significant attention in cancer therapy and diagnosis. Such consolidation is known as drug delivery systems (DDS) and can provide a reasonable alternative to enhance the selective delivery of drugs to tumors [45]–[47].

1.2. Drug Delivery Systems

The term DDS refers to engineered technologies for the targeted delivery and controlled release of therapeutic drugs [48]. The efficacy of such agents is significantly dependent on specific performance of the delivery method: an overdose would be harmful to the patient, whereas too low a concentration of the medication would produce non-therapeutic effect [49], [50]. For this

reason, the features of an ideal DDS must be: providing controlled and sustained release of drugs at therapeutic concentrations, high stability, intrinsic lower toxicity and selectivity [51]–[53]. Besides, such a system might be able to respond effectively to stimuli for release its cargo in the target tissue [54]. Thus, the drug could be efficiently transported, preventing its degradation in the biological environment and diminishing the toxicity in the healthy tissues [54]. Another important attribute associated with DDS is its function as theranostic agents, which is a concept that refers to the integration between imaging and therapy in a unique system [55].

1.3. Nanoparticles

DDS are commonly based on nanoobjects such as dendrimers, liposomes, polymeric systems, micelles, viruses, quantum dots, carbon nanotubes and metal oxide nanoparticles; with a size that is ranged between 1 and 100 nm (Figure 5) [56]. Those nanoobjects possess unique physical and chemical properties due to their high surface area and nanoscale size. Their optical properties, reactivity and other features are reported to be dependent on the size of the nanoobjects. Due to these characteristics, the latter nanoparticles are suitable candidates for various applications such as catalysis, imaging, energy-based research and environmental applications [57].

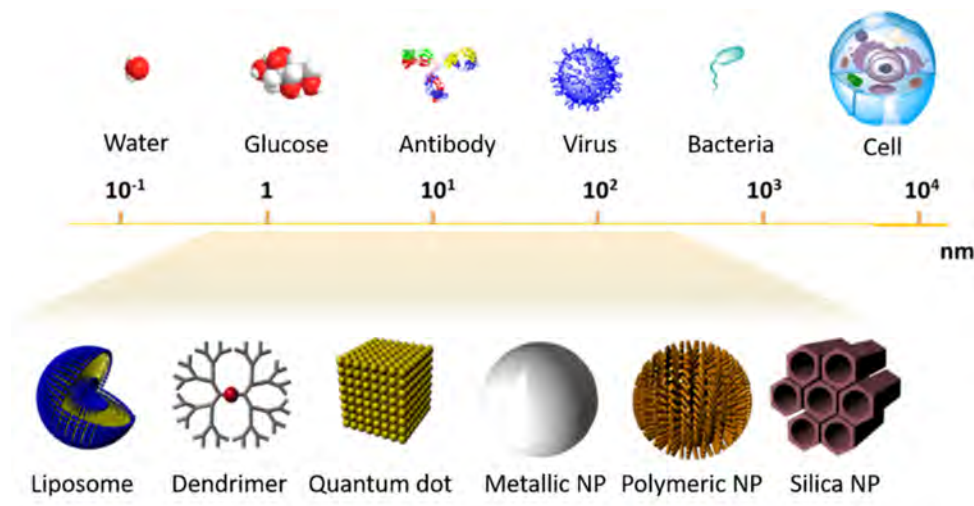


Figure 5. Size scale.

Arguably, in the last decade, nanomedicine has become the field that better capitalizes on the structural and physicochemical features of nanoparticles [58]. The size, shape and porosity of nanoparticles provide an end-less possibilities to build theranostic agents. The ideal features of such DDS agents are the following [58]:

1. Biocompatibility of the vehicle.
2. High loading and protection of the guest molecule.

3. Null release before reaching the target.
4. Efficient cellular uptake.
5. Effective endosomal escape to avoid the degradation of the drugs and enhance the therapeutic effect [59].
6. Controllable rate of release to achieve an effective local concentration.
7. Cell and tissue targeting.

Independently on the materials and technologies utilized for the construction of DDS based on nanoparticles, they can be easily classified in 2 main groups (Figure 6) [60], [61]:

- a. Organic nanostructures encompass all the polymeric materials such as nanospheres, nanocapsules, micelles, liposomes and dendrimers.
- b. Inorganic nanostructures encompass oxide metal nanoparticles, mesoporous silica nanoparticles (MSN) and carbon nanotubes.

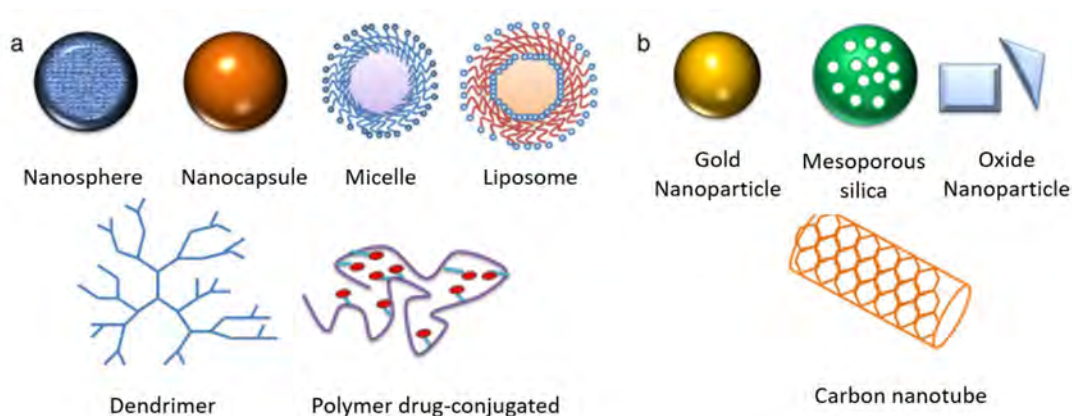


Figure 6. Nanostructural representation of organic (a) and inorganic (b) for the transport and release of drugs [60] .

For instance, liposomes were the first nanomaterial to be investigated as drug nanocarrier [62]. This nanoparticles are spherical vesicles mainly made of phospholipids and steroids such as cholesterol, bilayers, or other surfactants [62]. Commonly, the drug is incorporated inside the liposome after an encapsulation process. Afterwards, the drug is released according to the liposome composition and pH [62]. Similarly, dendrimers have also been used in many fields thanks to its polyvalency. However, it is in the field of DDS that has been widely studied due to its ability to ferry drugs, which can be either entrapped or functionalized within the dendrimer structure [63]. This fact enhances the solubility, stability and oral bioavailability of chemotherapeutic agents [63]. Besides, its high number of functional groups enables to add selectivity, by decoration of ligands, to the system [64].

As for inorganic nanostructures, gold nanoparticles have emerged as a novel platform for delivery or targeting of therapeutic agents [65]. These nanoparticles are characterized by its

inertness and non-toxicity. Generally, thiol linkages are functionalized on its surface due to the great affinity of this group with the gold nanoparticle surface. Thus, drugs or ligands can be attached thanks to this reactivity [65].

However, most of the systems available present weakness or limitations such as low loading capacity, poor biocompatibility or difficult preparations. In this context, MSN have emerged as the ideal nanoplatforms that allows the design of complex and selective DDS [66].

1.4. Mesoporous Silica Nanoparticles

MSN were discovered simultaneously in 1990 by two different investigation groups. Kuroda group from the Waseda University (Japan) and C. T. Kresage group from the Mobil Oil Corporation [67]. In the literature, these nanoparticles are known as MCM that stands for Mobil Composition of Matter. From this type, the most important are the MCM-41 (hexagonal bidimensional), MCM-48 (three-dimensional cubic) and MCM-50 (lamellar) (Figure 7) [68].

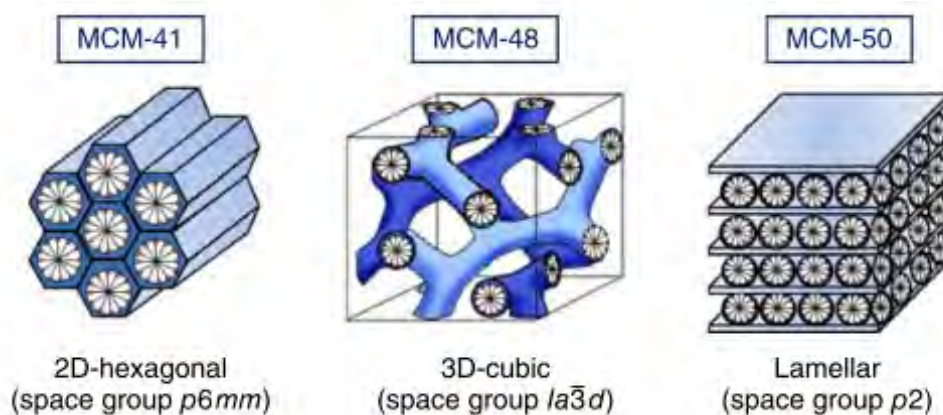


Figure 7. Structures of mesoporous materials: MCM-41, (2D-hexagonal, space group $p6mm$); MCM-48 (3D-cubic, space group $Ia\bar{3}d$); and MCM-50 (lamellar, space group $p2$). Reprinted with permission from [68]. Copyright 2014 Wiley-VCH Verlag GMBH & Co. KGAA, Weinheim.

Among this materials, MCM-41 are often used as nanocarriers for DDS purposes due to its physicochemical properties [69]:

1. High surface area ($>900 \text{ m}^2/\text{g}$).
2. Large pore volume ($>0.9 \text{ cm}^3/\text{g}$).
3. Tunable pore size with a narrow distribution (2-10 nm).
4. Chemical and thermal stability.
5. Low toxicity and biocompatibility with human body.
6. Easy to synthesize and functionalize.
7. Stable mesostructures.

Furthermore, the presence of pores provides two different surfaces to the nanoparticle: the external outer surface and the inner porous surface (Figure 8). This characteristic allows the selective functionalization of both surfaces of MSN with different moieties.

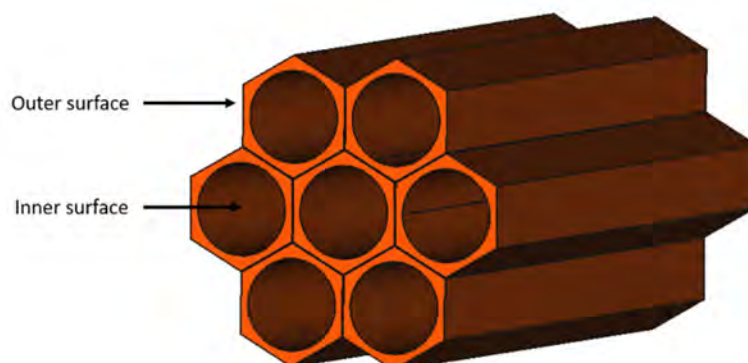


Figure 8. Schematic representation of MSNs channels.

1.4.1. Synthesis of Mesoporous Silica Nanoparticles

MSN are synthesised through a modification of the Stöber method which include the condensation of silica precursors such as sodium silicate, tetraethyl orthosilicate (TEOS) or tetramethylammonium silicate, in the presence of cationic surfactants, cetyltrimethylammonium bromide (CTAB), that act as structure-directing template in basic conditions (pH 11) and at a temperature between 30 °C and 60 °C [70], [71]. The MSN are formed by the sol-gel process catalysed in basic medium [72] (Figure 9).

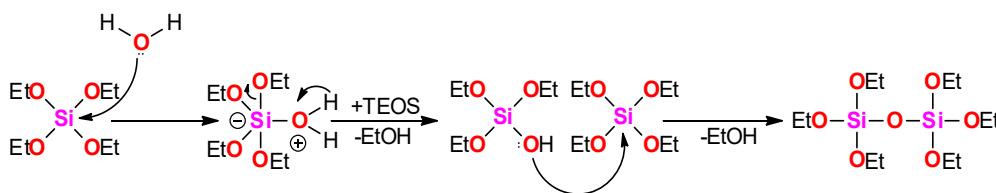


Figure 9. Mechanism of silica condensation.

First, Si-OH groups are formed by the hydrolysis of the alkoxide group. Afterwards, silanol moieties polymerize by condensation, forming three-dimensional structures linked by siloxane bonds (Si-O-Si). The following step needs the presence of a cylindrical template generated by the presence of a cationic surfactant, which will eventually generate the pores of the MSN. The negative charges of the silica species are attracted by the positive charge of the surfactant. Such a reaction would lead to the formation of tubular silica structures. Consequently, the size of the nanoparticle will increase until the negative charge introduced by the silica species is too high that it stops growing. Besides, a fine tune of the morphology, pore size and shape of the MSN

can be achieved by changing various variables such as rate of addition, temperature, agitation and the amount of catalyst used [73],[74]. Ultimately, the surfactant is removed from the silica structure by reflux in acidified ethanol, ionic exchange with ammonium nitrate in ethanol/methanol or calcination. The latter procedures allow the rupture of the electrostatic interaction present between the groups of the cationic surfactant heads and the anionic silicates. Hence the formation of the MSN is completely achieved (Figure 10) [75].

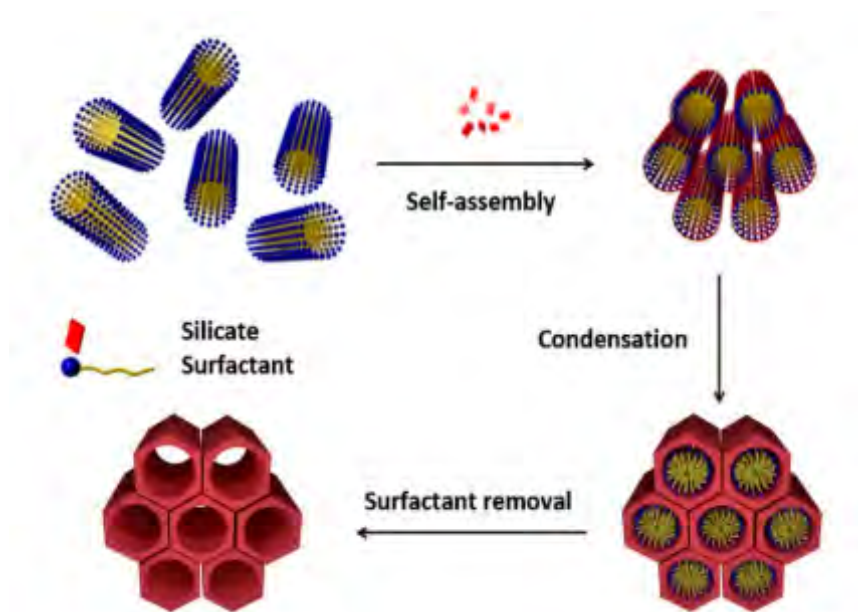


Figure 10. Preparation of MSN scheme [76].

As stated previously, a distinctive characteristic of MSN is the presence of two different surfaces: the external (surface) and the internal (pores). Thus, a regioselective modification both with inorganic or organic species of the nanoparticles, makes the nanomaterial very versatile and enables MSN to perform specialized tasks [77]. To do so, two different types of methodologies are typically used. The first method is carried out by grafting the surface of the MSN with organochlorosilanes or organoalkoxysilanes. The surface of the material must be dry enough in order to avoid self-condensation of the latter precursors in the presence of water (Figure 11) [76]. Alternatively, a simultaneous co-condensation within the reaction medium of the alkoxysilane precursor of the silica mesostructure. This method is able to homogeneously distribute organic groups on the inner surface of the pores. Moreover, the morphology of the molecular sieves can be more easily controlled in comparison with the grafting [73].

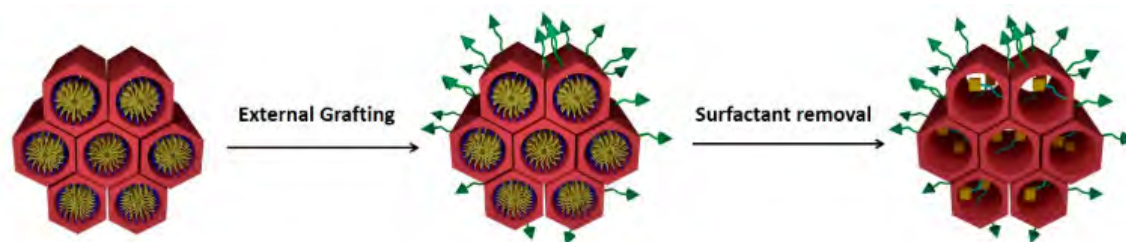


Figure 11. Regioselective di-functionalization of MCM-41 [76].

Nevertheless, either of the two methods has certain advantages. Grafting is a direct and fast modification of the surface of the MSN performed in one step. On the other hand, co-condensation leads to the formation of a homogeneous and uniform material.

1.4.2. MSN as drug delivery systems

The first report on the use of MSN for DDS was presented by the Vallet Regi group [78]. In this pioneering work, MCM-41 were loaded with ibuprofen. Then, the release of this drug was studied in a simulated body fluid. The authors showed that a proper tailoring of the molecular sieve allows control upon the cargo and release [78].

Generally, drugs are loaded inside the pores of the MSN by passive absorption. The mesoporous material is negatively charged due to the bulk hydroxyl groups of TEOS. Thereby, water-soluble positively charged molecules will be preferably loaded within the nanomaterial. Alternatively, the modification of the MSNs with functional groups such as carboxyl, phosphate, amine or sulfhydryl groups improve the adsorption of drugs with different charges into MSN [79]. As an example, DOX (**1**) was much better loaded within an MSN functionalized with $(\text{PO}_4)^{3-}$ than OH, COOH and NH_2 . This major loading is due to the significant interactions between this group and the drug [80].

Nonetheless, there are particular difficulties concerning the loading of hydrophobic drugs into the pores and on the surface of MSN. Typically, these drugs are dissolved in organic solutions and subsequently mixed with MSN dispersion. Finally, the MSN/drug complex formed is centrifuged to remove non-encapsulate drugs and vacuum dried to remove the undesired solvents. A major limitation of this procedure is the premature leakage of drugs before reaching the tumour site [81].

However, one of the main limitations that face MSN as DDS is the encapsulation of poorly soluble drugs, which may require the development of optimal methodologies to increase its loading such as adjustment of pH of the medium, contact time with the MSN, temperature and use of co-solvents [82]. This low loading implies the utilization of higher concentrations of nanocarrier, which can be harmful to patients, to obtain an appreciable therapeutic effect. Similarly, the

uncontrolled release of the therapeutic cargo before reaching the tumoral tissue can generate adverse side effects [83].

1.4.2.1. Design of an MSN as theranostic nanoplatform

Since the system described by Vallet Regi *et al.* [78] for the delivery of Ibuprofen, the control upon the release is one of the main challenges in the use of MSN as DDS. In this regard, the application of mechanical controls upon the pore openings have been broadly studied [84]. These mechanical control can be unlocked at will due to specific stimuli with the aim to selectively deliver the therapeutic cargo (Figure 12).

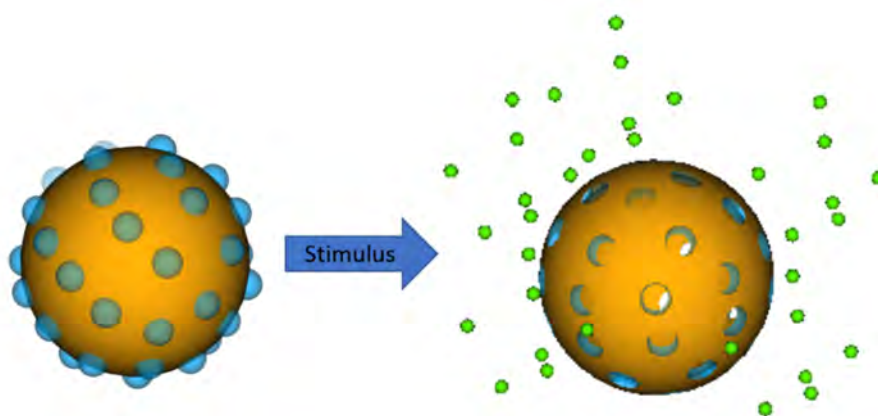


Figure 12. Nano gate triggered release by stimuli.

Two different strategies are employed in the designing of stimuli-responsive DDS:

- Endogenous stimuli: this type of stimuli is based on an internal/biological stimulus due to the diseased tissue such as dysregulation of pH, the high intracellular concentration of glutathione, reactive oxygen species, hypoxia and ATP concentrations [85]. Such microenvironment conditions can be cleverly exploited for enhancing drug action specificity by an appropriate selection of the DDS that will be prompt to be disrupted under these conditions, thus releasing the drugs [86].
- Exogenous stimuli: this type of stimuli are artificially applied from outside the tissue after administration of the DDS, and include temperature, light irradiation, ultrasounds and magnetic field [87]. The result of such action will eventually lead to the disruption of the system, releasing the entrapped cargo [86].

Table 1 classifies the different types of stimuli regarding its mechanism of action.

Table 1. Types of gate and stimulus.

Type of stimuli	Stimuli	Type of gates
Endogenous	Redox-Responsive	Disulphide linkage
	pH-Responsive	Hydrazone-linkage, Schiff base and carbamate
	Enzyme-Responsive	DDS degradation through different enzymes
	Ionic Microenvironment-Responsive	Acid or basic functional groups
Exogenous	Temperature-Responsive	Thermo-responsive polymers
	Photo/Light-Responsive	Photo-thermal effect, two-photon activation and upconverting nanoparticles
	Magnetic-Responsive	Hyperthermia and guided drug targeting (magnetic DDS)
	Ultrasound-Responsive	Disruption of the nanocarrier
	Electrical-Responsive	Oxidation-reduction reaction, disruption of the carrier and electrically disruption through temperature

However, among all the different stimuli-responsive possibilities presented in Table 1, pH-sensitive gates are commonly used due to the low pH value (pH 5.5-6) of cancerous cells [88]. The significant difference between numerous solid tumours and healthy tissue is the nutritional and metabolic environment [88]. The functional vasculature of tumours is often inadequate to supply the energy needs of the expanding population of tumour cells, leading to a deficiency of oxygen and many other nutrients. Thereby, the production of lactic acid under anaerobic conditions and the hydrolysis of ATP in an energy-deficient environment contribute to the acidic microenvironment [89]–[91].

Different strategies have been developed to control the release from MSN by applying mechanical controls over the pore openings. One of them implies the addition of bulky groups to block the pores mechanically (Figure 13 a)). For instance, Au or CdS nanocrystals can be located over the pore openings as gatekeepers for the encapsulated cargo. Then, the withdrawal of those groups via pH stimulus initiates cargo release [92]. An example of such a strategy was

used by Zhu *et al.* [93] and Du *et al.* [94] to preserve hydrophobic drugs within the pores of the MSN.

When these bulky groups are not covalently linked to the silica surface, they become nanomachines, such as “nanovalves” and “snap-top”. The main parts of these nanomachines are the static stalk, which is covalently attached to the surface of the particle, and a bulky cyclic moving component that is placed around the stalk *via* non-covalent interactions [95]. The pore opening is achieved by the large amplitude of motions between these two groups (Figure 13 b)) [95]. A considerable variety of nanovalves sensible to different stimuli have been synthesised. For instance, pH and redox stimuli sensitive nanovalves have been used to trigger the release of luminescent molecules for imaging [96], [97].

Another effective method to obtain a reliable pore capping is given by the coating of the MSN by polymers. These linkers can be either adsorbed or covalently bonded to the surface of the MSN. Polymers chains wrap around the particle surface, blocking multiple pores [98]. Later, under a particular stimulus, polymers can be detached from the silica framework liberating the cargo (Figure 13 c)) [98]. This strategy has been used to deliver chemotherapeutics drugs such as PTX or gentamicin properly stored within an MSN. When the polymeric layer degrades, the release of the cargo takes place [99]–[101].

Alternatively, a controllable release can be reached by forming chemical bonds directly onto the pore openings that can be cleaved upon stimulation (Figure 13 d)) [102]. For instance, glutathione sensitive bonds [103] are commonly used to the design of gatekeepers for drug delivery purposes along with acetals [104], imines [104] or hydrazones [105], [106]. Alkyl chains and sugars, containing a cleavable bond, have been functionalized on the MSN surface in order to preserve the cargo [107], [108]. Nevertheless, one of the most frequently functionalized moiety are PEGs chains [109]–[114]. These types of linkers enhance the biocompatibility, hydrophilicity, stability and biodegradability of the MSN. Besides, it offers sterical hindrance against other nanoparticles and blood components; hence its circulation time in blood stream is increased [115]. For instance, Li *et al.* [116] functionalized PEG chains on the silica surface by a disulphide bond with the aim to cap the pores and enhance the biocompatibility of the system. Subsequently, after a redox stimulus, the bond was broken releasing the cargo.

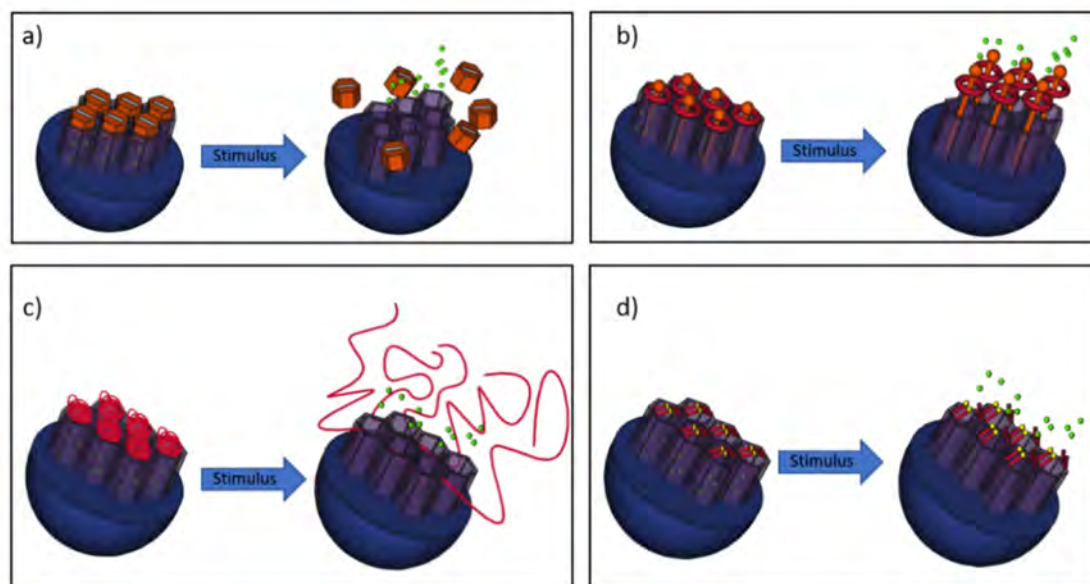


Figure 13. Relevant strategies for controlled release systems.

As has been stated, the design of the capping agent is essential to achieve a selective drug release. However, in some instances, the functionalization of this capping agents (amines groups) is crucial for the capping abilities of the system. In this regard, the end surface charge of functionalized moieties can play an essential role in the release trigger. This effect was studied by Martínez-Mañez *et al.* [117] who functionalized a series of alkyl chains on the pore outlets of mesoporous MCM-41. Besides, the researchers designed a dynamic simulation, where it was established that the presence of protonated polyamines induced a more effective obstruction of the pores due to the rigidity of the system than an alkyl chain of the same length (Figure 14).

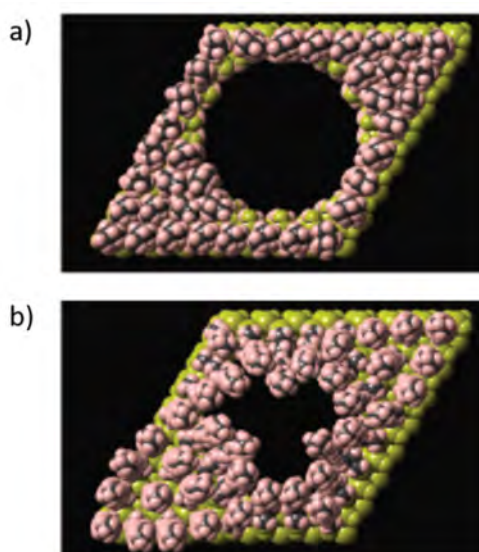


Figure 14. Simulation of MSN pore outlets functionalized with a) hexadecyl groups and b) protonated triamine $[-C_4H_8NH_2C_3H_6NH_2C_3H_6NH_2C_3H_7]^{3+}$ b). Reprinted with permission from [117]. Copyright 2012 American Chemical Society.

Another consideration of MSN as DDS is to deliver the drug to the target selectively. MSN can either accumulate in tumours passively or actively (Figure 15). Both approaches are able to deliver drugs specifically to the cancer cells and thus minimize the harmful toxicity to noncancerous cells [118].

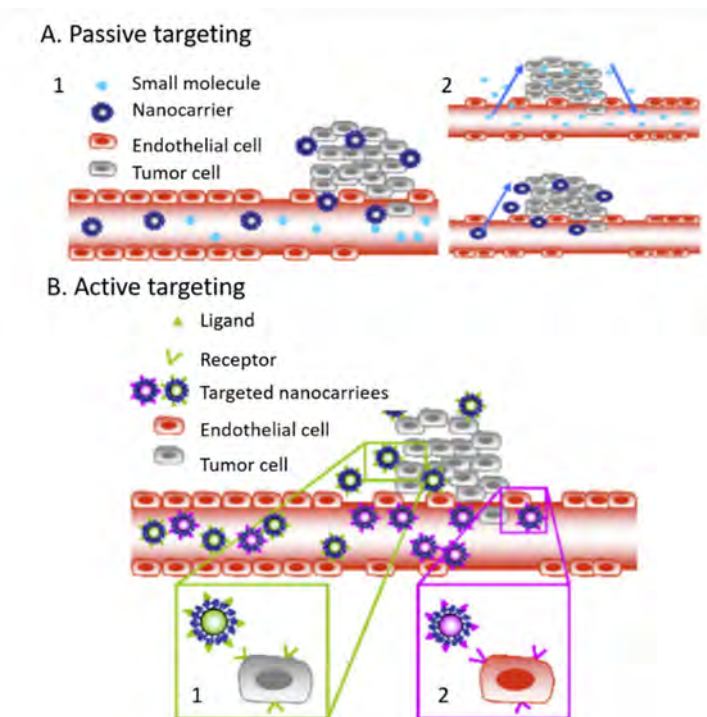


Figure 15. a) passive targeting and b) active targeting. Reprinted with permission from [119]. Copyright 2010 Elsevier.

Spontaneously, passive targeting is achieved by the accumulation of nanoparticles in the tumour tissue due to the EPR effect. Tumours higher than one cubic millimetre in size require oxygen and nutrient supply to proliferate at greater rates. Usually, their blood vessels are generally characterized by abnormalities such as the high proportion of proliferating endothelial cells, pericyte deficiency and aberrant basement membrane formation leading to an enhanced vascular permeability. Hence, macromolecules or nanoparticles can leave the blood vessels and accumulate in the adjacent tumour tissue but not in normal tissue [120].

It is noteworthy that among all the features present in an MSN, its shape, size and surface modifications are of great importance for passive targeting strategies [121]. As an example, to extravasate and accumulate inside the interstitial space, nanocarriers should have a size between 20 and 200 nm [119]. Besides, the nanoparticle shape also plays a key role in passive targeting. For instance, the best cellular uptake is achieved by MSN with a shape like rods and spheres, followed by cylinders and cubes. Curiously, the shape of the MSN can also show affinity towards a specific organ, thus a proper election of the MSN design must be considered [122].

Surface charge also influences nanoparticle uptake. Positively charged particles have been found to be taken up faster than neutral or negatively charged particles by cancerous cells. It is because the cellular membrane has a slightly negative charge and prefers binding of positively charged nanoparticles by electrostatic interaction [123].

On the other hand, as for active-targeting concern (Figure 15), ligands are attached at the surface of the nanocarrier with the aim to bind to appropriate receptors expressed in the cellular membrane. It is of great importance to choose a ligand to bind to a receptor overexpressed by tumour cells or tumour vasculature and not expressed by normal cells [119]. In this respect, different targeting moieties can be added to the MSN surface such as small molecules, short peptides, aptamers and whole antibodies or antibody fragments (Figure 16) [121].

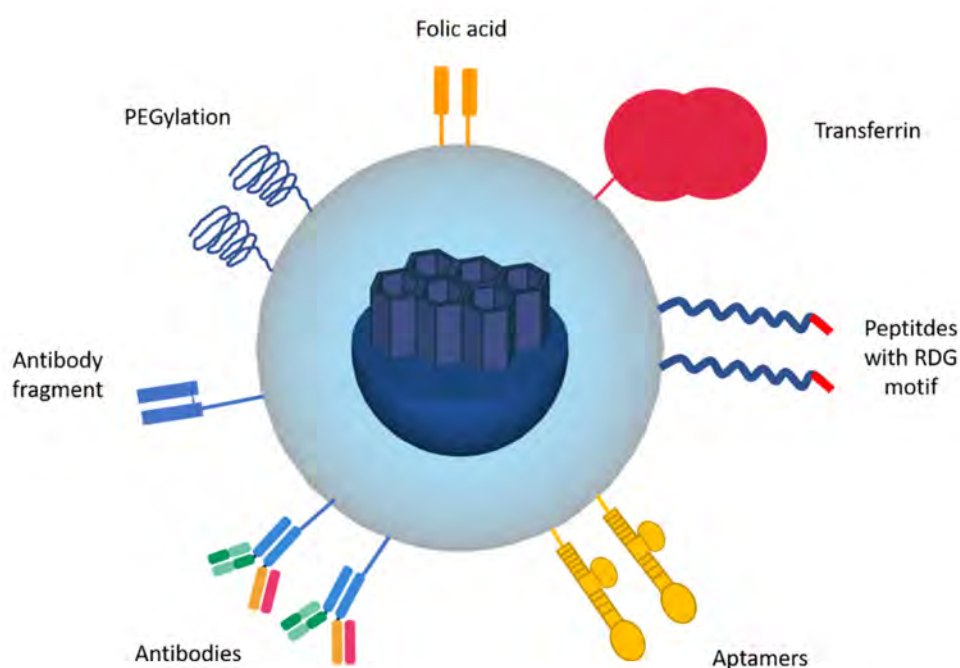


Figure 16. Ligands for active tumour targeting.

Folate receptor is commonly targeted because is overexpressed in many tumours in comparison with healthy tissues. Some authors have used it to selectively deliver chemotherapeutic drugs or siRNA to the target tissue [124], [125]. Similarly, hyaluronic acid (HA) has been used for its targeting properties as well as its biocompatibility and enzyme degradation [126]. The coating of MSN with this ligand shows selectivity towards cancerous cells that overexpress the CD44 receptor [127], [126]. Glycyrrhetic acid (GA) can be used as well as targeting ligand due to the abundant receptors that exist on the cellular membrane of hepatocarcinoma HepG2 cells [128]–[131]. This type of ligand has been used to enhance nanoparticle accumulation on HepG2 for DOX (**1**) delivery [132], [133]. A different approach is the use of glycoprotein transferrin to deliver DOX (**1**) in hepatocellular carcinoma cells [134]. Short peptides have also been

functionalized upon an MSN to improve the detection of tumour boundaries in magnetic resonance imaging [135]. But not only small molecules and peptides can be attached to the silica surface, complex molecules as aptamers can be used for tumour cell targeting. Aptamers are synthetic single-stranded DNA or RNA oligonucleotides that show affinity toward different targets such as nucleolin or epithelial cell adhesion molecule [136]. Ultimately, antibodies or antibody-fragments are also used for tumour targeting of DDS (Table 2) [121], [137].

Table 2. List of the approved antibodies for cancer therapy.

Antibody	Target
Cetuximab	Epidermal growth factor
Trastuzumab	Epidermal growth factor receptor 2
Bevacizumab	Vascular endothelial growth factor

1.4.2.2. Limitations and outlook of MSN as a theranostic agents

As it has been discussed up to now, a smart DDS based on MSN should meet two main prerequisites. First, MSN must preserve the cargo to avoid the premature leakage of the drugs before reaching the target side. Second, a high level of selectivity towards cancerous should be provided. The implementation of these two characteristics in an MSN entails a great level of complexity that usually implies a huge number of synthetic processes which could hamper the translation into the clinic.

An example of this complexity was reported by Song *et al.* [138]. The authors prepared a thermo/pH coupling sensitive polymer that acts as a “valve” to moderate the diffusion of drugs. Finally, folic acid was functionalized upon the polymer by a covalent bond to ensure target activity to the system. Surprisingly, the drugs were loaded after the assembling of the system. Hence low loading values were achieved, due to the decrease of the surface area by the introduction of the polymer and the ligand, folic acid. Even though the good targetability, the amount of therapeutic cargo was quite low producing an inefficient DDS. A different approach was proposed by Wang *et al.* [139] who first loaded DOX (**1**) inside the pores of the MSN achieving much better results than the previous authors. Later, the totality of the system was entrapped within a pH/reductive responsive chitosan particle in order to preserve the cargo. Lastly, FA was functionalized at the surface of the polymeric material. This approach is chemically complex and not efficient since covalent interactions were not present between the chitosan layer and the MSN. Thus, the system was not properly sealed and DOX (**1**) leakage occurred even at physiological pH or non-redox conditions. A similar problem was presented by

Zeng *et al.* [124]. The authors loaded DOX (**1**) inside the MSN and then wrapped it by the polymerization of dopamine, which is a pH sensible polymer. FA was functionalized on the polymer surface. Again, due to the low interactions between the MSN and the polymer, the release was uncontrollable at physiological pH.

To sum up, these nanocarriers still show serious issues to be used for its clinical applications. The integration between MSN and polymers is commonly used to build targeted DDS. Besides, more than 4 different steps are usually required in order to synthesise an MSN, which encompasses therapeutic cargo and targetability features. More importantly, the uncontrolled release of the drugs at physiological conditions completely hamper the use of this MSN as DDS. For all those reasons, the clinical translation of MSN is complicated because the system must assure low toxicity and immunogenicity in *in vivo* experiments. Besides, the lack of specific requirements for nanomedicine from FDA and the European Medicines Agency (EMA) compel that every novel nanocarrier must follow the same path as for small-molecules drugs, even if the transported drug alone has been already accepted for clinical use. This presumes that even the simplest nanocarrier encounters a lot of difficulties to get the market authorization [140].

1.5. Aims of the thesis

As has been depicted in section 1.1, although remarkable advancement in tumour biology and chemotherapy, adequate treatment of cancer is far from satisfactory. Insufficient drug dosage to the affected regions, rapid blood clearance, severe side effects and drug resistance are the main problems associated with these therapies. To overcome these drawbacks, a variety of nanoparticle-based drug delivery systems have been developed, including polymeric conjugates, micelles, liposomes, dendrimers and carbon nanotubes. In this regard, MSN present outstanding properties for drug delivery applications owing to their high specific surface area, uniform porosity, large pore volume, straightforward post-synthesis, and good biocompatibility. Such advantageous features have opened the door to the design of smart stimuli-responsive, which allows the selective release of the payload, DDS based on MSN. One of the most frequently investigated is the pH-triggered drug-delivery systems, which can respond to different pH values in diverse microenvironments. This type of strategy centers on constructing stable nanocarriers in blood circulation and then, due to a pH change, to release the cargo inside tumoral cells.

Nevertheless, the construction of this type of DDS is complex and requires the implementation of multiple steps in order to adequately preserve the cargo within the MSN and avoid the uncontrolled leakage before reaching the target side. Furthermore, such intricacy aggravates when more than one drug is ferried within an MSN with the aim to overcome the MDR effect.

Another important problem to consider is that only a partial amount of loaded drugs reach the target site due to some physiological limitations. Active targeting by using ligands attached to the DDS become such a good strategy to overcome these restrictions.

For this reason, in this PhD dissertation, it is proposed the synthesis of an easy to build pH-responsive DDS with the ability to co-deliver more than one drug selectively to the affected tissues employing a “radial-capping approximation” (Figure 17).

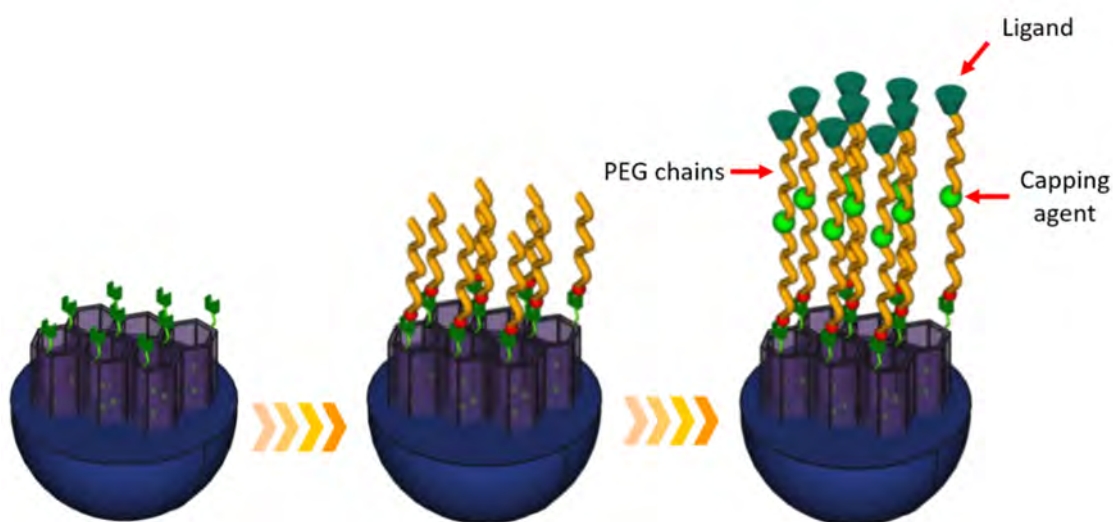


Figure 17. MSN representation following a radial-capping approximation.

This methodology proposed is simple; first, a hydrophobic drug could be loaded within the pores of the MSN. Then, PEG chains would be introduced onto the surface of the nanoparticle followed by a consecutive addition of a capping agent. Finally, the system would be completely assembled after the introduction of another PEG chain, which incorporates a ligand at its end. The breakthrough of this new approach is that the capping agent is indeed a drug. Thereby, the drug and the ligand will act as coating molecules as well as with their own activity. This new DDS would have the ability to co-deliver two drugs with different modes of action. This attribute opens the door to not only combine therapeutic agents but also combined therapies through the vehiculation of conjugates.

DOX (**1**) and CPT (**4**) have been reported to show a notably synergistic effect when they are administrated together (1.1.2). Thereby, their co-delivery by an MSN based on a radial-capping approximation is envisioned (Figure 17). However, it is anticipated low loading values of CPT (**4**) due to its insolubility. Thus, with the aim to overcome this drawback, TPT (**5**), which is a more soluble analogue of CPT (**4**), will be combined with DOX (**1**). Nevertheless, its low cytotoxicity prompts the synthesis of a prodrug of CPT (**4**). This new molecule will also be administrated with DOX (**1**). Lastly, the selectivity of this system towards hepatocarcinoma HepG2 cells will be

improved after the decoration of the MSN with the GA ligand. To do so, the ligand would be bonded over the capping agent, DOX (**1**), following the radial-capping approximation (Figure 17). On the other hand, the combination of a chemotherapeutic drug with a photosensitizer may become such a good alternative to overcome cancer. In this regard, the combined action of the ROS species, which are generated by light irradiation of a photosensitizer, together with the chemotherapeutic action of drugs **1** and **4** can induce different cytotoxic pathways, resulting in enhanced therapeutic efficacy. For this reason, it is proposed to co-deliver the latter drugs with a photosensitizer within an MSN to increase the chemo-photo activity of the treatment.

Therefore, the specific aims of this PhD thesis are summarized as follows:

1. To study the construction of a radial-capping system decorating the MSN surface with PEG chains to study the release behaviour of safranin.
2. To co-deliver DOX (**1**) and CPT (**4**) / TPT (**5**) employing the radial-capping approximation and to study its uptake and cytotoxicity in HeLa cells.
3. To develop a prodrug of CPT (**4**) with the aim to enhance its loading upon an MSN and to study its cytotoxicity effect with DOX (**1**) into two different tumoral cell lines.
4. To target HepG2 cells by means of a radial-capping construction upon an MSN using GA as a ligand to enhance tumour selectivity.
5. To develop a conjugate of CPT (**4**) able to enhance its solubility and deliver a photodynamic PS. Then, to study its loading upon an MSN and the cytotoxic effect in combination with DOX (**1**), and the uptake of this new MSN in HeLa cells.

Chapter 2. Results and discussion

Chapter 2. Results and discussion

2.1. Radial-capping of MSN with PEG chains

2.1.1. Introduction

One of the critical points for an efficient DDS based on MSN is its ability to deliver the chemotherapeutic drugs to the tumour tissue selectively. Thereby, it is of the paramount importance to preserve them inside the nanoparticles to prevent the possible side effects associated with the use of chemotherapeutic agents. To achieve this goal, the decoration of the MSN with PEGs chains has been proposed (1.4.2.1). Besides, it has been stated that this strategy enhances the colloidal stability of the system. In this regard, our group developed a radial-capping approach where a DOX-PEG moiety was introduced in the surface of an MSN (Figure 18). Preliminary studies showed a negligible release of the loaded drug (CPT (**4**)) and the drug at the surface of the MSN, DOX (**1**), at physiological pH.



Figure 18. MSN functionalized with DOX-PEG moiety.

This negligible release is rationalized in terms of the rigidity of the PEG chains. This effect is imparted by the presence of a protonated amino group of the DOX (**1**) drug. In fact, the zeta potential of this MSN was + 20 mV. Certainly, a possible explanation of this fact was found in a communication by Martínez-Mañez *et al.* [117]. As explained in section 1.4.2.1, these researchers run a computational simulation to study the capping behaviour of different alkyl chains attached to the pore outlets of the MSN. Their studies revealed that such linkers displayed high mobility due mainly to the lack of strong interactions between chains. Besides, they tend to freely and randomly move on the pore entrance only having occasional weak interactions with the neighbouring chains. As a result, the pore was in a continuous opening/closure process without altogether avoiding the release of the cargo. On the other

hand, a much better capping was obtained when a simulation was performed with protonated polyamines. The authors considered that such molecules strongly interact via electrostatic repulsion forces. The chains became rigid due to strong repulsive interactions between positively charged ammonium groups, which resulted in better pore coverage.

From these facts, it may be concluded that the behaviour displayed for the system represented in Figure 18 is strongly related to the presence of the protonated amino group of DOX, which is in agreement with the studies of Martínez-Mañez *et al.* [117]. Probably the PEG chains reorganize themselves in a rigid position preserving the cargo within the MSN. Therefore, to obtain further evidence of such hypothesis, a positive PEG chain (Figure 19 a)) and a neutral PEG chain (Figure 19 b)) of the same length have been functionalized to the MSN. Then, the capping capabilities of both systems have been tested, studying the release behaviour of a model drug.

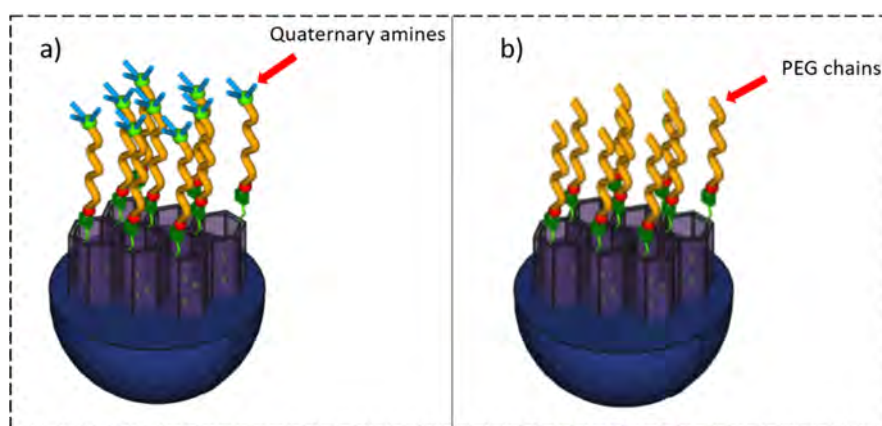


Figure 19. a) MSN capped with quaternary amines PEG chains and b) MSN capped with neutral PEG chains.

2.1.2. MSN capped with PEGs chains

To prove experimentally the results of Martínez-Mañez group, the synthesis of MSN decorated with PEGs **9** and **10** has been proposed (Figure 20).

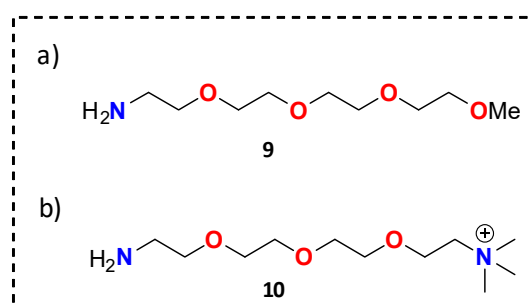


Figure 20. PEGs chains: a) 2,5,8,11-tetraoxatridecan-13-amine (**9**), b) 2-(2-(2-(2-aminoethoxy)ethoxy)ethoxy)-*N,N,N*-trimethylethanaminium (**10**).

Safranin (**11**) has been chosen as a model dye to be encapsulated within an MSN and study how its release is affected by the presence of the described PEGs (Figure 20). The decoration of the MSN with the PEGs **9** and **10** was carried out between the reaction of amine groups of the PEGs and isothiocyanate (NCS) groups, which are functionalized in the outer surface of the MSN. Our group developed a straightforward methodology to decorate aminated MSN with NCS [141]. Briefly, aminated MSN containing the surfactant (CTAB) ($\text{MSN}-(\text{NH}_2)_i(\text{CTAB})_o$) inside the pores were reacted with 1,1-thiocarbonyldi-2(1*H*)-pyridone (**12**) in dry toluene for 24 h [141]. Finally, the surfactant was removed in a mixture of NH_4NO_3 /methanol obtaining the $\text{MSN}-(\text{NH}_2)_i-(\text{NCS})_o$, which were satisfactorily synthesised and characterized [141]. Concisely, the $\text{MSN}-(\text{NH}_2)_i(\text{NCS})_o$ were spherical with a size of 100 nm.

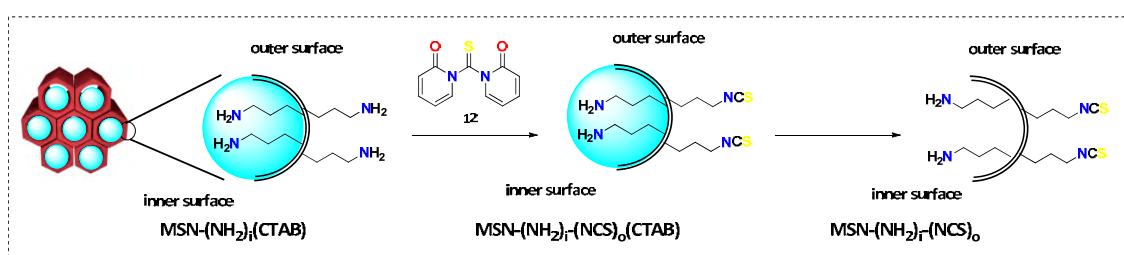


Figure 21. Regioselective synthesis of $\text{MSN}-(\text{NH}_2)_i-(\text{NCS})_o$.

Once in hand this nanomaterial, it was used to encapsulate safranin (**11**) as a model dye to study its release after the functionalization of $\text{MSN}-(\text{NH}_2)_i-(\text{NCS})_o$ with the amino PEGs (Figure 20). Briefly, $\text{MSN}-(\text{NH}_2)_i-(\text{NCS})_o$ were loaded with the dye by exposing the MSN to a solution of safranin (**11**) in EtOH. Then, the nanoparticles were reacted with PEGs **9** and **10** to seal the pores. Finally, the mixture was centrifuged and washed twice with ethanol. Thanks to the NCS chemistry, the only products present in the washing steps were the slight excess of the primary amine PEGs and the unloaded safranin (**11**) (Figure 22).

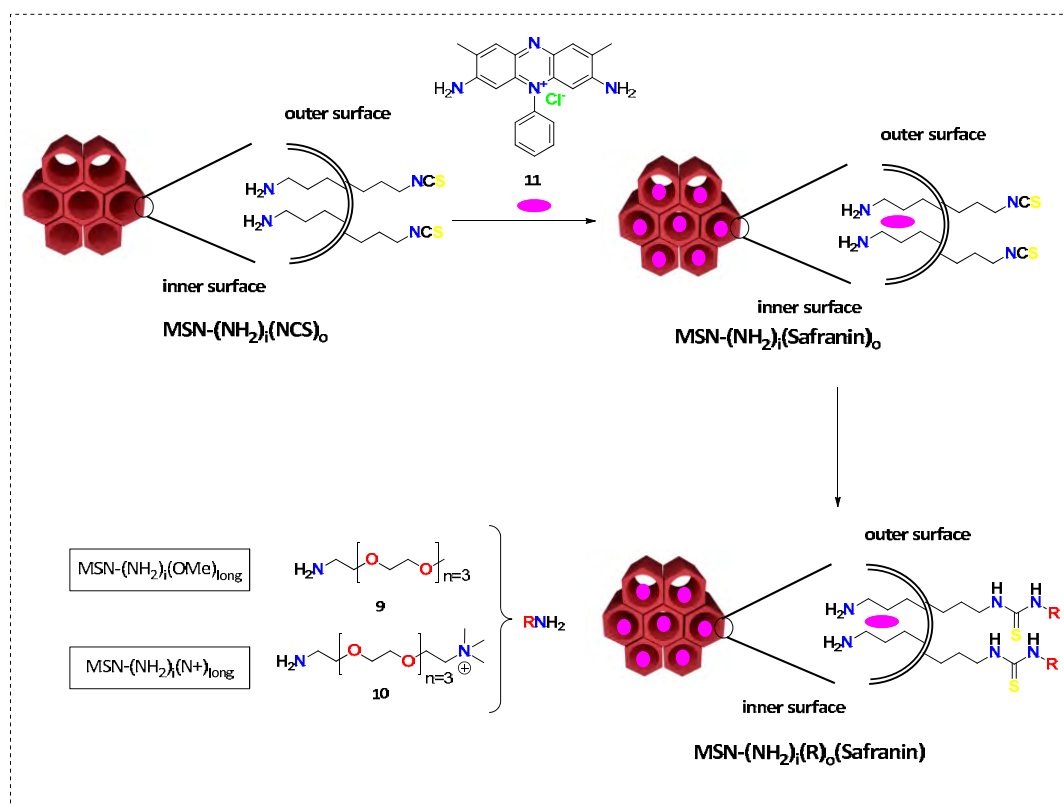


Figure 22. Loading of MSN-(NH₂)_i-(NCS)_o with safranin and functionalization with PEGs: 9 and 10.

Two different techniques showed the successful functionalization of the PEGs upon MSN. First, the infrared spectrum of MSN-(NH₂)_i-(NCS)_o and MSN-(NH₂)_i-(R)_o without the dye loaded were performed (Figure 23). The introduction of the isothiocyanate group was confirmed by the presence of two characteristic absorption bands around 2100 cm⁻¹ in the FTIR spectrum.

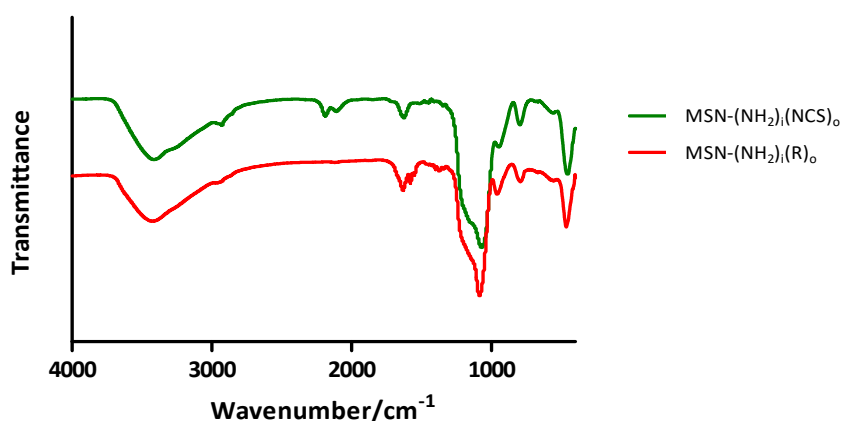


Figure 23. FTIR spectra of MSN-(NH₂)_i-(NCS)_o(CTAB), MSN-(NH₂)_i-(NCS)_o and MSN-(NH₂)_i-(R)_o.

Secondly, the disappearance of those bands validated the correct introduction of the PEGs 9 and 10 in the MSN (Figure 23). Moreover, the zeta potential of MSN-(NH₂)_i-(R)_o was also determined to analyse the contribution of the PEGs chains to the superficial charge of the MSN (Figure 24).

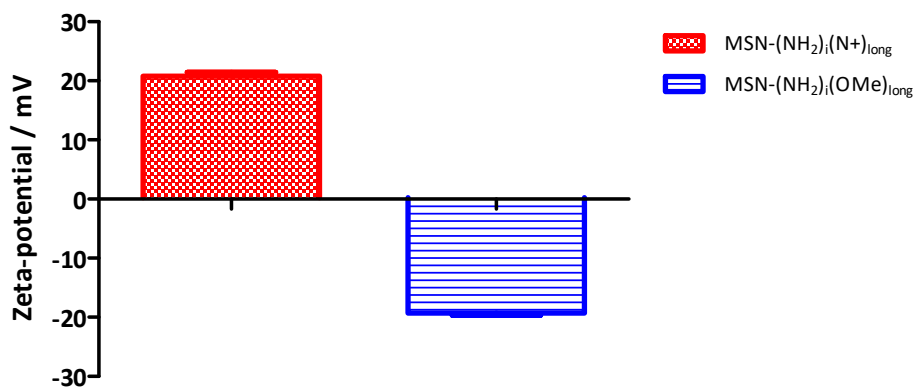


Figure 24. Zeta potential distribution of MSN-(NH₂)_i(N⁺)_{long} and MSN-(NH₂)_i(OMe)_{long}. Data represented as mean \pm SD ($n=3$).

From inspection of Figure 24, it can be concluded that the functionalization the MSN with a cationic PEG: MSN-(NH₂)_i(N⁺)_{long} highly increase the zeta potential value thanks to the presence of the quaternary amine at the end of the chain. Whereas, the functionalization with methoxy substituted PEG: MSN-(NH₂)_i(OMe)_{long} the mesoporous system experiment a high decrease of the zeta potential in comparison with the latter MSN.

Once MSNs were successfully functionalized with PEGs. The loading study of safranin (**11**) in the system and its subsequent release in a physiological medium (Figure 25) was performed. EtOH was used as a solvent and a 5% loading of the dye **11** was internalized within the pores of the MSN-(NH₂)_i(NCS)_o. Then, MSN were sealed through the addition amino PEGs **9** and **10** (Figure 22).

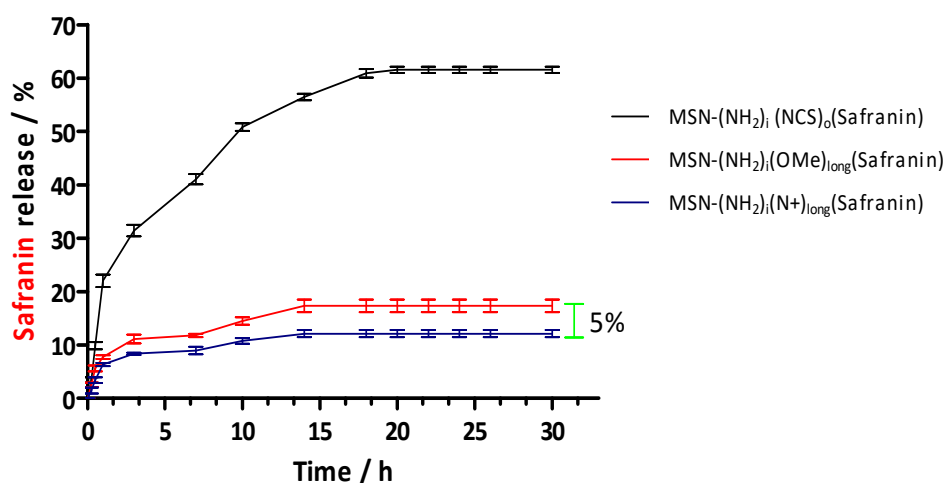


Figure 25. Release profile of Safranin: Aminated nanoparticles (MSN-(NH₂)_i(Safranin)_o), aminated nanoparticles functionalized with PEG **9** (MSN-(NH₂)_i(OMe)_{long}(Safranin)), aminated nanoparticles functionalized with PEG **10** (MSN-(NH₂)_i(N⁺)_{long}(Safranin)). Data represented as mean \pm SD ($n=3$).

The blocking effect of the amino PEGs **9** and **10** was clearly demonstrated by the release profile of safranin (**11**). For instance, non-functionalized MSNs show a safranin (**11**) release of 62% while

for MSN functionalized with PEGs: $(\text{MSN}-(\text{NH}_2)_i(\text{OMe})_{\text{long}}(\text{Safranin}))$ and $(\text{MSN}-(\text{NH}_2)_i(\text{N}^+)_{\text{long}}(\text{Safranin}))$ the release was just 17% and 12% respectively (Figure 25). From these results, it can be concluded that the presence of the quaternary amino PEGs improves in a 5% the capping capacity of the neutral PEG **10**. These results validate the hypothesis that cationic PEGs can cap better the pores than neutral PEGs.

2.1.3. Conclusions and Outlook

In summary, $\text{MSN}-(\text{NH}_2)_i(\text{NCS})_o$ have been satisfactorily loaded with a 5% of safranin (**11**) using EtOH as a solvent. Moreover, this MSN have been functionalized with primary amino PEGs chains to control the release of dye **11**. The proper introduction of these chains was corroborated by IR spectra and zeta potential measurements. MSN functionalized with cationic PEG chains show a highly positive zeta potential measurement (+ 20 mV), whereas functionalized MSN with methoxy (neutral) PEGs display a highly negative zeta potential measurement (- 20 mV). From release experiments, it was concluded that MSN decorated with cationic PEGs offered a better pore capping than neutral PEGs.

Hence, it seems reasonable to conclude that a quaternary amine may provide rigidity to the chains avoiding the open-closure motions due to the electrostatic repulsion of such groups (Figure 26 a)). Thereby, these results suggest that a similar effect is most likely to occur for the system with DOX-PEG moiety (Figure 26 b)). In addition, in this case, DOX (**1**) group does not only provides a cationic character to the capping, due to the presence of $-\text{NH}_2$ in the structure, but the bulkiness of the molecule also endows the stopper an improved capping efficiency.

Given these results, the radial capping system is validated for the design of DDS with a low drug leakage.

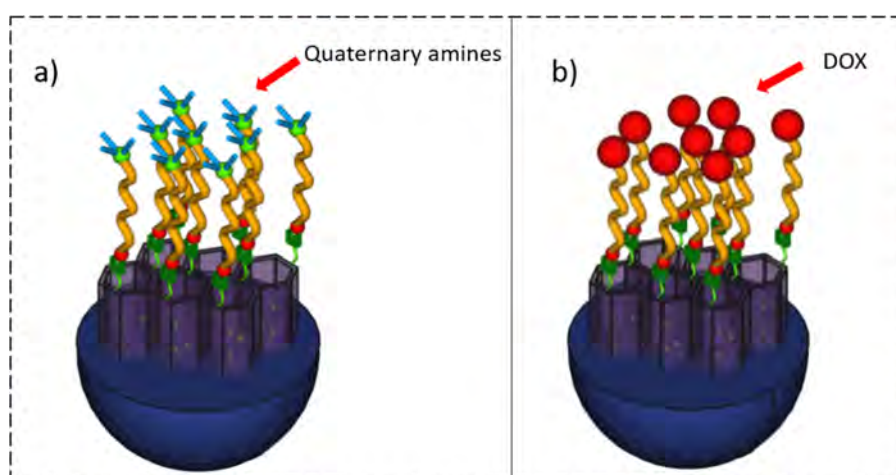


Figure 26. a) MSN capped with PEG/quaternary amines and b) MSN capped with DOX-PEG moiety.

2.2. Preparation of an MSN for dual DOX/CPT and DOX/TPT pH triggered delivery

2.2.1. Introduction

As has been stated in section 1.4.2, MSN have been used to deliver drugs to cancerous cells [142], [143]. However, the delivery of more than one drug has been scarcely described in the literature [3], [144]. In this regard, the development of the DOX-PEG moiety introduced in section 2.1, turns out to be such an ideal strategy to co-deliver more than one drug. As explained, the presence of the inner surface (pores) of the MSN lets the loading of any type of drug. Subsequently, the cargo is preserved after the functionalization of the pore outlets by the DOX-PEG moiety. In contrast to similar systems found in the literature [154],[155], this moiety efficiently capped the pores of the MSN thanks to the bulky group that represents the DOX (**1**) itself, together with the cationic character of the drug.

In particular, the combination of DOX (**1**) and CPT (**4**) has attracted considerable interest due to their potent inhibition of enzyme TOP1 and TOP2, respectively, leading to synergistic chemotherapy (1.1.3). Examples of such DDS have been reported in the literature [145]. However, the preparation of these systems is still complicated and entails the assembly of many different components that could hamper the practical use of these DDS. For this reason, our group developed a DDS able to co-deliver DOX (**1**) and CPT (**4**) through a pH-sensitive MSN (Figure 27) [74].

It is noteworthy that the cardiotoxicity side effect associated with the use of DOX (**1**) is diminished with this DDS. It is known that the two-electron reduction of the C-13 carbonyl group of the anthracycline side chain is the main rout of DOX (**1**) metabolism, supposedly implied in anthracycline-induced cardiotoxicity [146]. However, in the system proposed, this carbonyl group is linked with the PEG chain by a hydrazone bond (DOX-PEG moiety), inhibiting its cardiotoxicity issue (Figure 27).

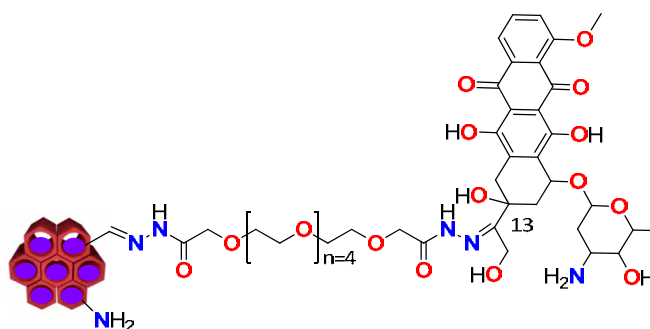


Figure 27. MSN for the codelivery of DOX (**1**) and CPT (**4**).

Moreover, in the design of this DDS, CPT (**4**) is encapsulated within the pores of the MSN in order to avoid the lactone opening. The opening of this ring leads to a less active and highly toxic drug [147]. It has been reported that the stability of the lactone form of CPT (**4**) strongly depends on the pH of the media (Figure 28) [147].

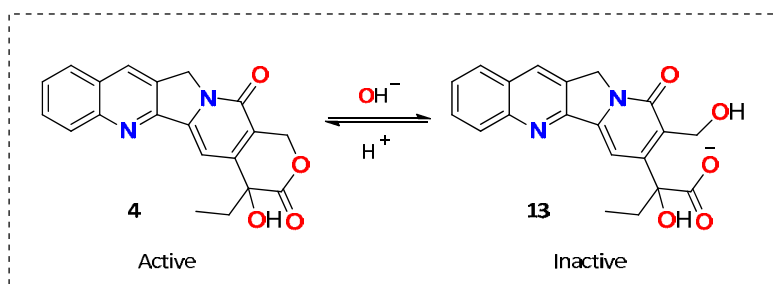


Figure 28. CPT (**4**) structure and equilibrium between the active lactone form and the inactive carboxylate form.

The preliminary results obtained by our group showed that the premature release of the hydrophobic CPT (**4**) at physiological pH (7.4) was avoided thanks to the proper capping with DOX (**1**) and its cationic character. Whereas at acidic pH, produced by tumoral cells, the MSN releases both drugs. However, the low loading of CPT (**4**) prompt us the preparation of a similar system with the more soluble TPT (**5**). This drug is a derivative analogue of CPT (**4**) that also acts as a DNA TOP1 inhibitor. It is expected that a higher amount of TPT (**5**) can be loaded in the MSN compared to CPT (**4**) [20], [148], [149].

Herein, in the present PhD dissertation, the dual DDS CPT (**4**) / DOX (**1**) has been used as a control to compare the effect of the enhanced solubility of TPT (**5**) in combination with DOX (**1**). The relative cell viabilities of these two DDS systems have been studied in HeLa cells. Furthermore, the cellular uptake of CPT (**4**) / DOX (**1**) DDS system have been studied in HeLa cells.

2.2.2. Preparation of MSN-(NH₂)_i(CHO)_o

The strategy developed by our group was based on a versatile system where a drug, in this case, CPT (**4**) or TPT (**5**), was loaded in an MSN. Then, a hydrolysable blocking linker was introduced and finally, DOX (**1**) was added to cap the system (Figure 29 a)). Two different components are needed in order to build the dual drug delivery system. First, a dihydrazide-polyethylene glycol linker **14** bonded with the MSN and DOX (**1**) by a pH scissile bond (hydrazone). Second, a bifunctionalized MSN with two different surfaces: the inner porous where CPT (**4**) or TPT (**5**) are loaded; and an aldehyde group located at the surface able to react with the PEG linker **14** (Figure 29 b)).

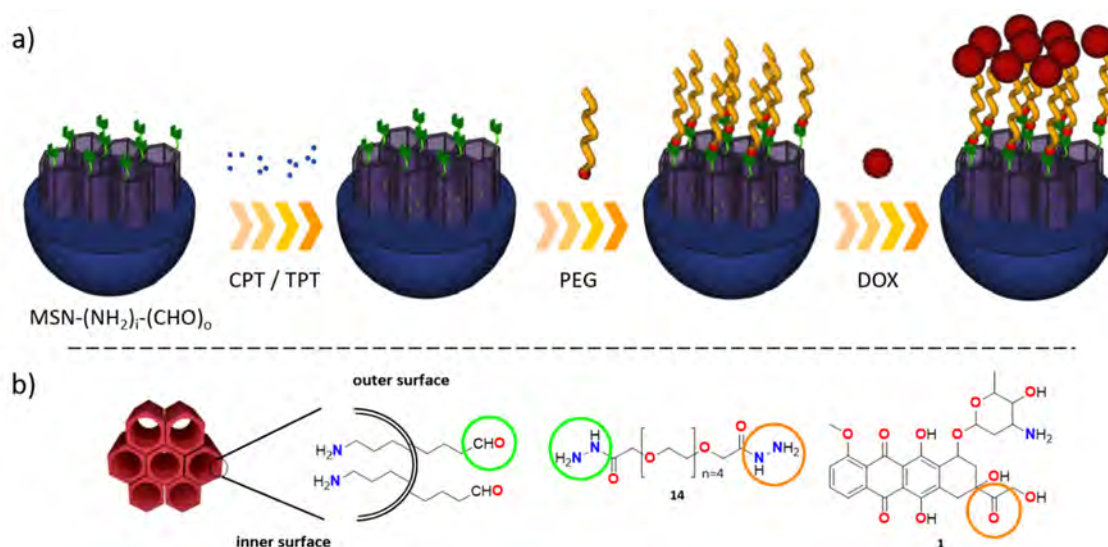


Figure 29. Dual DDS scheme.

Briefly, the preparation of amine-aldehyde MSNs requires two simple steps starting from MSN-(NH₂) (CTAB), which were reacted for 24 h with 2-isothiocyanate-1,1-dimethoxyethane (**15**) in toluene. It was important to perform this reaction using this solvent. Since under these conditions, the surfactant (CTAB) was preserved inside MSNs porous [150]. Afterwards, a treatment with NH₄NO₃ in EtOH removes the surfactant yielding MSN-(NH₂)_i(Acet)_o which was successfully transformed into the aldehyde group thanks to an acidic treatment affording the desired MSN-(NH₂)_i(CHO)_o (Figure 30).

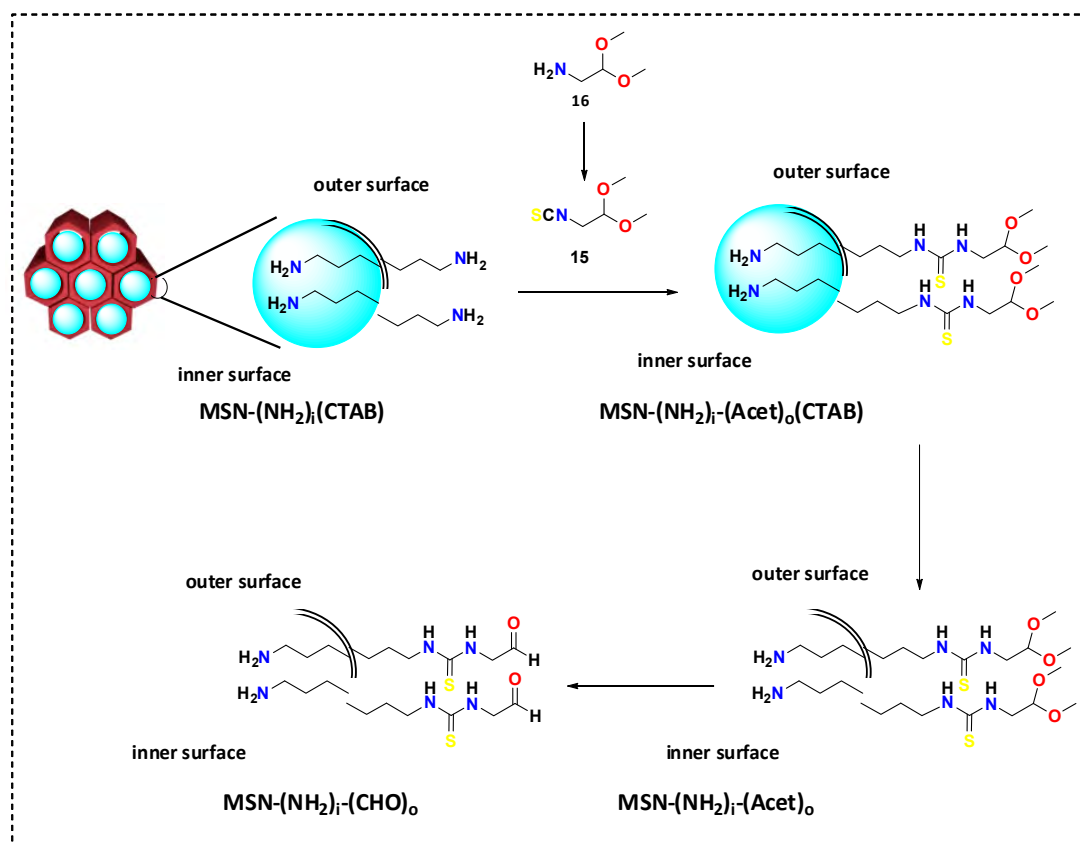


Figure 30. Synthesis of $\text{MSN}-(\text{NH}_2)_i(\text{CHO})_o$.

The as-synthesized bifunctionalized MSN were characterized [74], [151]. $\text{MSN}-(\text{NH}_2)_i(\text{CHO})_o$ had a size of 100 nm and zeta potential of -17 mV (Table 3). Moreover, the synthesized material was regular, homogeneous and round-shaped (Figure 31).

Table 3. $\text{MSN}-(\text{NH}_2)_i(\text{CHO})_o$ size and ζ potential (pH 5.5).

Size / nm	TEM	DLS	pdl	ζ -pot / mV
$\text{MSN}-(\text{NH}_2)$	100	142 ± 4	0.06 ± 0.02	-1 ± 4
$\text{MSN}-(\text{NH}_2)_i(\text{CHO})_o$	100	148 ± 5	0.19 ± 0.005	-17 ± 4

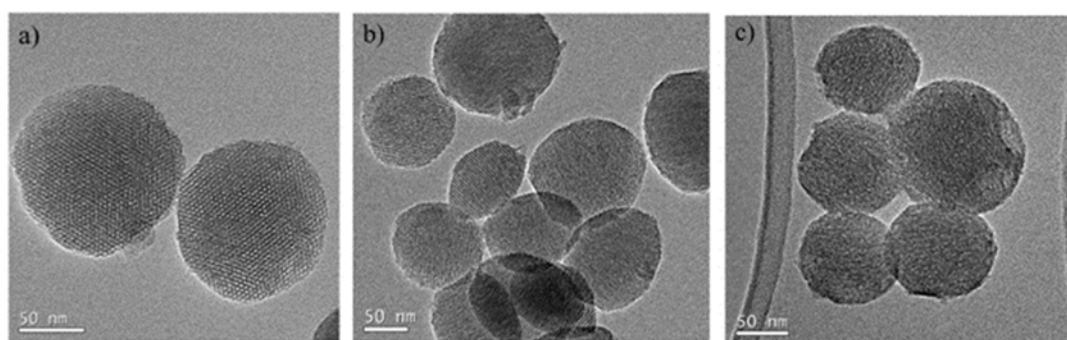


Figure 31. Transmission electron microscopy (TEM) micrographs of (a) $\text{MSN}-(\text{NH}_2)$, (b) $\text{MSN}-(\text{NH}_2)_i(\text{CHO})_o$ and (c) $\text{CPT@MSN-hyd-PEG-hyd-DOX}$ [151].

The next step entails the preparation of the requisite blocking linker. As explained before, a long dihydrazide polyethylene glycol chain (**14**) is believed to be an excellent blockage linker with the purpose of not only sealing the MSNs pores but also enhance the hydrophilicity of the nanoparticle in order to reduce the phagocytosis of macrophages [152]–[154]. In order to synthesize product **14**, tetraethylene glycol (**17**) is used as starting material, which by a nucleophilic substitution with ethyl bromoacetate (**18**) gives the diester PEG **19**. A final substitution with hydrazine results in the formation of 3,6,9,12,15-pentaoxaheptadecanedihydrazide (**14**) [155].

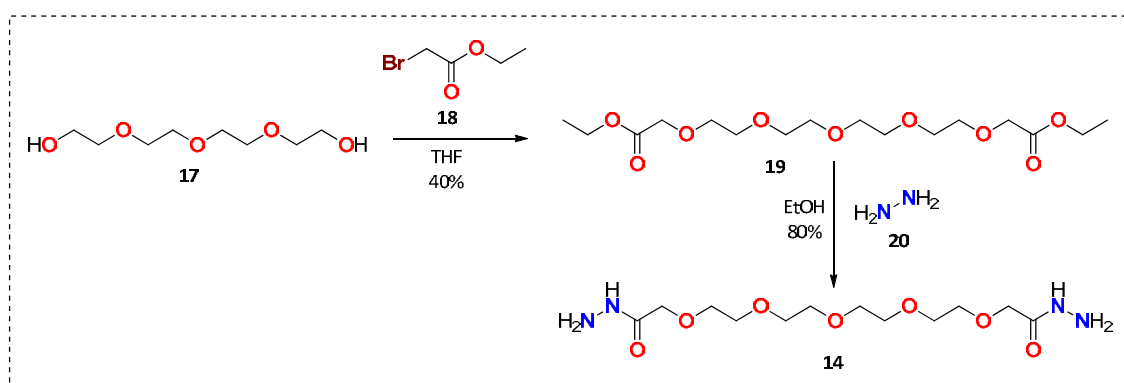


Figure 32. Schematic synthesis of 3,6,9,12,15-pentaoxaheptadecanedihydrazide (**14**).

2.2.3. Loading and release of the MSN

2.2.3.1. CPT / TPT and DOX loading

Once in hand, the vehicle and the capping linker, CPT (**4**) or TPT (**5**) was loaded inside the MSN porous. CPT (**4**) is a highly insoluble drug that is usually loaded using organic solvents such as MeOH, CHCl₃/MeOH, ACN/EtOH, DMSO and DMF [19], [93], [156]–[158]. In our hands, the mixture CHCl₃/MeOH allowed the most satisfactory loading, $1.36 \cdot 10^{-8}$ mol CPT·mg⁻¹ MSN, which corresponds to 3.1%. As for TPT (**5**), EtOH was used as a loading solvent achieving a value of $1.89 \cdot 10^{-7}$ mol TPT·mg⁻¹ MSN (8%). This TPT (**5**) loading value is in agreement with reported ones from literature [20], [159].

Then, an excess of PEG **14** was added to the solution in order to promote aldehyde MSNs reaction with only one of the terminal moieties of the linker to form a cleavable hydrazone bond. Afterwards, unreacted PEG **14** was eliminated by means of centrifugation to avoid any unwanted reaction in the next step. Finally, DOX (**1**) was added to the solution using EtOH as a solvent. This drug reacts with the other end of the PEG **14** chain yielding another hydrazone bond (Figure 27). Therefore, the systems CPT@MSN-hyd-PEG-hyd-DOX and TPT@MSN-PEG-hyd-DOX were

synthesized. Approximately, $7.06 \cdot 10^{-7}$ mol DOX·mg⁻¹ MSN were incorporated to the MSNs, which corresponds to 25%. In comparison with other hydrazone linkage systems, the values of DOX (1) loading that have been obtained are excellent [156], [160], [161]. Finally, the system CPT@MSN-hyd-PEG-hyd-DOX was characterized through TEM microscopy (Figure 31 (c)). The images confirm that the loading process did not erode the nanoparticles. Moreover, the mesopores of CPT@MSN-hyd-PEG-hyd-DOX were masked due to the drug loading and chemical modification of the surface.

2.2.3.2. Controlled drug release

The release profile of CPT (4) and TPT (5) from CPT@MSN-hyd-PEG-hyd-DOX and TPT@MSN-hyd-PEG-hyd-DOX were studied by UV-vis absorption spectroscopy at pH values of 4.0, 4.5, 5.5, 6.5 and 7.4 (Figure 33 a) and b)).

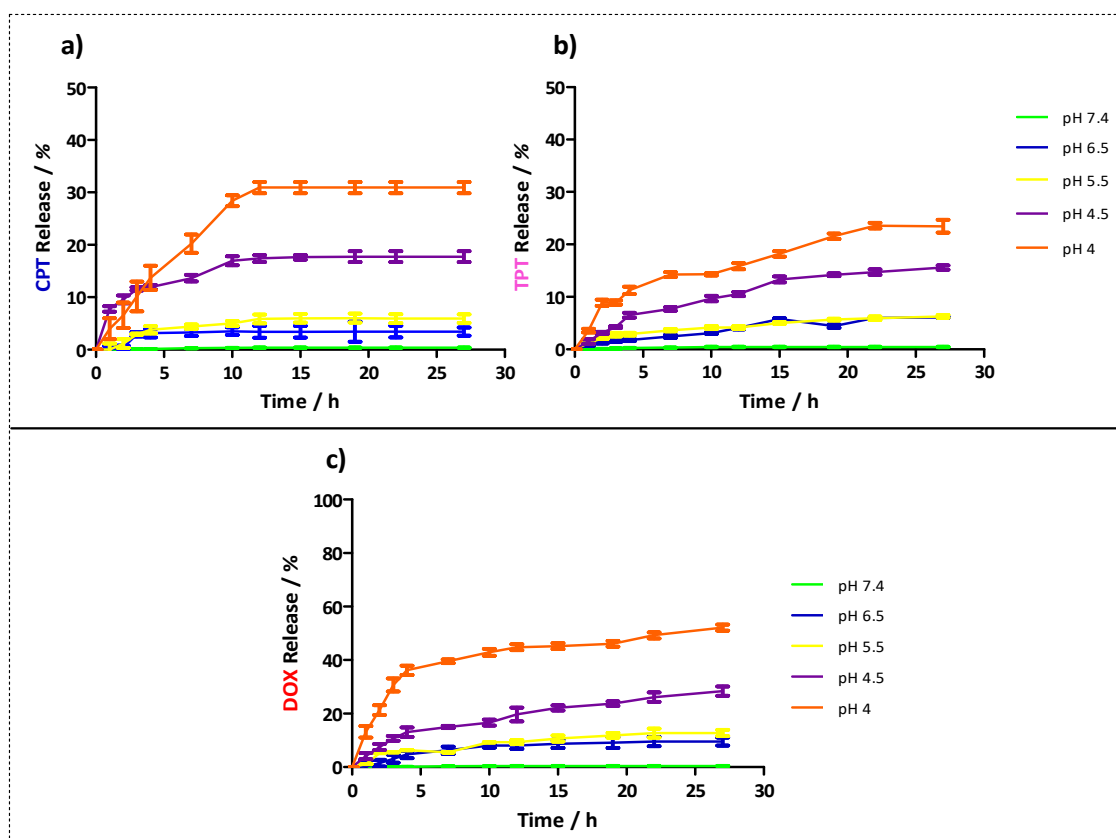


Figure 33. a) CPT (4), b) TPT (5) and DOX (1) release profile of CPT@MSN-hyd-PEG-hyd-DOX and TPT@MSN-hyd-PEG-hyd-DOX at different pH values under stirring at 100 rpm and $t=37$ °C. Data represented as mean \pm SD ($n=3$).

Both systems show a negligible release of CPT (4) and TPT (5) under neutral physiological conditions (pH 7.4) proving the stability of the hydrazone bond under this environment. Then, a gradual release was obtained under acidic conditions which agrees with the scission of the labile bond. Besides, this sustained-release might be ascribed to the physical absorption of the drug

inside the nanochannels [162]. Moreover, as has been demonstrated in section 2.1, DOX (**1**) plays a key role in the capping of the nanoparticle, since its presence would lead to a rigid tetraethylene glycol chains, due to the bulkiness of the molecule and the repulsive interaction between ammonium groups, providing an efficient pore closure.

CPT (**4**) release profile suggests that there is a burst release for 10 h, then it is maintained till 24 h. On the other hand, for TPT (**5**), the release was sustained for up than 24 h. These results suggest that TPT (**5**) release profile is governed by its higher solubility. Furthermore, the maximum amount of CPT (**4**) and TPT (**5**) liberated was determined at pH 4.0 for 24 h. Under these conditions, 31% and 23% of CPT (**4**) and TPT (**5**) were liberated respectively. These percentages correspond to 0.009 mg CPT·mg⁻¹ MSN and 0.018 mg TPT·mg⁻¹ MSN. Therefore, more TPT (**5**) was satisfactorily released in the medium than CPT (**4**) due to his high solubility that permits a better loading within an MSN.

On the other hand, DOX (**1**) release from CPT@MSN-hyd-PEG-hyd-DOX and TPT@MSN-hyd-PEG-hyd-DOX was also studied under the same pH conditions as CPT (**4**) and TPT (**5**) (Figure 33 c)). Under acidic conditions, a burst release of DOX (**1**) takes place with approximately 45%, 25% and 10% of the drug released within 20 h at pH 4.0, 4.5 and 5.5 respectively. It was hypothesized that this rapid release coincides with the cleavage of the hydrazone bond. It is worth noting that the DOX (**1**) release for the systems CPT@MSN-hyd-PEG-hyd-DOX and TPT@MSN-hyd-PEG-hyd-DOX was mostly the same due to the similarities of both systems.

2.2.4. Intracellular uptake

Uptake experiments were only performed for CPT@MSN-hyd-PEG-hyd-DOX due to the enormous resemblances with the MSN loaded with TPT (**5**) (TPT@MSN-hyd-PEG-hyd-DOX). To this end, cellular uptake and drug release were investigated by confocal laser microscopy (CLSM). To do so, a homogeneous suspension of CPT@MSN-hyd-PEG-hyd-DOX (50 µg MSN·mL⁻¹) was added to HeLa cells. After four hours of incubation blue and red fluorescence were observed in cell bodies, suggesting an efficient uptake and subsequent release of both drugs from the nanovehicle (Figure 34 b) and c)). On the other hand, Figure 34 d) illustrates merged fluorescence of DOX (**1**) and CPT (**4**), indicating the co-delivery of both drugs into the cells. As expected, free DOX (**1**) easily enters HeLa cell nucleus (Figure 34 c) yellow arrows), which is in agreement with the preferential accumulation of DOX (**1**) in this organelle [163]. These results demonstrate that after the uptake of the nano-vehicle DOX (**1**) was released by hydrolysis of the hydrazone bonds in response to the acidic environment found in the cell. By contrast, blue fluorescence of CPT (**4**), which has been released by diffusion from the pores of the nanoparticle, was only detected in the cytoplasmic matrix (Figure 34 b)).

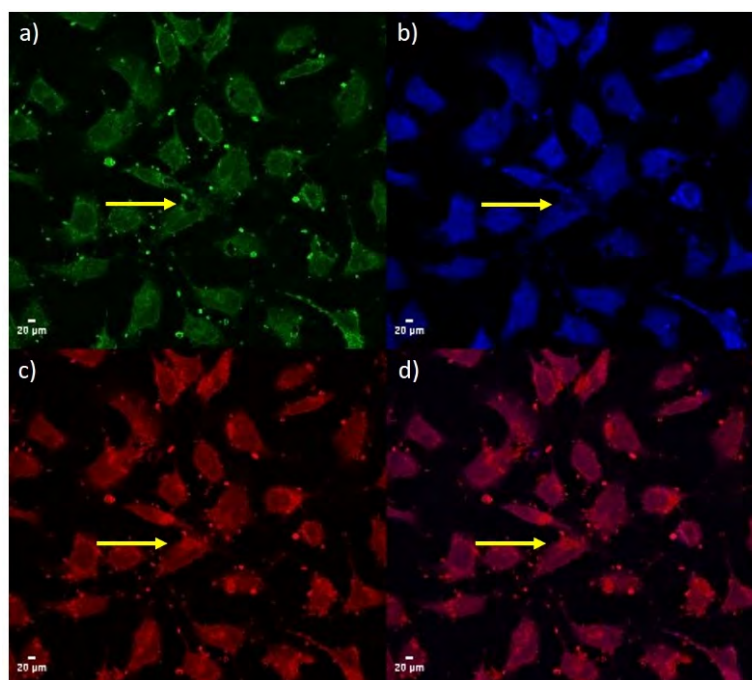


Figure 34. CLSM images of the uptake of CPT@MSN-hyd-PEG-hyd-DOX scale bar 20 μm . a) corresponds to fluorescein diacetate (FDA) fluorescence, b) CPT (**4**) fluorescence, c) DOX (**1**) fluorescence and d) DOX (**1**) and CPT (**4**) merged images [151].

Further confirmation of this efficient uptake of the DDS was obtained by flow cytometry (Figure 35). As depicted in section 1.4.2.1, highly positive surfaces can easily disrupt the negatively charge cytoplasmatic membrane due to electrostatic interactions. For this reason, it was hypothesized that the uptake of CPT@MSN-hyd-PEG-hyd-DOX was influenced and enhanced by the presence of at least partially protonated amino groups bonded to the sugar moiety of DOX (**1**), which was attached to the surface of the nanoparticle [164]. This hypothesis is consistent with the highly positive ζ -potential value measured for CPT@MSN-hyd-PEG-hyd-DOX (+ 20 mV).

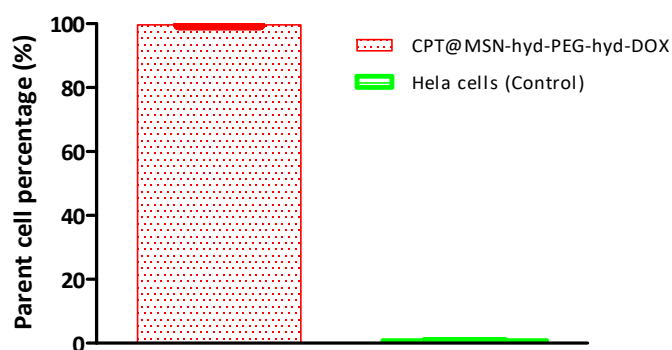


Figure 35. Flow cytometry analysis of the internalization of DOX (**1**) into HeLa cells using CPT@MSN-hyd-PEG-hyd-DOX. Data represented as mean \pm SD ($n=3$).

To gain insight into the uptake of CPT@MSN-hyd-PEG-hyd-DOX into HeLa cells the kinetics of the release of DOX (**1**) were studied using an IncuCyte[®]S3 live-cell analysis system. Thus,

monitoring DOX (1) fluorescence inside the cells revealed that after an incubation period of 3-4 h, an increase of the drug content took place (Figure 36 a) and b)).

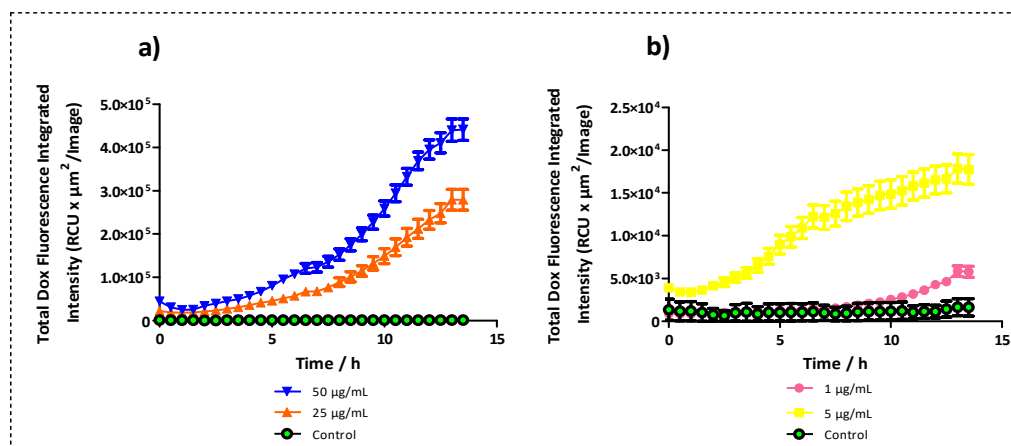


Figure 36. DOX (1) release kinetics in HeLa cells. Data represented as mean \pm SD ($n=3$) [151].

This initial period was ascribed to the uptake of the nanoparticle by the cell. Afterwards, a sustained increase of DOX (1) fluorescence during 14 h was observed and after a period of 25 h, cell death could be easily detected by inspection of the micrographs (Figure 37 c) and f)).

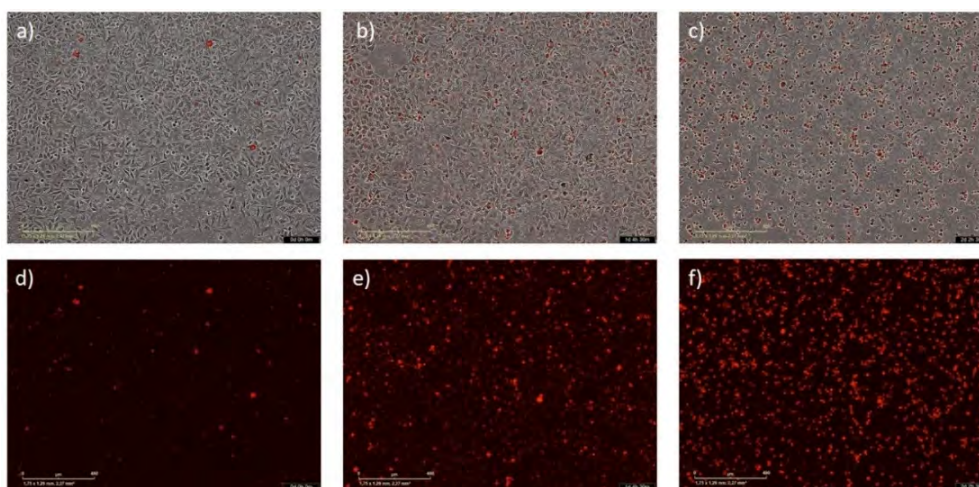


Figure 37. IncuCyte® images of CPT@MSN-hyd-PEG-hyd-DOX scale bar 400 μm . a), b) and c) corresponds to the bright field at 0 h, 25 h and 50 h, respectively. d), e) and f) corresponds to the red field at 0 h, 25 h and 50 h, respectively [151].

Furthermore, BIO-TEM was used to verify the intracellular uptake of individual nanoparticles (1) (Figure 38). As it can be observed in Figure 38 a), the endocytosed nanocarrier was principally accumulated within endosomes and/or lysosomes in the cytosol (2) of the cell. The confinement of the nanoparticles in such organelles would explain the acid hydrolysis of the hydrazone bonds which is responsible for the release of the drugs from the DDS. Although many groups of nanoparticles could be seen distributed around the nucleus (3), no nanoparticles appeared to be able to enter into this organelle. This is in agreement with reports that indicate the

impossibility of nanoparticles with a diameter over 100 nm to cross the nuclear membrane [165]. Figure 38 b) shows a cluster of nanoparticles that have escaped from the endosome, probably via cellular “sponge effects”, and entered into the cytoplasm. It is worth noting that the internalized nanoparticles still kept their spherical shape and structural integrity. Interestingly, in some micrographs, it was possible to observe characteristics ruffles of the plasma, suggesting an endocytosis process (Figure 38 c)).

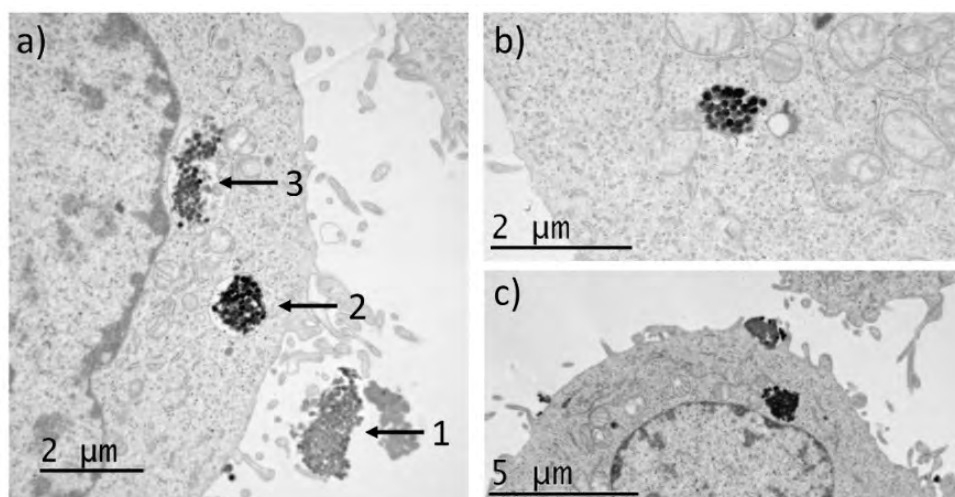


Figure 38. a) TEM images of HeLa cells incubated for 4 h with $50 \mu\text{g}\cdot\text{mL}^{-1}$ of CPT@MSN-hyd-PEG-hyd-DOX b) a cluster of nanoparticles that have escaped from the endosome c) internalization of the nanoparticles [151].

2.2.5. Cytotoxicity

To assess the cytotoxicity of CPT@MSN-hyd-PEG-hyd-DOX and TPT@MSN-hyd-PEG-hyd-DOX caused by the co-delivery of the drugs: CPT (**4**)-DOX (**1**) and TPT (**5**)-DOX (**1**), MTT assays in HeLa cell lines were carried out. Therefore, two control nanoparticles MSN-(NH₂) and MSN-(NH₂)(CHO)₆ were tested against drug-loaded nanoparticles: CPT@MSN-hyd-PEG-hyd, TPT@MSN-hyd-PEG-hyd, MSN-hyd-PEG-hyd-DOX, CPT@MSN-hyd-PEG-hyd-DOX and TPT@MSN-hyd-PEG-hyd-DOX at 1, 5, 25, 50 and 100 µg MSN·mL⁻¹ were added and incubated with the cells for 72 h (Figure 39).

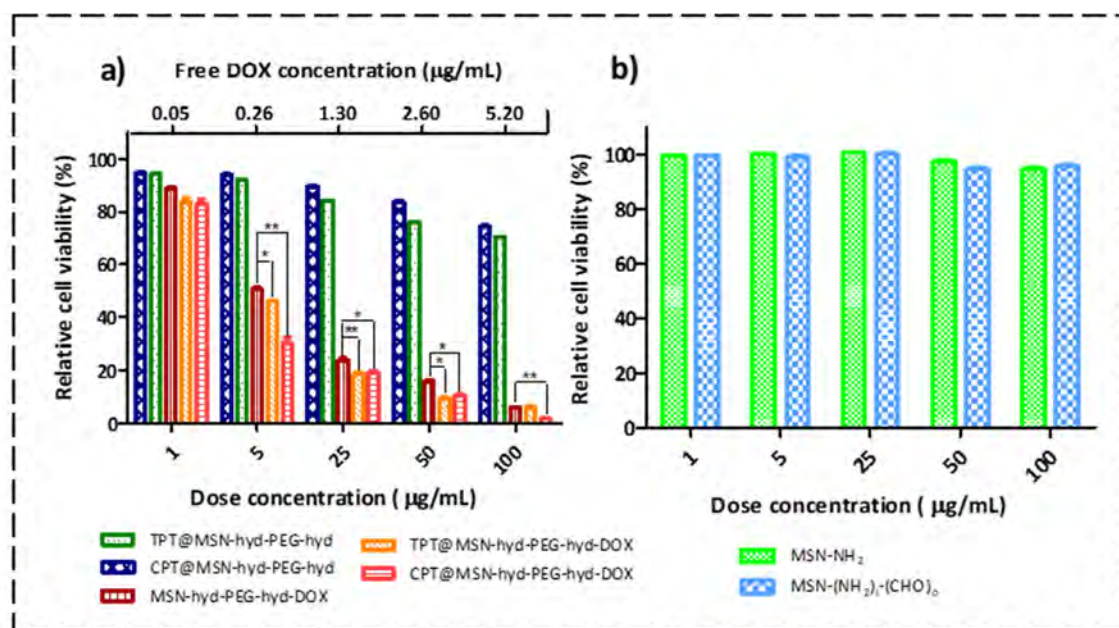


Figure 39. Cell viability of HeLa cells incubated with a) TPT@MSN-hyd-PEG-hyd, CPT@MSN-hyd-PEG-hyd, MSN-hyd-PEG-hyd-DOX, TPT@MSN-hyd-PEG-hyd-DOX and CPT@MSN-hyd-PEG-hyd-DOX and b) MSN-(NH₂) and MSN-(NH₂)₆(CHO)₆ for 72 h. Data represented as mean ± SD (n=3), *p<.05 and **p<.01. The concentration of free DOX (**1**) is the released drug at pH 5.5.

The viability assays revealed that control nanoparticles (Figure 39 b)) have no apparent toxicity on HeLa cells in a range of concentrations from 1 to 100 µg·mL⁻¹. Interestingly, DDS without any drug (MSN-(NH₂)₆(CHO)₆) shows viabilities higher than 90%, thus meaning that all the cytotoxic effect seen with CPT@MSN-hyd-PEG-hyd-DOX and TPT@MSN-hyd-PEG-hyd-DOX was solely due to the CPT (**4**) or TPT (**5**) and DOX (**1**) released from the DDS. Therefore, these DDS can be regarded as biocompatible.

By contrast, DOX (**1**) loaded MSN-hyd-PEG-hyd-DOX, reduces the viability of HeLa cells to 6% at doses of 100 µg·mL⁻¹. For this system, the half-maximal inhibitory concentration (IC₅₀) was 5 µg·mL⁻¹. This value is in the same order of magnitude of that of free DOX (**1**) (IC₅₀ 1.2 µg·mL⁻¹) [166]. But more importantly, it was found that the effect of the CPT (**4**)/ DOX (**1**) loaded

nanocarrier CPT@MSN-hyd-PEG-hyd-DOX was an increase in the cell death compared with nanoparticles loaded with DOX (**1**) (Figure 39 a)). For instance, cell viability at $5 \mu\text{g}\cdot\text{mL}^{-1}$ decrease from 50% (MSN-hyd-PEG-hyd-DOX) to 28% (CPT@MSN-hyd-PEG-hyd-DOX). However, the effect of the reduction in the relative cell viability in the case of TPT@MSN-hyd-PEG-hyd-DOX is less mark than CPT@MSN-hyd-PEG-hyd-DOX due to the higher IC_{50} of TPT (**5**) ($0.32 \mu\text{g}\cdot\text{mL}^{-1}$) in comparison with CPT (**4**) ($0.008 \mu\text{g}\cdot\text{mL}^{-1}$) [167], [168].

The calculated value of IC_{50} for CPT@MSN-hyd-PEG-hyd-DOX and TPT@MSN-hyd-PEG-hyd-DOX is $1.88 \mu\text{g}\cdot\text{mL}^{-1}$ and $5.30 \mu\text{g}\cdot\text{mL}^{-1}$ respectively. At those concentrations, the amount of free DOX released is $0.09 \mu\text{g}\cdot\text{mL}^{-1}$ (CPT@MSN-hyd-PEG-hyd-DOX) and $0.28 \mu\text{g}\cdot\text{mL}^{-1}$ (TPT@MSN-hyd-PEG-hyd-DOX) for the corresponding systems. The later values were calculated as the release of the drug at pH 5.5, which is the average pH found in the late-endosomes and lysosomes. At the same pH conditions, the calculated combination index (CI) value is 0.14 (at IC_{50}) for CPT@MSN-hyd-PEG-hyd-DOX and 0.31 (at IC_{50}) for TPT@MSN-hyd-PEG-hyd-DOX. These values are consistent with a synergistic interaction of the drugs and confirmed that the system CPT@MSN-hyd-PEG-hyd-DOX is more cytotoxic than TPT@MSN-hyd-PEG-hyd-DOX.

It is noteworthy that the systems CPT@MSN-hyd-PEG-hyd and TPT@MSN-hyd-PEG-hyd show non-significant toxicity in HeLa cells in comparison to the DOX-PEG functionalized systems. It is hypothesized, that cellular uptake of these MSN is hampered due to the presence of the neutral PEG chain (**14**) functionalized in the outer surface of the nanoparticle. It has been described in the literature that such systems cannot enter into the cells [169], hence the viability of the cell is not affected by CPT (**4**) or TPT (**5**).

Interestingly, the combined effect of the two systems (CPT@MSN-hyd-PEG-hyd-DOX and TPT@MSN-hyd-PEG-hyd-DOX) increases with time. Thus, at 24 h the effect of the combined treatment on cell death was mostly the same that was displayed in the presence of DOX (**1**) alone. However, at 48 h and more clearly at 72 h, cell viabilities decrease significantly. This delayed effect of CPT (**4**) and TPT (**5**) can be ascribed to the slow release of the drug from the pores (Figure 40). Similar results describing this time dependency synergism for co-delivery systems have been reported in the literature [170], [171]. All these observations are consistent with a combined effect between these two drugs and proves the successful co-delivery of DOX (**1**) and CPT (**4**)/TPT (**5**) to the cells [172], [173].

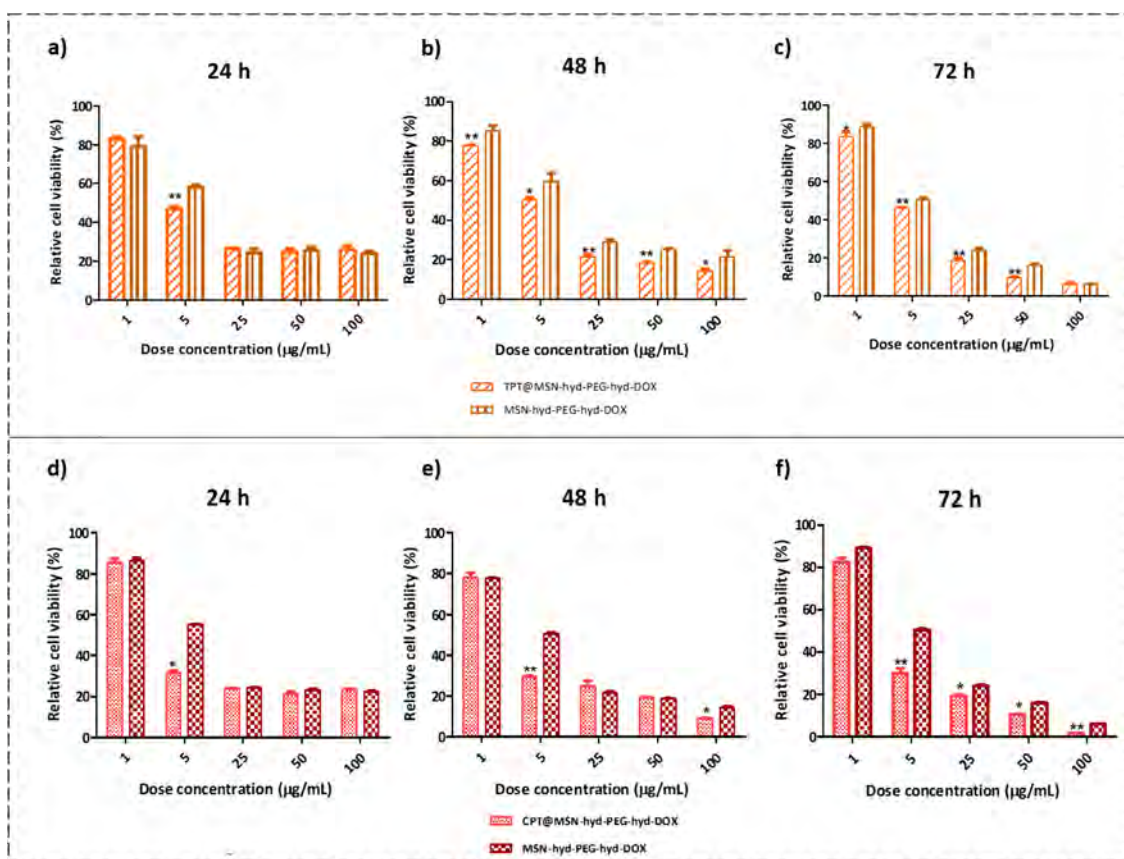


Figure 40. Cytotoxicity effect of a), b) and c) of TPT@MSN-hyd-PEG-hyd-DOX and MSN-hyd-PEG-hyd-DOX; d), e) and f) of CPT@MSN-hyd-PEG-hyd-DOX and MSN-hyd-PEG-hyd-DOX. Data represented as mean \pm SD ($n=3$), * $p < 0.05$ and ** $p < 0.01$.

2.2.6. Conclusions and Outlook

Bifunctionalized amino-aldehyde nanoparticles (MSN-(NH₂)_i(CHO)_o) of 100 nm have been synthesised for the dual vehiculation of CPT (**4**) / TPT (**5**) and DOX (**1**). A 3.1% of hydrophobic CPT (**4**) was successfully loaded within the pores of the MSN, while 8% of TPT (**5**) was as well internalized. Finally, the system was completed after the addition of PEG **14** and DOX (**1**) (25% loaded). The systems CPT@MSN-hyd-PEG-hyd-DOX and TPT@MSN-hyd-PEG-hyd-DOX are stable under physiological conditions (pH 7.4) with a negligible release of either CPT (**4**) / TPT (**5**) or DOX (**1**). On the other hand, under acidic conditions, a burst release of capping agent DOX (**1**) took place during the first 5 h. Besides, a more sustainable release was obtained for CPT (**4**) and TPT (**5**).

Even though more TPT (**5**) (0.018 mg TPT·mg⁻¹ MSN) was released in the medium than CPT (**5**) (0.009 mg CPT·mg⁻¹ MSN) at pH 4, its combined cytotoxicity with DOX (**1**) was lower than CPT (**4**). These results reflect the higher potency of CPT respect to TPT.

Additionally, this versatile nanocarrier has been proven to effectively enter inside HeLa cells and release the drugs inside them. In addition, BIO-TEM micrography has shown that MSN were accumulated within endosomes and located around the nucleus.

After this biological study, it can be stated that this dual DDS based on MSN is able to deliver CPT (**4**) / TPT (**5**) and DOX (**1**) in HeLa cells. Moreover, it was determined that the CPT (**4**) still provide a better synergistic effect with DOX (**1**) despite the lower loading in comparison of TPT (**5**). For this reason, to increase the loading of hydrophobic CPT (**4**), the derivatisation of this drug is envisioned to enhance its solubility.

2.3. Synthesis of a prodrug of CPT and study its synergistic effect with DOX.

2.3.1. Introduction

One of the most common problems of most anticancer drugs is its insolubility leading into a poor bioavailability which hampers the translation into the clinic [174], [19]. Therefore, it is of the highest importance to improve the solubility of these compounds. In this respect, different techniques can be applied to achieve that goal such as complexation of drugs, use of cosolvents, synthesis of pharmaceutical salts, prodrugs, particle size reduction technologies and others [175]. An elegant approach is the design of a biologically inactive prodrug with improved bioavailability, which can be metabolized in the body to produce the actual drug [176]. A representative example of one of this compounds is irinotecan (**21**) (Table 4), a camptothecin (**4**) analogue used in the treatment of gastroenteropancreatic tumors [177].

However, another approach to consider is the Pegylation strategy [178]. This technique is based on the derivatization of drugs with PEG chains. These linkers have repeating units of ethylene oxide that can bind to two or three water molecules. Thus, the solubility of insoluble small drugs such as docetaxel, paclitaxel or CPT (**4**) can be enhanced [178]. As an example, when paclitaxel is conjugated to high-molecular-weight PEG via an amino acid spacer, the water solubility remarkably enhanced [179], [180]. Besides, the afforded conjugate showed significant advantages in terms of high water solubility, without toxic excipients, and tumour environment-sensitive drug release [181]. Another illustration of this methodology was reported for CPT (**4**) with the aim to yield a more soluble compound [182], [183].

As explained in section 1.1.2, CPT (**4**) has been studied as an effective therapeutic agent since 1966. It exhibits a broad range of anticancer activity via the function of binding to the TOP1 and DNA complex. Unfortunately, low aqueous solubility limits its clinical use [184]. Therefore, a series of more soluble analogues such as TPT (**5**) or irinotecan (**21**) were developed in order to be implemented as an effective cancer therapy [185]. However, as can be observed in Table 4, the introduction of moieties upon the pyrrolo[3,4- β]-quinoline of CPT (**4**) structure displays a decrease in the cytotoxicity (IC_{50}).

Table 4. IC₅₀ values of camptothecin (**4**), topotecan (**5**) and irinotecan (**21**) at 24 h in HeLa cells ([186]–[188]).

Compound	Chemical Structure	IC ₅₀ (μM)
Camptothecin	The chemical structure of Camptothecin (4) is shown. It features a complex polycyclic core consisting of a tropane ring system fused to a piperidine ring, which is further fused to a lactone ring. A hydroxyl group is attached to the tropane ring, and a methyl group is attached to the piperidine ring. The lactone ring is part of a larger system that includes a quinoline-like ring.	0.44
Topotecan	The chemical structure of Topotecan (5) is shown. It is similar to Camptothecin but has a methylamino group (-NHCH ₃) attached to the tropane ring and a hydroxyl group (-OH) attached to the piperidine ring. The structure is shown as a hydrochloride salt (HCl).	9.09
Irinotecan	The chemical structure of Irinotecan (21) is shown. It features a complex polycyclic core similar to Camptothecin, but with a piperazine ring system attached to the tropane ring and a hydroxyl group (-OH) attached to the piperidine ring.	60.00

As has been stated, the chemical modifications upon CPT (**4**) in order to achieve a more soluble drug may lead to a loss of antitumor activity and significant alterations in the toxicological profile of the drug. Thereby, it is proposed to chemically modify CPT (**4**) with a short PEG chain to enhance its solubility but with the ability to scissile this linker within the cell in order to obtain the active drug CPT (**4**). In this regard, it has been reported that the glutathione-responsive disulphide linker attached in the hydrophobic drug can release the free CPT (**4**), thanks to the high concentration of glutathione (GSH) inside cancerous cells (2-8 mM) in comparison with plasma (1-2 μm) [189]. Thus, the therapeutic effect is not affected through the chemical modification, but the solubility is enhanced thanks to the hydrophilic PEG [189]. This strategy has been applied by the functionalization of an MSN with a disulphide PEG chain decorated with CPT (**4**). However, instead of loading the hydrophobic drug within the pores of the MSN, the researchers functionalized it in the outer surface of the nanomaterial [190], [191]. Thus, the lactone ring is prone to opening due to its exposure to the physiological medium (Figure 28) leading to an ineffective system. Therefore, in this PhD dissertation, it is proposed to chemically derive CPT (**4**) with a cleavable PEG chain to improve its solubility, and, its loading within an MSN.

2.3.2. Design of a Prodrug of CPT

As previously mentioned (2.2.1), CPT (**4**) can exist in two different forms: a therapeutically active lactone form and a therapeutically inactive carboxylate form (Figure 28). Thereby, it is of high importance to maintain it with the active form to perform coupling reactions and extend its

stability [192]. On the other hand, the hydroxyl group present in CPT (**4**) is an ideal group for chemical derivatization through alkylation or acylation. Besides, it has been reported that chemical modifications of this group does not disrupt the lactone ring [193].

Therefore, it is proposed to perform a “click” reaction upon the OH of CPT (**4**) to attach a cleavable disulphide PEG linker in order to enhance the solubility of this drug (Figure 41). Unlike the other CPT (**4**) analogues (Table 4), the derivatization of the drug by this site will maintain the therapeutic effect of CPT (**4**).

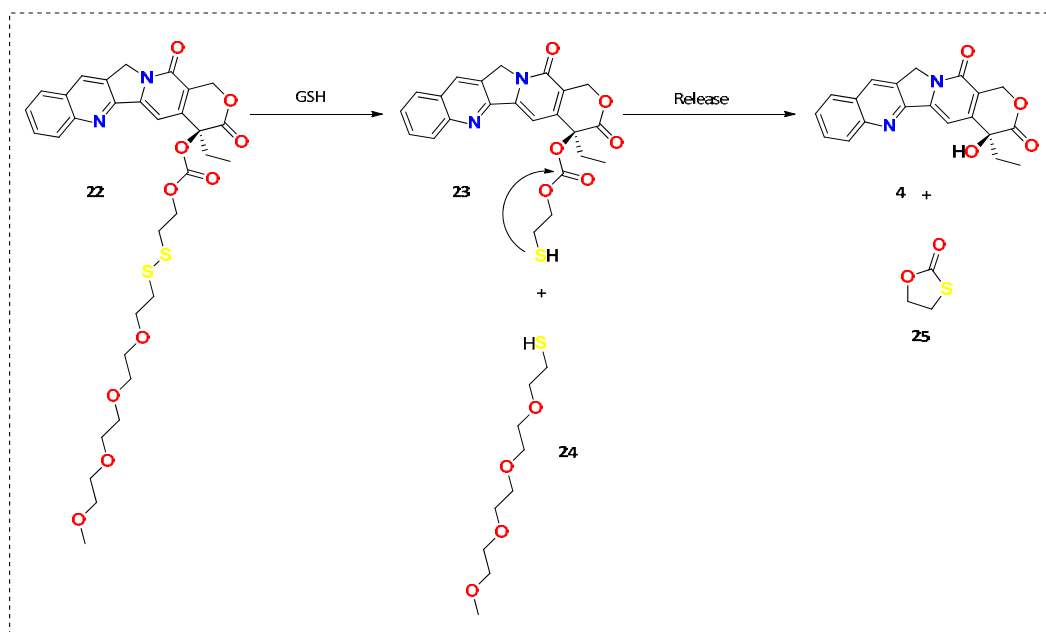


Figure 41. Cleavage of CPT-PEG (**22**) with GSH.

As it is illustrated in Figure 41, (S)-4-ethyl-3,14-dioxo-3,4,12,14-tetrahydro-1H-pyrano[3',4':6,7]indolizino[1,2-b]quinoline-4-yl 2,5,8,11-tetraoxa-14,15-dithiaheptadecan-17-yl carbonate (CPT-PEG) (**22**) contains a disulphide bond which in reductive conditions will be cleaved leading to the free drug. Figure 42 shows the retrosynthetic pathway for the obtention of molecule **22**.

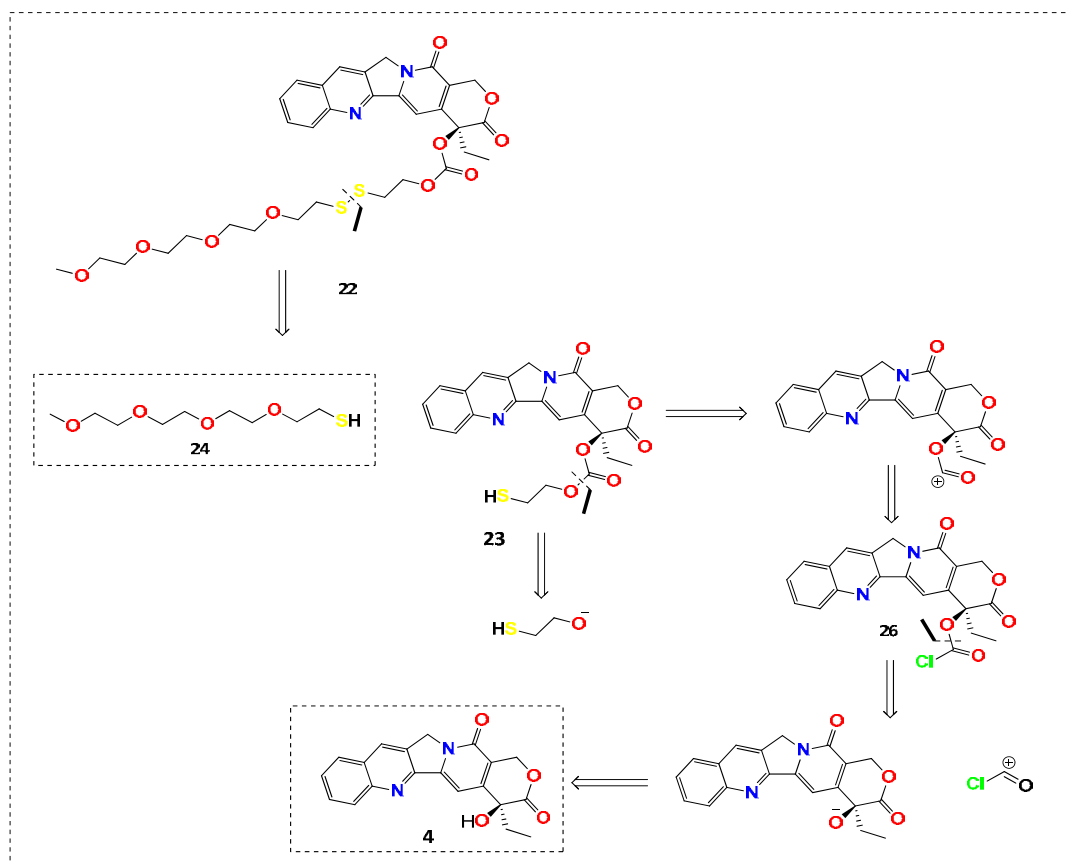


Figure 42. Retrosynthetic analysis of CPT-PEG (22).

2.3.2.1. Synthesis of PEG-SH (24)

Tetraethylene glycol monomethyl ether (27) was chosen as starting material to obtain a PEG with a thiol group in one end. First, PEG 28 is obtained through tosylation of OH using TsCl in THF. Then, PEG 28 underwent a nucleophilic substitution with the attack of thiourea. Finally, this group is hydrolysed with NaOH to give the thiol group. Then, PEG-SH (24) was obtained (Figure 43).

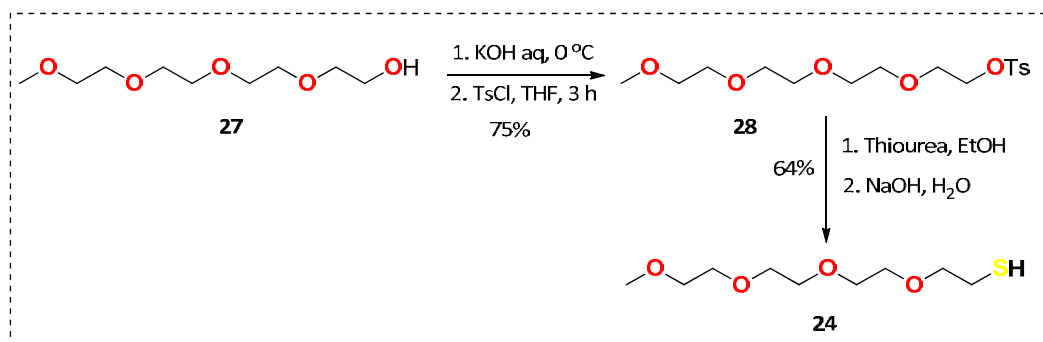


Figure 43. The synthetic pathway followed to obtain molecule PEG-SH (24).

In Figure 44 are depicted the $^1\text{H-NMR}$ spectra of tosyl intermediate **28** and PEG-SH **24**. The proper introduction of thiol group can be verified through the signals of the proton of $-\text{SH}$ (blue dot) with a chemical shift of 1.56 ppm (1H) and the neighbour $-\text{CH}_2$ (yellow dot) with a chemical shift of 2.68 ppm (2H) (Figure 44 b)). Moreover, the disappearance of the signals of the tosyl leaving group (purple and orange dots) (7.7 ppm and 7.3 ppm aromatic ring; 2.4 ppm $-\text{CH}_3$) also gives consistency to the accomplishment of the reaction (Figure 44 a)).

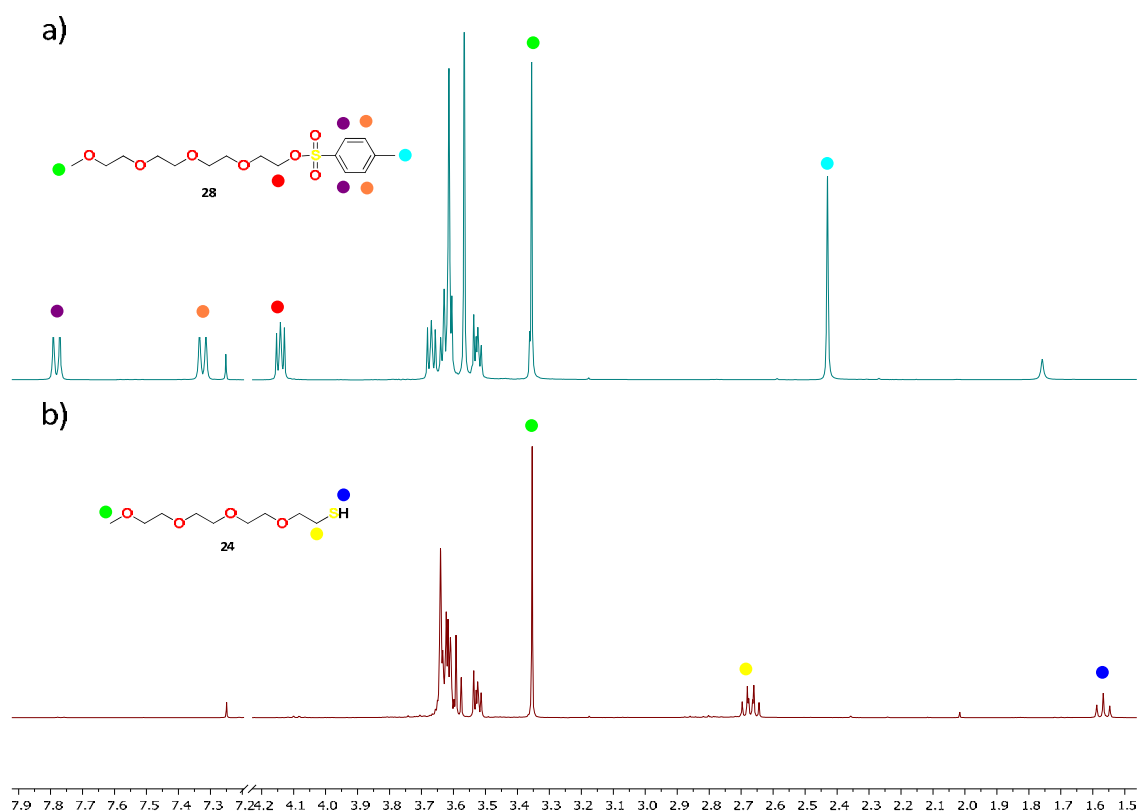


Figure 44. $^1\text{H-NMR}$ comparison between PEG (**28**) and PEG-SH (**24**).

2.3.2.2. Synthesis of CPT-PYR (**34**)

(Pyridin-2-yl)disulfanyl)alkyl carbonate derivative of CPT (**4**) (CPT-PYR (**34**)) was synthesized according to reported procedures [194], [195]. Briefly, 2-(2-pyridinildithiol)ethanol (**33**) was prepared by reacting 2-mercaptoethanol (**30**) with 2,2'-pyridyl disulphide (**31**) as described in the literature [109]. In this reaction, the only by-product was pyridine-2-thiol (**32**). The presence of molecule **32** turned to yellow the solution, which indicates the scission of the disulphide bridge of molecule the compound **31**. Then, CPT (**4**) was treated with triphosgene (**29**) in anhydrous conditions and the presence of DMAP. It was followed by a subsequent dropwise addition of a solution of 2-(2-pyridinildithiol)ethanol (**33**) to the mixture [108]. The main impurities were removed by flash silica gel column chromatography using 7:3 AcOEt:Cy eluent conditions to obtain (S)-4-ethyl-3,14-dioxo-3,4,12,14-tetrahydro-1H-

pyrano[3',4':6,7]indolizino[1,2-b]quinolin-4-yl (2-(pyridin-2-yl)disulfanyl)ethyl carbonate (CPT-PYR) (**34**) (Figure 45).

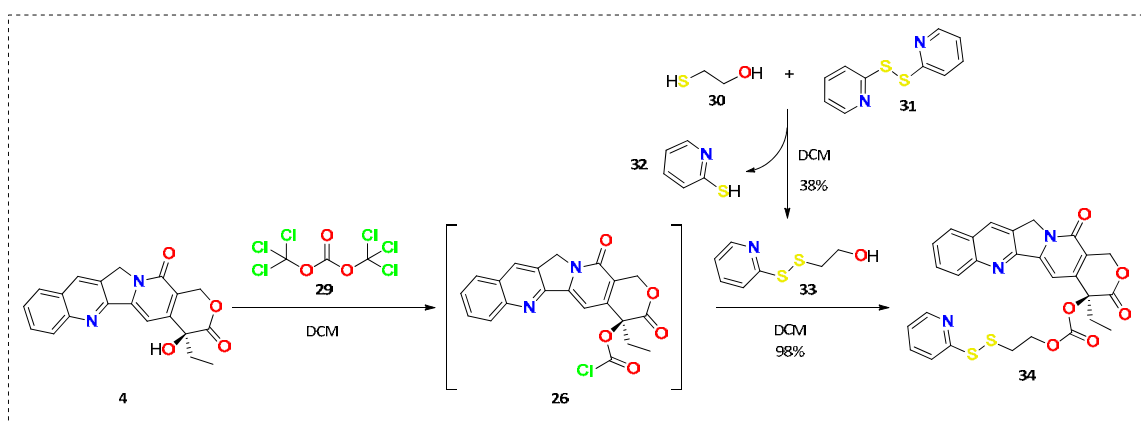


Figure 45. Synthesis of CPT-PYR (**34**).

2.3.2.3. Synthesis of CPT-PEG (**22**)

Finally, with PEG-SH (**24**) and CPT-PYR (**34**) already synthesised, the “click” reaction between these two molecules was performed (Figure 46).

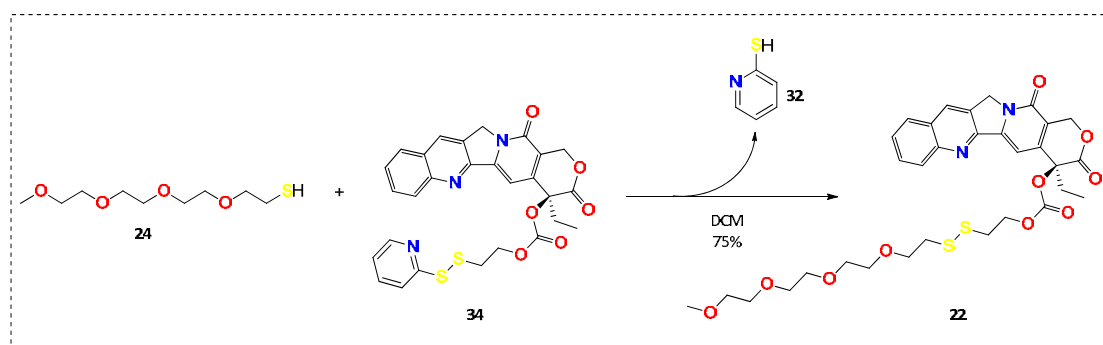


Figure 46. Synthesis of CPT-PEG (**22**).

In short, PEG-SH (**24**) was added to a solution of CPT-PYR (**34**) in anhydrous DCM with a rate of 10 mL/h. Then, the reaction was left 6 h at room temperature yielding CPT-PEG (**22**) and pyridine-2-thiol (**32**) as the only by-product. Finally, CPT-PEG (**22**) was purified using a silica gel chromatography with AcOEt.

Figure 47 shows the $^1\text{H-NMR}$ of CPT-PYR (**34**) and CPT-PEG (**22**). The main difference between the two spectra are the signals of the PEG chain (brown dot) with a chemical shift of 3.52-3.67 ppm (14H). Besides, the singlet at 3.3 ppm (3H) can be ascribed to the protons of the methoxy group (green dot). On the other hand, the disulphide bridge can also be detected thanks to the presence of the two $-\text{CH}_2$ adjacent; two triplets at 2.84 ppm (2H) (blue dot) and 2.93 ppm (2H) (purple dot) (Figure 47 b)).

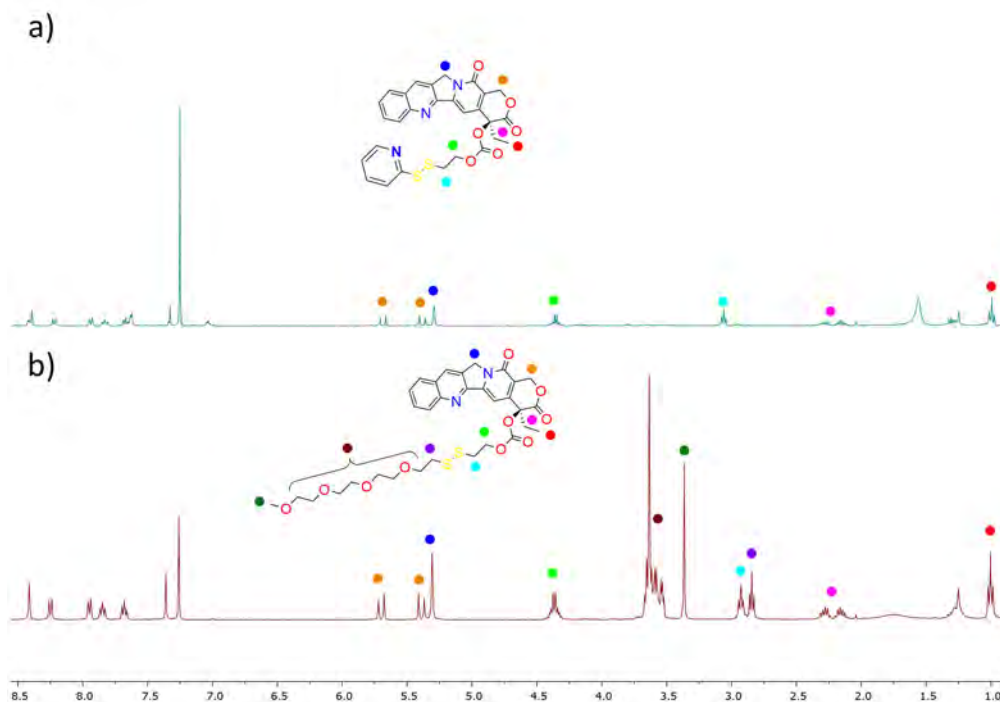


Figure 47. ¹H-NMR comparison between a) CPT-PYR (**34**) and b) CPT-PEG (**22**).

Further evidence of the synthesis of CPT-PEG (**22**) was obtained after characterization through High-Resolution Mass Spectrometry (HRMS). In Figure 48 is shown the data of ESI, which is in agreement with the exact mass of the desired molecule.

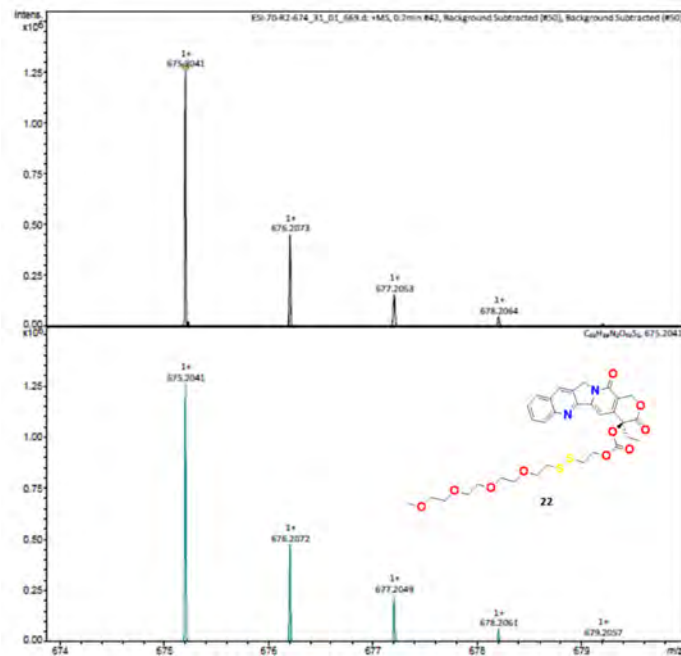


Figure 48. ESI-FIA-TOF spectrum of CPT-PEG (**22**).

2.3.2.4. Cleavage of CPT-PEG (22) with GSH

The proper cleavage of the disulphide bond was studied *in vitro* employing GSH 10 mM in PBS buffer pH 7.4, which is the concentration of this reductive compound inside cancerous cells, as a reductive agent (Figure 49) [189].

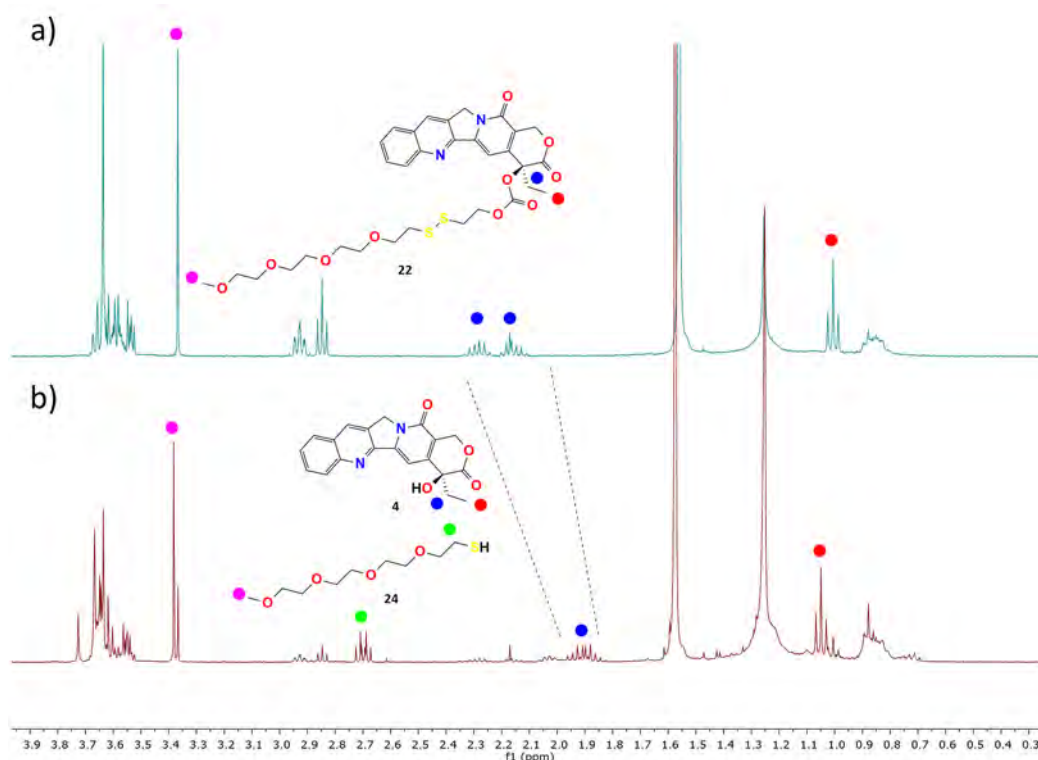


Figure 49. Cleavage study of CPT-PEG (22) with GSH 10 mM in PBS 7.4 for 1 h.

The scission of the disulphide bond can be studied monitoring the chemical shift of -CH₃ (red dot) of CPT-PEG (22) which is slightly deshielded from 1.01 ppm (Figure 49 a)) to 1.05 ppm (Figure 49 b)). Further evidence of the cleavage of the scissile bond can be confirmed by the signals of -CH₂ 2.70 ppm (2H) (green dot), which corresponds to the protons of the neighbouring carbon of the -SH group (Figure 49 b)). Besides, the -CH₃ of the methoxy group of PEG (24) can be inferred again (purple dot) and it is also slightly deshielded from 3.36 ppm (Figure 49 a)) to 3.38 ppm (Figure 49 b)). On the other hand, the chemical shift of the two diastereotopic protons of the ethyl group (blue dot) also gives consistent to the cleavage of the disulphide bond.

2.3.3. Loading of CPT-PEG (22)

Next, the loading of MSN with CPT-PEG (22) was carried out. As it is depicted in section 2.2.3.1, $\text{CHCl}_3/\text{MeOH}$ 4:1 showed the best loading conditions for CPT (4). Therefore, the same solvents were used to encapsulate CPT-PEG (22). As can be observed in Figure 50, the spectrum of CPT-PEG resembles the spectrum of CPT (4).

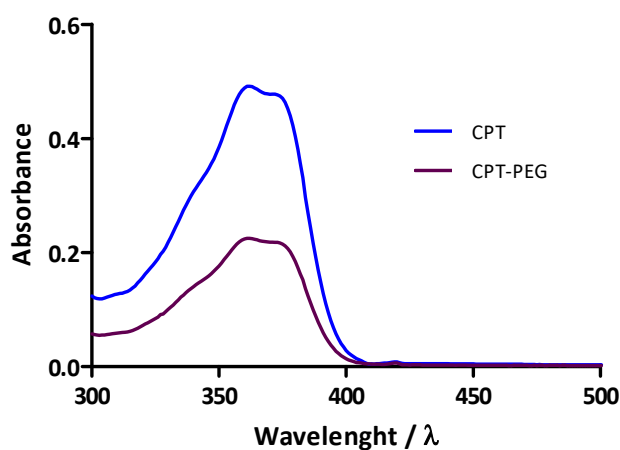


Figure 50. The shape of the absorption spectrum of CPT (4) and CPT-PEG (22) in $\text{CHCl}_3/\text{MeOH}$ 4:1.

A $6.3\% \pm 0.3$ of CPT-PEG (22) was internalized inside the pores of the MSN in comparison with $2.3\% \pm 0.4$ for CPT (4). Nevertheless, once inside the solid tumour and thanks to the reductive environment, CPT-PEG (22) would be cleaved, giving the free CPT (4), which in time will provide the cytotoxic activity (Figure 41). Therefore, a 30% more of CPT (4) will be adequately released it.

2.3.4. Construction of CPT-PEG@MSN-hyd-PEG-hyd-DOX

The capping was carried out following the methodology used for the system with TPT (5) and CPT (4) (2.2). Briefly, CPT-PEG (22) was loaded within the MSN utilizing $\text{CHCl}_3/\text{MeOH}$. Afterwards, the pores were blocked by the consecutive addition of dihydrazide polyethylene glycol chain (14) and DOX (1) (25% loaded) in ethanol (Figure 51).

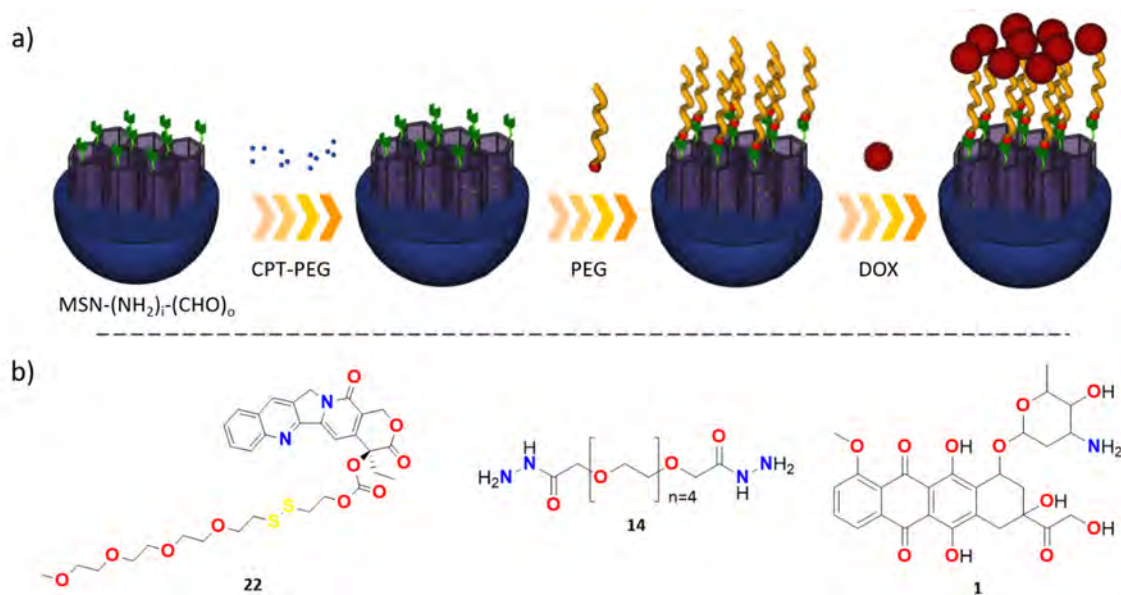


Figure 51. Preparation of the DDS with CPT-PEG (**22**).

2.3.4.1. Controlled drug release

The release profile of CPT-PEG (**22**) from CPT-PEG@MSN-hyd-PEG-hyd-DOX has been studied by UV-vis absorption spectroscopy at pH values of 4.0, 4.5, 5.5, 6.5 and 7.4 (Figure 52).

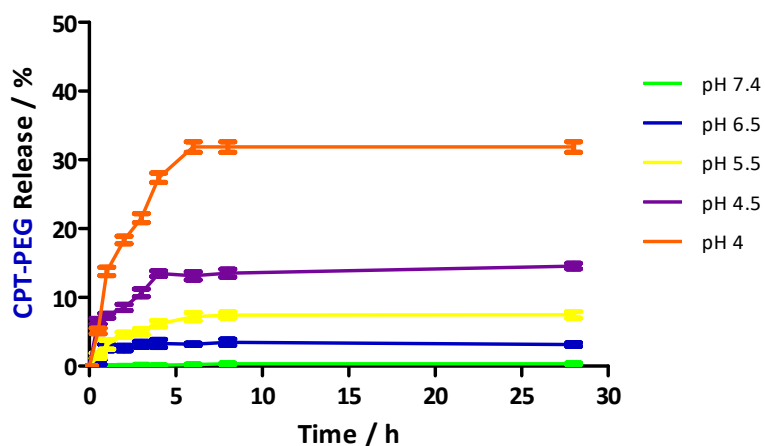


Figure 52. CPT-PEG (**22**) release profile of CPT-PEG@MSN-hyd-PEG-hyd-DOX at different pH values under stirring at 100 rpm and at $t=37$ °C. Data represented as mean \pm SD ($n=3$).

As well as the other systems (2.2.3.2), at physiological pH (7.4), the release was negligible, confirming the stability of CPT-PEG@MSN-hyd-PEG-hyd-DOX. On the other hand, when the acidity of the media increased, a burst release of the drug takes place in the range of 5 h. Then, a sustainable release is kept for more than 10 h.

As expected, for DOX (**1**) release, the profile was similar for the one obtained in system CPT@MSN-hyd-PEG-hyd-DOX (Figure 33 c)), where a burst release of DOX takes place at pH 4 liberating a 45% of the drug in the medium due to the scission of the hydrazone bond.

2.3.5. Cytotoxicity

The cytotoxicity of CPT-PEG@MSN-hyd-PEG-hyd-DOX was assessed against MSN-hyd-PEG-hyd-DOX and CPT@MSN-hyd-PEG-hyd-DOX (in a concentration range of 1-100 $\mu\text{g}\cdot\text{mL}^{-1}$) in HeLa and HepG2 cells by MTT cell viability assay for 72 h (Figure 53 a) and b)). The performance of this experiment revealed a decrease in the relative cell viability at 5 $\mu\text{g}\cdot\text{mL}^{-1}$ from 65% (MSN-hyd-PEG-hyd-DOX) to 43% (CPT-PEG@MSN-hyd-PEG-hyd-DOX) in HeLa cells (Figure 53 a)). In contrast, in HepG2 cells, a similar result was obtained at the same concentration, where the cytotoxicity was decreased from 85% (MSN-hyd-PEG-hyd-DOX) to 63% (CPT-PEG@MSN-hyd-PEG-hyd-DOX) (Figure 53 b)). But more importantly, it is at 25 $\mu\text{g}\cdot\text{mL}^{-1}$ of MSN, where an increase in the cell death was found for CPT-PEG@MSN-hyd-PEG-hyd-DOX in HepG2 cells achieving a viability of only 17%, whereas for MSN-hyd-PEG-hyd-DOX the cell viability was 47% (Figure 53 b)).

The calculated values of IC_{50} for CPT-PEG@MSN-hyd-PEG-hyd-DOX and CPT@MSN-hyd-PEG-hyd-DOX in HeLa and HepG2 cells are displayed in Table 5. For HeLa cells, both nanoparticles systems show a similar IC_{50} value of 2.70 $\mu\text{g}\cdot\text{mL}^{-1}$ and 2.73 $\mu\text{g}\cdot\text{mL}^{-1}$ for CPT-PEG@MSN-hyd-PEG-hyd-DOX and CPT@MSN-hyd-PEG-hyd-DOX, respectively. Whereas for HepG2 cells, the newly synthesised CPT-PEG@MSN-hyd-PEG-hyd-DOX exhibit a significant improvement of IC_{50} (7.70 $\mu\text{g}\cdot\text{mL}^{-1}$) in comparison to the former CPT@MSN-hyd-PEG-hyd-DOX (9.88 $\mu\text{g}\cdot\text{mL}^{-1}$). Most importantly, specially, the CI value achieved for the CPT-PEG system is lower (0.54) than the CPT system (0.68). Thus, the synergistic effect has been enhanced.

Table 5. IC_{50} and CI values of CPT-PEG@MSN-DOX (CPT-PEG@MSN-hyd-PEG-hyd-DOX) and CPT@MSN-DOX (CPT@MSN-hyd-PEG-hyd-DOX) in HeLa and HepG2 cells at 72 h.

Cell line	IC_{50} ($\mu\text{g}\cdot\text{mL}^{-1}$)	
	CPT-PEG@MSN-DOX	CPT@MSN-DOX
HeLa	2.70	2.73
HepG2	7.70	9.88
Cell line	CI	
HeLa	0.67	0.21
HepG2	0.54	0.65

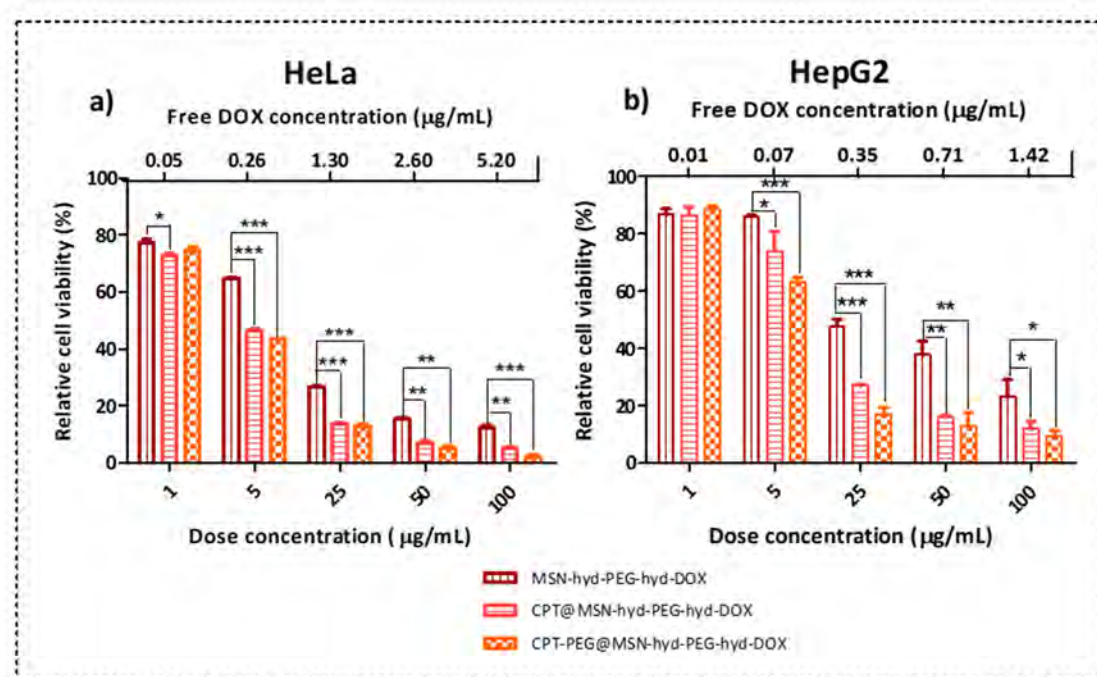










Figure 53. Cell viability of a) HeLa cells and b) HepG2 incubated with MSN-hyd-PEG-hyd-DOX, CPT@MSN-hyd-PEG-hyd-DOX and CPT-PEG@MSN-hyd-PEG-hyd-DOX for 72 h. Data represented as mean \pm SD ($n=3$), * $p<.05$, ** $p<.01$ and *** $p<0.0001$. The concentration of free DOX (**1**) is the released drug at pH 5.5 for HeLa cells and pH 6.5 for HepG2 cells.

The results obtained are rationalized in term of differences in the metabolism of the cells. First, it has been reported that the presence of DOX (**1**) has an apparent effect in glutathione depletion; this outcome is higher for HeLa than HepG2 cells [196]. Thereby, it is hypothesized that the low level of GSH in HeLa cells is not enough to completely cleave the disulphide bond of CPT-PEG (**22**), whereas, for HepG2, the amount of CPT-PEG (**22**) cleaved is higher. Hence more CPT (**4**) is released in the medium and the toxicity of the system CPT-PEG@MSN-hyd-PEG-hyd-DOX is improved in comparison to CPT@MSN-hyd-PEG-hyd-DOX (Figure 53 a) and b)).

Second, this fact is enhanced due to the different pH environments of the two cell lines. From the literature it is known that HepG2 cells display a less acidic endosomal pH (pH 6 \sim 6.7) than HeLa [197]–[199]. Thus, less DOX (**1**) is released in the medium. Conversely, the low pH of the endosomes (pH 5.5) of HeLa cells permits a higher release of the cargo, raising the toxicity of the MSN at lower concentrations [198]. Eventually, such effect is strongly related to the amount of “free” CPT (**4**) from CPT-PEG (**22**) liberated within the cells. As mentioned above, the amount of DOX (**1**) in the medium has an effect on GSH depletion, which regulates the scission of the disulphide bridge. For this reason, since the pH in HeLa cells is more acid than HepG2 cells, a higher amount of DOX (**1**) is released in the medium, which decreases the amount of GSH responsible for the scissions of the disulphide bond of CPT-PEG (**22**). On the contrary, the higher pH in HepG2 cells releases less quantity of DOX (**1**) in the medium, hence the decrease of GSH

does not take place, which lets the scissions of the disulphide bond producing more “free” CPT (**4**) (Table 6). This hypothesis is consistent to the cytotoxic profiles obtained for CPT-PEG@MSN-hyd-PEG-hyd-DOX in comparison with CPT@MSN-hyd-PEG-hyd-DOX for HeLa and HepG2 cells.

Table 6. Effect of the pH of the cell on CPT (**4**) release from CPT-PEG (**22**).

HeLa	 pH	 DOX	 GSH	 CPT
HepG2	 pH	 DOX	 GSH	 CPT

2.3.6. Conclusions and Outlook

A new prodrug of CPT (**4**) with a PEG attached to the hydroxyl moiety has been synthesised (CPT-PEG) (**22**). The disulphide bridge of this new prodrug is labile under reductive conditions of the cancerous cells, releasing the active CPT (**4**). Notably, the loading of CPT-PEG (**22**) within an MSN has increase (6.3%) in comparison with CPT (**4**) (2.3%). This rise in the loading represents a 30% more of CPT % internalized within an MSN in contrast with the former system CPT@MSN-hyd-PEG-hyd-DOX. Furthermore, the system was stable under physiological conditions (pH 7.4), where no-release took place. Whereas, under acidic conditions, a burst/sustained release occurred. The system shows an apparent synergistic effect in comparison with MSN-hyd-PEG-hyd-DOX in HeLa and HepG2. Noteworthy, the cytotoxic activity of the synthesised system was higher in HepG2 cells.

Given the results obtained, it has been confirmed that the functionalization of CPT (**4**) by the hydroxyl group lets the attachment of short PEG **24** that increase its solubility. Moreover, the suitability of the system against HepG2 cells in comparison to HeLa cells has been noticed. Thereby, the next step to further increase the selectivity of this new system towards this particular cell line is to add selective ligands to the as-synthesized system.

2.4. Glycyrrhetic acid-functionalized MSN for the co-delivery of DOX/CPT-PEG for targeting HepG2 cells

2.4.1. Introduction

As has been explained in section 1.4.2.1, the accumulation of nanoparticles in the solid tumor can be achieved in principle by two general mechanisms; through a passive or active targeting [200]. In general, passive targeting is based on the accumulation of MSN in the tumor tissue due to the well-known EPR effect [201]. However, an improvement of this selectivity can be obtained by using active targeting, which involves the functionalization of the nanoparticle with antibodies, aptamers or small-molecule ligands [202], [203]. These small-molecule ligands can recognize and bind specifically to receptors that are overexpressed by cancer cells [204]. The overexpression of the receptors is usually to the advantage of tumor growth and spread [205].

The active targeting mechanism has been used to fight the Hepatocellular carcinoma, which is the primary cancer of the liver [206]. This terrible disease is the third leading cause of cancer death affecting more than half a million people across the world [207], [208]. Even though different chemotherapeutic agents have been approved for the treatment of this type of cancer, there remains an urgent need for the development of selective strategies [209]. It has been reported that human hepatocellular carcinoma HepG2 cells possess a significant number of glycyrrhetic acid (GA) receptors in its membrane [128]–[131]. This particular feature has been exploited to modify the surface of nanoparticles with this ligand to enhance the concentration of the nanocarrier in the tumoral tissue (**1**) [132], [133]. Thereby, to improve the targeting efficacy of the MSNs synthesised in section 2.3 (CPT-PEG@MSN-hyd-PEG-hyd-DOX), the functionalization of the system with GA is envisioned. For this purpose, taking advantage of the radial-capping approximation, the GA ligand would be placed over the DOX (**1**) drug (Figure 54). Thus, both GA and DOX (**1**) will act as pore capping agents preserving the cargo within the MSN. It is noteworthy the simplicity of the methodology presented in comparison with the systems presented in section 1.4.2.2 [124], [138], [139]. Besides, the stability of those systems is unstable under physiological conditions, since leakage of the cargo takes place.

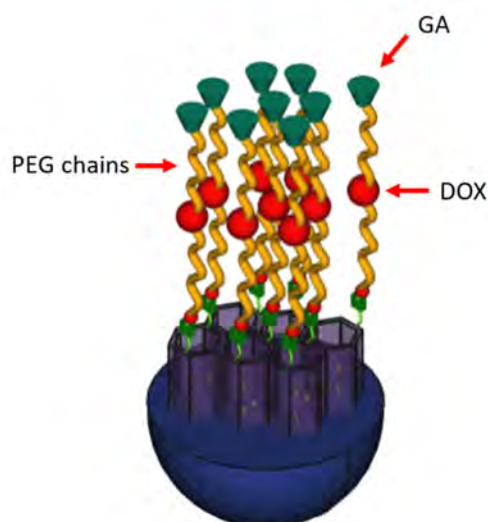


Figure 54. Schematic representation of MSN functionalized with GA.

2.4.2. Synthesis of the target ligand

The decoration of the MSN with the GA ligand would rely on the presence of the -NH_2 group of the DOX (**1**) drug, which plays a crucial role owing to its reactivity (Figure 55).

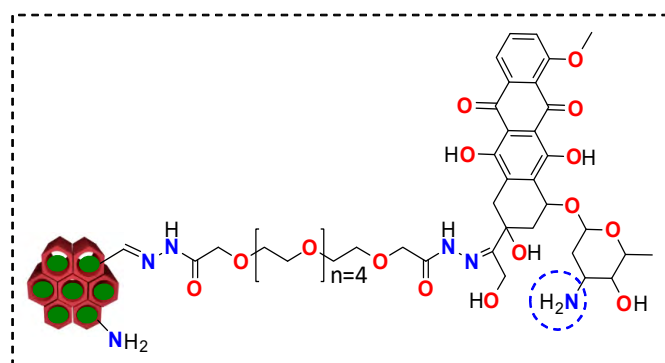


Figure 55. CPT-PEG@MSN-hyd-PEG-hyd-DOX system.

A search in the literature reveals that the chemistry of the amino group has been exploited to build pH-sensitive systems through the formation of a benzoic-imine bond between a linker and DOX (**1**) (Figure 56) [210], [211]. In general, the imine bond is less stable in physiological environments than acetals and hydrazones. Nevertheless, the aromatic imine bond enhances its stability due to the π -conjugated effect [212].

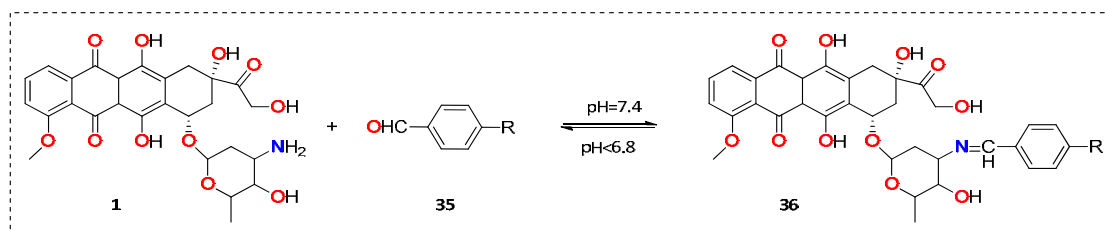


Figure 56. Dynamic interaction between DOX (**1**) and benzaldehyde (**35**) via pH-sensitive benzoic-imine bond.

However, little attention has been paid for the decoration of the MSN using Schiff-bases for drug delivery purposes [213]–[218]. To the best of our knowledge, the further functionalization of MSN with benzoic-imine bonds to attach ligands have not been described in the literature.

In this PhD dissertation, it is proposed to bond the GA ligand to the DOX (**1**) of CPT-PEG@MSN-hyd-PEG-hyd-DOX system by means of an aromatic-imine bond. This approach allows the easy incorporation of the ligand using the functional group of the outer drug of the system (Figure 57).

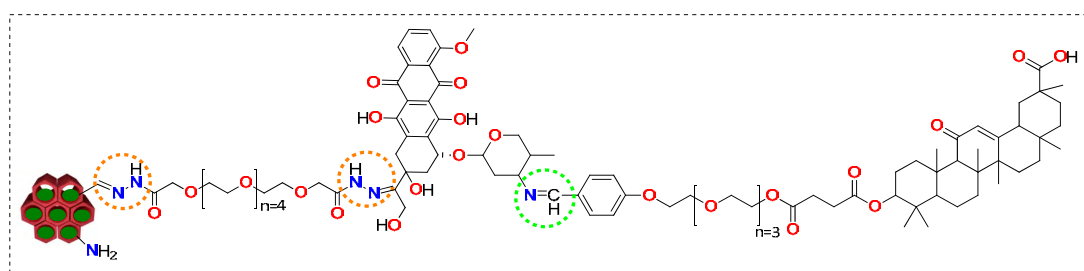


Figure 57. DDS with GA targeting (CPT-PEG@MSN-hyd-PEG-hyd-DOX-PEG-GA).

This system presents two different cleavable bonds. The imine bond (green circle) located in the outer part of the system that will be cleaved at weakly acidic pH (6.8) while the hydrazone bond (orange circle) will be cleaved at more acidic pH (4.5).

The rationale for the design of this smart DDS relies on the targeting of the tumoral cells located in the liver, thanks to a passive targeting that would accumulate the MSNs in the tumor. Then, the ligand will recognize the overexpressed receptors of the HepG2 cells, allowing the selective uptake of the system within the cells. Once inside the endosome, part of this imine bond would be rapidly cleaved due to its acidity. Later, the hydrazone bonds will be cleaved, releasing the drugs within the cytoplasm (Figure 58). It is noteworthy that the imine bond can be only cleaved outside the tumoral cells due to the weak acidity pH of the surroundings. However, this fact is not expected to happen in healthy tissues because there is not such pH. In the event that there is a premature cleavage of the benzoic-imine bond, the presence of the protonated amino group of the DOX (**1**) would enhance the uptake of the MSN in the tumoral cell. However, it is expected

that the bond would be stable due to the π -conjugation. Hence, the MSN uptake would be mainly driven by the ligand-receptor interaction.

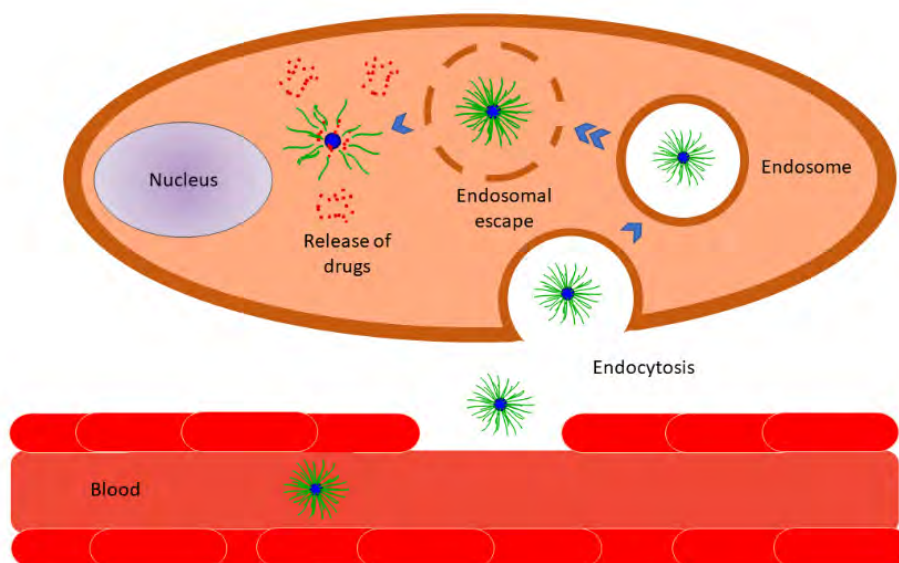


Figure 58. MSN uptake by passive and active targeting.

2.4.2.1. Synthesis of the targeting linker

Exploiting the radial-capping design, it is proposed to prepare a benzaldehyde attached to a PEG linker with a GA ligand located in one end of the chain. In Figure 59, the retrosynthetic analysis of this new linker is depicted.

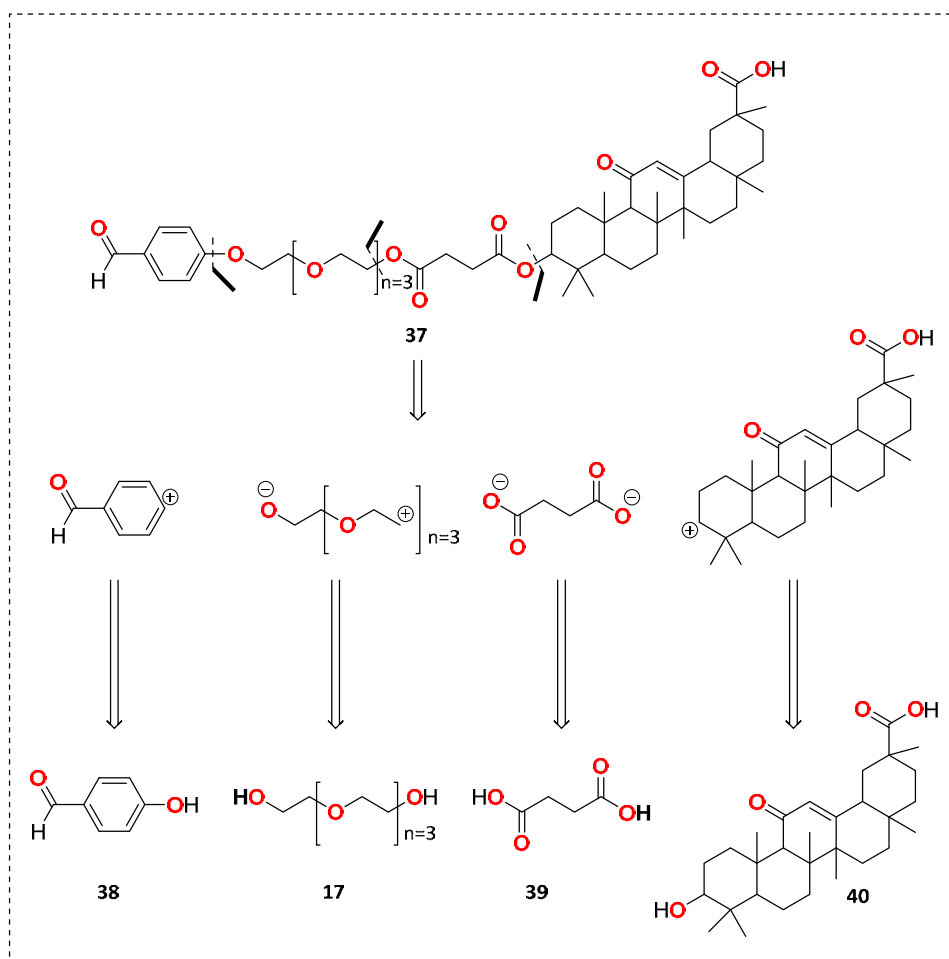


Figure 59. Retrosynthetic analysis of PEG **37**.

2.4.2.2. Synthesis of benz-PEG (**42**)

In order to synthesise the linker **42**, tetraethylene glycol (**17**) is used as a starting material. The monotosylation of this molecule with 4-toluenesulfonyl chloride yields to PEG tosylate **41**. Compound **41** is then reacted with 4-hydroxybenzaldehyde (**38**) to give the final product 4-(2-(2-(2-hydroxyethoxy)ethoxy)ethoxy)ethoxy)benzaldehyde (benz-PEG) (**42**) (Figure 60) [219].

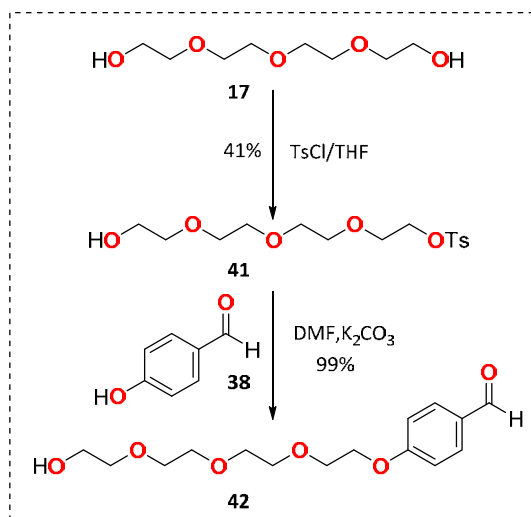


Figure 60. Schematic synthesis of benz-PEG (42).

The presence of a singlet at 9.8 ppm (1H) (pink dot) confirms the introduction of the benzaldehyde moiety. Such signal corresponds to the hydrogen of the aldehyde group (Figure 61 b)). Besides, the removal of the aromatic signals of the tosyl group (blue and green dots) and the -CH₃ (red dot) signals indicate the successful introduction of the benzaldehyde group (Figure 61 b)).

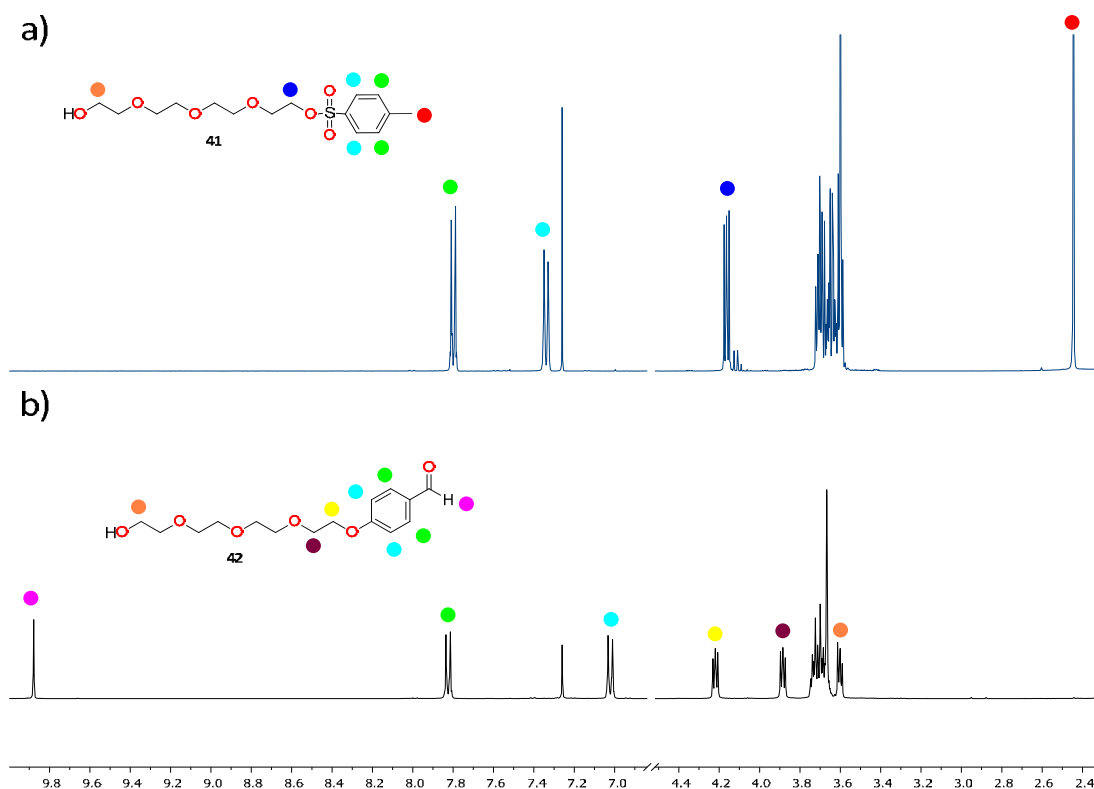


Figure 61. ¹H-NMR comparison between PEG 41 a) and PEG 42 b).

2.4.2.3. Synthesis of GA anhydride (44)

GA (**40**) contains a carboxylic acid in the C₃₀ position of the structure, which is essential for its targeting properties [220], [221]. On the other hand, the hydroxyl group located at the C₃ position has little influence on the targeting ability [222], [223]. Thus, the derivatization of the hydroxyl group has been investigated in the literature to synthesise GA (**40**) conjugates [220]. For this reason, the modification of the hydroxyl group is pursued to attach the benz-PEG (**42**) already synthesised. In this regard, following reported methodologies, the synthesis of compound **44** was performed by reaction of succinic anhydride with GA (**40**) (Figure 62) [131].

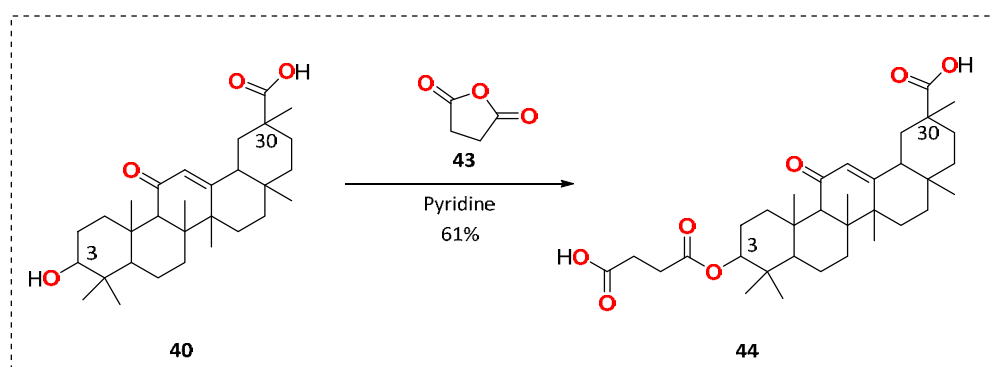


Figure 62. GA with carboxylic acid (**44**).

2.4.2.4. Synthesis of benz-PEG-GA (45)

The introduction of benz-peg (**42**) to acid **44** was carried out by means of the Steglich reaction using DMAP as a catalyst and DCC as a coupling agent. The compounds were left overnight at room temperature to give the final product 10-((1-(4-formylphenoxy)-13-oxo-3,6,9,12-tetraoxahexadecan-16-oyl)oxy)-2,4a,6a,6b,9,9,12a-heptamethyl-13-oxo-1,2,3,4,4a,5,6,6a,6b,7,8,8a,9,10,11,12,12a,12b,13,14b-icosahydricene-2-carboxylic acid (benz-PEG-GA) (**45**) (Figure 63) [224].

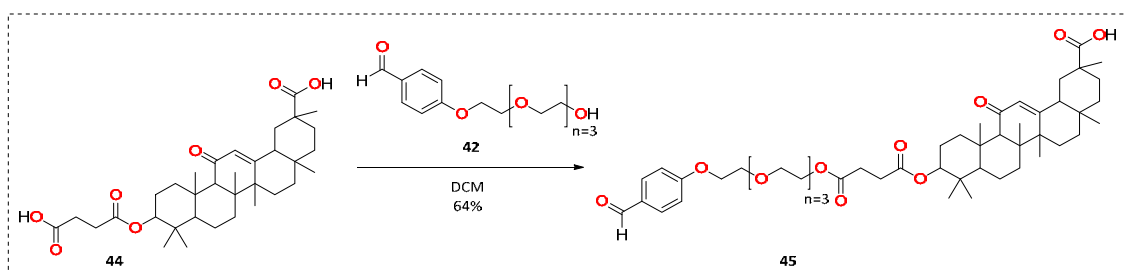


Figure 63. Synthesis of benz-PEG-GA (**45**).

The correct introduction of the benz-PEG (**42**) was confirmed by the presence of the PEG chain signals at 3.6-3.8 ppm (10 H) and the corresponding characteristic proton of the aldehyde group

(orange dot), which can be located at 9.8 ppm (1H) (Figure 64 b)). Besides, the chemical shift of the 3-carboxybutyloxy signals 2.63 ppm (2 H) and 2.65 ppm (2 H) (red dot) to 4.1 ppm (2 H) (brown dot) confirms the formation of the ester (Figure 64).

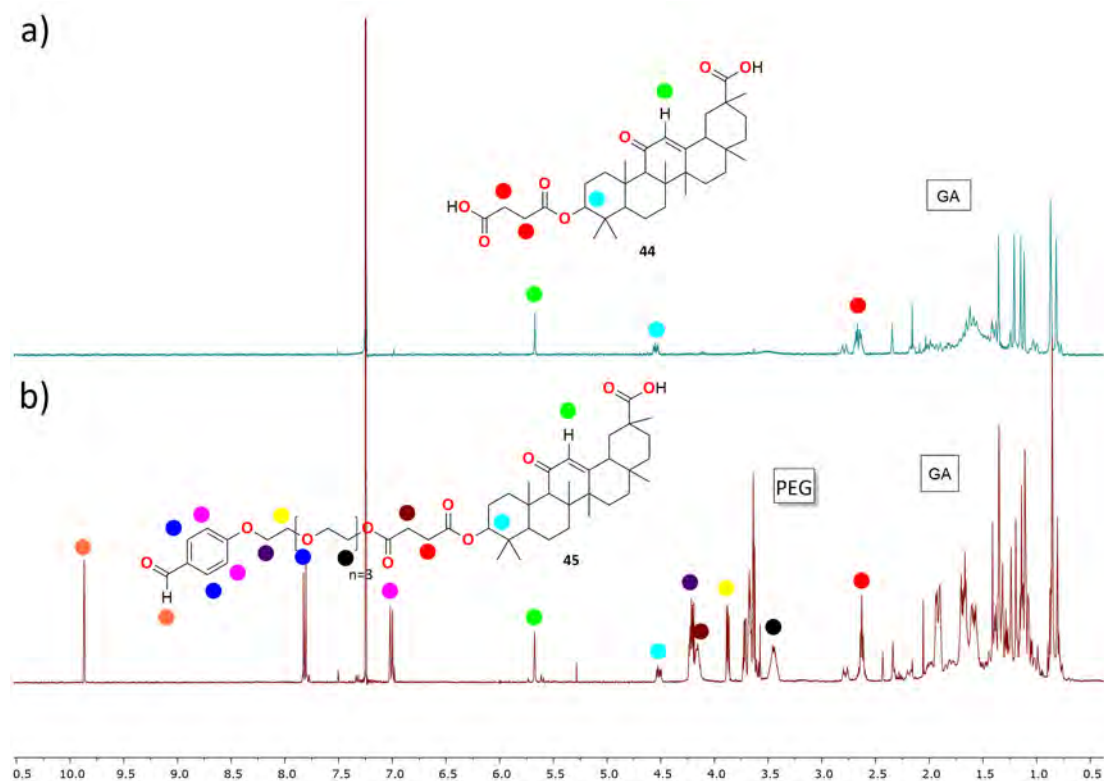


Figure 64. ¹H-RMN comparison between (44) and (45).

Additional proofs of the synthesis of benz-PEG-GA (45) were obtained through HRMS. Figure 65 shows the ESI of the molecule (45), which is in agreement with the theoretical spectrum for the same compound.

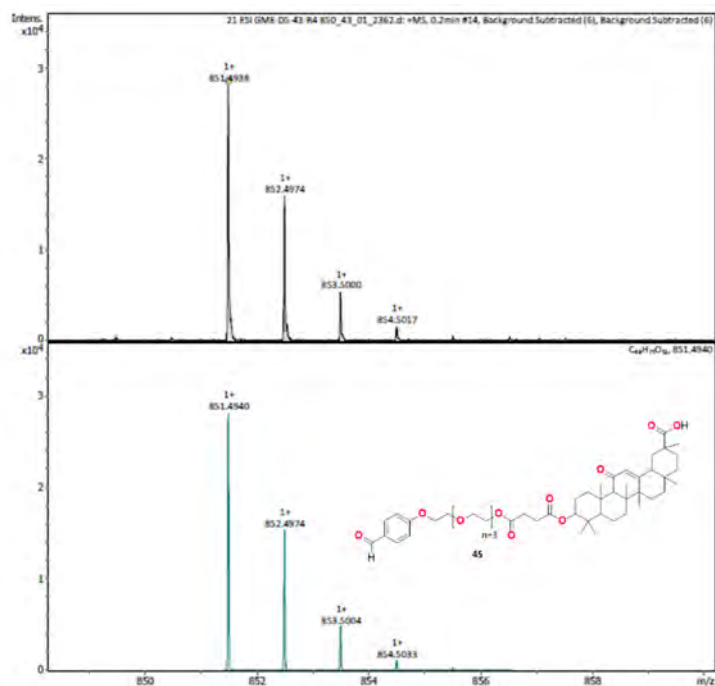


Figure 65. ESI-FIA-TOF-spectrum of benz-PEG-GA (**47**).

2.4.3. Construction of the system

After the synthesis of benz-PEG-GA (**45**), the system was built by imine formation with CPT-PEG@MSN-hyd-PEG-hyd-DOX (Figure 66).

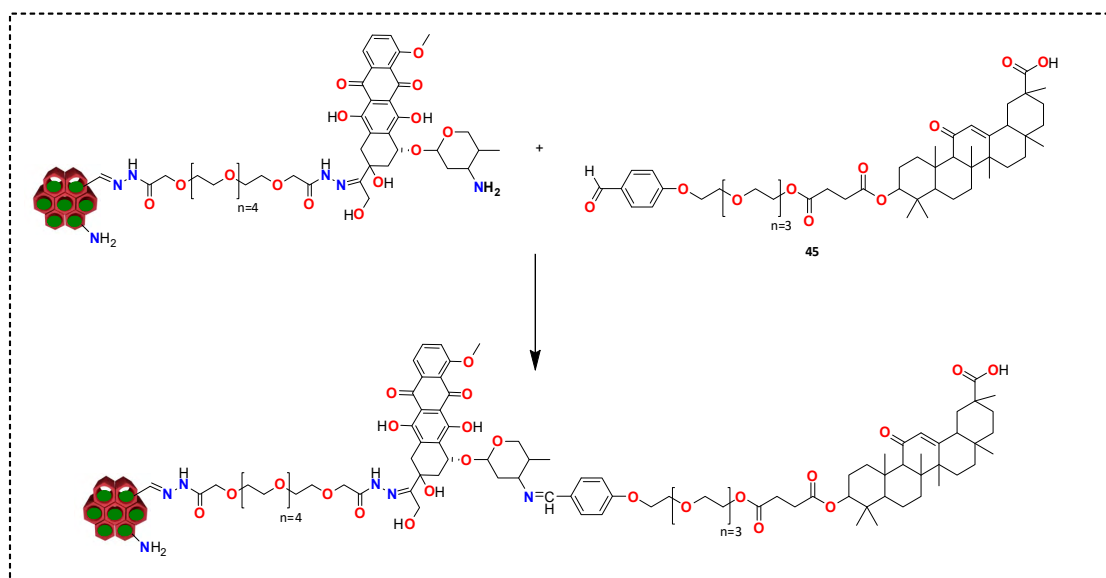


Figure 66. Synthesis of the DDS with GA targeting.

This reaction was carried out following a reported methodology by Pan *et al.* [210]. The authors attached an amino polyethylene glycol to the $-NH_2$ group of DOX (**1**) through the formation of a benzoic-imine bond at pH 8.5. Thus, the same conditions were applied to functionalize benz-

PEG-GA (**45**) to CPT-PEG@MSN-hyd-PEG-hyd-DOX. In parallel, as a control system, benz-PEG (**42**) was likewise reacted upon the MSN (Figure 67).

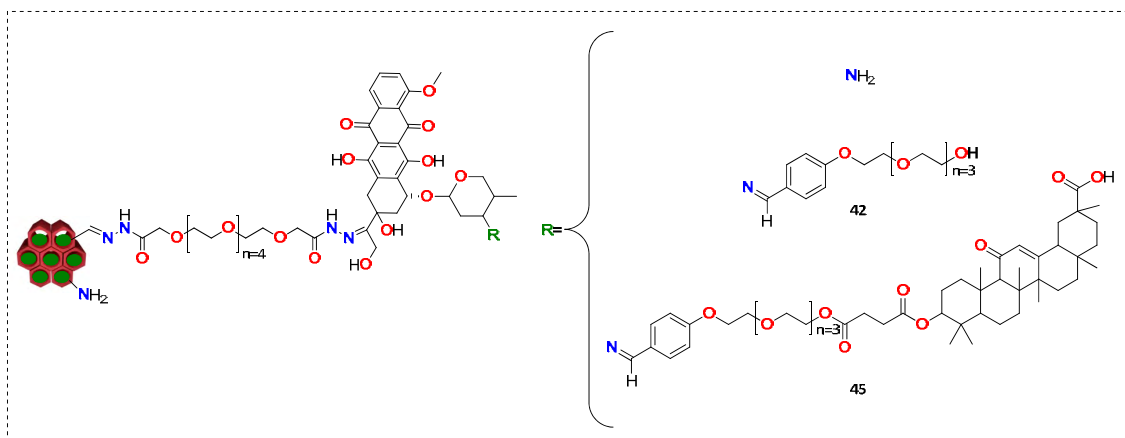


Figure 67. Functionalization of CPT-PEG@MSN-hyd-PEG-hyd-DOX with PEG (**42**) and (**45**).

Next, the zeta potential was determined in order to assess the contribution of each PEG to the MSN in comparison with the starting system (CPT-PEG@MSN-hyd-PEG-hyd-DOX) (Figure 68).

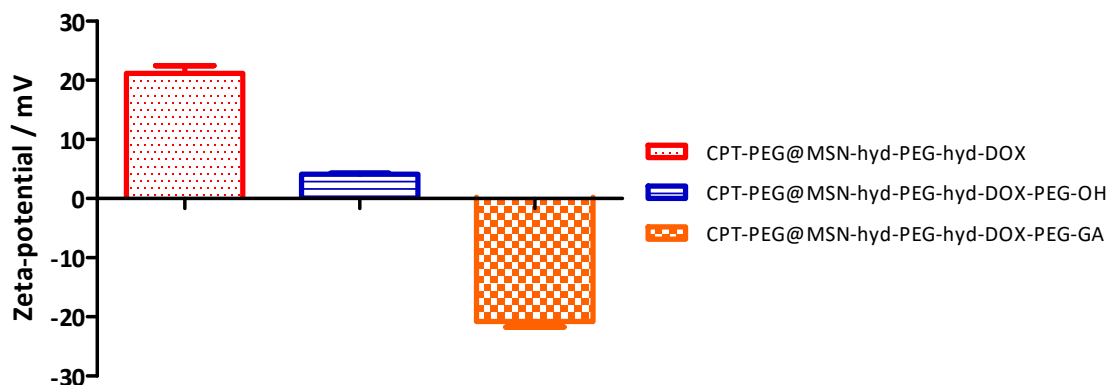


Figure 68. Zeta potential distribution of CP-PEG@MSN-hyd-PEG-hyd-DOX, CPT-PEG@MSN-hyd-PEG-hyd-DOX-PEG-OH and CPT-PEG@MSN-hyd-PEG-hyd-DOX-PEG-GA. Data represented as mean \pm SD ($n=3$). Data measurements pH 5.5.

System CPT-PEG@MSN-hyd-PEG-hyd-DOX show a zeta potential of + 21 mV. This value is consistent with the presence of the protonated amino group bonded to the sugar moiety of DOX (**1**). Whereas, for CPT-PEG@MSN-hyd-PEG-hyd-DOX-PEG-GA the potential was completely reverted, with a negative value of - 20 mV, which is in accordance to reported ones in the literature for similar systems due to the presence of the carboxylic acid of GA (**40**) [118]. Contrary, for the MSN functionalized with a benz-PEG (**42**), the zeta potential value found was + 4 mV.

2.4.4. Cellular uptake and intracellular distribution

Flow cytometry was carried out in order to compare the uptake of CPT-PEG@MSN-hyd-PEG-hyd-DOX-PEG-OH, CPT-PEG@MSN-hyd-PEG-hyd-DOX-PEG-GA and CPT-PEG@MSN-hyd-PEG-hyd-DOX in HepG2 cells (Figure 69 a)). The same experiment was performed as well with HeLa cells as a control due to the absence of GA receptors in its cytoplasmic membrane (Figure 69 b)).

As expected, decorated nanoparticles with GA (**40**) show more affinity for HepG2, with a 73% of DOX (**1**) fluorescence, than HeLa cells, with an 11% of DOX (**1**) fluorescence. Therefore, the ability of CPT-PEG@MSN-hyd-PEG-hyd-DOX-PEG-GA system to discriminate between cancer liver cells HepG2 and HeLa cells has been proved. On the other hand, CPT-PEG@MSN-hyd-PEG-hyd-DOX presents the highest uptake in both cell lines, with nearly 100% of DOX (**1**) fluorescence, independently on the presence of GA (**40**) receptors. It is hypothesized that the high zeta potential value (+ 20 mV) is responsible for the disruption of the cytoplasmic membrane, enhancing the uptake in both cell lines [148]. Finally, CPT-PEG@MSN-hyd-PEG-hyd-DOX-PEG-OH internalizes neither HepG2, 2% of DOX (**1**) fluorescence, nor HeLa cells, 9% of DOX (**1**) fluorescence. This type of MSN does not present any target ligand; hence non-internalization is expected for HepG2 cells. Besides, its charge is not positive enough (+ 4 mV) to disrupt the membrane of HeLa cells.

From the results obtained, it can be stated that the latter MSNs follows different uptake pathways. For instance, CPT-PEG@MSN-hyd-PEG-hyd-DOX may follow endocytosis mediated by the electrostatic interaction between the cationic character of the system and the negative cell membrane [218]. Contrarily, CPT-PEG@MSN-hyd-PEG-hyd-DOX-PEG-GA is most likely to follow receptor-mediated endocytosis because of the presence of the GA (**40**) ligand [130].

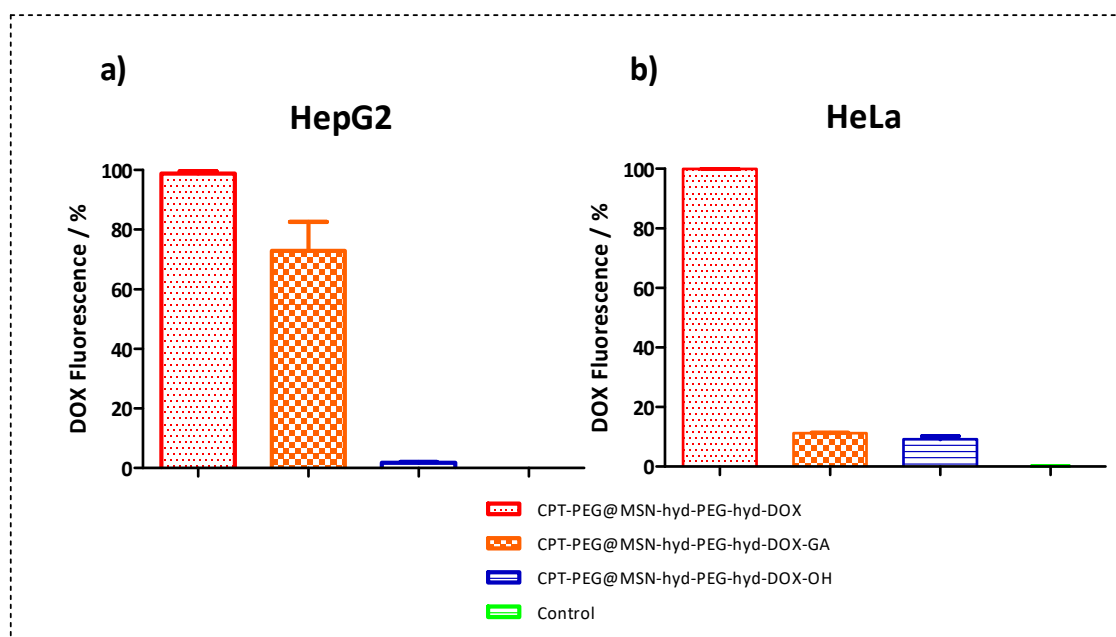


Figure 69. Flow cytometry analysis of HepG2 cells a) and HeLa cells b) that were incubated with CPT-PEG@MSN-hyd-PEG-hyd-DOX, CPT-PEG@MSN-hyd-PEG-hyd-DOX-PEG-GA, CPT-PEG@MSN-hyd-PEG-hyd-DOX-PEG-OH for 4 h at $100 \mu\text{g}\cdot\text{mL}^{-1}$. Data represented as mean \pm SD ($n=3$).

Additional evidence of the uptake was obtained through CLSM images for each DDS in HepG2 cells for 4 h (Figure 70). From inspection of Figure 70, it can be inferred how the DOX (**1**) fluorescence is high for the CPT-PEG@MSN-hyd-PEG-hyd-DOX and low for the targeted system with GA (**40**) after 4 h. Moreover, DOX (**1**) is principally located in the nucleus of the cells, which colocalize with the DAPI channel (Figure 70 c)), probably due to the rapidly bounding of this drug with the chromosomal DNA [225]. For CPT-PEG@MSN-hyd-PEG-hyd-DOX-PEG-OH (Figure 70 h)), the internalization within the HepG2 cells is nearly null due to the low interaction of the system with the cytoplasmatic membrane. This result is in agreement with the work of Vallet-Regi *et al.* [169], which reported that although pegylated MSN can indeed increase the circulation on the bloodstream, the uptake is hampered by the presence of PEG chains.

These results are consistent with the cytotoxicity assays performed in section 2.2.5 and 2.3.5. Thus, the low toxicity of the only loaded CPT (**4**), TPT (**4**) and CPT-PEG (**22**) MSN systems is derived for their inability to enter inside the cells.

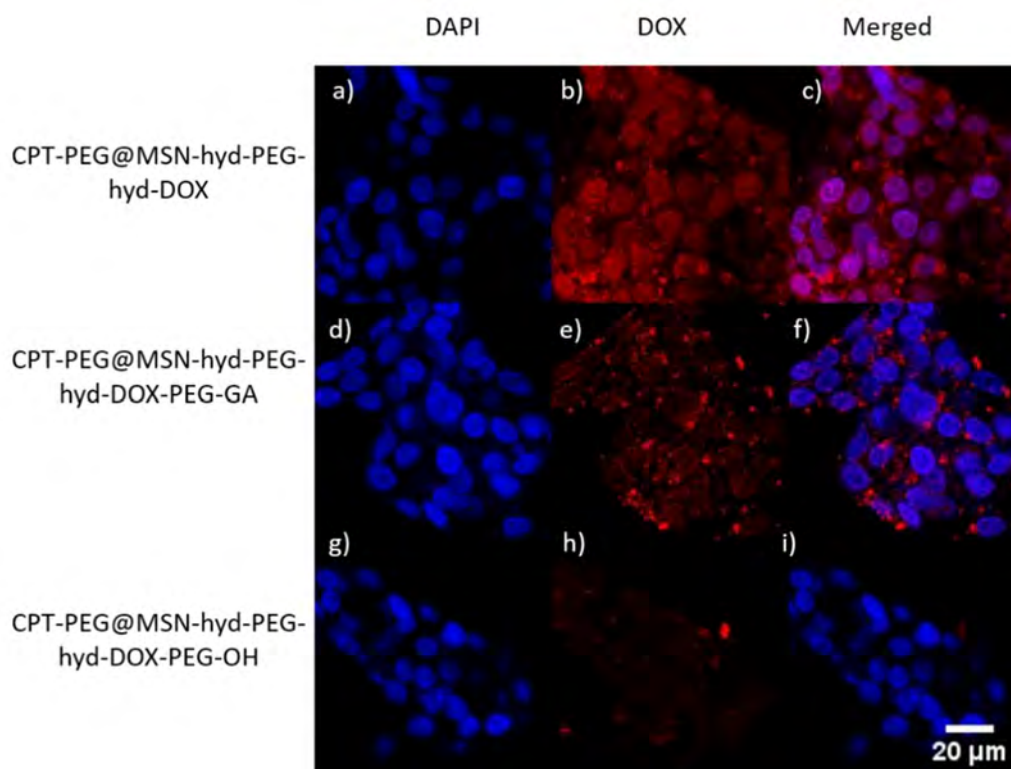


Figure 70. CLSM images of HepG2 cells incubated with CPT-PEG@MSN-hyd-PEG-hyd-DOX a), CPT-PEG@MSN-hyd-PEG-hyd-DOX-PEG-GA b) and CPT-PEG@MSN-hyd-PEG-hyd-DOX-PEG-OH d) at 37 °C for 4 h at 100 $\mu\text{g}\cdot\text{mL}^{-1}$. Scale bar 20 μm . Blue: dapi, red: DOX

In order to gain insight into the uptake of the systems, the kinetics of CPT-PEG@MSN-hyd-PEG-hyd-DOX and CPT-PEG@MSN-hyd-PEG-hyd-DOX-PEG-GA were studied in HepG2 cells from 1 h to 24 h (Figure 71).

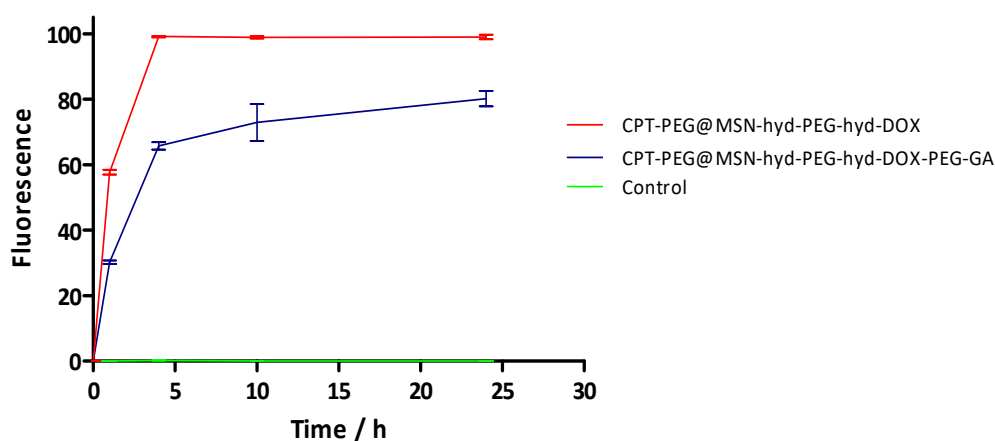


Figure 71. Kinetics of CPT-PEG@MSN-hyd-PEG-hyd-DOX and CPT-PEG@MSN-hyd-PEG-hyd-DOX-PEG-GA by Flow Cytometry of HepG2 cells at 1, 4, 10 and 24 h at 100 $\mu\text{g}\cdot\text{mL}^{-1}$. Data represented as mean \pm SD ($n=3$).

After a careful inspection of Figure 71, it can be established that the untargeted system (CPT-PEG@MSN-hyd-PEG-hyd-DOX) reaches a plateau after 4 h of incubation achieving 100% of internalization. Whereas for the GA (40) system (CPT-PEG@MSN-hyd-PEG-hyd-DOX-PEG-GA),

the maximum uptake efficiency at 10 h was 74-80%. Even at higher exposure times (24 h), the internalization did not increase, suggesting that the GA (**40**) receptors were completely saturated, thus preventing endocytosis.

The internalization of MSN in HepG2 cells was further studied by CLSM, labelling the endosomes of the cells with primary antibody RAB7, for two different periods of time: 1 h (Figure 72) and 10 h (Figure 73).

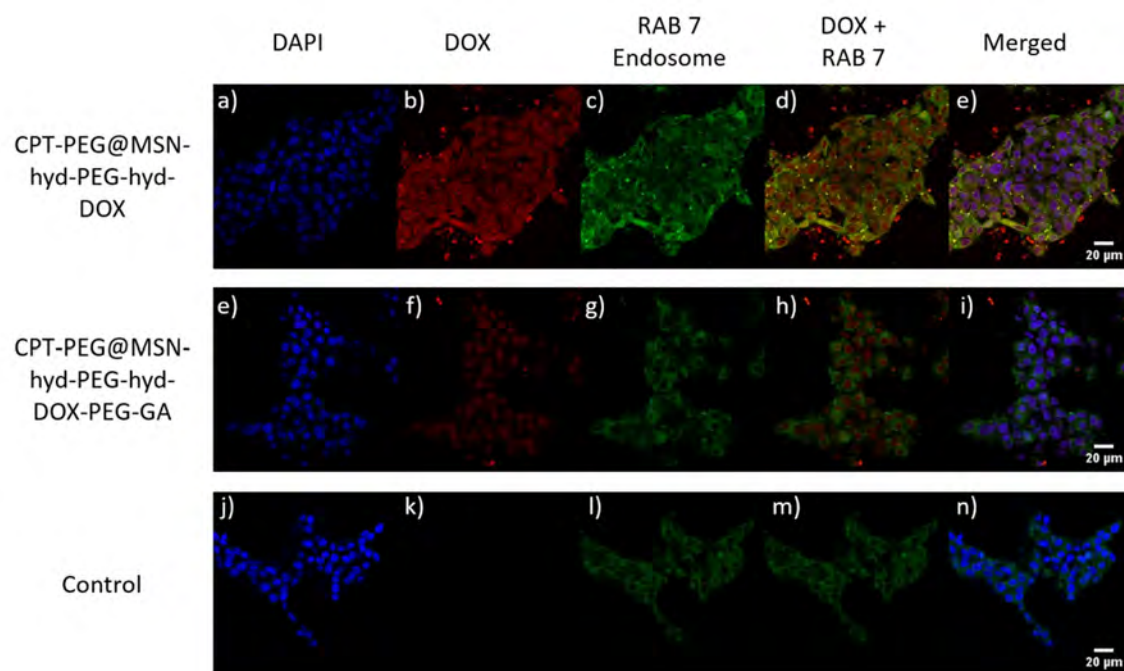


Figure 72. CLSM images of the uptake of CPT-PEG@MSN-hyd-PEG-hyd-DOX and CPT-PEG@MSN-hyd-PEG-hyd-DOX-PEG-GA (100 μg·mL⁻¹) at 37 °C for 1 h at 100 μg·mL⁻¹. Scale bar 20 μm. Blue: dapi, red: DOX, green: RAB7.

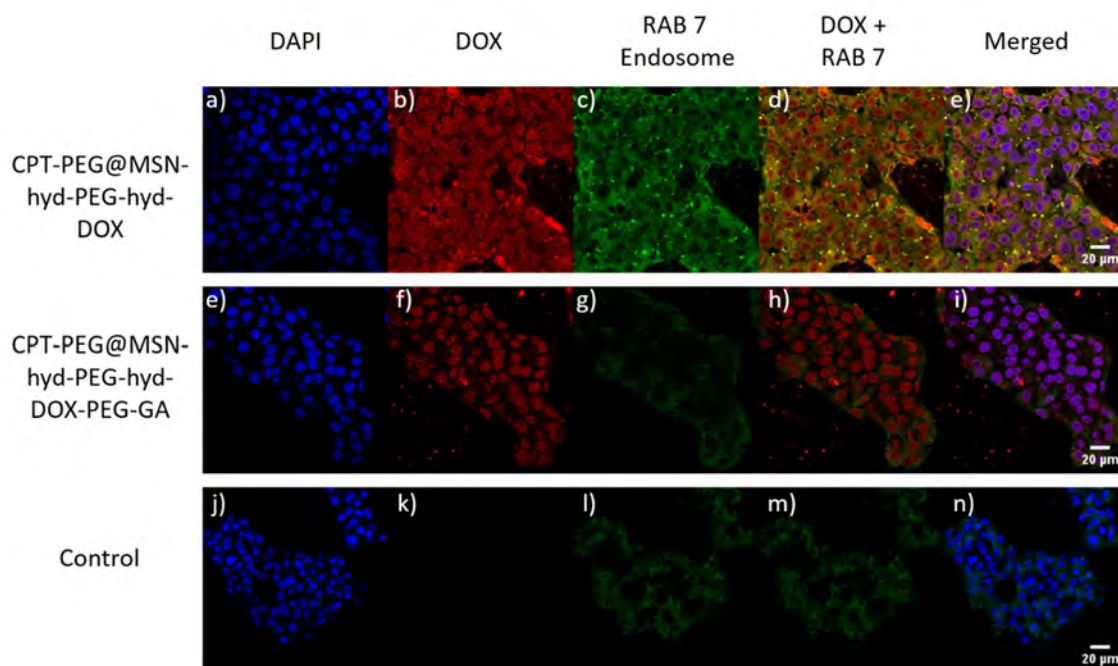


Figure 73. CLSM images of the uptake for 10 h of CPT-PEG@MSN-hyd-PEG-hyd-DOX and CPT-PEG@MSN-hyd-PEG-hyd-DOX-PEG-GA ($100 \mu\text{g}\cdot\text{mL}^{-1}$) at 37°C for 10 h at $100 \mu\text{g}\cdot\text{mL}^{-1}$. Scale bar $20 \mu\text{m}$. Blue: dapi, red: DOX, green: RAB7.

From inspection of (Figure 72 b)) and (Figure 72 f)) it can be assessed a difference in DOX (1) fluorescence for CPT-PEG@MSN-hyd-PEG-hyd-DOX and CPT-PEG@MSN-hyd-PEG-hyd-DOX-PEG-GA. The untargeted MSN system displays a higher amount of DOX (1) fluorescence in comparison with GA (40) decorated MSN. These results are in agreement with the kinetic study performed, which suggest that CPT-PEG@MSN-hyd-PEG-hyd-DOX was more rapidly internalized within the cells at 1 h than CPT-PEG@MSN-hyd-PEG-hyd-DOX-PEG-GA (Figure 71). In this sense, a similar result was obtained at 10 h for the same MSN systems (Figure 73 b)) and (Figure 73 f)) only detecting an increase of DOX (1) fluorescence.

However, it should be noted a main distinction regarding DOX (1) distribution in the cell organelles. For instance, DOX (1) released from CPT-PEG@MSN-hyd-PEG-hyd-DOX can be found either the endosomes or the nucleus of the cell (Figure 73 d)) due to their colocalization (yellow fluorescence). On the other hand, DOX (1) fluorescence from CPT-PEG@MSN-hyd-PEG-hyd-DOX-PEG-GA was only detected within the nucleus of the cell (Figure 73 h)). These results are attributed to the endosomal escape capabilities of the MSN systems. In this sense, the colocalization of endosomes and DOX (1) released from CPT-PEG@MSN-hyd-PEG-hyd-DOX demonstrated the presence of this system within this organelle (Figure 73 d)). Highly positive MSN, such as this MSN (+ 20 mV), tend to be trapped within endosomes due to its inability to disrupt the endosomal membrane [226]. Differently, DOX (1) fluorescence from CPT-PEG@MSN-hyd-PEG-hyd-DOX-PEG-GA does not colocalize with endosomes (Figure 73 h)) suggesting that a rapid endosome escape occurs. This assumption agrees with the anionic character of this

nanoparticle (- 20 mV). It has been reported that negatively charged MSN are prompt to escape to the endosome via the proton sponge effect. Besides, more negatively charged nanoparticles would escape more easily from endosomes of cancer cells owing to their high buffering capacity [226]. For this reason, released DOX (**1**) is mainly found in the nuclei ((Figure 72 f) and Figure 73 f)).

2.4.5. Cytotoxicity

The cytotoxicities of MSN systems: CPT-PEG@MSN-hyd-PEG-hyd-DOX, CPT-PEG@MSN-hyd-PEG-hyd-DOX-PEG-OH and CPT-PEG@MSN-hyd-PEG-hyd-DOX-PEG-GA were determined by measuring the growth inhibition of HepG2 cells using the MTT assay (Figure 74).

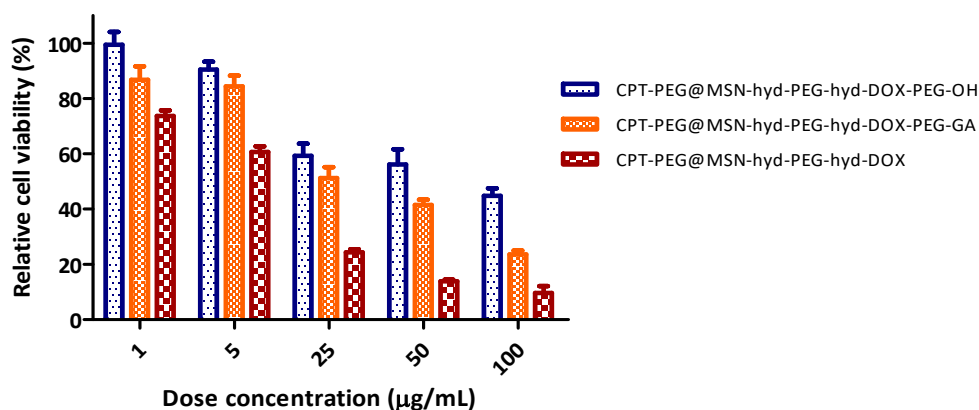


Figure 74. Cell viability of HepG2 cells incubated with CPT-PEG@MSN-hyd-PEG-hyd-DOX-PEG-OH, CPT-PEG@MSN-hyd-PEG-hyd-DOX-PEG-GA and CPT-PEG@MSN-hyd-PEG-hyd-DOX for 72 h. Data represented as mean \pm SD ($n=3$).

As expected, the relative cell viabilities obtained are consistent with the uptake experiments. In this sense, control nanoparticles (CPT-PEG@MSN-hyd-PEG-hyd-DOX-PEG-OH) shows the lowest cytotoxicity due to its inability to be internalized within the cells. On the other hand, targeted system (CPT-PEG@MSN-hyd-PEG-hyd-DOX-PEG-GA) exhibit the second cytotoxicity accordingly with his uptake capability. Lastly, starting system CPT-PEG@MSN-hyd-PEG-hyd-DOX shows the highest cytotoxicity in accordance with his high uptake.

2.4.6. Conclusions and Outlook

GA ligand has been successfully attached to the DOX (**1**) drug located in the outer surface of the CPT-PEG@MSN-hyd-PEG-hyd-DOX system by means of a benzoic-imine bond. To do so, aldehyde benz-PEG-GA (**45**) has been synthesised and characterized by $^1\text{H-NMR}$ and HRMS. The as-synthesized MSN were characterized by usual methods. As expected, GA labelled MSN show a negative zeta potential (- 20 mV), which is consistent with the presence of the carboxylic acid of the GA moiety at the surface of the nanoparticle [118].

Uptake cytometry assays have demonstrated that the GA system is selectively internalized by HepG2 cells. Besides, DOX (**1**) released from CPT-PEG@MSN-hyd-PEG-hyd-DOX-PEG-GA is rapidly localized in the nuclei. This result is rationalized in terms of efficient endosomal escape ascribed to the presence of the anionic charge of GA (**40**) ligand.

Although the targeting towards HepG2 cells is clearly improved with the GA (**40**) ligand, the uptake capability of the starting system CPT-PEG@MSN-hyd-PEG-hyd-DOX is higher than CPT-PEG@MSN-hyd-PEG-hyd-DOX-PEG-GA due to its cationic character. It is suggested that this uptake behaviour is responsible for the cytotoxicities displayed for the MSN systems.

This result opens the door to the functionalization of different ligands in order to provide different modes of selectivity to the system. Finally, on the current time *in vivo* experiments are being carried out to determine the affinity of the synthesised targeting system to the liver and the reduction of the tumoral tissue located in it.

2.5. Delivery of chemotherapeutic drugs and a PDT drug based on an MSN

2.5.1. Introduction

In chapter 2.2, it has been demonstrated how the co-delivery of DOX (**1**) and CPT (**4**) to HeLa cells by MSN results in a strong synergistic effect. Moreover, the derivatisation of the insoluble CPT (**4**) with a PEG chain has increased its solubility, achieving better loading values inside the MSN, as well as an improvement in cell mortality in HepG2 cells. However, combined chemotherapeutic agents not always can counteract the MDR effect due to the possibility of cells to develop other mechanisms to eliminate or fight against chemical drugs [227]. This drawback can be overcome with the combination of therapies. For instance, the combination of photodynamic therapy (PDT) with chemotherapy have shown promise results to overcome such effect [39].

In short, the mechanism of PDT is based upon three pillars: a photosensitizer (PS), light and molecular oxygen (Figure 75). None of these agents is individually toxic, but the combination of these three factors cause cellular and tissue damage [228].

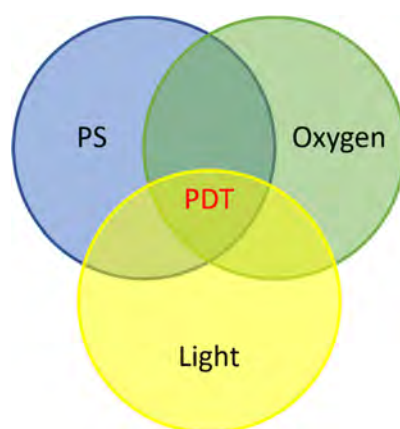


Figure 75. PDT factors.

The mechanism of action of photodynamic therapy is based on the photochemical production of ROS species after irradiation of a PS with light. This process leads to the transfer of one electron to a higher-energy orbital (Figure 76). Thus, the specie derived from such reaction is very unstable and emits this excess of energy as fluorescence and/or heat [229]. Instead, an excited PS may undergo an intersystem crossing to form a more stable triplet state. The evolution of this state follows two kinds of mechanism: type I and type II. Type I occurs when the PS reacts directly with an organic molecule in a cellular microenvironment, acquiring a hydrogen atom or electron to form a radical. The following autoxidation of the reduced PS

produces a superoxide anion radical (O_2^*) or hydroxyl (OH^*) (Figure 76) [230]. In contrast, type II mechanism refers to the transfer of energy from triplet state to molecular oxygen leading to the formation of singlet oxygen (1O_2) (Figure 76). The formation of these species is responsible for the cytotoxicity of PDT. The toxicity can be inter-related from the direct cytotoxic effect on cells, driven by ROS formation, and the damage to the tumour vasculature.

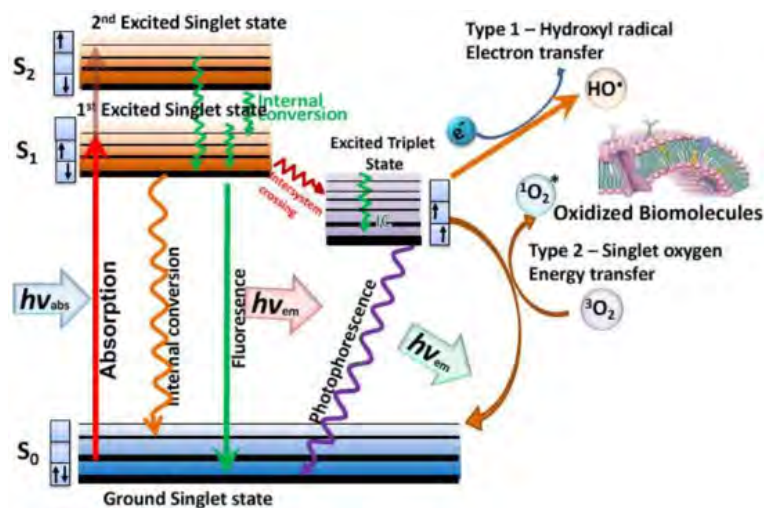


Figure 76. Schematic illustration of photodynamic therapy [231].

PDT is a doubly selective therapy because the active species, 1O_2 and ROS, are formed by irradiation of a laser and can diffuse only through 0.01-0.02 μm from the treated area. Therefore, the cellular damage is restricted to a very narrow space depending on the localization of the PS [230], [232].

Most of the PS used in cancer therapy are based on the tetrapyrrole backbone and have extended π -conjugation system making them highly planar and hydrophobic [233]. The first PS was Photofrin, a purified form of a water-soluble mixture of porphyrins. However, the relative low absorbance (630 nm) and long-lasting skin photosensitivity encourage the substitution of this PS by a second generation of these molecules [233]. In this regard, phthalocyanines (Pcs) have become an ideal PS due to their own intense absorption in the phototherapeutic window, high stability, biocompatibility and the tuneability of optical and photophysical properties modifying the core [234], [235].

This kind of compounds have been scarcely used in combination with DOX (**1**) or CPT (**4**) for cancer treatment. There is just one example in the literature where a Pc is combined with DOX (**1**) and subsequently encapsulated within nanoparticles. In 2017, Ng and Lo *et al.* [236], proposed to functionalize DOX (**1**) with an hydrolysable linker to Pc. Afterwards, the conjugated was grafted to the walls of the MSN via azide-alkyne cycloaddition reaction. Like similar systems, the PS and DOX (**1**) are released to the media by scission of the bond in cancerous cells. Finally,

irradiation of the PS induces the photo-damage of the PDT, which is combined with the action of the chemotherapeutic drug.

To the best of our knowledge, there are no reports that combined, DOX (**1**) and CPT (**4**), with a Pc employing MSNs as a DDS. Hence, following our radial-capping approach, it is proposed to create a regioselective MSN which will act with two different modes of action. The well-known synergistic effect between DOX (**1**) and CPT (**4**), which has been carefully studied in 2.2.5., in combination with the photodynamic activity of a particular type of Pc (**46**) (Figure 77) [237].

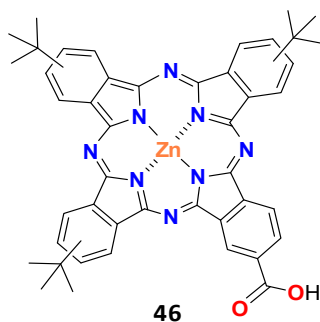


Figure 77. Molecular structure of zinc carboxyphthalocyanine (TT1).

According to this plan, TT1 (**46**) would be attached to CPT (**4**) with a cleavable PEG linker (Figure 78 b)). The presence of this PEG is expected to prevent the formation of aggregates and enhance the solubility of the PS [238]. This fact would improve the loading of the conjugate within the pores of the MSN. Then, the system would be capped by means of the dihydrazide PEG (**14**) and DOX (**1**), following the methodology presented in section 2.2 (Figure 78 a)).

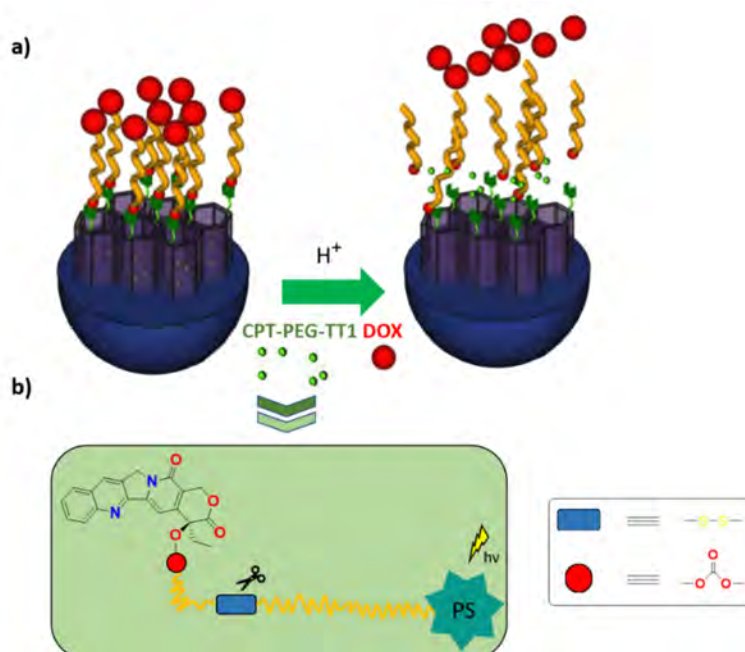


Figure 78. a) MSN carrying a combination of two therapies; b) Schematic illustration of the structural compounds of the conjugate.

2.5.2. Design of TT1-PEG-CPT conjugate (47)

As has been depicted in section 2.3, the functionalization of a cleavable PEG linker enhance the solubility of hydrophobic drugs and permits the selective release of the active drugs within the cancerous cells. Thereby, cognizant the procedure of attaching PEG linkers to CPT (**4**), the derivatisation of one of its ends is used to add the PS. As it is illustrated in Figure 79, the proposed conjugate contains a disulphide bridge that will be cleaved due to the reductive environment of cancerous cells, which possesses a higher concentration of GSH than the physiological medium [239], [240].

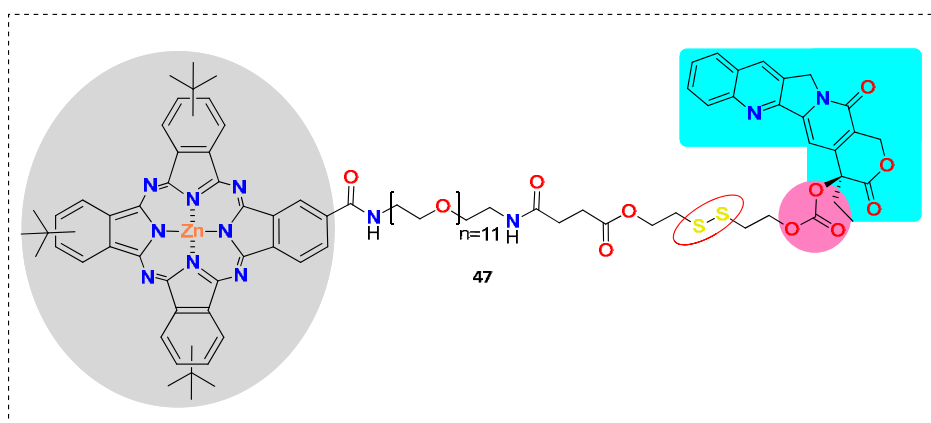


Figure 79. TT1-PEG-CPT conjugate (**47**). Key bonds to the synthesis of **47** are remarked by red circles.

2.5.2.1. Synthesis of TT1-PEG-CPT (47)

In Figure 80 is depicted the retrosynthetic pathway to synthesis TT1-PEG-CPT (47).

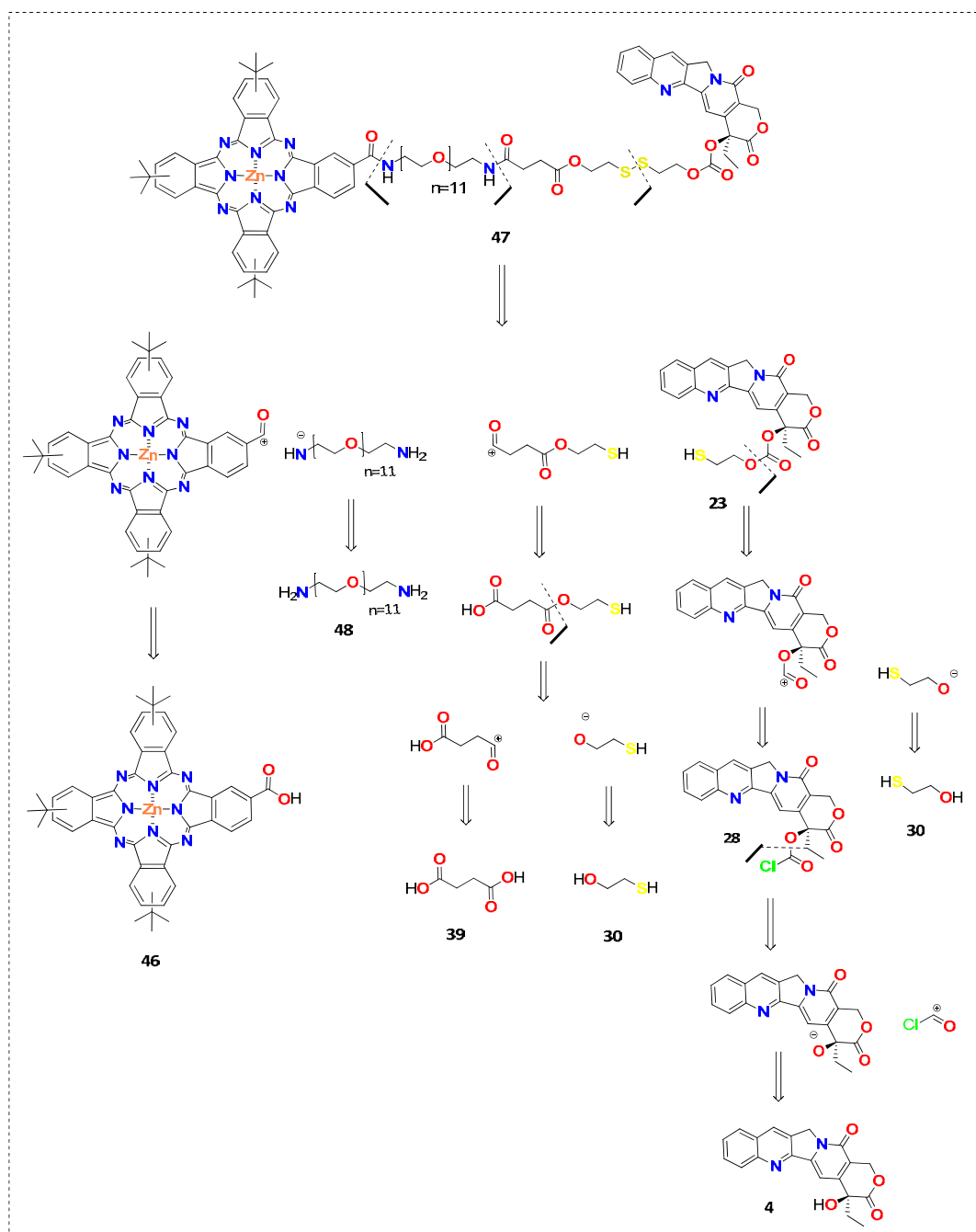


Figure 80. Retrosynthetic analysis of compound 47.

As can be observed in Figure 80, both drugs are linked through two different amide bonds. To form the first amide bond with a reductive disulphide bond, the reaction of CPT-PYR (34) with 2-mercaptoethanol (30) was carried out, leading to the formation of alcohol 49. Finally, the carboxylic acid was obtained by reaction led by the alkoxide formation through DMAP providing (S)-4-(2-((2-(((4ethyl-3,14-dioxo-3,4,12,14-tetrahydro-1H-pyrano[3',4':6,7]indolizino[1,2-

b]quinoline-4-yl)oxy)carbonyl) oxy)ethyl) disulfanyl)ethoxy) -4-oxobutanoic acid (CPT-COOH) (**50**) (Figure 81) [241].

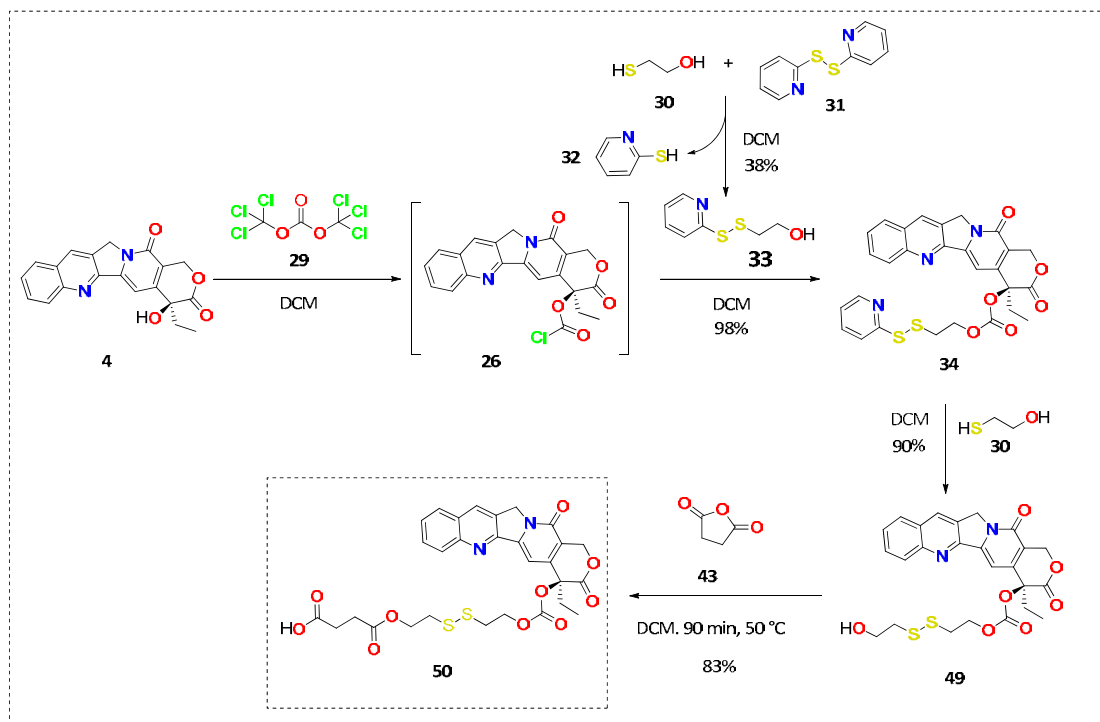


Figure 81. Synthetic route for the obtention of CPT-COOH (**50**).

The spectrum of CPT-COOH (**50**) obtained (Figure 82) is in agreement with reported data [241]. The signal at 3.7 ppm (2H) (red dot), corresponding to the adjacent carbon from alcohol group **49**, is shifted to higher field, 4.25 ppm (2H) (blue dot), after the addition of the ester moiety **50** (Figure 82 b)).

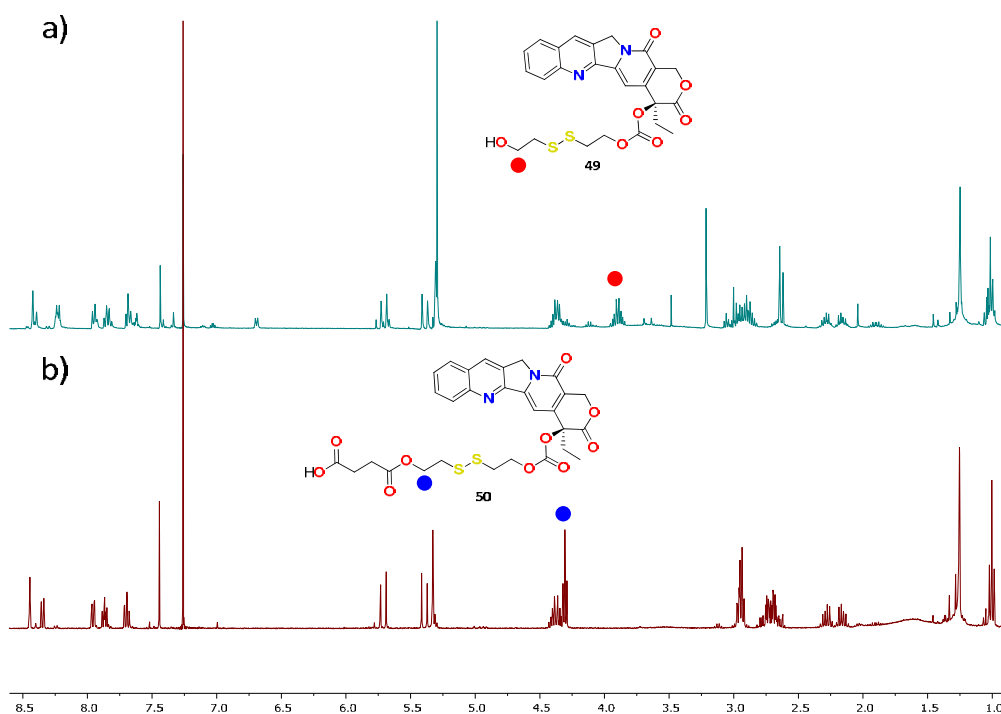


Figure 82. $^1\text{H-NMR}$ spectra comparison between compounds **49** a) and **50** b).

The second amide bond can be introduced to TT1 **46** after activation of the carboxylic acid with NHS to yield **51**. This compound was a gift from Tomas Torres group. Then, amide formation was carried out by reaction between amino PEG **52** and compound **51** in THF during 16 h to yield product **53** (Figure 83).

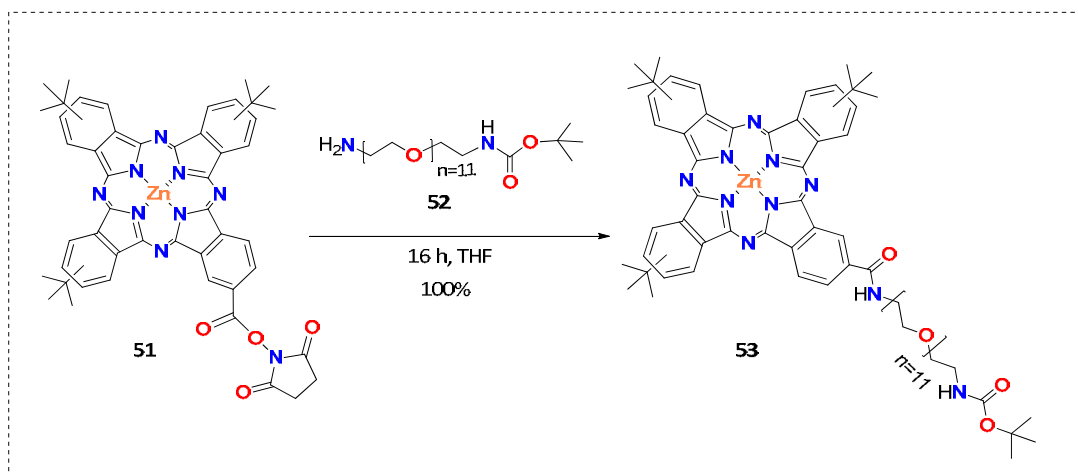


Figure 83. Synthesis of compound **53**.

Unexpectedly, the product cannot be identified through $^1\text{H-NMR}$ due to the phthalocyanine broad signals at the aromatic region. Although, *tert*-butyl protons can be identified at 1.43 ppm (27 H) and 1.44 ppm (9H) belonging to *tert*-butyl protons of the aromatic ring and *tert*-butyl protons adjacent to carbamate moiety, respectively (Figure 84).

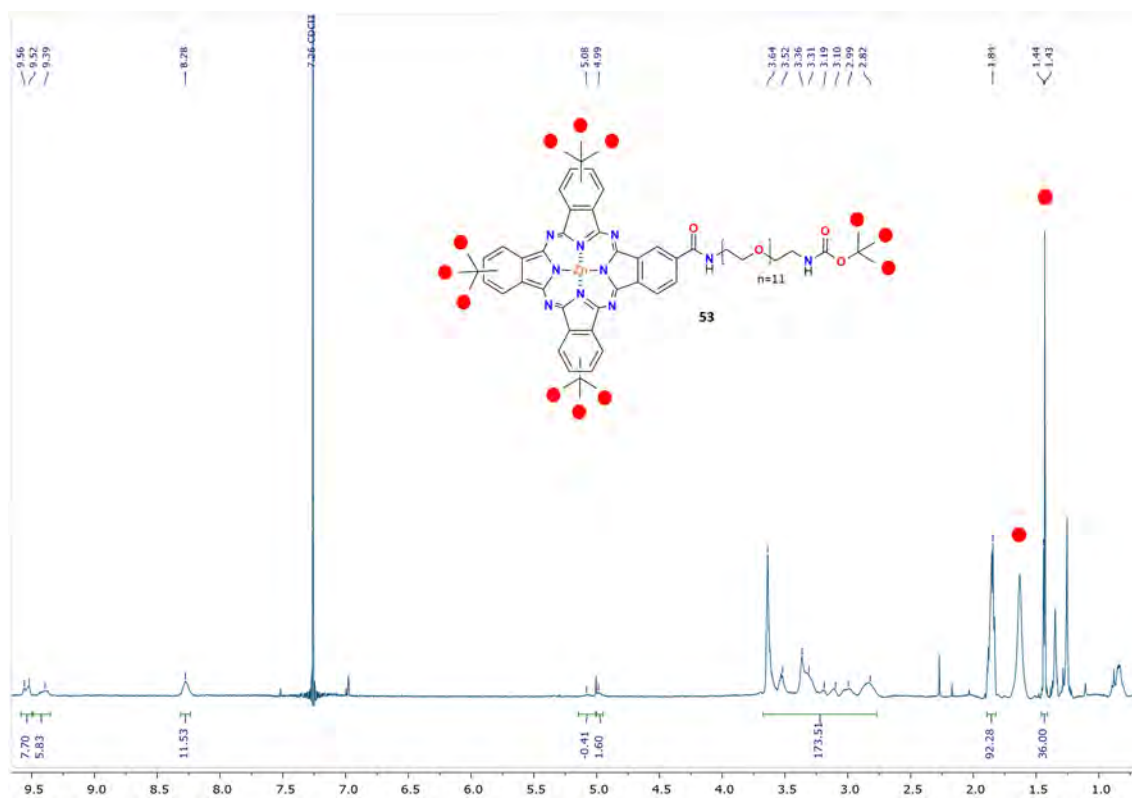


Figure 84. ¹H-NMR spectra of compound **53**.

Further support for the assignment of compound **53** was obtained by ESI. Figure 85 shows the data of ESI, which is in agreement to the exact mass of the desired molecule **53**.

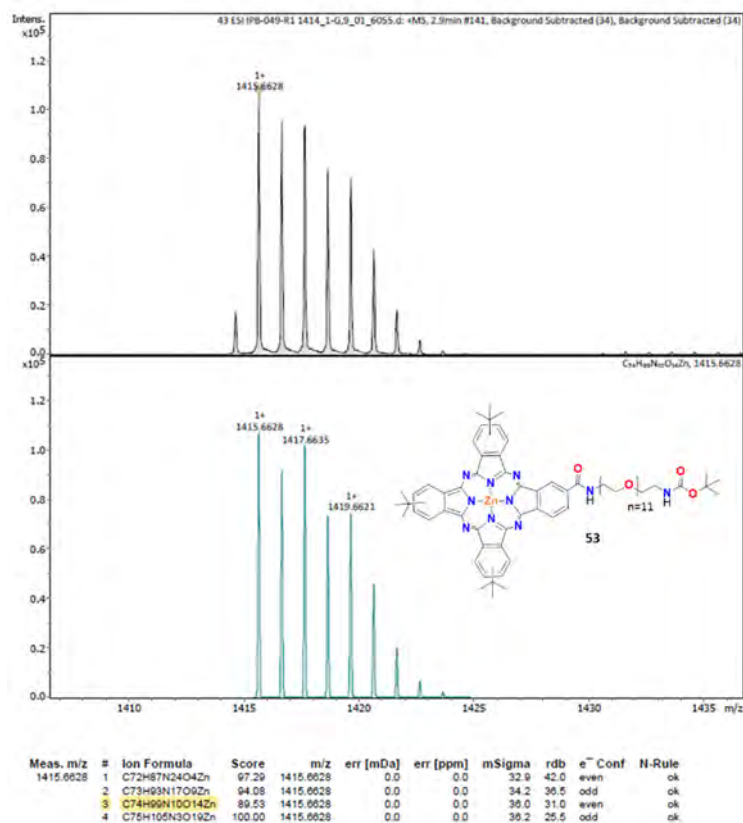


Figure 85. ESI-FIA-TOF spectrum of **53**.

The following goal was to activate carboxylic acid of **50** to react with the deprotected amine **54** (Figure 86). Thereby, after the deprotection of **53** with TFA in DCM, the activation *in situ* of the carboxylic acid **50** was achieved using PyBOP [242]. This coupling reagent has been chosen due to its excellent performance in high weight molecules such as peptides [243]. The mechanism of action of this coupling reagent starts on the deprotonation of carboxylic acid by a base yielding a carboxylate, which in turn, attack the electrophile position of the phosphonium salt of PyBOP. Once the activated acid is formed (HOBt), the primary amine attacks leading to the formation of the amide (**47**) (TT1-PEG-CPT) [244].

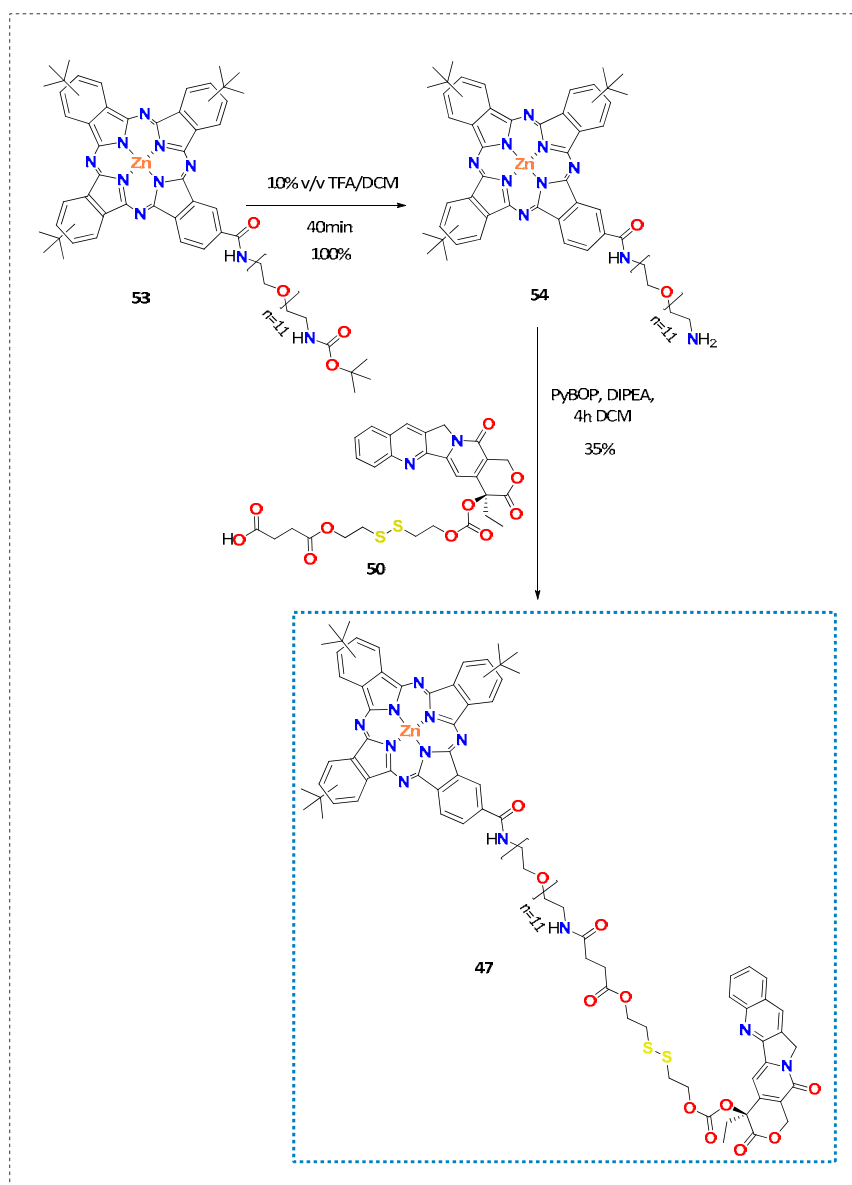


Figure 86. Synthesis of compound **47**.

Finally, the purification of this new compound was accomplished by silica gel column chromatography. After the proper elimination of the undesired reactants and reagents with AcOEt, TT1-PEG-CPT (**47**) was eluted with a gradient mixture from 99:1 DCM:MeOH to 9:1 DCM:MeOH. A blue sticky solid was obtained, which was further purified/dried after 2-3 washing steps with pentane and methyl *tert*-butyl ether. Hence, a blue crystal solid product was finally achieved and eventually, $^1\text{H-NMR}$ was successfully registered in CDCl_3 (Figure 87).

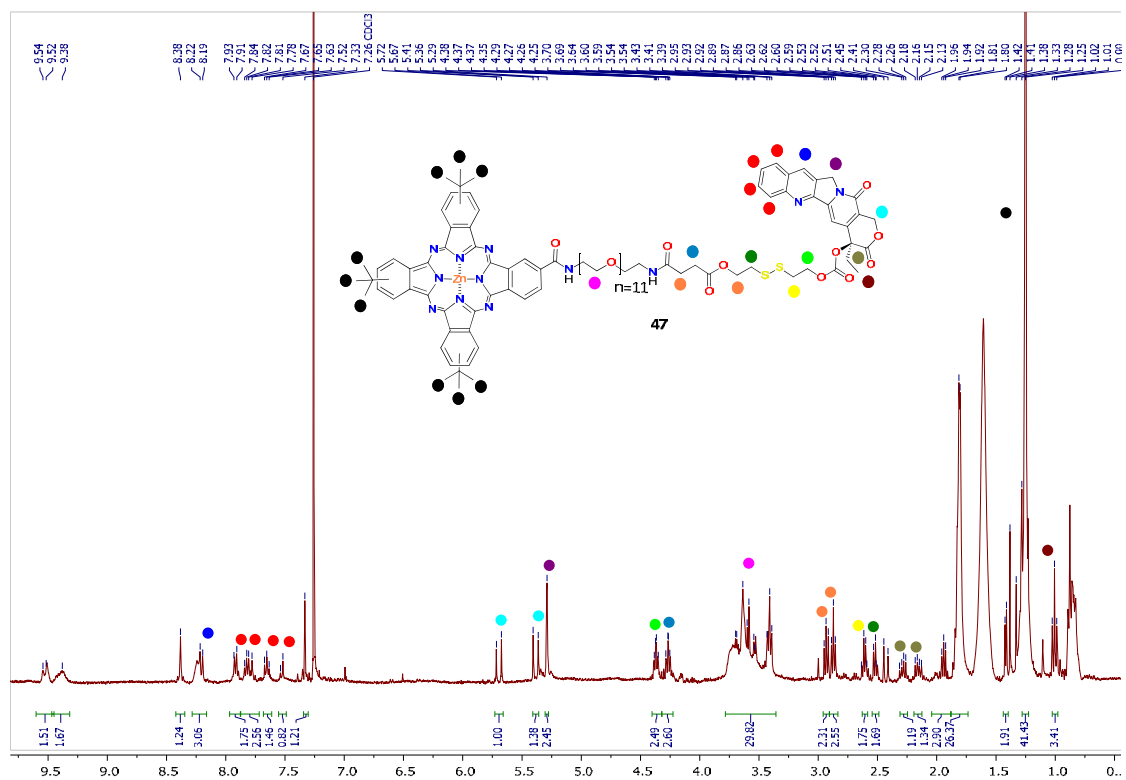
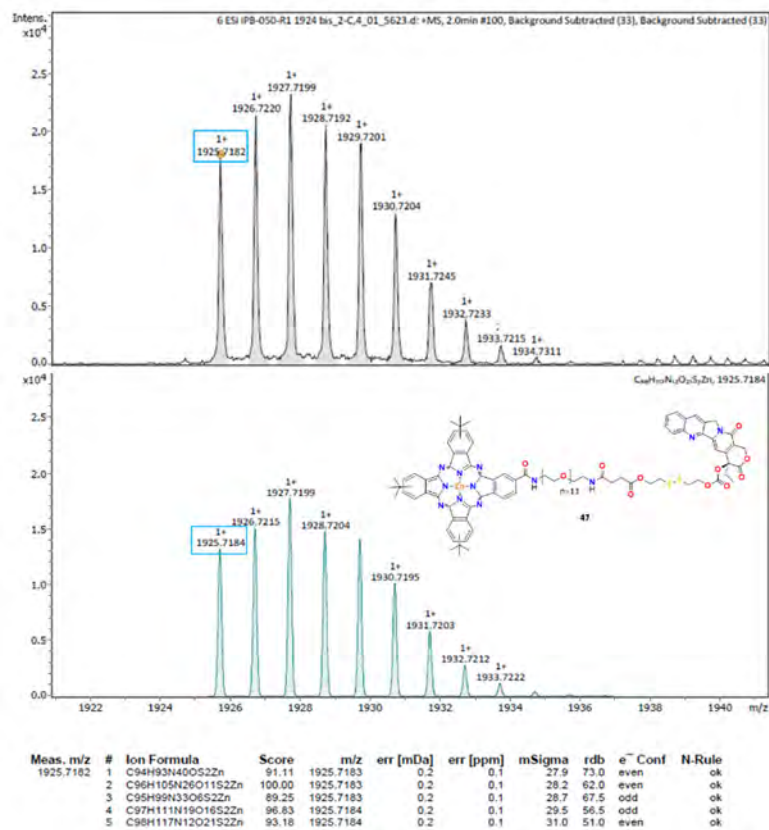


Figure 87. $^1\text{H-NMR}$ spectrum in CDCl_3 of TT1-PEG-CPT (**47**).

Further evidence of the accomplishment of the reaction was obtained after the characterization given through HRMS. The most abundant peak is 1927.7199 m/z , that corresponds to the exact molecular mass of 1925.7184 g/mol in agreement with the chemical formula of the desired product **47**.

Figure 88. ESI-FIA-TOF spectrum of **47**.

2.5.2.2. Cleavage of TT1-PEG-CPT (**47**)

In order to assess the chemical behaviour of the linker under reductive conditions, the cleavage study of TT1-PEG-CPT (**47**) was carried out by *tlc* using the 7:3 dioxane:Cy as eluents. A sample of **47** was treated with propane-1,3-dithiol (**55**). From inspection of Figure 89, it was noticed the appearance of a new fluorescence spot more polar, belonging to CPT (**4**). Besides, it was also observed a colour change from red purplish to red fluorescence, which is hypothesized to be the compound **56**, in agreement of non-aggregated phthalocyanine. Furthermore, the cleavage of the disulphide bridge, which involved the release mechanism of CPT (**4**) driven by GSH, leads with an intramolecular cyclisation providing the 1,3-oxathiolan-2-one (**25**) and thiirane (**57**) [245].

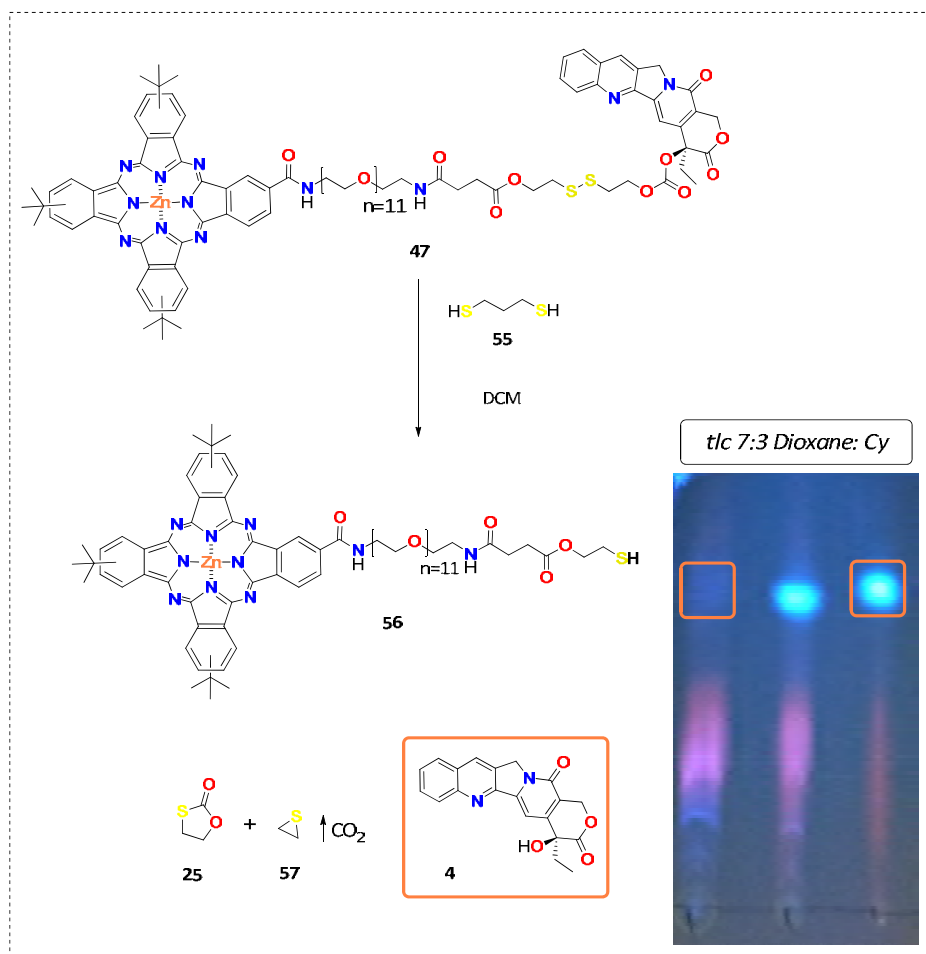


Figure 89. Disulphide bridge cleavage monitored by tlc 7:3 Dioxane: Cy. Spot of CPT (**4**) circled in orange.

2.5.3. Construction of the DDS

The functionalized nanoparticles ($\text{MSN}-(\text{NH}_2)_i(\text{CHO})_o$) developed in section 2.2 were used to load the TT1-PEG-CPT (**47**) and DOX (**1**). This process was delineated in Figure 90.

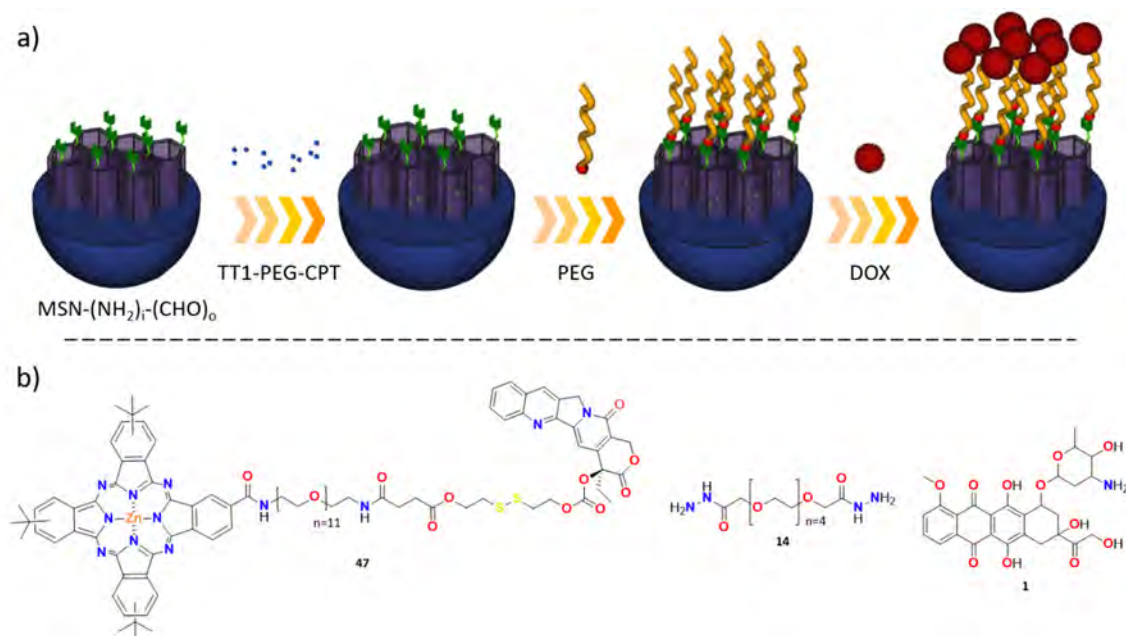


Figure 90. Construction of the DDS loaded with TT1-PEG-CPT (**47**).

2.5.3.1. Loading of the TT1-PEG-CPT (**49**) into $\text{MSN}-(\text{NH}_2)_i(\text{CHO})_o$

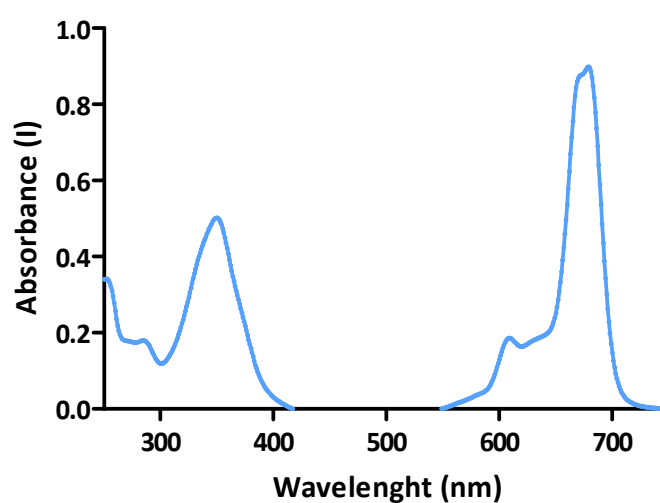
The first step entails the loading of the conjugate. Thus, different dissolvent mixture to achieve the best loading of CPT-TT1-PEG (**47**) were explored. According to Lo *et al.* [236], [246], and Chang *et al.* [247], DMF and DMSO are the most reported solvents mostly used for solubilizing phthalocyanine conjugates. In our hands, these conditions were not optimal for the loading. It should be noted that MSN are better dispersed in polar protic organic solvents such as MeOH or EtOH [248], [249]. Besides, those solvents enhance the embedding of drugs into the porous.

The best loading conditions were achieved with MeOH obtaining an 8% of TT1-PEG-CPT (**47**) within the nanochannels of the MSN (Table 7).

Table 7. Values of Q band in nm and loading in % of solvents used to load TT1-PEG-CPT (**47**).

Solvent	λ_{\max} / nm	Loading / %
CHCl ₃ /MeOH 4:1	684	6
DMF	680	2
DMSO/MeOH 4:1	680	4
MeOH	679	8

A well-resolved shape spectrum in MeOH was obtained (Figure 91).

**Figure 91.** Shape of absorption spectrum of TT1-PEG-CPT (**47**) in MeOH.

The electronic absorption spectrum of the conjugate **47** in MeOH is typical for monomeric nonaggregate phthalocyanines [250]. Apart from an intense and sharp Q band at 679 nm, it can be detected a broadband at 350 nm and a weak vibrionic band at 609 nm.

After the entrapment of TT1-PEG-CPT (**47**), the construction of the DDs system (TT1-PEG-CPT@MSN-hyd-PEG-hyd-DOX) was carried out following the capping with the PEG linker (**14**) and DOX (**1**) (2.2) (Figure 90).

2.5.3.2. Release of TT1-PEG-CPT (47)

Release experiments were performed at pH 4, pH 5.5 and pH 7.4 to mimic the physiological and tumoral cells environments. The UV/Vis absorption spectrum of the conjugate **47** in acetate buffer at pH 4 was registered (Figure 92).

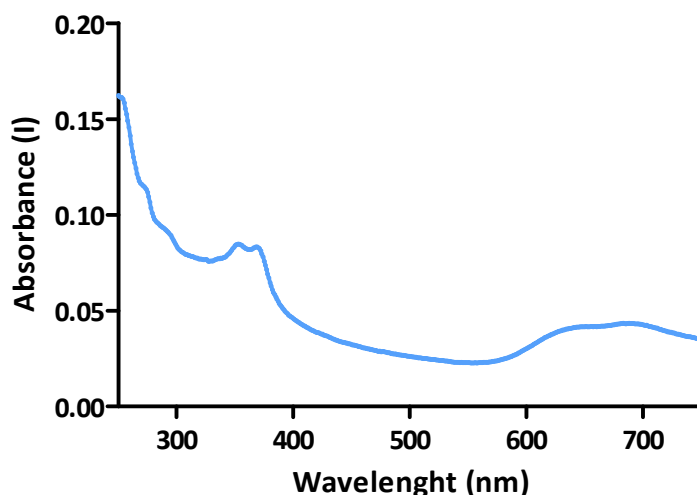


Figure 92. Absorption spectrum shape of TT1-PEG-CPT (**47**) in acetate buffer (0.1M NaAcO/0.1M AcOH) pH 4.

As expected, the characteristic bands of a Pc (Figure 91) emerged with low intensity and broad shape, remarking the Q band, lower than the band at 350 nm. These features correspond to the presence of a high level of aggregates of the conjugate **47**, caused by its low solubility in aqueous media [238]. Therefore, the amount of TT1-PEG-CPT (**47**) released cannot be accurately calculated. For this reason, an extraction with CHCl_3 of the target molecule is envisioned due to the high solubility of the compound in this solvent.

In Figure 93 a), is represented the release of the conjugate **47** for 24h. A burst release of the conjugate takes place during the first 2 h. Subsequently, a gradual release was obtained, achieving a total amount of 6% released. It is hypothesized that the low release can be attributed to the high insolubility of this molecule in water.

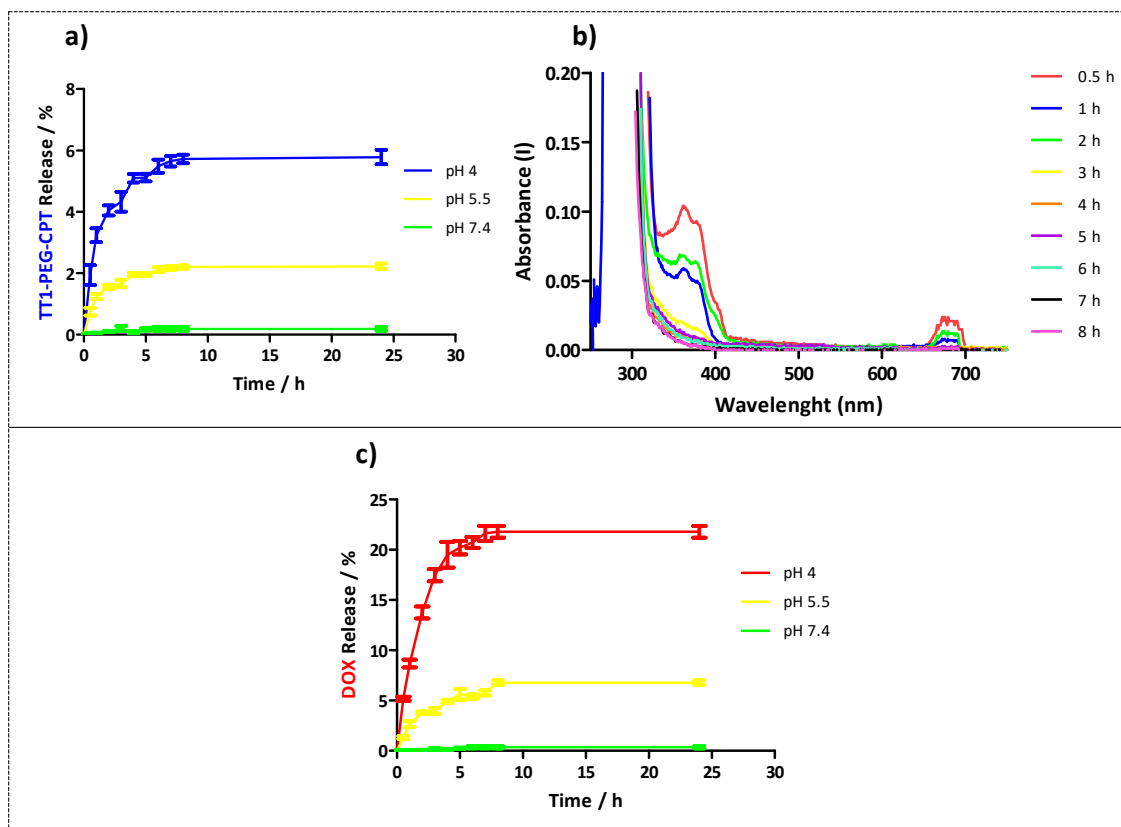


Figure 93. a) TT1-PEG-CPT (**47**) release profile at pH 4, pH 5.5 and pH 7.4 values under stirring at 100 rpm and $t=37$ °C b) Absorption supernatants of TT1-PEG-CPT (**47**) in CHCl_3 from pH 4 and c) DOX (**1**) release at pH 4, pH 5.5 and pH 7.4 values under stirring at 100 rpm and $t=37$ °C.

On the other hand, in Figure 93 b) the absorbance of supernatants extracted from aqueous acetate buffer (pH 4) with CHCl_3 is shown. From inspection of Figure 93 b), it can be concluded that compound **47** can be disaggregated after the extraction with the organic solvent. Conjugate **47** can be observed again in its monomeric form instead of heterogeneous aggregates. Even though the less level of aggregation presented in CHCl_3 than in aqueous media, the shape of Q-band presents lower intensity than in Figure 91.

On the other hand, a burst release of DOX (**1**) was obtained after 8 h for pH 4 and pH 5.5. Then a sustainable release was kept till 24 h (Figure 93 c)).

2.5.4. Cellular uptake and intracellular distribution

To corroborate the endocytosis of the nanoparticle, TT1-PEG-CPT@MSN-hyd-PEG-hyd-DOX, was quantitatively analysed by fluorescence flow cytometry in HeLa cells for 4 h (Figure 94). It can be assessed that nearly 100% of the system was effectively internalized within HeLa cells. The internalization is consistent with previous results (2.2.4), that can be ascribed to the cationic character of the MSN produced by the protonated $-\text{NH}_2$ of DOX (**1**) [151].

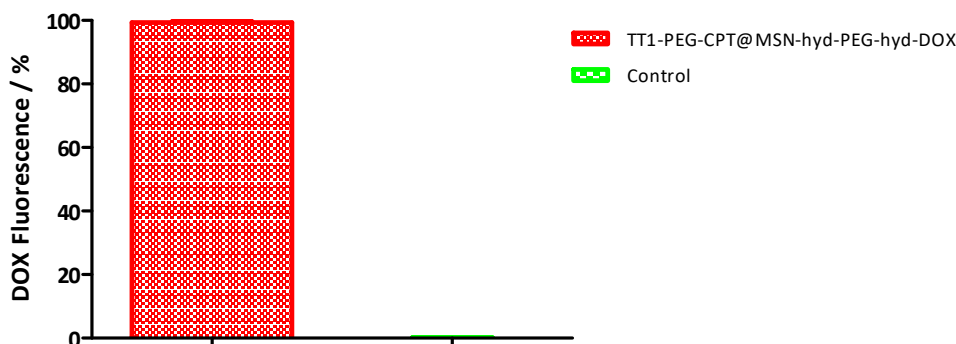


Figure 94. Flow cytometry analysis of HeLa cells that were incubated with TT1-PEG-CPT-PEG@MSN-hyd-PEG-hyd-DOX for 4 h at $100 \mu\text{g}\cdot\text{mL}^{-1}$.

More evidence of the cellular internalization was obtained after CLSM acquisition, which was employed to monitor cellular uptake, sense intracellular DOX (1) release and image the cancer cells. The protocol is as follows: HeLa cells were incubated with $100 \mu\text{g}\cdot\text{mL}^{-1}$ of TT1-PEG-CPT@MSN-hyd-PEG-hyd-DOX for 4 h at 37°C . As can be observed in Figure 95, MSN are internalized through endosome since DOX (1) and primary antibody rab7 (endosome) colocalize (Figure 95 d)). Besides, DOX (1) can be detected inside the nucleus of the cell, which is a well-known feature of this drug (Figure 95 e)). It seems that the endosome formation is strictly related to the presence of nanoparticles in the medium since fewer endosomes are present in the control cells (Figure 95 g)).

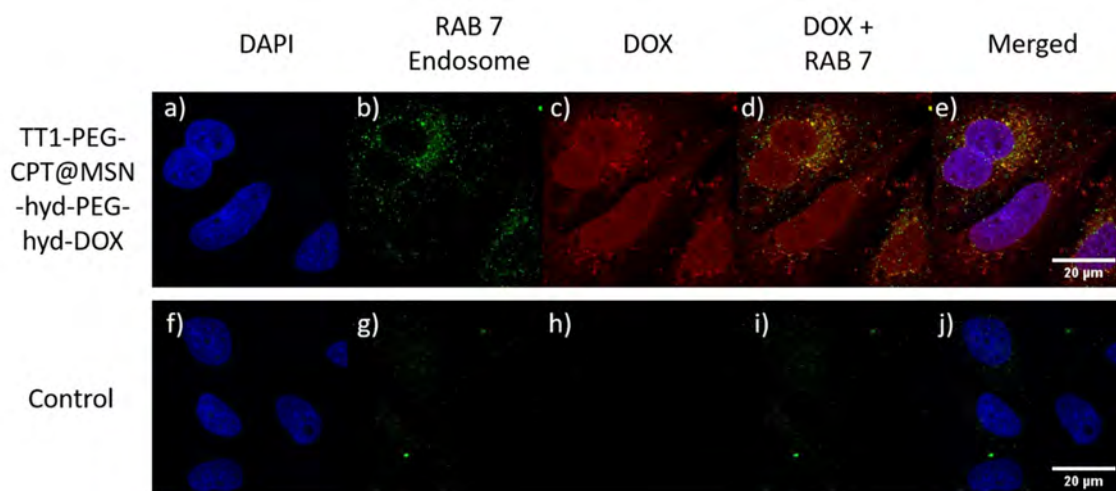


Figure 95. CLSM of the uptake of TT1-PEG-CPT@MSN-hyd-PEG-hyd-DOX at 37°C for 4 h at $100 \mu\text{g}\cdot\text{mL}^{-1}$. Scale bar $20 \mu\text{m}$. Blue: dapi; red: DOX; green: RAB 7.

No stain protocols with nuclear staining have been performed to assess the release of CPT within the cytoplasm of the cell (Figure 96). To do so, $100 \mu\text{g}\cdot\text{mL}^{-1}$ of MSN (TT1-PEG-CPT@MSN-hyd-PEG-hyd-DOX) were incubated for 4 h in HeLa cells. Afterwards, cell images indicated blue, red

and purple staining in cell bodies, suggesting the efficient uptake and subsequent release of the three drugs from the MSN. Blue staining (Figure 96 a)) implied the release of CPT (**4**) molecules from the nanopores of the particles, whereas the intense red (Figure 96 b)) signified the DOX (**1**) fluorescence. Both drugs can be detected in the nucleus and cytoplasm of HeLa cells. On the other hand, Pc (**56**) was only released on the cytoplasm of the cell (purple staining) (Figure 96 d)), which is in agreement for this type of PS [236].

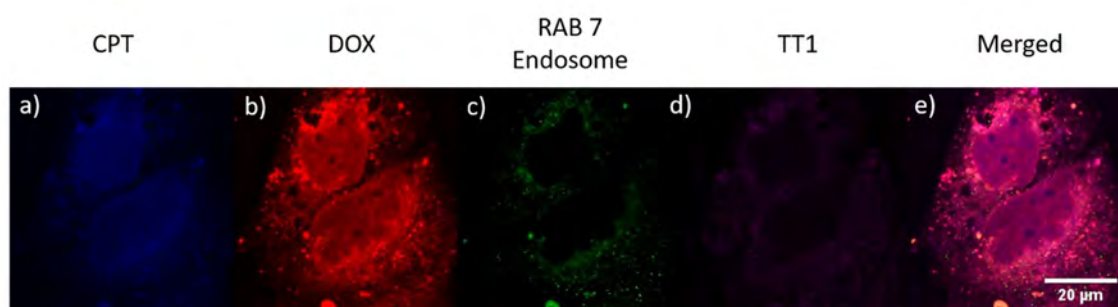


Figure 96. CLSM of the uptake of TT1-PEG-CPT@MSN-hyd-PEG-hyd-DOX at 37°C for 4 h at 100 $\mu\text{g}\cdot\text{mL}^{-1}$. Scale bar 20 μm . Blue: CPT; red: DOX; green: RAB 7; purple: Pcs.

2.5.5. Cytotoxicity

To assess the cytotoxicity of the new system, the MTT assay was adopted to compare the viability test of HeLa cells after incubation with different MSNs (TT1-PEG-CPT@MSN-hyd-PEG-hyd-DOX, TT1-PEG-CPT@MSN-hyd-PEG-hyd and MSN-hyd-PEG-hyd-DOX) for 72 h. As revealed in Figure 97, cell viability decreases at higher concentration of TT1-PEG-CPT@MSN-hyd-PEG-hyd-DOX and MSN-hyd-PEG-hyd-DOX. Whereas for TT1-PEG-CPT@MSN-hyd-PEG-hyd the cytotoxicity was negligible against HeLa cells at concentrations up to 100 $\mu\text{g}\cdot\text{mL}^{-1}$.

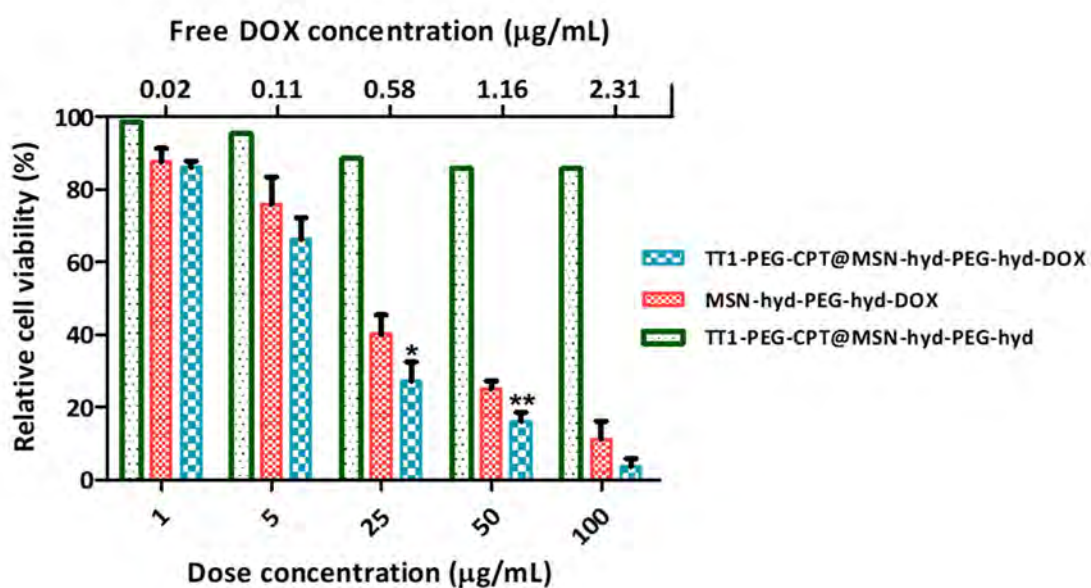


Figure 97. Cell viability of HeLa cells incubated with TT1-PEG-CPT@MSN-hyd-PEG-hyd-DOX, MSN-hyd-PEG-hyd-DOX and TT1-PEG-CPT@MSN-hyd-PEG-hyd for 72 h. Data represented as mean \pm SD ($n=3$), * $p<0.05$ and ** $p<0.01$. The concentration of free DOX is the released drug at pH 5.5.

A synergistic effect can be detected for TT1-PEG-CPT@MSN-hyd-PEG-hyd-DOX in comparison with the other systems (TT1-PEG-CPT@MSN-hyd-PEG-hyd and MSN-hyd-PEG-hyd-DOX). The calculated IC_{50} for TT1-PEG-CPT@MSN-hyd-PEG-hyd-DOX was $8.36 \mu\text{g}\cdot\text{mL}^{-1}$ and is equivalent to the release of $0.19 \mu\text{g}\cdot\text{mL}^{-1}$ of free DOX (**1**) and $0.002 \mu\text{g}\cdot\text{mL}^{-1}$ of CPT (**4**) from TT1-PEG-CPT (**47**). These values have been calculated as the release of drugs at pH 5.5, which is the average pH found in late-endosomes and lysosomes of HeLa cells [198]. At the same pH conditions, the calculated CI value is 0.46 (at IC_{50}), which is consistent with a synergistic interaction of the drugs. It is worth noting that this value has been obtained only considering the contribution of CPT (**4**). It is expected that under red light, the CI will decrease due to the generation of singlet oxygen and ROS species of the Pcs [251]. These results are in agreement with previous data result of viability with CPT(**4**)/DOX (**1**) system constructed by our group [151].

2.5.6. Conclusions and Outlook

A synthetic pathway has been developed to synthesise a double sensitive pH-glutathione conjugate of CPT with a Pc attached through a PEG chain, TT1-PEG-CPT (**47**). This new compound **47** has been characterized by $^1\text{H-NMR}$ and HRMS. Besides, its cleavage under reductive conditions has been assessed in the presence of propane-1,3-dithiol (**55**). The cleavage of the disulphide bond assures the liberation of CPT (**4**) and Pegylated TT1 **54** inside the cancerous cells.

A loading of 8% of conjugate TT1-PEG-CPT (**47**) within an MSN was achieved using MeOH as a solvent. This value is in agreement to similar systems found in the literature for Pcs [246]. In addition, the stability of the system has been tested in physiological conditions (pH 7.4) obtaining a null release of the conjugate **47** and DOX (**1**). On the other hand, under acidic environment, a burst sustained release was observed for both drugs at 24 h.

The cytotoxicity of the system TT1-PEG-CPT@MSN-hyd-PEG-hyd-DOX has been tested against HeLa cells achieving a synergistic effect in comparison with MSN-hyd-PEG-hyd-DOX and TT1-PEG-CPT@MSN-hyd-PEG-hyd. The uptake experiments show 100% of internalization in the same cell line for 4 h. Moreover, the CLSM micrographs show the release of all the drugs inside the cells.

The photodynamic activity of TT1-PEG-CPT@MSN-hyd-PEG-hyd-DOX will be determined under light irradiation. These experiments will be performed in the future at the laboratory of professor Ng in The Chinese University of Hong Kong.

Chapter 3. Experimental Part

Chapter 3. Experimental Part

3.1. Instrumentation

TEM Microscopy was carried out using a JEOL microscope model JEM 2011 in *Universitat Autònoma de Barcelona (UAB)*.

Bio-TEM Microscopy of HeLa cells was performed using a JEOL microscope model JEM-1400 in (UAB).

Fluorescence Confocal Microscope was carried out using a multiphoton spectral Leica model TCS SP5 (UAB) and Leica model SP8 lighting (IQS).

Uptake Kinetic experiments were carried out using an IncuCyte® S3 Live-cell Analysis System (Essen Bioscience, Ann Arbor, MI).

Flow cytometry was performed using a flow cytometer (NovoCyte, ACEA Biosciences, Inc.)

Porous surface nitrogen physisorption analysis was conducted on a Micromeritics Gemini V surface area and pore size analyser. Pore size distribution curves were obtained from analysis of the absorption portion of the isotherms using BJH (Barrett-Joyner-Halenda) method.

Dynamic Light scattering (DLS) size and ζ -potential measurements were obtained by Malvern Zetasizer Nano Series ZEN 3600.

Infrared Spectra (FTIR) was recorded in a Thermo Scientific Nicolet iS10 FTIR spectrometer with Smart iTr. Values are reported in wavenumbers (cm^{-1}). The notation used is KBr (potassium bromide plates) and film (evaporated film from chloroform).

UV-Vis Absorption spectra was recorded in a Thermo Scientific 300 UV-Vis spectrophotometer.

Nuclear Magnetic Resonance spectra ($^1\text{H-NMR}$ and $^{13}\text{C-NMR}$) were recorded on a Varian 400-NMR spectrometer with frequency generators for ranges $^1\text{H-}^{19}\text{F}$ and $^{15}\text{N-}^{31}\text{P}$, temperature control system, automatic tuning probe and sample introduction robot 50 positions ($^1\text{H-NMR}$ at 400 MHz and $^{13}\text{C-NMR}$ at 100.6 MHz). Chemical shifts are reported in $^1\text{H-NMR}$ spectra and to solvent signal of CDCl_3 (77.0 ppm), DMSO-d_6 (39.5 ppm), or methanol-d_4 (49.0 ppm) in $^{13}\text{C-NMR}$ spectra. Coupling constants are reported in Hertz (Hz). Spectral splitting patterns are designed as: s (singlet), d (doublet), t (triplet), q (quartet), dd (doublet of doublets), ddd (doublet of doublet of doublets), m (complex multiplet) and brs (broad signal).

High Resolution Mass Spectrometry (HRMS) was conducted on a VG AutoSpec (Micromass Instruments) Trisector EBE of high resolution spectrometer operating in FAB or EI mode and on

Biotoff II (Bruker) apparatus in ESI-TOF mode at *Servicio de Espectroscopia de Masas (Universidad de Santiago de Compostela)*.

3.2. Protocols

TEM Microscopy

Samples were ultrasonically dispersed in EtOH for 1 h at a concentration of $0.1 \text{ mg}\cdot\text{mL}^{-1}$ and deposited on an amorphous, porous carbon grid. Sometimes, initial concentration is too high and 1/10 or 1/100 dilutions need to be carried out. Sonication must be applied 15 min before using the microscope.

Porous surface

After numerous tests processes it was determined that:

- CTAB removal must be completely achieved.
- MSNs must be washed several times with water and ethanol and final ethanol solutions must be removed under reduced pressure.
- Final solid samples must be sonicated until the formation of a free powdered solid.
- MSNs must be treated in a lyophilizer at 0.05 mBar, $-0.759 \text{ }^\circ\text{C}$, 24 h, prior to conduct adsorption experiments directly inside BET tubs.
- More or less 15 mg are needed.

Dynamic Light scattering (DLS)

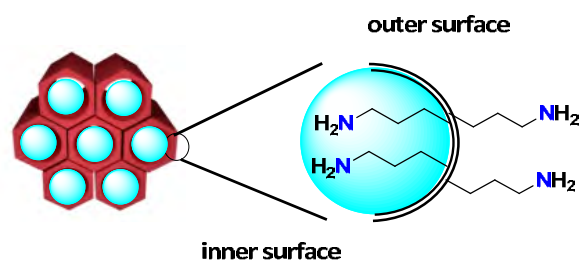
Samples were prepared at a concentration of $0.1 \text{ mg}\cdot\text{mL}^{-1}$ in EtOH for size measurements and $0.05 \text{ mg}\cdot\text{mL}^{-1}$ in H_2O for the zeta measurements. Better results are obtained if MSNs have just been synthesized and have not been dried. Sonication must be applied 1 h before using DLS. Sometimes, samples need to be filtered in a $0.45 \text{ }\mu\text{m}$ nylon filter. Normally, in order to adjust concentration range, the initial concentration must be diluted 1/10 or 1/3. No results can be achieved by DLS measurements if CTAB is still present in MSNs matrix or if there is any fluorescent molecule attached to MSNs.

Infrared Spectra (FTIR)

Well dried MSNs need to be obtained. To do so, final solvent is evaporated under reduced pressure and samples have been placed in a vacuum desiccator at $60 \text{ }^\circ\text{C}$ for 24 h.

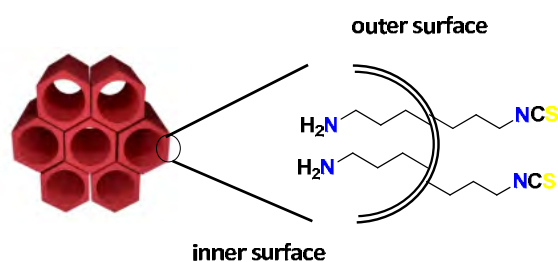
3.3. Synthetic part of chapter 2.1.

3.3.1. Synthesis of Amino MSNs with CTAB (MSN-NH₂ (CTAB)) [141]

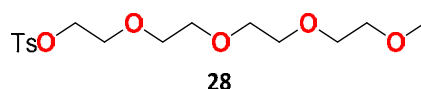


A solution of 0.2 g of CTAB and 100 mL of NH₄OH (0.2 M) was stirred at 1100 rpm for 30 minutes at 60 °C. Then, 1.6 mL of 0.2 M dilute TEOS (in absolute ethanol) was added dropwise by an automatic injector for 20 minutes. The solution was stirred at 1100 rpm for 5 h at 60 °C. Afterwards, 1.6 mL of 12% v/v APTES (in absolute ethanol) and 1.6 mL of 1 M dilute TEOS (in absolute ethanol) were added to the solution dropwise. The solution was stirred at the same rpm and temperature for another 1 h. Then, the solution was aged at 60 °C for 24 h. Solid samples were collected by centrifugation at 13,000 rpm for 13 min and were washed and dispersed with deionized water in order to avoid CTAB elimination.

3.3.2. Synthesis of isothiocyanate MSNs ((MSN)-(NH₂)_i(NCS)_o) [141]

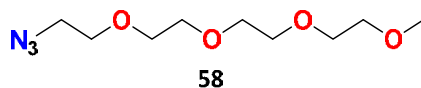


54 mg of MSN-NH₂ (CTAB) were dissolved in 20 mL of dry toluene and stirred at 50 °C for 24 h. Then, 42 mg (0.180 mmol, 20 eq.) of thiocarbonyld-2(1*H*)-pyridone (**13**) were added and the mixture was stirred at room temperature for 24 h. Solid samples were collected by centrifugation at 13,000 rpm for 13 min and then washed with absolute EtOH twice. Then, the surfactant component was eliminated by adding to the dispersion 30 mL of 0.1 M NH₄NO₃ methanolic solution for 24 h. Solid samples were collected by centrifugation and then washed and dispersed with absolute EtOH and water. The solvent was evaporated under reduced pressure and the resulting MSN-(NH₂)_i(NCS)_o were stored dry.

3.3.3. Synthesis of tetra(ethylene glycol) methyl ether tosylate (**28**) [252]

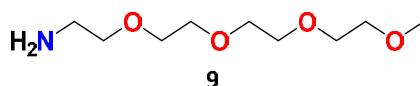
2 mL (10.0 mmol) of tetraethyleneglycol monomethyl ether (**27**) in 10 mL of THF was added to a solution of 4.50 g of KOH (80.2 mmol) in 40 mL H₂O. The resulting mixture was stirred for 1 h at 0 °C. Then 1.91 g (10.0 mmol) of p-toluensulfonyl chloride in 10 mL of THF was added dropwise to the reaction mixture during 1 h at 0 °C. The mixture was stirred for additional 3 h. The solution was poured onto 1 M HCl and the organic solvent was evaporated. The residue was extracted three times with chloroform and the organic phase dried over MgSO₄, filtered and the solvent was removed by rotary evaporation. The transparent crude product was used for the next step without further purification. Yield: (**28**) 2.74 g (η = 75%).

¹H-NMR (400 MHz, CDCl₃) δ 7.78 (d, 2H), 7.32 (d, 2H), 4.15 – 4.12 (m, 2H), 3.68 – 3.65 (m, 2H), 3.63 – 3.60 (m, 6H), 3.56 (m, 4H), 3.52 (m, 2H), 3.35 (s, 3H), 2.43 (s, 3H).

3.3.4. Synthesis of 1-Azido-2-[2-[2-[2-(methoxyethoxy)ethoxy]ethoxy]ethane (**58**) [253]

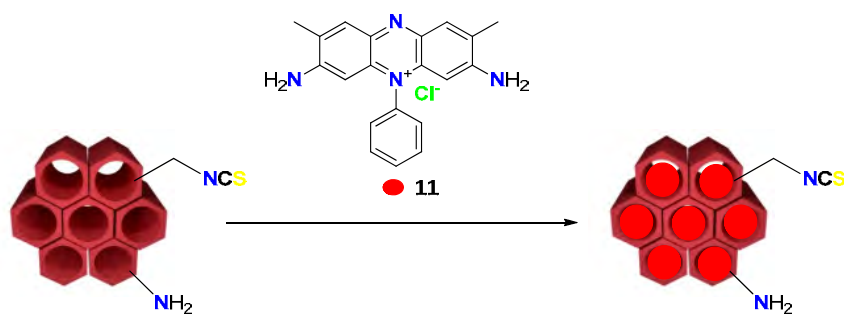
2.74 g (7.5 mmol) of tetra(ethylene glycol) methyl ether tosylate (**28**) was dissolved in ethanol (50 mL) and 1.20 g (18.5 mmol) of sodium azide were added. The solution was heated under reflux overnight or until TLC (10% MeOH in CHCl₃) showed no starting material. The solvent was removed under vacuum and DCM was added to the residue. The organic layer was extracted with water (3 times) and dried over MgSO₄, filtered and the solvent was removed by rotary evaporation. Yield: (**58**) 1.02 g (η = 58%).

¹H-NMR (400 MHz, CDCl₃) δ 3.66 – 3.59 (brs, 12H), 3.53 – 3.49 (brs, 2H), 3.37 – 3.33 (overlapping multiplets, 5H).

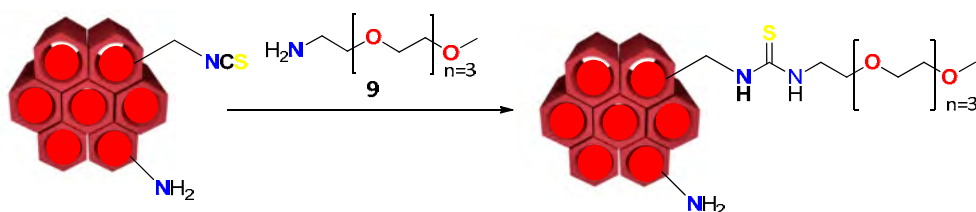
3.3.5. Synthesis of triethylene glycol 2-aminoethyl methyl ether (**9**) [254]

100 mg (0.239 mmol) of compound **58** and 15 mg Pd/C were dissolved in 20 mL of MeOH and stirred at room temperature for 1 h under H₂ atmosphere. The mixture was filtered and the solid was washed with MeOH. The filtrate was concentrated to afford triethylene glycol 2-aminoethyl methyl ether (**9**). Yield: (**9**) 88 mg ($\eta=100\%$).

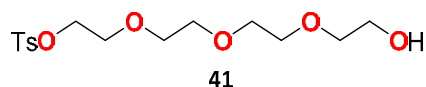
¹H-NMR (400 MHz, CDCl₃) δ 3.68 – 3.57 (overlapping multiplets, 12H), 3.52 – 3.48 (brs, 2H), 3.36 (s, 3H), 2.86 (t, 2H).

3.3.6. Safranin loading in MSN-(NH₂)_i-(NCS)

100 mg of MSN-(NH₂)_i-(NCS)_o were dissolved in 75 mL of absolute ethanol and stirred vigorously at room temperature for 1 h. Then, 67 mg of Safranin (**11**) (0.190 mmol) were added and the mixture was stirred at room temperature for 24 h. Finally, solid samples were collected by centrifugation at 13,000 rpm for 13 min. Nanoparticles were washed with ethanol once. Safranin loading content (%LC=[entrapped drug/nanoparticles weight] x 100) was quantified by UV-vis spectroscopy (518 nm) from the supernatant.

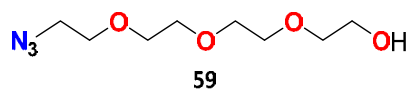
3.3.7. Functionalization of Safranin loaded MSN-(NH₂)_i-(NCS)_o with (9) (MSN-(NH₂)_i(OMe)_{long})

10 mg of MSN-(NH₂)_i-(NCS)_o loaded with Safranin O dye (**14**) were dissolved in 10 mL of acetonitrile in a round-bottomed flask. 40 mg (0.19 mmol) of triethylene glycol 2-aminoethyl methyl ether (**9**) were added to the solution. The mixture was stirred at room temperature in the dark for 30 min. Solid samples were collected by centrifugation at 13,000 rpm for 13 minutes and then washed with acetonitrile twice. The solvent was evaporated under reduced pressure and the resulting MSN-(NH₂)_i(OMe)_{long} were stored dry.

3.3.8. Synthesis of tetraethylene glycol monotosylate (**41**) [255]

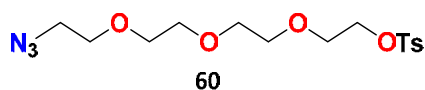
5.0 g (4.44 mL, 25.7 mmol) of tetraethylene glycol (**17**) were dissolved in 5 mL of THF anhydrous. Then, 1.68 g (42.0 mmol) of NaOH dissolved in 10 mL of H₂O were added to the latter solution. The mixture was cooled to 0 °C on an ice bath and stirred for 20 min. Afterwards a solution of 4.87 g (26.0 mmol) of TsCl in 20 mL THF was added to the mixture and stirred for 2 h at 0 °C. Then, the mixture was poured on water and extracted with DCM (5 x 30 mL). The combined organic phase was washed with water (2 x 30 mL), dried over MgSO₄, and evaporated under reduced pressure. The crude was purified through a silica gel column chromatographic with AcOEt:Cy mixtures (80:20). The product **41** was collected and the solvent removed by rotatory evaporation. Yield: (**41**) 3.78 g (η=42%).

¹H-NMR (400 MHz, CDCl₃) δ 7.79 (d, 2H), 7.35 (d, 2H), 4.15 (t, 2H), 3.73 – 3.67 (m, 4H), 3.67 – 3.61 (m, 4H), 3.61 – 3.58 (m, 6H), 2.44 (s, 3H).

3.3.9. Synthesis of 2-(2-(2-(2-azidoethoxy)ethoxy)ethoxy)ethan-1-ol (**59**) [256]

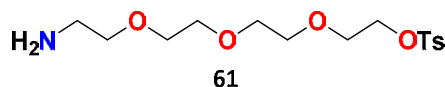
3.78 g (10.8 mmol) of compound **41** were dissolved in 50 mL of EtOH. Then, 5.47 g (84.1 mmol) of NaN₃ were added at room temperature, and the mixture was stirred vigorously at 70 °C for 18 h. The resulting mixture was poured on water and distilled under reduced pressure to 1/3 of its volume, in order to evaporate EtOH. The water phase was extracted three times with AcOEt, and the combined organic phase was dried over MgSO₄. The solvent was removed by rotatory evaporation. Yield: (**59**) 1.66 g (η=70 %).

¹H-NMR (400 MHz, CDCl₃) δ 3.73 (t, 2H), 3.70 – 3.65 (m, 10H), 3.61 (t, 2H), 3.40 (t, 2H).

3.3.10. Synthesis of 2-(2-(2-(2-azidoethoxy)ethoxy)ethoxy)ethyl 4-methylbenzenesulfonate (**60**) [257]

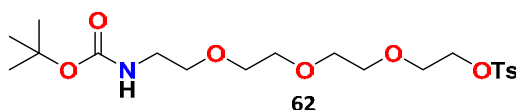
1.67 g (7.62 mmol) of compound **59** were dissolved in 10 mL of DCM anh. Then 1.1 mL (7.89 mmol) of Et₃N and 92 mg (0.76 mmol) of DMAP were added, and the mixture was stirred vigorously at 0 °C in an ice bath for 15 min. 1.44 g (7.55 mmol) of TsCl dissolved in 10 mL of DCM were added dropwise to the mixture and it was stirred at 0 °C for 30 more minutes. Then, the mixture was stirred at room temperature for 24 h. The resulting mixture was washed with HCl 0.1 M (3 x 15 mL), brine (2 x 15 mL) and water (2 x 20 mL) and dried over MgSO₄. The solvent was removed by rotatory evaporation. Yield: (**60**) 2.18 g (η=77%).

¹H-NMR (400 MHz, CDCl₃) δ 7.80 (d, 2H), 7.34 (d, 2H), 4.16 (t, 2H), 3.71 – 3.66 (m, 4H), 3.66 – 3.63 (m, 4H), 3.59 (m, 4H), 3.38 (t, 2H), 2.44 (s, 3H).

3.3.11. Synthesis of 2-(2-(2-(2-aminoethoxy)ethoxy)ethoxy)ethyl 4-methylbenzenesulfonate (**61**) [258]

7.5 g (20.1 mmol) of compound **61** and 0.8 g of Pd/C 10% were dissolved in MeOH (150 mL) and stirred at room temperature for 5 h under H₂ atmosphere. TLC showed the reaction completed. The mixture was filtered and the solid was washed with MeOH. The filtrate was concentrated to afford the desired compound **61**. The colourless oil was used in next step without further purification. Yield: (**61**) 6.8 g (η =97%)

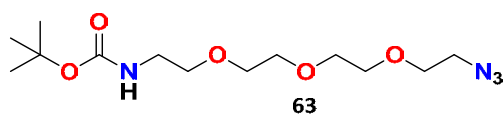
¹H-NMR (400 MHz, CDCl₃) δ 7.78 (d, 2H), 7.32 (d, 2H), 4.14 (t, 2H), 3.68 (t, 2H), 3.61 – 3.55 (m, 8H), 3.51 (t, 2H), 3.33 – 3.22 (m, 2H), 2.43 (s, 3H).

3.3.12. Synthesis of 2,2-dimethyl-4-oxo-3,8,11,14-tetraoxa-5-azahexadecan-16-yl 4-methylbenzenesulfonate (**62**) [259]

0.31 g (0.910 mmol) of compound **61** were dissolved in 5 mL of DCM and added to a solution of di-tert-butyl dicarbonate (0.15 g, 0.68 mmol) in DCM (5 mL). The reaction mixture was stirred for 2 h at 0 °C in an ice bath. Then, the mixture was washed with brine and with water and dried over MgSO₄. The solvent was removed by rotatory evaporation. Yield: (**61**) 138 mg (η =34%).

¹H-NMR (400 MHz, CDCl₃) δ 7.80 (d, 2H), 7.34 (d, 2H), 4.16 (t, 2H), 3.69 (t, 2H), 3.63 – 3.56 (m, 8H), 3.52 (t, 2H), 3.30 (m, 2H), 2.45 (s, 3H), 1.43 (s, 9H).

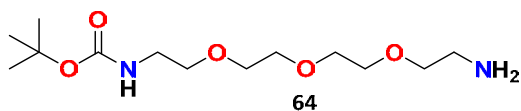
3.3.13. Synthesis of tert-butyl-(2-(2-(2-(2-azidoethoxy) ethoxy) ethoxy) ethyl) carbamate (**63**) [260]



0.14 g (0.312 mmol) of compound **62** were dissolved in 20 mL of EtOH. Then 0.10 g (1.54 mmol) of NaN₃ was added at room temperature, and the mixture was stirred vigorously at 70 °C for 18 h. The resulting mixture was poured on water and distilled under reduced pressure to 1/3 of its volume, in order to evaporate EtOH. The water phase was extracted three times with AcOEt, and the combined organic phase was dried over MgSO₄. The solvent was removed by rotatory evaporation. Yield: (**63**) 99 mg (η=99%).

¹H-NMR (400 MHz, CDCl₃) δ 3.70 – 3.60 (brs, 10H), 3.54 (t, 2H), 3.39 (t, 2H), 3.32 (m, 2H), 1.44 (s, 9H).

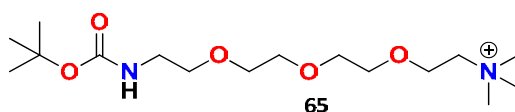
3.3.14. Synthesis of tert-butyl (2-(2-(2-(2-aminoethoxy)ethoxy)ethoxy)ethyl)carbamate (**64**) [260]



99 mg (0.311 mmol) of compound **63** were dissolved in dry THF (5 mL). 96 mg (0.365 mmol) of triphenyl phosphine were added to the solution. Then 1.0 mL of H₂O was added, after which the mixture was heated under reflux at 75 °C for 18 h. The reaction mixture was diluted with water (7 mL) and washed with toluene (5 mL) and stirred for 10 min at room temperature. Then the aqueous layer was evaporated under reduced pressure. The product was diluted with DCM and dried over MgSO₄. The solvent was removed by rotatory evaporation. Yield: (**64**) 28 mg (η=31%).

¹H-NMR (400 MHz, CDCl₃) δ 3.69 – 3.59 (brs, 8H), 3.56 – 3.48 (m, 4H), 3.31 (m, 2H), 2.87 (t, 2H), 1.44 (s, 9H).

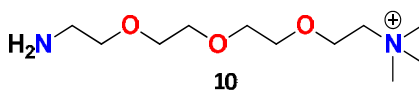
3.3.15. Synthesis of N,N,N,2,2-pentamethyl-4-oxo-3,8,11,14-tetraoxa-5-azahexadecan-16-aminium (65) [261]



77 mg (0.264 mmol) of compound **64** was dissolved in 5 mL of ACN and 139 mg (1.0 mmol) of K_2CO_3 were added. The mixture was stirred at room temperature for 30 min. Then, 58.0 μ L of MeI were added and the mixture was heated under reflux at 85 °C for 20 h. After cooling down at room temperature, K_2CO_3 was removed by filtration and solvent was removed by rotatory evaporation. Yield: (**65**) 85 mg (η =97%).

1H -NMR (400 MHz, $CDCl_3$) δ 4.02 (brs, 4H), 3.70 (t, 2H), 3.63 (t, 2H), 3.60 (brs, 4H), 3.52 (t, 2H), 3.46 (s, 9H), 3.30 (m, 2H), 1.44 (s, 9H).

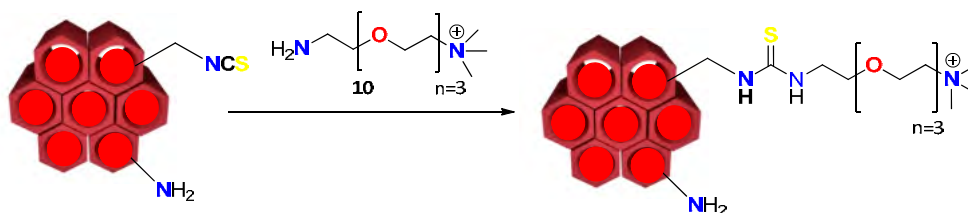
3.3.16. Synthesis of 2-(2-(2-(2-aminoethoxy)ethoxy)ethoxy)-N,N,N-trimethylethan-1-aminium (10)



5 mL (6.53 mmol) of TFA 5% in DCM was added to 161 mg (0.480 mmol) of compound **65**. The mixture was stirred at 0 °C in an ice bath for 40 min. The product was purified by precipitation in diethyl ether. Yield: (**10**) 47 mg (η =42%).

1H -NMR (400 MHz, CD_3OD) δ 4.04 – 3.97 (m, 2H), 3.80 – 3.71 (m, 10H), 3.68 (t, 2H), 3.28 (s, 9H), 3.19 (t, 2H).

3.3.17. Functionalization of Safranin loaded MSN-(NH₂)_i-(NCS)_o with (10) (MSN-(NH₂)_i(N⁺)_{long})

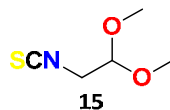


10 mg of MSN-(NH₂)_i-(NCS)_o loaded with Safranin O dye (**11**) were dissolved in 10 mL of acetonitrile in a round-bottomed flask. 40.0 mg (0.17 mmol) of PEG **10** and 0.2 mL of TEA were added to the solution. The mixture was stirred at room temperature in the dark for 30 min. Solid samples were collected by centrifugation at 13,000 rpm for 13 minutes and then washed with acetonitrile twice. The solvent was removed by rotatory evaporation and the resulting MSN-(NH₂)_i(N⁺)_{long} were stored dry.

3.3.18. Release experiments [141]

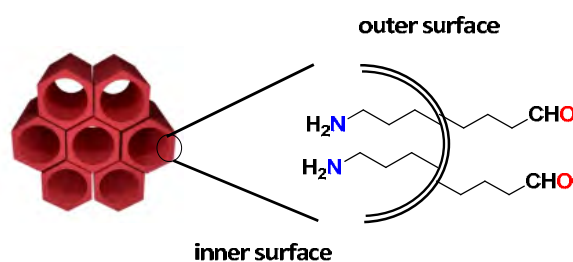
Release experiments were performed at pH 7.4 (PBS buffer). For each release study, MSNs (10 mg) were dispersed by sonication (2 min) in the buffer solution (1.5 mL) and kept at 37 °C, while being stirred (100 rpm). At every designated interval, buffer solutions were taken out for analysis and centrifugated (13,000 rpm, 13 min). The solid residues were dispersed in fresh buffer solution (1.5 mL). The quantities of safranin (**11**) released into the buffer solution were measured by UV-vis absorption spectroscopy at 518 nm.

3.4. Synthetic part of chapter 2.2.

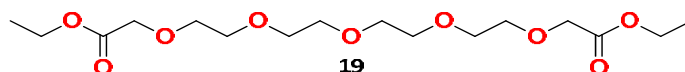
3.4.1. Synthesis of 2-isothiocyanate-1,1-dimethoxyethane (**15**) [151]

0.2 mL (1.9 mmol) of 2,2-dimethoxyethan-1-amine (**16**) was dissolved in 10 mL of DCM anhydrous. Then, 0.6 g (2.6 mmol, 1.4 eq) of 1,1'-thiocarbonyldi-2(1*H*)-pyridone (**13**) was added. The mixture was stirred at room temperature for 24 h. The solvent was washed twice with bicarbonate and removed by rotary evaporation. Yield: (**15**) 0.16 g ($\eta = 60\%$).

$^1\text{H-NMR}$ (400 MHz, CDCl_3): δ 4.46 (t, 1H), 3.60 (d, 2H), 3.43 (s, 9H).

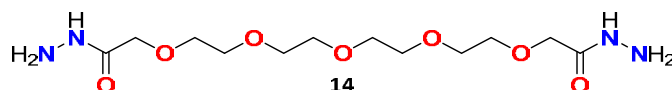
3.4.2. Synthesis of bifunctionalized amino-aldehyde ($\text{MSN}-(\text{NH}_2)_i(\text{CHO})_o$) [151]

0.2 g of $\text{MSN}-(\text{NH}_2)$ (CTAB) were reacted with 0.1 g (0.68 mmol, 4 eq.) of 2-isothiocyanate-1,1-dimethoxyethane (**15**) in 50 mL of toluene. 24 h later, MSNs were washed twice with toluene and ethanol and then the surfactant was eliminated with 30 mL of 0.1 M NH_4NO_3 yielding $(\text{MSN}-(\text{NH}_2)_i(\text{Acet})_o)$. Then MSNs were washed with methanol and acetal protecting groups were removed by stirring MSNs in HCl solution for 6 h.

3.4.3. Synthesis of diethyl 3,6,9,12,15-pentaoxaheptadecanedioate (**19**) [151]

1.7 mL (9.8 mmol) of tetraethyleneglycol (**17**) in 20 mL of anhydrous THF and with 1.2 g (0.05 mol, 5 eq.) of NaH were added and stirred at 0°C for 30 min. Then, the solution was heated at 80 °C until colour change from yellow to brown, 6 h. 3.3 mL (34 mmol, 3.4 eq.) of ethyl bromoacetate was added to the solution and left in the reflux for 24 h. The white precipitate was filtered, and the solvent was removed by rotatory evaporation. Then, the final oil was digested for 24 h in Cy to obtain product dimethyl-3,6,9,12,15-pentaoxaheptadecanedioate (**19**). Yield (**19**): 1.41 g ($\eta=40\%$).

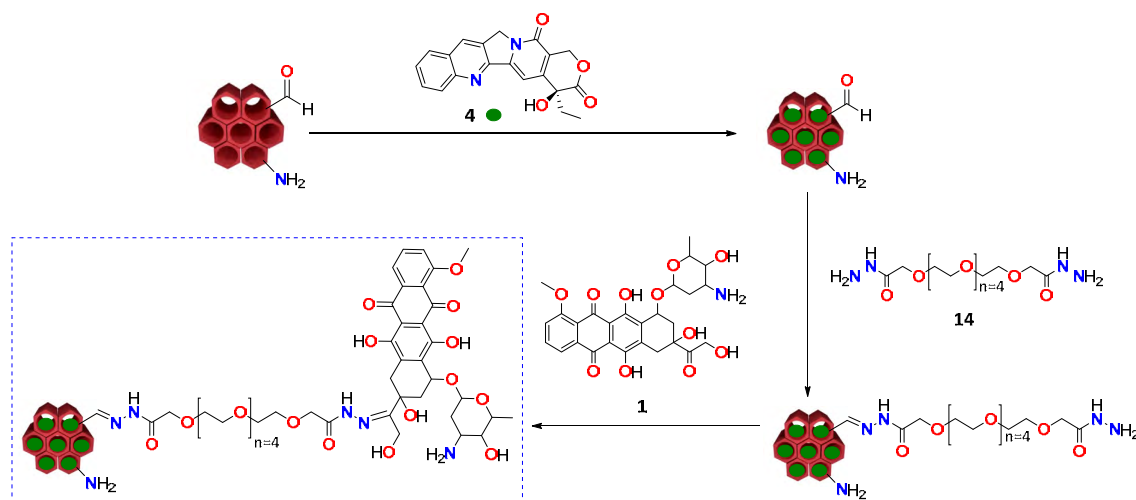
$^1\text{H NMR}$ (400 MHz, CDCl_3) δ 4.26-4.17 (m, 4H), 4.15 (s, 4H), 3.78-3.6 (m, 16H), 1.29 (t, $J=7.2$ Hz, 6H).

3.4.4. Synthesis of dimethyl 3, 6, 9, 12, 15 pentaoxaheptadecanedihydrazide (**14**) [151]

0.8 g ($2.4 \cdot 10^{-3}$ mol) diester PEG **19** were dissolved in 25 mL of EtOH and 0.6 mL (2.1 eq.) of NH_2NH_2 were added. After 24 h of reflux, the eluent is eliminated at reduced pressure to give and oil, which after been washed with EtOH/Cy/DCM gave the product 3,6,9,12,15-pentaoxaheptadecanedihydrazide (**14**). Yield (**14**): 0.60 g ($\eta=80\%$).

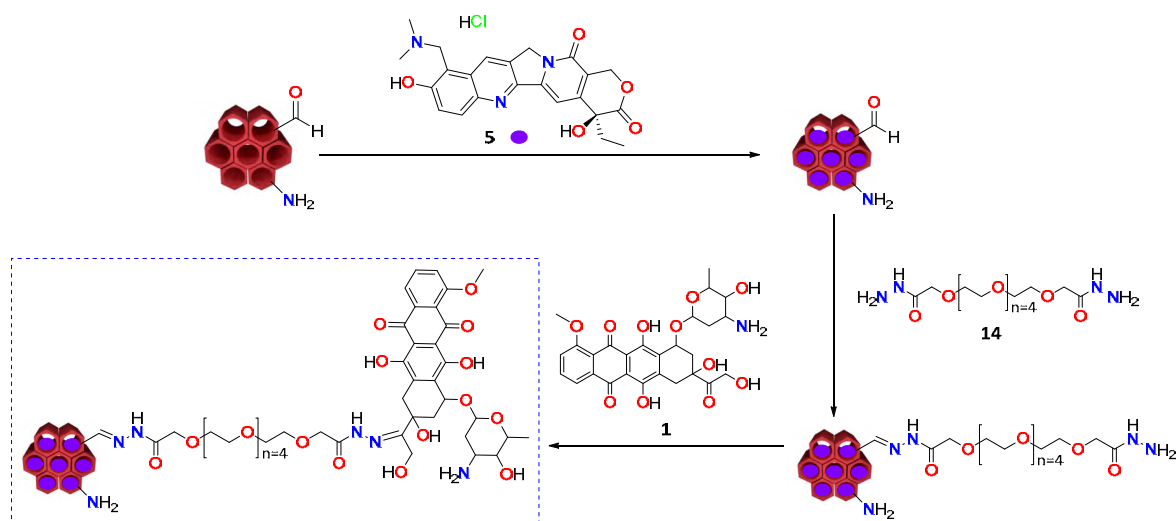
$^1\text{H NMR}$ (400 MHz, CDCl_3) δ 6.81 (brs, 6H), 4.07 (s, 4H), 3.71-3.64 (m, 16H).

3.4.5. Dual CPT@MSN-hyd-PEG-hyd-DOX [151]



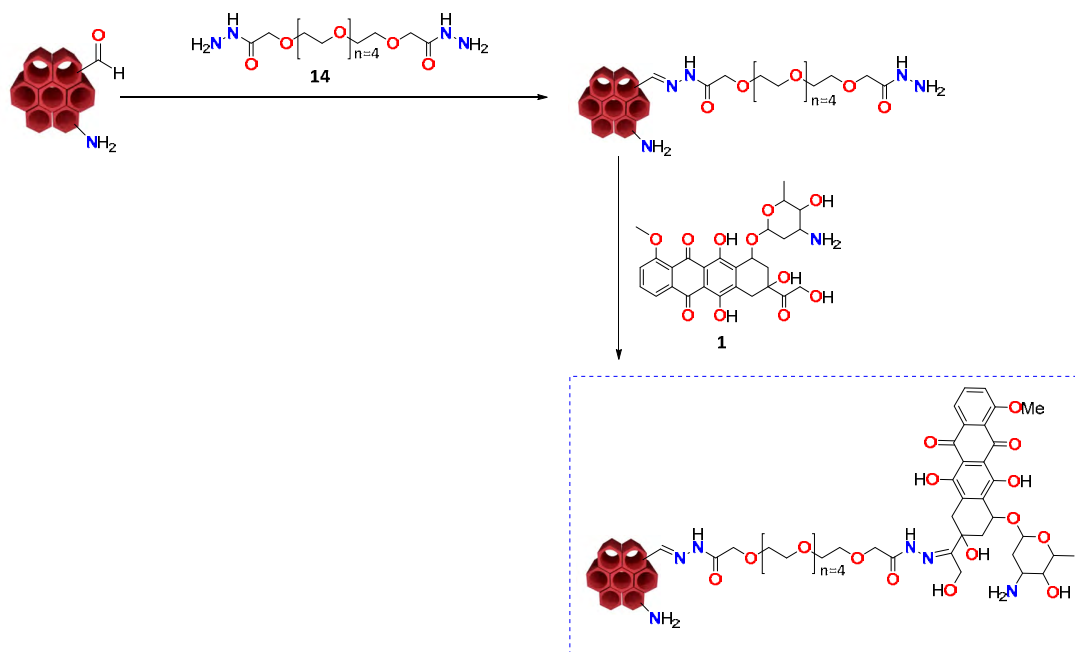
18 mg ($5.16 \cdot 10^{-5}$ mol) of CPT (**4**) was dissolved in 35 mL of CHCl_3 with the aid of sonication at 60 °C until total dissolution of the drug was achieved. Then, CPT (**4**) solution was added to a stirred suspension of $\text{MSN}-(\text{NH}_2)_i(\text{CHO})_o$ (30 mg) in MeOH (25 mL). Afterwards (24 h), a solution dihydrazide-PEG (**14**) (0.080 g, $2.36 \cdot 10^{-4}$ mol) in MeOH (20 mL) was added. After 24 h, MSNs were centrifuged (13,000 rpm for 13 minutes), and the supernatant was collected to quantify the loading of the drug by UV-vis spectroscopy (354 nm). Then, the resulting MSNs were dispersed in a solution of DOX (**1**) (21 mg, $3.6 \cdot 10^{-5}$ mol) in MeOH (20 mL). Finally, after 48 h MSNs were washed with MeOH (three times) and H_2O (three times) until no red supernatant was obtained and then lyophilized. DOX (**1**) and CPT (**4**) loading content ($\% \text{LC} = [\text{entrapped drug}/\text{nanoparticles weight}] \times 100$) were quantified by UV-vis spectroscopy (490 and 354 nm, respectively) from the supernatant (the amount of CPT (**4**) released to the supernatant during the pore capping was subtracted from the initial value of loaded drug (CPT@MSN- $(\text{NH}_2)_i(\text{CHO})_o$)).

3.4.6. Dual TPT@MSN-hyd-PEG-hyd-DOX [151]



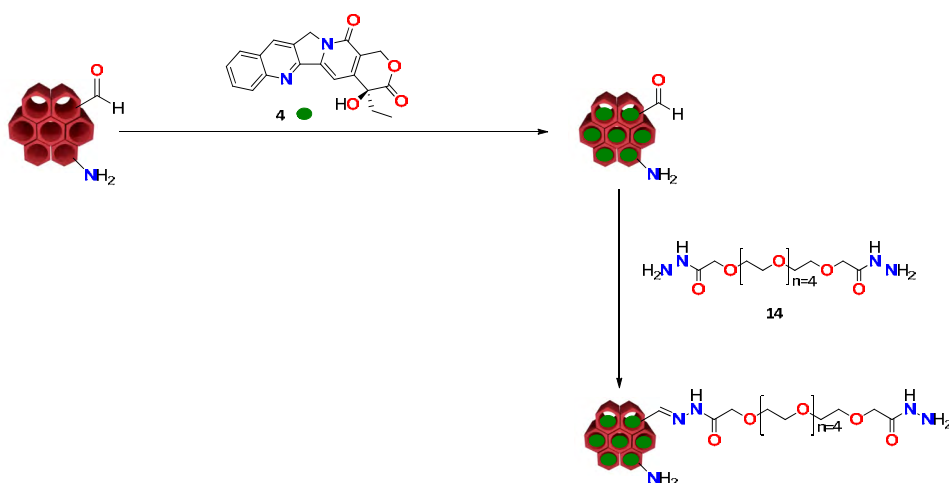
18 mg ($4.27 \cdot 10^{-5}$ mol) of TPT (**5**) were dissolved in 35 mL of ethanol with the aid of sonication until total dissolution of the drug was achieved. Then, TPT (**5**) solution was added to a stirred suspension MSN-(NH₂)_i(CHO)_o (30 mg) in ethanol (25 mL) (700 rpm, 23 °C). Afterwards (24 h), a solution dihydrazide-PEG (**14**) (0.080 g, $2.36 \cdot 10^{-4}$ mol) in MeOH (20 mL) was added. After 24 h, MSNs were centrifuged (13,000 rpm for 13 minutes), and the supernatant was collected to quantify the loading of the drug by UV-vis spectroscopy (385 nm). Then, the resulting MSNs were dispersed in a solution of DOX (21 mg, $3.6 \cdot 10^{-5}$ mol) in MeOH (20 mL). Finally, after 48 h MSNs were washed with MeOH (three times) and H₂O (three times) until no red supernatant was obtained and then lyophilized. DOX (**1**) and TPT (**5**) loading content (%LC=[entrapped drug/nanoparticles weight] x 100) were quantified by UV-vis spectroscopy (490 and 385 nm, respectively) from the supernatant (the amount of TPT (**5**) released to the supernatant during the pore capping was subtracted from the initial value of loaded drug (TPT@MSN-(NH₂)_i(CHO)_o).

3.4.7. Synthesis of MSN-hyd-PEG-hyd-DOX [151]



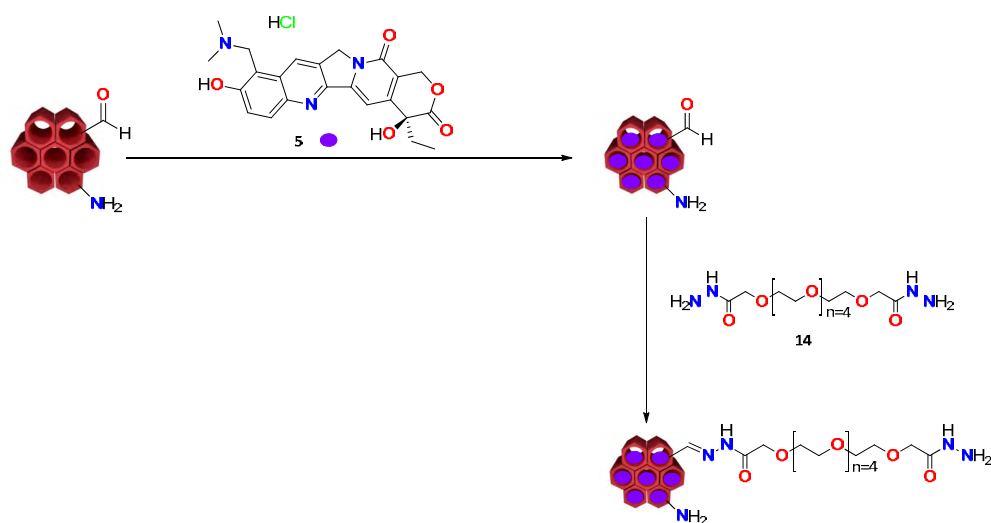
To MSN-(NH₂)_i(CHO)_o (30 mg) in MeOH (30 mL) a solution of dihydrazide-PEG (**14**) (0.080 g, 2.36·10⁻⁴ mol) in MeOH (20 mL) was added. Then, after 48 h, MSNs were centrifuged, washed with MeOH and the supernatant was collected. Afterward, DOX (**1**) (21 mg, 3.6·10⁻⁵ mol) was added to the resulting MSNs suspended in MeOH (20 mL). Finally, after 48 h MSNs were washed with MeOH (three times) and H₂O (three times), until no red supernatant was obtained and then lyophilized. DOX (**1**) loading was quantified by UV-vis spectroscopy (490 nm) from the supernatant.

3.4.8. Synthesis of CPT@MSN-hyd-PEG-hyd



18 mg ($5.16 \cdot 10^{-5}$ mol) of CPT (**4**) was dissolved in 35 mL of CHCl_3 with the aid of sonication at 60 °C until total dissolution of the drug was achieved. Then, CPT (**4**) solution was added to a stirred suspension of $\text{MSN}-(\text{NH}_2)_i(\text{CHO})_o$ (30 mg) in MeOH (25 mL). Afterwards (24 h), a solution dihydrazide-PEG (**14**) (0.080 g, $2.36 \cdot 10^{-4}$ mol) in MeOH (20 mL) was added. After 24 h, MSNs were centrifuged (13,000 rpm for 13 minutes), and the supernatant was collected to quantify the loading of the drug by UV-vis spectroscopy (354 nm). Finally, MSNs were washed with MeOH (three times) and H_2O (three times) and then lyophilized.

3.4.9. Synthesis of TPT@MSN-hyd-PEG-hyd



18 mg ($4.27 \cdot 10^{-5}$ mol) of TPT (**5**) were dissolved in 35 mL of ethanol with the aid of sonication until total dissolution of the drug was achieved. Then, TPT (**5**) solution was added to a stirred suspension MSN-(NH₂)_i(CHO)_o (30 mg) in ethanol (25 mL) (700 rpm, 23 °C). Afterwards (24 h), a solution dihydrazide-PEG (**14**) (0.080 g, $2.36 \cdot 10^{-4}$ mol) in MeOH (20 mL) was added. After 24 h, MSNs were centrifuged (13,000 rpm for 13 minutes), and the supernatant was collected to quantify the loading of the drug by UV-vis spectroscopy (385 nm). Finally, MSNs were washed with MeOH (three times) and H₂O (three times) and then lyophilized.

3.4.10. Release experiments of CPT@MSN-(NH₂)_i(PEG-DOX)_o and TPT@MSN-(NH₂)_i(PEG-DOX)_o [151]

Release experiments were performed at pH 7.4 (PBS buffer), pH 6.5 (phosphate buffer, 0.2M NaH₂PO₄/0.2m Na₂HPO₄), pH 5.5, 4.5 and 4 (acetate buffer, 0.1M NaAcO/0.1 M AcOH). For each release study, MSNs (10 mg) were dispersed by sonication (2 min) in the buffer solution (1.5 mL) and kept at 37 °C, while being stirred (100 rpm). At every designated interval, buffer solutions were taken out for analysis and centrifugated (13,000 rpm, 13 min). The solid residues were dispersed in fresh buffer solution (1.5 mL). The quantities of the drugs released into the buffer solution were measured by UV-vis absorption spectroscopy at 490 nm for DOX (**1**), 354 nm for CPT (**4**) and 385 nm for TPT (**5**).

3.4.11. *In vitro* cytotoxicity [151]

In vitro cytotoxicity was performed using the MTT assay in HeLa cells. Experiments were carried out in 96-well plates (0.1 mL/well) where 10,000 cells/well were seeded using complete DMEM media (10% FBS, 1% glutamine, 1% penicillin/streptomycin). Twenty-four hours later, cells were incubated with MSNs for 24, 48 and 72 h at 37 °C and 5% CO₂. After a washing step with PBS, the MTT solution was added (0.5 mg/mL). Cells were incubated for 3 h at 37 °C and 5% CO₂, the MTT solution was removed, and formazan crystals were dissolved in 0.1 mL of DMSO. Finally, formazan absorbance was measured at 560 nm.

3.4.12. Confocal microscopy for cellular internalization [151]

Uptake experiments were carried out on glass coverslips. 180,000 HeLa cells/well were seeded using complete DMEM media (10% FBS, 1% glutamine and 1% penicillin/streptomycin). Twenty-four hours later, cells were incubated with 50 µg·mL⁻¹ CPT@MSN-hyd-PEG-hyd-DOX for 4 h at 37 °C and 5% CO₂. Then, cells were washed with PBS and fixed with 10% formalin. Finally, cells were observed in a fluorescence confocal microscopy (multiphoton spectral Leica model TCS SP5).

3.4.13. Bio-TEM [151]

Two million HeLa cells were seeded onto a Petri dish in a complete DMEM medium and incubated at 37 °C with 5% CO₂ atmosphere for 24 h. Next, medium was removed, and cells were incubated in a new medium supplemented with CPT@MSN-hyd-PEG-hyd-DOX at 50 µg·mL⁻¹ for 4 h. Then, cells were fixed, first with 2% glutaraldehyde buffered in 0.1 M sodium cacodylate at room temperature for 1 h and afterward, with 2% osmium tetroxide containing 1.5% of potassium ferricyanide buffered in 0.1 M sodium cacodylate for 90 min at room temperature. Finally, samples were dehydrated in grading alcohols (70%, 90% and 100%) and included in Epon for at least 24 h at 60 °C. Thin slides were cut using microtome, deposited on copper grids, and stained with 5% uranyl acetate and 0.4% lead citrate. Observations were performed with transmission electron microscope (JEOL microscope model JEM-1400).

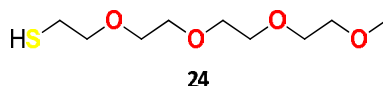
3.4.14. Flow cytometry [151]

HeLa cells were seeded at a density of 20,000 cells/well in 96-well plates with complete DMEM media (10% FBS, 1% glutamine and 1% penicillin/streptomycin) and incubated at 37 °C, 5% CO₂ for 24 h. Then, 50 µg·mL⁻¹ CPT@MSN-hyd-PEG-hyd-DOX were added, and after 4 h incubation period, cells were prepared for flow cytometry. Briefly, cells were washed with PBS and harvested with 40 µL of trypsin per well. After a few minutes, 120 µL of complete DMEM were added, to stop trypsin reaction, and cells were fixed with 100 µL of paraformaldehyde 2%. DOX (1) internalization was measured by flow cytometry.

3.4.15. IncuCyte® S3 live-cell analysis [151]

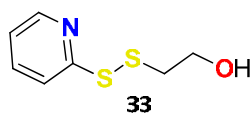
Uptake kinetics experiment were carried out in 96-well plates (0.1 mL/well) where 15,000 HeLa cells/well were seeded using complete DMEM media (10% FBS, 1% glutamine and 1% penicillin/streptomycin). Twenty-four hours later, cells were incubated with CPT@MSN-hyd-PEG-hyd-DOX (1-50 µg·mL⁻¹) for 13.5 h and 50.5 h at 37 °C and 5% CO₂. DOX release was monitored with IncuCyte® S3 live-cell analysis system, capturing live-cell images every 30 min.

3.5. Synthetic part of chapter 2.3.

3.5.1. Synthesis of 2,5,8,11-tetraoxatridecane-13-thiol (**24**) [262]

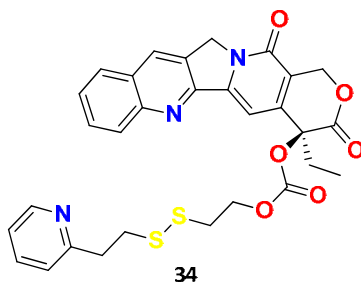
To a 50 mL reaction flask were added 1.85 g (17.0 mmol) of compound **28**, anhydrous EtOH (10 mL), 0.39 g (17.0 mmol) of thiourea and distilled H₂O (7 mL). The flask was fitted with a condenser and nitrogen inlet, and the reaction mixture was refluxed for 3 h. A solution of 0.81 g (20.4 mmol) of NaOH in distilled H₂O (5 mL) was added and refluxed continued overnight. The reaction mixture was concentrated to approximately 10 mL, diluted with distilled H₂O (5 mL), neutralized with concentrated HCl, and extracted with CH₂Cl₂ (3 x 5 mL). The solution was dried over MgSO₄, evaporated to dryness and distilled (50 °C/1mm). Yield: (**24**) 1.18 g (η= 64%).

¹H NMR (400 MHz, Chloroform-d) δ 3.68 – 3.57 (m, 13H), 3.54 (dd, J = 5.8, 3.5 Hz, 2H), 3.37 (s, 3H), 2.68 (dt, J = 8.2, 6.5 Hz, 2H), 1.58 (t, J = 8.2 Hz, 1H).

3.5.2. Synthesis of 2-(Pyridyl-disulfanyl)ethanol (**33**) [263]

0.3 g (1.36 mmol) of 2,2'-pyridyldisulphide (**31**) was dissolved in DCM (5 ml) and 78 μl (64 mg, 0.82 mmol) of 2-mercaptoethanol (**30**) dissolved in DCM (5 ml) was added to the mixture dropwise over 30 minutes. The mixture was stirred overnight. The result crude was purified through a silica gel column chromatographic with Cy:AcOEt mixtures 8:2. The product (**33**) was collected and the solvent was removed by rotatory evaporation. Yield: (**33**) 96.9 mg (η=38 %).

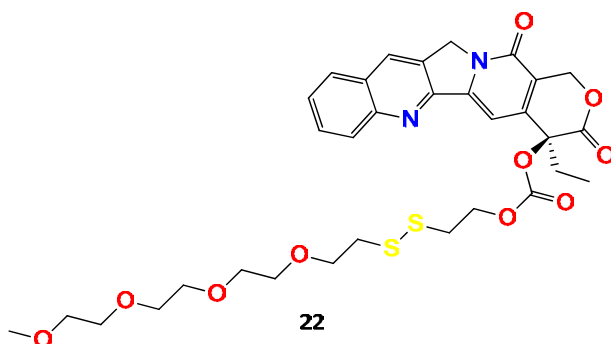
¹H NMR (400 MHz, CDCl₃) δ(ppm): δ 8.49 (d, J=4.7 Hz, 1H), 7.57 (t, J=8.1 Hz, 1H), 7.40 (d, J = 8.0 Hz, 1H), 7.19 – 7.08 (m, 1H), 3.85 – 3.74 (m, 2H), 2.98 – 2.87 (m, 2H).

3.5.3. Synthesis of Camptothecin-(4-pyridyldisulfanyl)ethyl carbonate (CPT-PYR) (**34**) [263]

A solution of 167 mg (1.36 mmol) of DMAP, 100 mg (0.33 mmol) of CPT (**4**) and 55 mg (0.18 mmol) of triphosgene were dissolved in anhydrous DCM (30 ml). The solution was reacted at room temperature. After 15 minutes, 55 mg (0.18 mmol) of compound **33** was added to the solution, and the mixture was stirred vigorously at room temperature for 18 h under argon atmosphere. The reaction was quenched by washing the organic layer with brine and dried using anhydrous MgSO_4 . The result crude was purified through a silica gel column chromatographic with AcOEt. The product **34** was collected and the solvent was removed by rotatory evaporation to yield the pure product as a yellow solid. Yield: (**34**) 91 mg ($\eta=98\%$).

$^1\text{H NMR}$ (400 MHz, CDCl_3) $\delta(\text{ppm})$: 8.54 (s, 1H), 8.50 (s, 1H), 8.37 (d, $J = 8.6$ Hz, 1H), 7.98 (d, $J = 7.4$ Hz, 2H), 7.89 (t, $J = 7.7$ Hz, 1H), 7.72 (q, $J = 7.1, 6.7$ Hz, 1H), 7.58 (s, 1H), 7.34 (s, 1H), 5.69 (d, $J = 17.3$ Hz, 1H), 5.39 (d, $J = 17.4$ Hz, 1H), 5.34 (s, 2H), 4.35 (t, $J = 6.0$ Hz, 2H), 3.18 (t, $J = 6.0$ Hz, 2H), 2.27 (m, 1H), 2.17 (m, 1H), 1.01 (t, $J = 7.2$ Hz, 3H).

3.5.4. Synthesis of (S)-4-ethyl-3,14-dioxo-3,4,12,14-tetrahydro-1H-pyrano[3',4':6,7]indolizino[1,2-b]quinolin-4-yl (2,5,8,11-tetraoxa-14,15-dithiaheptadecan-17-yl) carbonate (CPT-PEG) (**22**)



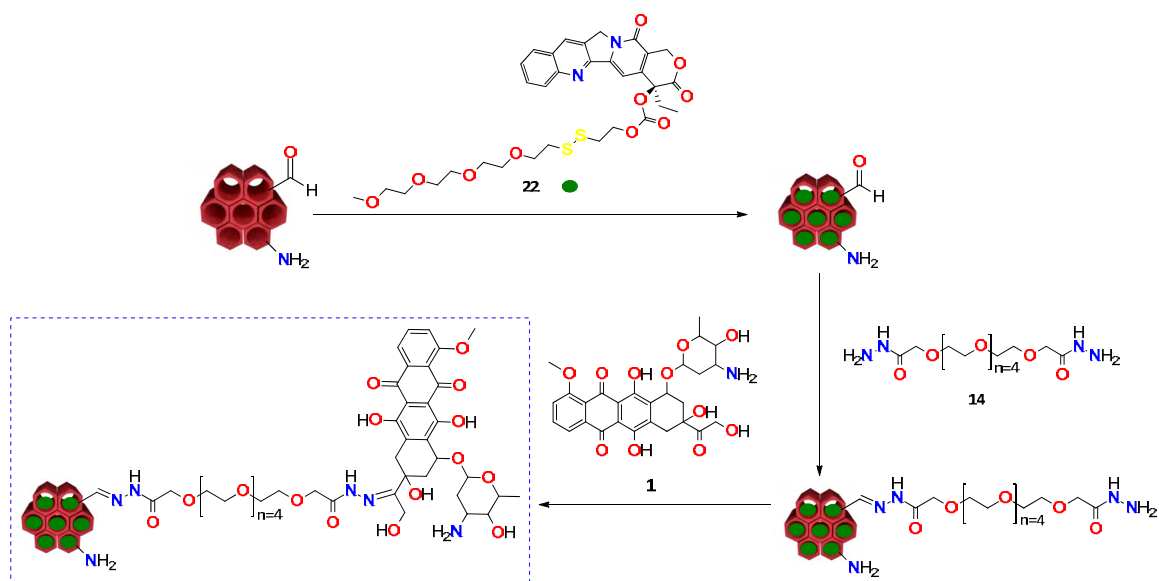
50 mg (0.08 mmol) of camptothecin-(4-pyridyldisulfanyl)ethyl carbonate (**34**) was dissolved in DCM. 20 mg (0.08 mmol) of 2,5,8,11-tetraoxatridecane-13-thiol (**24**) was dissolved in DCM (5 ml) and added to the solution dropwise over 30 minutes. The mixture was stirred for 6 h at room temperature. The result crude was purified through a silica gel column chromatographic with ACOEt. The product **22** was collected and the solvent was removed by rotatory evaporation. Yield: (**22**) 43 mg (η = 75%).

$^1\text{H NMR}$ (400 MHz, Chloroform-*d*) δ 8.41 (s, 1H), 8.25 (d, J = 8.5 Hz, 1H), 7.95 (d, J = 8.1 Hz, 1H), 7.85 (ddd, J = 8.4, 6.8, 1.4 Hz, 1H), 7.68 (t, J = 7.5 Hz, 1H), 7.36 (s, 1H), 5.70 (d, J = 17.2 Hz, 1H), 5.39 (d, J = 17.3 Hz, 1H), 5.31 (s, 2H), 4.37 (d, J = 7.2 Hz, 1H), 3.63 (s, 5H), 3.36 (s, 3H), 2.93 (td, J = 6.9, 1.7 Hz, 2H), 2.84 (t, J = 6.5 Hz, 2H), 2.29 (dd, J = 14.2, 7.3 Hz, 1H), 2.15 (dd, J = 14.2, 7.3 Hz, 1H), 1.00 (t, J = 7.5 Hz, 3H).

$^{13}\text{C NMR}$ (100 MHz, Chloroform-*d*) δ 167.40 , 157.42 , 153.60 , 152.32 , 148.81 , 146.42 , 145.78 , 131.54 , 130.99 , 129.69 , 128.65 , 120.56 , 96.41 , 78.12 , 77.36 , 72.08 , 70.74 , 70.65 , 70.49 , 69.54 , 67.22 , 66.82 , 59.18 , 50.17 , 38.73 , 36.57 , 32.05 , 7.79 .

ESI-MS m/z : calcd. 674.20 found 675.20 (M-H).

3.5.5. Dual CPT-PEG@MSN-hyd-PEG-hyd-DOX [151]



18 mg ($2.66 \cdot 10^{-5}$ mol) of CPT-PEG (**22**) were dissolved in 35 mL of CHCl_3 with the aid of sonication at 60 °C until total dissolution of the drug was achieved. Then, CPT-PEG (**22**) solution was added to a stirred suspension $\text{MSN}-(\text{NH}_2)_i(\text{CHO})_o$ (30 mg) in MeOH (25 mL) (700 rpm, 23 °C). Afterwards (24 h), a solution dihydrazide-PEG (**14**) (0.080 g, $2.36 \cdot 10^{-4}$ mol) in MeOH (20 mL) was added. After 24 h, MSNs were centrifuged, and the supernatant was collected to quantify the loading of the drug by UV-vis spectroscopy (354 nm). Then, the resulting MSNs were dispersed in a solution of DOX (**1**) (21 mg, $3.6 \cdot 10^{-5}$ mol) in MeOH (20 mL). Finally, after 48 h MSNs were washed with MeOH (three times) and H_2O (three times) until no red supernatant was obtained and then lyophilized. DOX (**1**) and CPT-PEG (**22**) loading content ($\% \text{LC} = [\text{entrapped drug} / \text{nanoparticles weight}] \times 100$) were quantified by UV-vis spectroscopy (490 and 354 nm, respectively) from the supernatant (the amount of CPT-PEG (**22**) released to the supernatant during the pore capping was subtracted from the initial value of loaded drug (CPT-PEG@MSN-(NH_2)_i(CHO)_o)).

3.5.6. Release experiments of CPT-PEG@MSN-hyd-PEG-hyd-DOX [151]

Release experiments were performed at pH 7.4 (PBS buffer), pH 6.5 (phosphate buffer, 0.2M NaH₂PO₄/0.2m Na₂HPO₄), pH 5.5, 4.5 and 4 (acetate buffer, 0.1M NaAcO/0.1 M AcOH). For each release study, MSNs (10 mg) were dispersed by sonication (2 min) in the buffer solution (1.5 mL) and kept at 37 °C, while being stirred (100 rpm). At every designated interval, buffer solutions were taken out for analysis and centrifugated (13,000 rpm, 13 min). The solid residues were dispersed in fresh buffer solution (1.5 mL). The quantities of the drugs released into the buffer solution were measured by UV-vis absorption spectroscopy at 490 nm for DOX (1) and 354 nm for CPT-PEG.

3.5.7. *In vitro* cytotoxicity [151]

In vitro cytotoxicity was performed using the MTT assay in HeLa and HepG2 cells. Experiments were carried out in 96-well plates (0.1 mL/well) where 10,000 cells/well were seeded using complete DMEM media (10% FBS, 1% glutamine, 1% penicillin/streptomycin). Twenty-four hours later, cells were incubated with MSNs for 24, 48 and 72 h at 37 °C and 5% CO₂. After a washing step with PBS, the MTT solution was added (0.5 mg/mL). Cells were incubated for 3 h at 37 °C and 5% CO₂, the MTT solution was removed, and formazan crystals were dissolved in 0.1 mL of DMSO. Finally, formazan absorbance was measured at 560 nm.

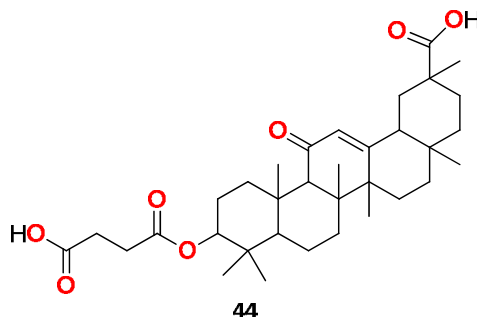
3.6. Synthetic part of chapter 2.4.

3.6.1. Synthesis of 4-(2-(2-(2-(2-hydroxyethoxy) ethoxy) ethoxy) ethoxy) benzaldehyde (benz-PEG) (**42**) [264]

0.73 g (6 mmol) of 4-hydroxybenzaldehyde (**40**), 2.10 g (6 mmol) of tetraethylene glycol monotosylate (**41**) and 2.50 g (18.1 mmol) of K_2CO_3 were dissolved in dry MeCN (50 mL). The solution was heated at reflux under a nitrogen atmosphere for 3 days. After the addition of CH_2Cl_2 (50 mL), the mixture was filtered and the precipitate was washed with CH_2Cl_2 (2 \times 50 mL). The organic filtrates were combined and the solvents were evaporated to afford the crude as a pale orange oil. The product **42** was used in the next step without further purification. Yield: (**42**) 1.80 g (η = 99%).

1H NMR (400 MHz, $CDCl_3$) δ (ppm): 2.60 (t, j =5.9 Hz, 1H), 3.77-3.56 (m, 12H), 3.92-3.87 (m, 2H), 4.25-4.20 (m, 2H), 7.05-6.99 (m, j =8,4 Hz, 2H), 7.86-7.80 (m, j =8.4 Hz, 2H).

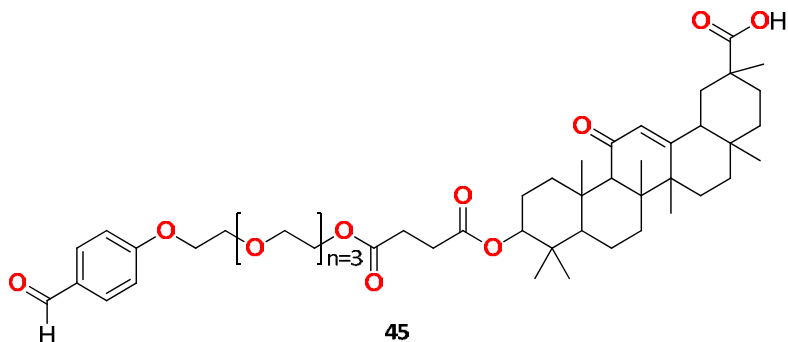
3.6.2. Synthesis of 10-((3-carboxypropanoyl)oxy)-2,4a,6a,6b,9,9,12a-heptamethyl-13-oxo-1,2,3,4,4a,5,6,6a,6b,7,8,8a,9,10,11,12,12a,12b,13,14b-icosahydricene-2-carboxylic acid (**44**) [129]



4.7 g (10.0 mmol) of GA (**40**), 2.2 g (22.0 mmol) of succinic anhydride (**43**) were mixed with anhydrous pyridine (80 mL). The reaction mixture was agitated and heated at 80 °C for 48 h. After removal of solvent, the residue was dissolved in CHCl₂ (80 mL), washed with HCl (1 mol/l, 20 mL x 3), and extracted with CH₂Cl₂ (30 mL x 3). The CH₂Cl₂ layers were combined and dried with MgSO₄. The solvent was removed by rotatory evaporation, and the residual solid was purified through silica column chromatograph (hexane:AcOEt = 1:1) to afford product **44**. Yield: (**44**) 3.5 g (η=61%).

¹H NMR (400 MHz, CDCl₃) δ (ppm): 0.83 (s, 3H), 0.90 (s, 6H), 1.14 (s, 3H), 1.18 (s, 3H), 1.24 (s, 3H), 1.38 (s, 3H), 2.38 (s, 1H), 2.66-2.74 (d, 4H), 2.80 (d, 1H), 4.55-4.59 (dd, 1H).

3.6.3. Synthesis of 10-((1-(4-formylphenoxy)-13-oxo-3,6,9,12-tetraoxahexadecan-16-oyl)oxy)-2,4a,6a,6b,9,9,12a-heptamethyl-13-oxo-1,2,3,4,4a,5,6,6a,6b,7,8,8a,9,10,11,12,12a,12b,13,14b-icosahydricene-2-carboxylic acid (benz-PEG-GA) (**45**) [118]



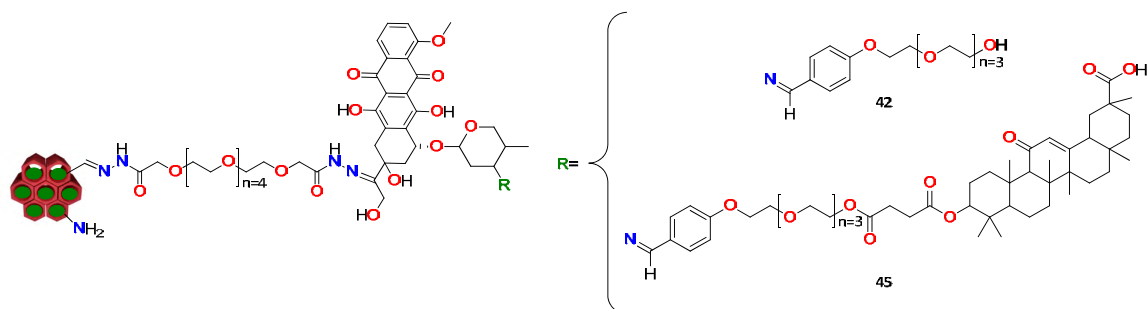
50 mg (0.08 mmol) of compound **44** and 23 mg (0.07 mmol) of benz-PEG (**42**) were dissolved in 4 mL of anhydrous DCM. The reaction mixture was agitated for 10 minutes at 0 °C. Then, 13 mg (0.1 mmol) of DMAP and 18 mg (0.08 mmol) of DCC were dissolved in 5 mL of anhydrous DCM. This solution was added to the latter and keep overnight at room temperature under nitrogen atmosphere. Finally, the organic layer was washed with water (2 x 50 mL), dried with MgSO₄, filtered and evaporated in vacuo to afford benz-PEG-GA (**45**). Yield: (**45**) 47 mg (η =64%).

¹H NMR (400 MHz, CDCl₃) δ 9.87 (s, 1H), 7.86 – 7.77 (m, J = 8.4 Hz, 2H), 7.00 (m, J = 8.4 Hz, 2H), 5.67 (s, 1H), 4.52 (dd, J = 11.6, 4.8 Hz, 1H), 4.26 – 4.18 (m, 4H), 4.14 (d, J = 9.6 Hz, 2H), 3.91 – 3.85 (m, 2H), 3.76 – 3.56 (m, 8H), 3.51 – 3.39 (m, 4H), 2.83 – 2.74 (m, 1H), 2.68 – 2.59 (m, 2H), 2.38 (s, 1H), 1.38 (s, 3H), 1.24 (s, 3H), 1.18 (s, 3H), 1.14 (s, 3H), 0.90 (s, 6H), 0.83 (s, 3H).

¹³C NMR (100 MHz, CDCl₃) δ 200.26 , 190.94 , 172.19 , 170.21 , 163.93 , 157.54 , 132.05 , 130.10 , 128.35 , 114.97 , 81.15 , 71.39 , 70.29 , 69.34 , 67.84 , 63.86 , 61.73 , 55.10 , 49.59 , 46.80 , 45.49 , 43.31 , 39.60 , 38.17 , 36.99 , 33.87 , 31.96 , 29.88 , 27.66 , 26.99 , 24.76 , 23.53 , 18.76 , 17.76 , 16.16.

ESI-MS m/z : calcd. 850.49 found 851.49 (M-H).

3.6.4. Dual conjugate CPT-PEG@MSN-hyd-PEG-hyd-DOX-PEG-OH and CPT-PEG@MSN-hyd-PEG-hyd-DOX-PEG-GA [210]



5 mg of MSNs (CPT-PEG@MSN-hyd-PEG-hyd-DOX) was placed in a round-bottomed flask with 10 mL of basic water (pH 8.5). Then an excess amount of benz-PEG (**42**) or benz-PEG-GA (**45**) were added to the solution. The mixture was stirred at room temperature for 24 h. Solid samples were collected by centrifugation at 13,000 rpm for 13 minutes, washing with basic water (pH 8.5), twice. Solvent was eliminated and MSNs were stored dry yielding CPT-PEG@MSN-hyd-PEG-hyd-DOX-PEG-OH and CPT-PEG@MSN-hyd-PEG-hyd-DOX-PEG-GA.

3.6.5. *In vitro* cytotoxicity [151]

In vitro cytotoxicity was performed using the MTT assay in HepG2 cells. Experiments were carried out in 96-well plates (0.1 mL/well) where 10,000 cells/well were seeded using complete DMEM media (10% FBS, 1% glutamine, 1% penicillin/streptomycin). Twenty-four hours later, cells were incubated with MSNs (CPT-PEG@MSN-hyd-PEG-hyd-DOX, CPT-PEG@MSN-hyd-PEG-hyd-DOX-PEG-OH and CPT-PEG@MSN-hyd-PEG-hyd-DOX-PEG-GA) for 24, 48 and 72 h at 37 °C and 5% CO_2 . After a washing step with PBS, the MTT solution was added (0.5 mg/mL). Cells were incubated for 3 h at 37 °C and 5% CO_2 , the MTT solution was removed, and formazan crystals were dissolved in 0.1 mL of DMSO. Finally, formazan absorbance was measured at 560 nm.

3.6.6. Flow cytometry [151]

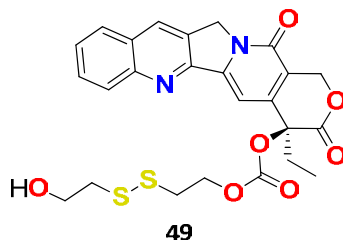
HeLa and HepG2 cells were seeded at a density of 20,000 cells/well in 96-well plates with complete DMEM media (10% FBS, 1% glutamine and 1% penicillin/streptomycin) and incubated at 37 °C, 5% CO₂ for 24 h. Then, 100 µg·mL⁻¹ of CPT-PEG@MSN-hyd-PEG-hyd-DOX, CPT-PEG@MSN-hyd-PEG-hyd-DOX-PEG-OH and CPT-PEG@MSN-hyd-PEG-hyd-DOX-PEG-GA were added, and after 1 h, 4 h, 10 h and 24 h incubation period, cells were prepared for flow cytometry. Briefly, cells were washed with PBS and harvested with 40 µL of trypsin per well. After a few minutes, 120 µL of complete DMEM were added, to stop trypsin reaction, and cells were fixed with 100 µL of paraformaldehyde 2%. DOX internalization was measured by flow cytometry.

3.6.7. Confocal microscopy for cellular internalization [151]

Uptake experiments were carried out on glass coverslips. 200,000 HepG2 cells/well were seeded using complete DMEM media (10% FBS, 1% glutamine and 1% penicillin/streptomycin). Twenty-four hours later, cells were incubated with 100 µg·mL⁻¹ of CPT-PEG@MSN-hyd-PEG-hyd-DOX, CPT-PEG@MSN-hyd-PEG-hyd-DOX-PEG-OH and CPT-PEG@MSN-hyd-PEG-hyd-DOX-PEG-GA for 1 h, 4 h and 10 h at 37 °C and 5% CO₂. For immunofluorescence, cells were fixed with 10% formalin in PBS for 10 minutes at room temperature. After 3 washing steps with PBS, cells were permeabilized using 0.1% Triton-X-100 in PBS for 10 minutes at room temperature. Then, cells were blocked using 5% milk powder in PBS for 1 h at room temperature. Subsequently, cells were incubated with mouse monoclonal anti-Rab7 primary antibody diluted in the blocking solution overnight at 4 °C followed by three PBS washing steps. The secondary antibody, goat anti-mouse Alexa fluor 555, was diluted in the blocking solution and incubated for 1 h at room temperature. Afterwards, nuclei were stained using DAPI at 1:1000 for 10 minutes at room temperature. Finally, cells were observed in a fluorescence confocal microscopy (Leica model SP8 lighting).

3.7. Synthetic part of chapter 2.5.

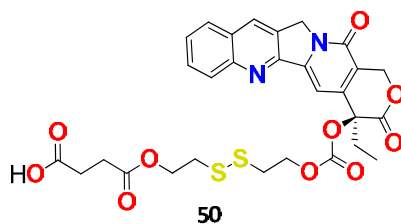
3.7.1. Synthesis of (S)-4-ethyl-3,14-dioxo-3,4,12,14-tetrahydro-1H-pyrano[3',4':6,7]indolizino[1,2-b]quinolin-4-yl (2-((2-hydroxyethyl)disulfanyl)ethyl) carbonate (49) [241]



80 mg (0.142 mmol) of CPT-PYR (**34**) were dissolved in DCM (8 mL), followed by the slow addition (19.8 mL) of 20 μ L (0.277 mmol) of 2-mercaptoethanol (**30**) dissolved in 5 mL of DCM. Then, the mixture was stirred 12 h at room temperature. Finally, the crude was washed with bicarbonate and brine three times each one and concentrated by rotatory evaporation obtaining a brown oil (**49**). Yield: (**49**) 100 mg (η =90%).

¹H-NMR (300 MHz, CDCl₃) δ (ppm): 8.42 (s, 1H), 8.23 (d, J = 8.5 Hz, 1H), 7.95 (d, J = 8.0 Hz, 1H), 7.87 – 7.81 (m, 1H), 7.72 – 7.64 (m, 2H), 7.44 (s, 1H), 5.71 (d, J = 17.2 Hz, 1H), 5.39 (d, J = 17.2 Hz, 1H), 4.40 – 4.33 (m, 2H), 3.94 – 3.84 (m, 2H), 3.12 – 2.78 (m, 5H), 2.23.

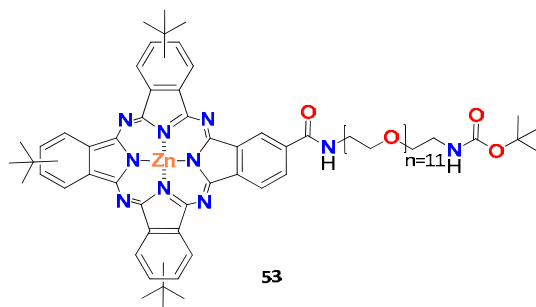
3.7.2. Synthesis of (*S*)-4-(2-((2-(((4-ethyl-3,14-dioxo-3,4,12,14-tetrahydro-1*H*-pyrano[3',4':6,7]indolizino[1,2-*b*]quinolin-4-yl) oxy) carbonyl) oxy) ethyl) disulfanyl) ethoxy)-4-oxobutanoic acid (**50**) [241]



400 mg (4.00 mmol) of succinic anhydride (**43**), 204 mg (0.38 mmol) of compound **49** and 19 mg (0.16 mmol) of DMAP were dissolved in anhydrous DCM (200 mL). The reaction mixture was stirred overnight at room temperature and then washed with water (1 × 100 mL), 50 mM HCl aqueous solution (1 × 100 mL), and brine (1 × 100 mL). The organic layer was separated and dried over anhydrous Na₂SO₄. The solution of product **50** was concentrated by rotatory evaporation. Yield: (**50**) 201 mg (η =83%).

¹H-NMR (300 MHz, CDCl₃) δ (ppm): 8.44 (s, 1H), 8.32 (d, *J* = 8.4 Hz, 1H), 7.95 (d, *J* = 8.2 Hz, 1H), 7.86 (ddd, *J* = 8.5, 6.9, 1.4 Hz, 1H), 7.69 (ddd, *J* = 8.1, 7.0, 1.1 Hz, 1H), 7.43 (s, 1H), 5.71 (d, *J* = 17.3 Hz, 1H), 5.39 (d, *J* = 17.3 Hz, 1H), 5.32 (s, 2H), 4.46–4.25 (m, 4H), 3.00–2.86 (m, 4H), 2.79–2.61 (m, 4H), 2.37–2.07 (m, 2H), 1.01 (t, *J* = 7.5, 3H).

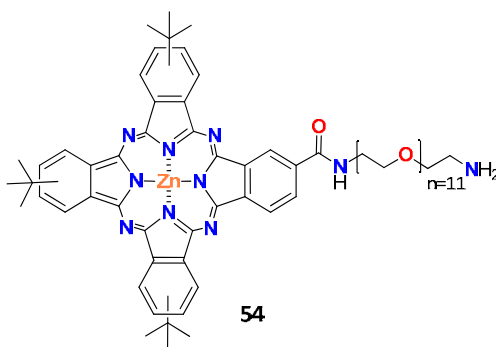
3.7.3. Synthesis of TT1-PEG-NHBOC (56)



80 mg (0.09 mmol) of Phthalocyanine **51** was dissolved in 5 mL anhydrous THF. Then, 116 mg (0.18 mmol, 3 equivalents) of PEG linker **52** were dissolved in 10 mL of THF and added to the solution. The mixture was stirred 12 h at RT. The crude was washed with 100 mL of HCl 1M twice, 100 mL of saturated solution of Na₂CO₃ and 100 mL of water. The product **53** was concentrated by rotatory evaporator.

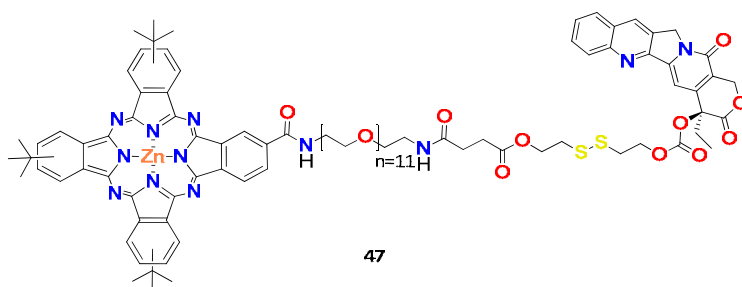
¹H-NMR (400 MHz, CDCl₃) δ (ppm): 9.56 – 9.39 (m, 9H Ar. Pc), 8.28 (m, 7H Ar. Pc), 5.08-4.99 (m, 3H), 3.64-2.83 (m, 128H PEG), 1.44 (s, 9H *tert*-butyl), 1.43 (s, 27H *tert*-butyl ar.). IR (evap. film): 3341.8 (N-H); 2954.8-2868.2 (C-H ar.) 1712.5-1613.7 (C=O); 1392.2-1255.4 (C-O) cm⁻¹.

ESI-MS *m/z*: calcd. 1414.66 found 1415.66 (M-H).

3.7.4. Synthesis of TT1-PEG-NH₂ (54)

37 mg (0.26 mmol) of compound **53**, were dissolved in 10 mL of anhydrous DCM. The mixture was cooled at 0 °C and stirred for 30 minutes. Then, 1 mL (13 mmol) of trifluoroacetic acid (TFA) was added dropwise. Afterwards, the mixture was stirred for 1.5 h at 0 °C and the solvent was removed at vacuum. The product **54** is directly utilized in the next step without further purification.

3.7.5. Synthesis of TT1-PEG-CPT (47)



35 mg (0.027 mmol) of compound **54** were dissolved in 3 mL of anhydrous DCM. Followed by the addition of 16 mg (0.029 mmol, 1.1 eq.) of compound **50** and 14 mg (0.02 mmol, 1 eq.) of benzotriazol-1-yl-oxytrityrrolidinophosphonium hexafluorophosphate. 2 drops of DIPEA were added to the mixture and it was stirred for 4 h. Then, the mixture was washed trice with brine and the organic layer was removed by rotatory evaporation. A gradient flash silica chromatographic column was performed starting from AcOEt eluent conditions, gradually changed to DCM and finally to 95:5 DCM:MeOH. Finally, crude **47** is washed with water and centrifugated twice, repeating the same process with *tert*-butyl ether. The isolated product **47** was obtained as a blue solid. Yield: (**47**) 18 mg (η =35%).

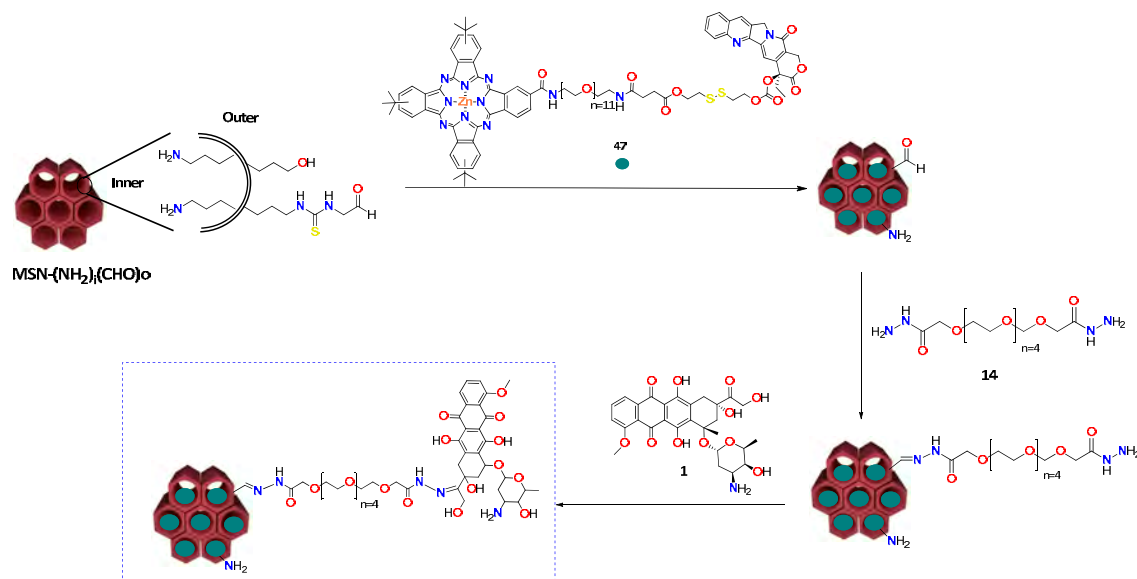
¹H-NMR (400 MHz, DMSO-*d*₆) δ (ppm): 9.9-7.7 (m 12H; Pc-H), 8.7-5.2 (m 10H; Ar_{CPT}-H), 4.3 (m 2H; CH₂) 3.8-3.3 (br 48H, PEG-H), 3.0 (m 2H; CH₂) 2.9 (M 2H; CH₂), 2.4 (M 2H; CH₂), 2.3 (M 2H; CH₂), 2.2 (M 2H; CH₂), 1.8 (m 27H; C(CH₃)₃), 0.8 ppm (m 3H; CH₃).

¹H-NMR (400 MHz, CDCl₃) δ (ppm): 9.51-7.78 (m 12H; Pc-H), 8.38-5.29 (m 10H; Ar_{CPT}-H), 4.38 (m 2H; CH₂) 3.64-3.39 (br 46 H, PEG-H), 2.93 (m 2H; CH₂) 2.89 (m 2H; CH₂), 2.63 (m 2H; CH₂), 2.60 (M 2H; CH₂), 2.28 (M 2H; CH₂), 2.18 (m 27H; C(CH₃)₃), 1.01 ppm (m 3H; CH₃).

ESI-MS m/z: calcd 1924,71 found 1925,72 (M-H).

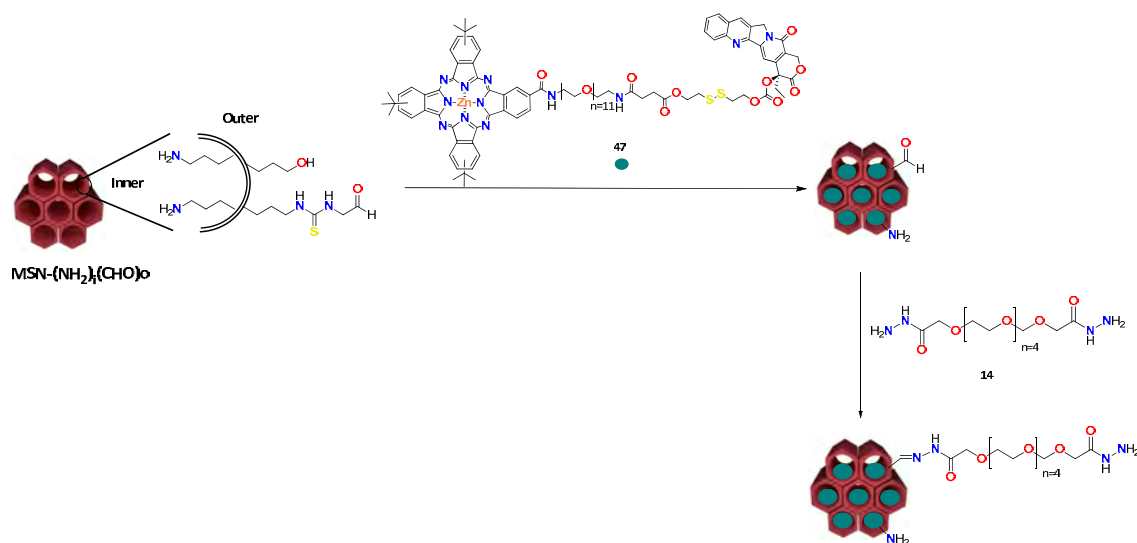
UV/Vis (MeOH) $\lambda_{\text{m\acute{a}x.}$ (ϵ)= 679, 674, 609, 350 nm

3.7.6. Dual conjugate TT1-PEG-CPT@MSN-hyd-PEG-hyd-DOX



1.4 mg ($7.27 \cdot 10^{-7}$ mol) of TT1-PEG-CPT (**47**) were dissolved in 3 mL of CHCl_3 with the aid of sonication until total dissolution of the conjugate was achieved. Then, TT1-PEG-CPT (**47**) solution was added to a stirred suspension $\text{MSN}-(\text{NH}_2)_i(\text{CHO})_o$ (5 mg) in MeOH (5 mL) (700 rpm, 23 °C). Afterwards (48 h), a solution of dihydrazide-PEG (**14**) (0.054 g, $1.60 \cdot 10^{-4}$) in MeOH (15 mL) was added. After 24 h, MSNs were centrifuged, and the supernatant was collected to quantify the loading of the conjugate **47** by UV-vis spectroscopy (679 nm). Then, the resulting MSNs were dispersed in a solution of DOX (**1**) (21 mg, $3.6 \cdot 10^{-5}$ mol) in EtOH (20 mL). Finally, after 48 h MSNs were washed with EtOH (three times) and H_2O (three times) until no red supernatant was obtained and then lyophilized. DOX (**1**) and TT1-PEG-CPT (**47**) loading content (%LC=[entrapped drug/nanoparticles weight] x 100) were quantified by UV-vis spectroscopy (490 and 679 nm, respectively) from the supernatant (the amount of TT1-PEG-CPT (**47**) released to the supernatant during the pore capping was subtracted from the initial value of loaded drug (TT1-PEG-CPT@MSN-(NH_2) $_i$ (CHO) $_o$)).

3.7.7. Synthesis of TT1-PEG-CPT@MSN-hyd-PEG-hyd



1.4 mg ($7.27 \cdot 10^{-7}$ mol) of TT1-PEG-CPT (**47**) were dissolved in 3 mL of CHCl_3 with the aid of sonication until total dissolution of the conjugate was achieved. Then, TT1-PEG-CPT (**47**) solution was added to a stirred suspension MSN-(NH_2)₄(CHO)₆ (5 mg) in MeOH (5 mL) (700 rpm, 23 °C). Afterwards (48 h), a solution of dihydrazide-PEG (**14**) (0.054 g, $1.60 \cdot 10^{-4}$) in MeOH (15 mL) was added. After 24 h, MSNs were centrifuged, and the supernatant was collected to quantify the loading of the conjugate **47** by UV-vis spectroscopy (679 nm). Finally, MSNs were washed with EtOH (three times) and H₂O (three times) and then lyophilized.

3.7.7. Release experiments of TT1-PEG-CPT@MSN-hyd-PEG-hyd-DOX [151]

Release experiments were performed at pH 7.4 (PBS buffer), pH 5.5 and 4 (acetate buffer, 0.1M NaAcO/0.1 M AcOH). MSNs (10 mg) were dispersed by sonication (2 min) in the buffer solution (1.5 mL) and kept at 37 °C, while being stirred (100 rpm). At every designated interval, buffer solutions were taken out for analysis. The resulting precipitate was isolated by centrifugation at 13,000 rpm for 13 minutes. 0.8 mL of the supernatant was extracted and stored in order to calculate the concentration of TT1-PEG-CPT (**47**) through UV/Vis spectroscopy. The Eppendorf was refilled again with 1 mL of the previous buffer. When the release was accomplished, 1,2 mL of CHCl_3 was added to each sample to extract the conjugate **47** from buffer solution and 1 mL was taken to measure the absorbance samples at 244 nm through UV-light. Then, the values were interpolated in a calibration curve.

3.7.8. *In vitro* cytotoxicity

In vitro cytotoxicity was performed using the MTT assay in HeLa cell line. A concentration of 10,000 cells per well is chosen. Cells are seeded using complete DMEM media (10% FBS, 1% glutamine, 1% penicillin/streptomycin) into 96 well plate ($\mu\text{L}/\text{well}$). 24 h later, cells were incubated with MSN-hyd-PEG-hyd-DOX, TT1-PEG-CPT@MSN-hyd-PEG-hyd and TT1-PEG-CPT@MSN-hyd-PEG-hyd-DOX for 24, 48 and 72 h at 37 °C and 5% CO₂. After a washing step with PBS, the MTT solution was added (0.5 mg/mL). Cells were incubated for 3 h at 37 °C and 5% CO₂. MTT solution was removed and formazan crystals were dissolved in 0.1 mL of DMSO. Finally, formazan absorbance was measured at 560 nm.

The statistical study was performed using an unpaired *t-student* test, double tailed and with a confidence interval of 95%.

3.7.9. Flow cytometry

HeLa cells were seeded at a density of 20,000 cells/well in 96-well plates with complete DMEM media (10% FBS, 1% glutamine and 1% penicillin/streptomycin) and incubated at 37 °C, 5% CO₂ for 24 h. Then, 100 $\mu\text{g}\cdot\text{mL}^{-1}$ of TT1-PEG-CPT@MSN-hyd-PEG-hyd-DOX were added, and after 4 h incubation period, cells were prepared for flow cytometry. Briefly, cells were washed with PBS and harvested with 40 μL of trypsin per well. After a few minutes, 120 μL of complete DMEM were added, to stop trypsin reaction, and cells were fixed with 100 μL of paraformaldehyde 2%. DOX internalization was measured by flow cytometry.

3.7.10. Confocal microscopy for cellular internalization [151]

Uptake experiments were carried out on glass coverslips. 180,000 HeLa cells/well were seeded using complete DMEM media (10% FBS, 1% glutamine and 1% penicillin/streptomycin). Twenty-four hours later, cells were incubated with TT1-PEG-CPT@MSN-hyd-PEG-hyd-DOX for 4 h at 37 °C and 5% CO₂. For immunofluorescence, cells were fixed with 10% formalin in PBS for 10 minutes at room temperature. After 3 washing steps with PBS, cells were permeabilized using 0.1% Triton-X-100 in PBS for 10 minutes at room temperature. Then, cells were blocked using 5% milk powder in PBS for 1 h at room temperature. Subsequently, cells were incubated with mouse monoclonal anti-Rab7 primary antibody diluted in the blocking solution overnight at 4 °C followed by three PBS washing steps. The secondary antibody goat anti-mouse Alexa fluor 555 diluted in the blocking solution and incubated for 1 h at room temperature. If required, nuclei

were stained using DAPI (Sigma-Aldrich) at 1:1000 for 10 minutes at room temperature. Finally, cells were observed in a fluorescence confocal microscopy (Leica model SP8 lighting).

Chapter 4. Conclusions

Chapter 4. Conclusions

1. The functionalization of the outer surface of MSN with PEG's functionalized with quaternized amine end-groups provided a highly effective capping methodology. This new procedure has been termed: radial-capping. The effectiveness of these chains in the pore capping has been assessed studying the release of Safranin under physiological conditions. From these experiments, it has been determined that the presence of a cationic moiety at the end of PEGs chains offered a better pore capping than those with neutral groups PEGs of the same length.
2. A pH-triggered DDS for the co-delivery of drugs based on the so called radial-capping approach has been synthesized. CPT / TPT have been loaded within the pores of the MSN. Then, the system was capped by the addition of a DOX-PEG moiety in the surface of the MSN. The stability of the as-prepared DDS, CPT@MSN-hyd-PEG-hyd-DOX / TPT@MSN-hyd-PEG-hyd-DOX, was studied under physiological conditions, showing a negligible release of the drugs, thus, reducing the intrinsic toxicity of the treatment. On the other hand, under acidic conditions a burst and sustained release take places. Uptake experiments have demonstrated that CPT@MSN-hyd-PEG-hyd-DOX internalizes within HeLa cells and are located within endosomes in the cytoplasm. Moreover, the release of the drugs leads to a synergistic effect that is more evident for the combination of DOX and CPT than the combination of DOX and TPT.
3. The cytotoxicity of the as-synthesized DDS, CPT@MSN-hyd-PEG-hyd-DOX, was improved by increasing the loading content of CPT inside the MSN. To do so, a soluble prodrug of CPT has been synthesised by the addition of a cleavable PEG chain. A 6.3% of this prodrug, CPT-PEG, was loaded within the nanochannels of an MSN, which corresponds to 31% of extra "free" drug in comparison with CPT. The system was assembled following the radial-capping based on the functionalization of the DOX-PEG-moiety in the outer surface of the MSN. The synthesized CPT-PEG@MSN-hyd-PEG-hyd-DOX shows higher cytotoxicity in HepG2 cells than Hela cells in comparison with the starting CPT@MSN-hyd-PEG-hyd-DOX.
4. The targeting capability of the CPT-PEG@MSN-hyd-PEG-hyd-DOX system towards HepG2 cells was improved by the decoration of the surface of the nanoparticle with the Glycyrrhetic acid (GA) ligand. For this purpose, a benzaldehyde moiety attached to a

PEG linker with a GA ligand located in one end has been synthesized and characterized by $^1\text{H-NMR}$ and HRMS. Then, the linker was attached to the DDS by imine formation with the amino group of the outer DOX of CPT-PEG@MSN-hyd-PEG-hyd-PEG-DOX. Uptake analysis has demonstrated that CPT-PEG@MSN-hyd-PEG-hyd-PEG-DOX-PEG-GA is able to discriminate between HeLa and HepG2 cells, showing higher endocytosis in the latter cell line. Besides, the anionic character of the system derived from the carboxylic acid of the GA moiety enhances the endosomal escape.

5. A pH-triggered DDS for the co-delivery of DOX and a cleavable conjugate Phthalocyanine-CPT has been prepared. This DDS was designed for the combination of chemo- and photodynamic therapies of cancer. To do so, a synthetic pathway to attach CPT and phthalocyanine with a cleavable PEG linker was developed. This new conjugate improves the solubility of both drugs. In this regard, 8% of loading within an MSN was achieved. Thus, employing the same radial-capping approximation, the DOX-PEG moiety was attached to the outer surface of the nanomaterial. Release of the three drugs from TT1-PEG-CPT@MSN-hyd-PEG-hyd-DOX was confirmed by CLSM, displaying the presence of phthalocyanine, CPT and DOX inside the cell. Besides, the synergistic effect between CPT and DOX was assessed in HeLa cells.

List of publications and presentations

Publications

M. C. Llinàs, G. Martínez-Edo, A. Cascante, I. Porcar, S. Borrós, and D. Sánchez-García, "Preparation of a mesoporous silica-based nano-vehicle for dual DOX / CPT pH-triggered delivery," *Drug Deliv.*, vol. 25, no. 1, pp. 1137–1146, 2018.

G. Martínez-Edo, A. Balmori, I. Pontón, A. Martí del Rio, and D. Sánchez-García, "Functionalized Ordered Mesoporous Silicas (MCM-41): Synthesis and Applications in Catalysis," *Catalysts*, vol. 8, no. 12, p. 617, Dec. 2018.

G. Martínez-Edo, M. C. Llinàs, G. Anguera, A. Gibert, and D. Sánchez-García, "Functionalized mesoporous silica nanoparticles with 2,7,12,17-tetraphenylporphycene," *J. Porphyrins Phthalocyanines*, vol. 23, no. 1, pp. 1–5, Feb. 2019.

G. Martínez-Edo, M. C. Llinàs, S. Borrós, and D. Sánchez-García, "Isothiocyanate-Functionalized Mesoporous Silica Nanoparticles as Building Blocks for the Design of Nanovehicles with Optimized Drug Release Profile," *Nanomaterials*, vol. 9, no. 9, p. 1219, 2019.

Congresses

ICREA Conference on Functional Nanocontainers, 17-20 of October 2016, CaixaForum Auditorium Tarragona (Spain). Poster presentation.

I Jornada de Doctorands del IQS, 16-17 of May 2019, IQS School of Engineering (Spain). Poster and Oral presentation.

Congreso Internacional Duchenne Parent Project España, 7-9 of June 2019, Madrid (Spain).

Onzena Trobada de Joves Investigadors dels Països Catalans, 28-30 of January 2020, Escola Politècnica Superior d'Enginyeria de Vilanova i la Geltrú (Spain). Oral presentation.

Chapter 5. Bibliography

Chapter 5. Bibliography

- [1] S. Senapati, A. K. Mahanta, S. Kumar, and P. Maiti, "Controlled drug delivery vehicles for cancer treatment and their performance," *Signal Transduction and Targeted Therapy*, vol. 3, no. 1, p. 7, 2018.
- [2] J. S. Bertram, "The molecular biology of cancer," *Mol. Aspects Med.*, vol. 21, no. 1, pp. 167–223, 2001.
- [3] F. Muhammad *et al.*, "Responsive delivery of drug cocktail via mesoporous silica nanolamps," *J. Colloid Interface Sci.*, vol. 434, pp. 1–8, 2014.
- [4] M. Shurin, "Cancer as an immune-mediated disease," *ImmunoTargets Ther.*, vol. 1, p. 6, 2012.
- [5] K. D. Miller *et al.*, "Cancer treatment and survivorship statistics, 2019," *CA. Cancer J. Clin.*, vol. 69, no. 5, pp. 363–385, 2019.
- [6] D. W. Kufe *et al.*, *Holland-Frei Cancer Medicine, 6th edition*. 2003.
- [7] Z. Li, W. Song, M. Rubinstein, and D. Liu, "Recent updates in cancer immunotherapy: A comprehensive review and perspective of the 2018 China Cancer Immunotherapy Workshop in Beijing," *J. Hematol. Oncol.*, vol. 11, no. 1, pp. 1–15, 2018.
- [8] S. Kruger *et al.*, "Advances in cancer immunotherapy 2019 - Latest trends," *J. Exp. Clin. Cancer Res.*, vol. 38, no. 1, pp. 1–11, 2019.
- [9] World Health Organization, "Summary of global update on provision of preventive chemotherapy in 2017 and progress towards ensuring timely supplies and management," *Wkly. Epidemiol. Rec.*, vol. 39, no. 93, pp. 508–520, 2018.
- [10] K. D. Miller, R. L. Siegel, and A. Jemal, "Cancer Treatment & Survivorship Facts & Figures 2016-2017," *Am. Cancer Soc.*, vol. 15, no. 12, pp. 1–41, 2016.
- [11] A. Pearce *et al.*, "Incidence and severity of self-reported chemotherapy side effects in routine care: A prospective cohort study," *PLoS One*, vol. 12, no. 10, pp. 1–12, 2017.
- [12] I. J. Fidler, "The organ microenvironment and cancer metastasis," *Differentiation*, vol. 70, no. 9–10, pp. 498–505, 2002.
- [13] L. Chen *et al.*, "Multifunctional Redox-Responsive Mesoporous Silica Nanoparticles for Efficient Targeting Drug Delivery and Magnetic Resonance Imaging," *ACS Appl. Mater. Interfaces*, vol. 8, no. 49, pp. 33829–33841, 2016.
- [14] H. S. Abandansari, M. Abuali, M. R. Nabid, and H. Niknejad, "Enhance chemotherapy

- efficacy and minimize anticancer drug side effects by using reversibly pH- and redox-responsive cross-linked unimolecular micelles,” *Polymer (Guildf)*, vol. 116, pp. 16–26, 2017.
- [15] T. Bagnyukova, I. G. Serebriiskii, Y. Zhou, E. A. Hopper-Borge, E. A. Golemis, and I. Astsaturov, “Chemotherapy and signaling: How can targeted therapies supercharge cytotoxic agents?,” *Cancer Biology and Therapy*, vol. 10, no. 9, pp. 839–853, 2010.
- [16] O. Tacar, P. Sriamornsak, and C. R. Dass, “Doxorubicin: an update on anticancer molecular action, toxicity and novel drug delivery systems,” *J. Pharm. Pharmacol.*, vol. 65, no. 2, pp. 157–170, 2013.
- [17] M. Grimaldi *et al.*, “Long-term effects after treatment with platinum compounds, cisplatin and [Pt(O,O'-acac)(γ -acac)(DMS)]: Autophagy activation in rat B50 neuroblastoma cells,” *Toxicol. Appl. Pharmacol.*, vol. 364, pp. 1–11, 2019.
- [18] K. Tsujii, T. Hattori, A. Imaoka, T. Akiyoshi, and H. Ohtani, “5-Fluororacil-Induced Gastrointestinal Damage Impairs the Absorption and Anticoagulant Effects of Dabigatran Etexilate,” *J. Pharm. Sci.*, vol. 107, no. 5, pp. 1430–1433, 2018.
- [19] J. Lu, M. Liong, J. I. Zink, and F. Tamanoi, “Mesoporous silica nanoparticles as a delivery system for hydrophobic anticancer drugs,” *Small*, vol. 3, no. 8, pp. 1341–1346, 2007.
- [20] B. Shen, K. Zhao, S. Ma, D. Yuan, and Y. Bai, “Topotecan-loaded mesoporous silica nanoparticles for reversing multi-drug resistance by synergetic chemoradiotherapy,” *Chem. - An Asian J.*, vol. 10, no. 2, pp. 344–348, 2015.
- [21] A. Montecucco, F. Zanetta, and G. Biamonti, “Molecular mechanisms of etoposide,” *EXCLI J.*, vol. 14, pp. 95–108, 2015.
- [22] T. A. H. Järvinen *et al.*, “Amplification and deletion of topoisomerase II α associate with ErbB-2 amplification and affect sensitivity to topoisomerase II inhibitor doxorubicin in breast cancer,” *Am. J. Pathol.*, vol. 156, no. 3, pp. 839–847, 2000.
- [23] S. Samuel, T. Nguyen, and H. A. Choi, “Pharmacologic Characteristics of Corticosteroids,” *J. Neurocritical Care*, vol. 10, no. 2, pp. 53–59, 2017.
- [24] J. D. Martin *et al.*, “Dexamethasone Increases Cisplatin-Loaded Nanocarrier Delivery and Efficacy in Metastatic Breast Cancer by Normalizing the Tumor Microenvironment,” *ACS Nano*, vol. 13, no. 13, pp. 6396–6408, 2019.
- [25] B. A. Chabner and E. S. Chabner, “Mitotic inhibitors,” *Journal of Thoracic Oncology*, vol. 6. NIH Public Access, pp. 1791–1792, 1994.

- [26] P. Chowdhury *et al.*, "Tannic acid-inspired paclitaxel nanoparticles for enhanced anticancer effects in breast cancer cells," *J. Colloid Interface Sci.*, vol. 535, pp. 133–148, 2019.
- [27] E. Yechiel, "Interactive Vehicles in Synergistic Cosmeceuticals: Advances in Nanoencapsulation, Transportation, Transfer, and Targeting," in *Delivery System Handbook for Personal Care and Cosmetic Products: Technology, Applications and Formulations*, Elsevier Inc., 2005, pp. 303–319.
- [28] A. M. Butt, M. C. Iqbal, M. Amin, and H. Katas, "Synergistic effect of pH-responsive folate-functionalized poloxamer 407-TPGS-mixed micelles on targeted delivery of anticancer drugs," *Int. J. Nanomedicine*, vol. 10, pp. 1321–1334, 2015.
- [29] K. M. Camacho, S. Kumar, S. Menegatti, D. R. Vogus, A. C. Anselmo, and S. Mitragotri, "Synergistic Antitumor Activity of Camptothecin-Doxorubicin Combinations and their Conjugates with Hyaluronic Acid HHS Public Access," *J Control Release*, vol. 210, pp. 198–207, 2015.
- [30] Z. Y. Li *et al.*, "One-pot construction of functional mesoporous silica nanoparticles for the tumor-acidity-activated synergistic chemotherapy of glioblastoma," *ACS Appl. Mater. Interfaces*, vol. 5, no. 16, pp. 7995–8001, 2013.
- [31] N. A. Patankar, J. Pritchard, M. Van Grinsven, M. Osooly, and M. B. Bally, "Topotecan and doxorubicin combination to treat recurrent ovarian cancer: The influence of drug exposure time and delivery systems to achieve optimum therapeutic activity," *Clin. Cancer Res.*, vol. 19, no. 4, pp. 865–877, 2013.
- [32] T. H. Guthrie, L. J. McElveen, E. S. Porubsky, and J. D. Harmon, "Cisplatin and doxorubicin. An effective chemotherapy combination in the treatment of advanced basal cell and squamous carcinoma of the skin," *Cancer*, vol. 55, no. 8, pp. 1629–1632, 1985.
- [33] X. L. Guo *et al.*, "Co-delivery of cisplatin and doxorubicin by covalently conjugating with polyamidoamine dendrimer for enhanced synergistic cancer therapy," *Acta Biomater.*, vol. 84, pp. 367–377, 2019.
- [34] C. Dong *et al.*, "A Protein-Polymer Bioconjugate-Coated Upconversion Nanosystem for Simultaneous Tumor Cell Imaging, Photodynamic Therapy, and Chemotherapy," *ACS Appl. Mater. Interfaces*, vol. 8, no. 48, pp. 32688–32698, 2016.
- [35] N. Ando *et al.*, "Surgery plus chemotherapy compared with surgery alone for localized squamous cell carcinoma of the thoracic esophagus: A Japan Clinical Oncology Group Study - JCOG9204," *J. Clin. Oncol.*, vol. 21, no. 24, pp. 4592–4596, 2003.

- [36] P. G. Rose *et al.*, "Concurrent cisplatin-based radiotherapy and chemotherapy for locally advanced cervical cancer," *N. Engl. J. Med.*, vol. 340, p. 1145, 1999.
- [37] E. C. Ko, D. Raben, and S. C. Formenti, "The integration of radiotherapy with immunotherapy for the treatment of non-small cell lung cancer," *Clinical Cancer Research*, vol. 24, no. 23, pp. 5792–5806, 2018.
- [38] N. Bhalla, R. Brooker, and M. Brada, "Combining immunotherapy and radiotherapy in lung cancer," *Journal of Thoracic Disease*, vol. 10, pp. S1447–S1460, 2018.
- [39] W. Fan *et al.*, "A smart upconversion-based mesoporous silica nanotheranostic system for synergetic chemo-/radio-/photodynamic therapy and simultaneous MR/UCL imaging," *Biomaterials*, vol. 35, no. 32, pp. 8992–9002, 2014.
- [40] L. F. De Freitas and M. R. Hamblin, "Antimicrobial photoinactivation with functionalized fullerenes," in *Nanobiomaterials in Antimicrobial Therapy: Applications of Nanobiomaterials*, Elsevier Inc., 2016, pp. 1–27.
- [41] D. Dave, U. Desai, and N. Despande, "Photodynamic Therapy: A View through Light," *J. Orofac. Res.*, vol. 2, pp. 82–86, 2012.
- [42] C. Chen *et al.*, "Hyaluronic acid conjugated polydopamine functionalized mesoporous silica nanoparticles for synergistic targeted chemo-photothermal therapy," *Nanoscale*, vol. 11, no. 22, pp. 11012–11024, 2019.
- [43] E. A. Dubikovskaya, S. H. Thorne, T. H. Pillow, C. H. Contag, and P. A. Wender, "Overcoming multidrug resistance of small-molecule therapeutics through conjugation with releasable octaarginine transporters.," *Proc. Natl. Acad. Sci. U. S. A.*, vol. 105, no. 34, pp. 12128–33, 2008.
- [44] W. Li *et al.*, "Synthesis and Evaluation of Camptothecin Antibody-Drug Conjugates," *ACS Med. Chem. Lett.*, vol. 10, no. 10, pp. 1386–1392, 2019.
- [45] N. Nasongkla *et al.*, "Multifunctional polymeric micelles as cancer-targeted, MRI-ultrasensitive drug delivery systems," *Nano Lett.*, vol. 6, no. 11, pp. 2427–2430, 2006.
- [46] S. Maleki Dizaj, M. Barzegar-Jalali, M. H. Zarrintan, K. Adibkia, and F. Lotfipour, "Calcium carbonate nanoparticles as cancer drug delivery system," *Expert Opin. Drug Deliv.*, vol. 12, no. 10, pp. 1649–1660, 2015.
- [47] R. Chouhan and A. Bajpai, "Real time in vitro studies of doxorubicin release from PHEMA nanoparticles," *J. Nanobiotechnology*, vol. 7, no. 1, p. 5, 2009.
- [48] K. M. Shakesheff, "Drug delivery systems," in *Handbook of Biodegradable Polymers:*

- Isolation, Synthesis, Characterization and Applications*, 2011, pp. 363–378.
- [49] S. Ezrahi, A. Aserin, and N. Garti, “Basic principles of drug delivery systems – the case of paclitaxel,” *Adv. Colloid Interface Sci.*, vol. 263, pp. 95–130, 2019.
- [50] G. Tiwari *et al.*, “Drug delivery systems: An updated review,” *Int. J. Pharm. Investig.*, vol. 2, no. 1, p. 2, 2012.
- [51] H. S. Kim, X. Sun, J. H. Lee, H. W. Kim, X. Fu, and K. W. Leong, “Advanced drug delivery systems and artificial skin grafts for skin wound healing,” *Adv. Drug Deliv. Rev.*, vol. 146, pp. 209–239, 2019.
- [52] K.-N. Yang, C.-Q. Zhang, W. Wang, P. C. Wang, J.-P. Zhou, and X.-J. Liang, “pH-responsive mesoporous silica nanoparticles employed in controlled drug delivery systems for cancer treatment,” *Cancer Biol. Med.*, vol. 11, no. 1, pp. 34–43, 2014.
- [53] M. Hecht, E. Climent, M. Biyikal, F. Sancenón, R. Martínez-Máñez, and K. Rurack, “Gated hybrid delivery systems: En route to sensory materials with inherent signal amplification,” *Coord. Chem. Rev.*, vol. 257, no. 17–18, pp. 2589–2606, 2013.
- [54] J. L. Vivero-Escoto, I. I. Slowing, V. S. Y. Lin, and B. G. Trewyn, “Mesoporous silica nanoparticles for intracellular controlled drug delivery,” *Small*, vol. 6, no. 18, pp. 1952–1967, 2010.
- [55] Z. Ma *et al.*, “A theranostic agent for cancer therapy and imaging in the second near-infrared window,” *Nano Res.*, vol. 12, no. 2, pp. 273–279, 2019.
- [56] M. C. Llinàs and D. Sánchez-garcía, “Nanopartículas de sílice: preparación y aplicaciones en biomedicina,” *Afinidad LXXI*, vol. 565, no. 565, pp. 20–31, 2014.
- [57] I. Khan, K. Saeed, and I. Khan, “Nanoparticles: Properties, applications and toxicities,” *Arab. J. Chem.*, vol. 12, no. 7, pp. 908–931, 2019.
- [58] M. D. Mauricio *et al.*, “Nanoparticles in Medicine : A Focus on Vascular Oxidative Stress,” *Oxid. Med. Cell. Longev.*, vol. 2018, pp. 1–20, 2018.
- [59] S. A. Smith, L. I. Selby, A. P. R. Johnston, and G. K. Such, “The Endosomal Escape of Nanoparticles: Toward More Efficient Cellular Delivery,” *Bioconjug. Chem.*, vol. 30, no. 2, pp. 263–272, 2019.
- [60] Y. Rojas-Aguirre, K. Aguado-Castrejón, and I. González-Méndez, “La nanomedicina y los sistemas de liberación de fármacos: ¿la revolución de la terapia contra el cáncer?,” *Educ. Quim.*, vol. 27, no. 4, pp. 286–291, 2016.
- [61] V. P. Torchilin, “Multifunctional, stimuli-sensitive nanoparticulate systems for drug

- delivery," *Nat. Rev. Drug Discov.*, vol. 13, no. 11, pp. 813–827, 2014.
- [62] A. Z. Wilczewska, K. Niemirowicz, K. H. Markiewicz, and H. Car, "Nanoparticles as drug delivery systems," *Pharmacol. Reports*, vol. 64, no. 5, pp. 1020–1037, 2012.
- [63] A. S. Chauhan, "Dendrimers for Drug Delivery," *Molecules*, vol. 23, no. 4, pp. 1–9, 2018.
- [64] E. Abbasi *et al.*, "Dendrimers: Synthesis, applications, and properties," *Nanoscale Res. Lett.*, vol. 9, no. 1, pp. 1–10, 2014.
- [65] P. Ghosh, G. Han, M. De, C. K. Kim, and V. M. Rotello, "Gold nanoparticles in delivery applications," *Adv. Drug Deliv. Rev.*, vol. 60, no. 11, pp. 1307–1315, 2008.
- [66] Y. Song, Y. Li, Q. Xu, and Z. Liu, "Mesoporous silica nanoparticles for stimuli-responsive controlled drug delivery: advances, challenges, and outlook," *Int. J. Nanomedicine*, vol. Volume 12, pp. 87–110, 2016.
- [67] M. Vallet-Regí, L. Ruiz-González, I. Izquierdo-Barba, and J. M. González-Calbet, "Revisiting silica based ordered mesoporous materials: medical applications," *J. Mater. Chem.*, vol. 16, no. 1, pp. 26–31, 2006.
- [68] M. Colilla, "Silica-based Ceramics: Mesoporous Silica," in *Bio-Ceramics with Clinical Applications*, Chichester, UK, 2014, pp. 109–151.
- [69] I. I. Slowing, J. L. Vivero-Escoto, C. W. Wu, and V. S. Y. Lin, "Mesoporous silica nanoparticles as controlled release drug delivery and gene transfection carriers," *Advanced Drug Delivery Reviews*, vol. 60, no. 11, pp. 1278–1288, 2008.
- [70] S. H. Wu and H. P. Lin, "Synthesis of mesoporous silica nanoparticles," *Chem. Soc. Rev.*, vol. 42, no. 9, pp. 3862–3875, 2013.
- [71] N. I. Vazquez, Z. Gonzalez, B. Ferrari, and Y. Castro, "Synthesis of mesoporous silica nanoparticles by sol–gel as nanocontainer for future drug delivery applications," *Boletín la Soc. Española Cerámica y Vidr.*, vol. 56, no. 3, pp. 139–145, 2017.
- [72] F. Hoffmann, M. Cornelius, J. Morell, and M. Fröba, "Silica-Based Mesoporous Organic–Inorganic Hybrid Materials," *Angew. Chemie Int. Ed.*, vol. 45, no. 20, pp. 3216–3251, 2006.
- [73] G. Martínez-Edo, A. Balmori, I. Pontón, A. Martí del Rio, and D. Sánchez-García, "Functionalized Ordered Mesoporous Silicas (MCM-41): Synthesis and Applications in Catalysis," *Catalysts*, vol. 8, no. 12, p. 617, 2018.
- [74] M. C. Llinàs, "New functionalization methodologies of mesoporous silica nanoparticles (MSNs) for biomedical applications.," Universitat Ramon Llull, 2016.

- [75] N. Lang and A. Tuel, "A fast and efficient ion-exchange procedure to remove surfactant molecules from MCM-41 materials," *Chem. Mater.*, vol. 16, no. 10, pp. 1961–1966, 2004.
- [76] M. H. Lim and A. Stein, "Comparative studies of grafting and direct syntheses of inorganic-organic hybrid mesoporous materials," *Chem. Mater.*, vol. 11, no. 11, pp. 3285–3295, 1999.
- [77] N. Izza Taib, S. Endud, and M. Nasir Katun, "Functionalization of Mesoporous Si-MCM-41 by Grafting with Trimethylchlorosilane," *Int. J. Chem.*, vol. 3, no. 3, 2011.
- [78] M. Vallet-Regi, A. Rámila, R. P. Del Real, and J. Pérez-Pariente, "A new property of MCM-41: Drug delivery system," *Chem. Mater.*, vol. 13, no. 2, pp. 308–311, 2001.
- [79] T. Li *et al.*, "Recent advancements in mesoporous silica nanoparticles towards therapeutic applications for cancer," *Acta Biomater.*, vol. 89, pp. 1–13, 2019.
- [80] H. Meng *et al.*, "Engineered design of mesoporous silica nanoparticles to deliver doxorubicin and p-glycoprotein siRNA to overcome drug resistance in a cancer cell line," *ACS Nano*, vol. 4, no. 8, pp. 4539–4550, 2010.
- [81] F. Chen *et al.*, "Ultrasmall targeted nanoparticles with engineered antibody fragments for imaging detection of HER2-overexpressing breast cancer," *Nat. Commun.*, vol. 9, no. 1, pp. 1–11, 2018.
- [82] A. M. Pandele, C. Andronescu, A. Ghebur, S. A. Garea, and H. Iovu, "New biocompatible mesoporous silica/polysaccharide hybrid materials as possible drug delivery systems," *Materials (Basel)*, vol. 12, no. 1, pp. 1–14, 2018.
- [83] V. Delplace, P. Couvreur, and J. Nicolas, "Recent trends in the design of anticancer polymer prodrug nanocarriers," *Polymer Chemistry*, vol. 5, no. 5, pp. 1529–1544, 2014.
- [84] R. R. Castillo, D. Lozano, B. González, M. Manzano, I. Izquierdo-Barba, and M. Vallet-Regí, "Advances in mesoporous silica nanoparticles for targeted stimuli-responsive drug delivery: an update," *Expert Opinion on Drug Delivery*, vol. 16, no. 4, pp. 415–439, 2019.
- [85] M. Faal Maleki *et al.*, "Endogenous stimuli-responsive linkers in nanoliposomal systems for cancer drug targeting," *Int. J. Pharm.*, vol. 572, p. 118716, 2019.
- [86] A. Raza, T. Rasheed, F. Nabeel, U. Hayat, M. Bilal, and H. M. N. Iqbal, "Endogenous and exogenous stimuli-responsive drug delivery systems for programmed site-specific release," *Molecules*, vol. 24, no. 6, pp. 1–21, 2019.
- [87] H. Hatakeyama, "Recent advances in endogenous and exogenous stimuli-responsive nanocarriers for drug delivery and therapeutics," *Chem. Pharm. Bull.*, vol. 65, no. 7, pp.

- 612–617, 2017.
- [88] Y. Song, Y. Li, Q. Xu, and Z. Liu, “Mesoporous silica nanoparticles for stimuli-responsive controlled drug delivery: advances, challenges, and outlook,” *Int. J. Nanomedicine*, vol. 12, pp. 87–110, 2017.
- [89] M. Karimi, H. Mirshekari, M. Aliakbari, Z. Sahandi, and M. R. Hamblin, “Smart mesoporous silica nanoparticles for controlled-release drug delivery,” *Nanotechnol. Rev.*, vol. 5, no. 2, pp. 1–26, 2016.
- [90] I. F. Tannock and D. Rotin, “Acid pH in Tumors and Its Potential for Therapeutic Exploitation,” *Cancer Res.*, vol. 49, no. 16, pp. 4373–4384, 1989.
- [91] S. Tavakol, “Acidic pH derived from cancer cells may induce failed reprogramming of normal differentiated cells adjacent tumor cells and turn them into cancer cells,” *Med. Hypotheses*, vol. 83, no. 6, pp. 668–672, 2014.
- [92] J. L. Vivero-Escoto, I. I. Slowing, V. S. Y. Lin, and B. G. Trewyn, “Mesoporous silica nanoparticles for intracellular controlled drug delivery,” *Small*, vol. 6, no. 18, pp. 1952–1967, 2010.
- [93] F. Muhammad *et al.*, “Responsive delivery of drug cocktail via mesoporous silica nanolamps,” *J. Colloid Interface Sci.*, vol. 434, pp. 1–8, 2014.
- [94] S. Zhou, H. Sha, X. Ke, B. Liu, X. Wang, and X. Du, “Combination drug release of smart cyclodextrin-gated mesoporous silica nanovehicles †,” *Chem. Commun*, vol. 51, pp. 7203–7206, 2015.
- [95] K. K. Cotí *et al.*, “Mechanised nanoparticles for drug delivery,” *Nanoscale*, vol. 1, no. 1, pp. 16–39, Sep. 2009.
- [96] S. N. Kane, A. Mishra, and A. K. Dutta, “Preface: International Conference on Recent Trends in Physics (ICRTP 2016),” *J. Phys. Conf. Ser.*, vol. 755, no. 1, 2016.
- [97] T. D. Nguyen, Y. Liu, S. Saha, K. C. F. Leung, J. F. Stoddart, and J. I. Zink, “Design and optimization of molecular nanovalves based on redox-switchable bistable rotaxanes,” *J. Am. Chem. Soc.*, vol. 129, no. 3, pp. 626–634, 2007.
- [98] Q. Fu *et al.*, “Control of Molecular Transport Through Stimuli-Responsive Ordered Mesoporous Materials,” *Adv. Mater.*, vol. 15, no. 15, pp. 1262–1266, 2003.
- [99] E. Bringas *et al.*, “Triggered release in lipid bilayer-capped mesoporous silica nanoparticles containing SPION using an alternating magnetic field,” *Chem. Commun.*, vol. 48, no. 45, pp. 5647–5649, 2012.

- [100] H. Meng *et al.*, "Use of a lipid-coated mesoporous silica nanoparticle platform for synergistic gemcitabine and paclitaxel delivery to human pancreatic cancer in mice," *ACS Nano*, vol. 9, no. 4, pp. 3540–3557, 2015.
- [101] Q. Yan *et al.*, "Gated Mesoporous Silica Nanocarriers for Hypoxia-Responsive Cargo Release," *ACS Appl. Mater. Interfaces*, vol. 11, no. 27, pp. 24377–24385, 2019.
- [102] N. K. Mal, M. Fujiwara, and Y. Tanaka, "Photocontrolled reversible release of guest molecules from coumarin-modified mesoporous silica," *Nature*, vol. 421, no. 6921, pp. 350–353, 2003.
- [103] L. Chen *et al.*, "Multifunctional Redox-Responsive Mesoporous Silica Nanoparticles for Efficient Targeting Drug Delivery and Magnetic Resonance Imaging," *ACS Appl. Mater. Interfaces*, vol. 8, no. 49, pp. 33829–33841, 2016.
- [104] Q. Zhou, L. Zhang, T. H. Yang, and H. Wu, "Stimuli-responsive polymeric micelles for drug delivery and cancer therapy," *Int. J. Nanomedicine*, vol. 13, pp. 2921–2942, 2018.
- [105] C. H. Lee *et al.*, "Intracellular pH-responsive mesoporous silica nanoparticles for the controlled release of anticancer chemotherapeutics," *Angew. Chemie - Int. Ed.*, vol. 49, no. 44, pp. 8214–8219, 2010.
- [106] J. Fan, G. Fang, X. Wang, F. Zeng, Y. Xiang, and S. Wu, "Targeted anticancer prodrug with mesoporous silica nanoparticles as vehicles," *Nanotechnology*, vol. 22, no. 45, pp. 1–11, 2011.
- [107] D. He *et al.*, "Noncovalent assembly of reduced graphene oxide and alkyl-grafted mesoporous silica: an effective drug carrier for near-infrared light-responsive controlled drug release," *J. Mater. Chem. B*, vol. 3, no. 27, pp. 5588–5594, 2015.
- [108] E. Niemelä, D. Desai, Y. Nkizinkiko, J. E. Eriksson, and J. M. Rosenholm, "Sugar-decorated mesoporous silica nanoparticles as delivery vehicles for the poorly soluble drug celestrol enables targeted induction of apoptosis in cancer cells," *Eur. J. Pharm. Biopharm.*, vol. 96, pp. 11–21, 2015.
- [109] M. Grimaldi *et al.*, "Long-term effects after treatment with platinum compounds, cisplatin and [Pt(O,O'-acac)(γ -acac)(DMS)]: Autophagy activation in rat B50 neuroblastoma cells," *Toxicol. Appl. Pharmacol.*, vol. 364, pp. 1–11, 2019.
- [110] Y. Wang *et al.*, "Redox-responsive mesoporous silica as carriers for controlled drug delivery: A comparative study based on silica and PEG gatekeepers," *Eur. J. Pharm. Sci.*, vol. 72, pp. 12–20, 2015.

- [111] J. Jiao *et al.*, "Redox and pH dual-responsive PEG and chitosan-conjugated hollow mesoporous silica for controlled drug release," *Mater. Sci. Eng. C*, vol. 67, pp. 26–33, 2016.
- [112] L. C. Fonseca, A. J. De Paula, D. S. T. Martinez, and O. L. Alves, "How does the chain length of PEG functionalized at the outer surface of mesoporous silica nanoparticles alter the uptake of molecules?," *New J. Chem.*, vol. 40, no. 9, pp. 8060–8067, 2016.
- [113] C. P. Tsai, C. Y. Chen, Y. Hung, F. H. Chang, and C. Y. Mou, "Monoclonal antibody-functionalized mesoporous silica nanoparticles (MSN) for selective targeting breast cancer cells," *J. Mater. Chem.*, vol. 19, no. 32, pp. 5737–5743, 2009.
- [114] Y. Cui, H. Dong, X. Cai, D. Wang, and Y. Li, "Mesoporous silica nanoparticles capped with disulfide-linked PEG gatekeepers for glutathione-mediated controlled release," *ACS Appl. Mater. Interfaces*, vol. 4, no. 6, pp. 3177–3183, 2012.
- [115] K. Rahme and N. Dagher, "Chemistry Routes for Copolymer Synthesis Containing PEG for Targeting, Imaging, and Drug Delivery Purposes," *Pharmaceutics*, vol. 11, no. 7, p. 327, 2019.
- [116] Y. Cui, H. Dong, X. Cai, D. Wang, and Y. Li, "Mesoporous silica nanoparticles capped with disulfide-linked PEG gatekeepers for glutathione-mediated controlled release," *ACS Appl. Mater. Interfaces*, vol. 4, no. 6, pp. 3177–3183, 2012.
- [117] E. Aznar *et al.*, "Delivery modulation in silica mesoporous supports via alkyl chain pore outlet decoration," *Langmuir*, vol. 28, no. 5, pp. 2986–2996, 2012.
- [118] W. W. Qi *et al.*, "Doxorubicin-Loaded Glycyrrhetic Acid Modified Recombinant Human Serum Albumin Nanoparticles for Targeting Liver Tumor Chemotherapy," *Mol. Pharm.*, vol. 12, no. 3, pp. 675–683, 2015.
- [119] F. Danhier, O. Feron, and V. Pr at, "To exploit the tumor microenvironment: Passive and active tumor targeting of nanocarriers for anti-cancer drug delivery," *J. Control. Release*, vol. 148, no. 2, pp. 135–146, 2010.
- [120] J. Fang, H. Nakamura, and H. Maeda, "The EPR effect: Unique features of tumor blood vessels for drug delivery, factors involved, and limitations and augmentation of the effect," *Advanced Drug Delivery Reviews*, vol. 63, no. 3, pp. 136–151, 2011.
- [121] A. Watermann and J. Brieger, "Mesoporous silica nanoparticles as drug delivery vehicles in cancer," *Nanomaterials*, vol. 7, no. 7, pp. 1–17, 2017.
- [122] X. Huang *et al.*, "The shape effect of mesoporous silica nanoparticles on biodistribution,

- clearance, and biocompatibility in vivo,” in *ACS Nano*, 2011, vol. 5, no. 7, pp. 5390–5399.
- [123] A. E. Nel *et al.*, “Understanding biophysicochemical interactions at the nano-bio interface,” *Nature Materials*, vol. 8, no. 7, pp. 543–557, 2009.
- [124] W. Cheng *et al.*, “pH-Sensitive Delivery Vehicle Based on Folic Acid-Conjugated Polydopamine-Modified Mesoporous Silica Nanoparticles for Targeted Cancer Therapy,” *ACS Appl. Mater. Interfaces*, vol. 9, no. 22, pp. 18462–18473, 2017.
- [125] X. Qi *et al.*, “Targeting CD133+ laryngeal carcinoma cells with chemotherapeutic drugs and siRNA against ABCG2 mediated by thermo/pH-sensitive mesoporous silica nanoparticles,” *Tumor Biol.*, vol. 37, no. 2, pp. 2209–2217, 2016.
- [126] Z. Luo, Y. Dai, and H. Gao, “Development and application of hyaluronic acid in tumor targeting drug delivery,” *Acta Pharm. Sin. B*, vol. 9, pp. 1099–1112, 2019.
- [127] F. Du and W. Wang, “Hyaluronic acid-modified mesoporous silica-coated superparamagnetic Fe₃O₄ nanoparticles for targeted drug delivery,” pp. 5785–5797, 2019.
- [128] M. Nassiri Asl and H. Hosseinzadeh, “Review of pharmacological effects of glycyrrhiza sp. and its bioactive compounds,” *Phytotherapy Research*, vol. 22, no. 6, pp. 709–724, 2008.
- [129] R. Feng *et al.*, “Glycyrrhetic acid-modified PEG-PCL copolymeric micelles for the delivery of curcumin,” *React. Funct. Polym.*, vol. 111, pp. 30–37, 2017.
- [130] L. Zhang, J. Yao, J. Zhou, T. Wang, and Q. Zhang, “Glycyrrhetic acid-graft-hyaluronic acid conjugate as a carrier for synergistic targeted delivery of antitumor drugs,” *Int. J. Pharm.*, vol. 441, no. 1–2, pp. 654–664, 2013.
- [131] Q. Tian, X.-H. Wang, W. Wang, C.-N. Zhang, P. Wang, and Z. Yuan, “Self-assembly and liver targeting of sulfated chitosan nanoparticles functionalized with glycyrrhetic acid,” *Nanomedicine Nanotechnology, Biol. Med.*, vol. 8, no. 6, pp. 870–879, 2012.
- [132] C. Zhang *et al.*, “Doxorubicin-loaded glycyrrhetic acid-modified alginate nanoparticles for liver tumor chemotherapy,” *Biomaterials*, vol. 33, no. 7, pp. 2187–2196, 2012.
- [133] W. Huang *et al.*, “Glycyrrhetic acid-modified poly(ethylene glycol)-b-poly(γ -benzyl L-glutamate) micelles for liver targeting therapy,” *Acta Biomater.*, vol. 6, no. 10, pp. 3927–3935, 2010.
- [134] X. Chen, H. Sun, J. Hu, X. Han, H. Liu, and Y. Hu, “Transferrin gated mesoporous silica nanoparticles for redox-responsive and targeted drug delivery,” *Colloids Surfaces B Biointerfaces*, vol. 152, pp. 77–84, 2017.

- [135] S. K. Sweeney, Y. Luo, M. A. O'Donnell, and J. G. Assouline, "Peptide-mediated targeting mesoporous silica nanoparticles: A novel tool for fighting bladder cancer," *J. Biomed. Nanotechnol.*, vol. 13, no. 2, pp. 232–242, 2017.
- [136] M. Babaei *et al.*, "Synthesis of theranostic epithelial cell adhesion molecule targeted mesoporous silica nanoparticle with gold gatekeeper for hepatocellular carcinoma," *Nanomedicine*, vol. 12, no. 11, pp. 1261–1279, 2017.
- [137] P. N. Durfee *et al.*, "Mesoporous Silica Nanoparticle-Supported Lipid Bilayers (Protocells) for Active Targeting and Delivery to Individual Leukemia Cells," *ACS Nano*, vol. 10, no. 9, pp. 8325–8345, 2016.
- [138] X. Liu *et al.*, "A dual responsive targeted drug delivery system based on smart polymer coated mesoporous silica for laryngeal carcinoma treatment," *New J. Chem.*, vol. 38, no. 10, pp. 4830–4836, 2014.
- [139] C. Chen *et al.*, "A self-targeting and controllable drug delivery system constituting mesoporous silica nanoparticles fabricated with a multi-stimuli responsive chitosan-based thin film layer," *Int. J. Biol. Macromol.*, vol. 122, pp. 1090–1099, 2019.
- [140] M. Vallet-Regí, M. Colilla, I. Izquierdo-Barba, and M. Manzano, "Mesoporous Silica Nanoparticles for Drug Delivery :," *Molecules*, vol. 23, no. 47, pp. 1–19, 2017.
- [141] G. Martínez-Edo, M. C. Llinàs, S. Borrós, and D. Sánchez-García, "Isothiocyanate-Functionalized Mesoporous Silica Nanoparticles as Building Blocks for the Design of Nanovehicles with Optimized Drug Release Profile," *Nanomaterials*, vol. 9, no. 9, p. 1219, 2019.
- [142] J. M. Rosenholm, E. Peuhu, J. E. Eriksson, C. Sahlgren, and M. Lindén, "Targeted Intracellular Delivery of Hydrophobic Agents using Mesoporous Hybrid Silica Nanoparticles as Carrier Systems," *Nano Lett.*, vol. 9, no. 9, pp. 3308–3311, 2009.
- [143] A. Popat, B. P. Ross, J. Liu, S. Jambhrunkar, F. Kleitz, and S. Z. Qiao, "Enzyme-Responsive Controlled Release of Covalently Bound Prodrug from Functional Mesoporous Silica Nanospheres," *Angew. Chemie Int. Ed.*, vol. 51, no. 50, pp. 12486–12489, 2012.
- [144] Y. Liu, B. Huang, J. Zhu, K. Feng, Y. Yuan, and C. Liu, "Dual-generation dendritic mesoporous silica nanoparticles for co-delivery and kinetically sequential drug release," vol. 8, pp. 40598–40610, 2018.
- [145] Q. L. Li *et al.*, "pH and Glutathione Dual-Responsive Dynamic Cross-Linked Supramolecular Network on Mesoporous Silica Nanoparticles for Controlled Anticancer

- Drug Release,” *ACS Appl. Mater. Interfaces*, vol. 7, no. 51, pp. 28656–28664, 2015.
- [146] A. Mordente, E. Meucci, A. Silvestrini, G. Martorana, and B. Giardina, “New Developments in Anthracycline-Induced Cardiotoxicity,” *Curr. Med. Chem.*, vol. 16, no. 13, pp. 1656–1672, 2009.
- [147] Z. Li *et al.*, “Camptothecin nanocolloids based on N,N,N-trimethyl chitosan: Efficient suppression of growth of multiple myeloma in a murine model,” *Oncol. Rep.*, vol. 27, no. 4, pp. 1035–1040, 2012.
- [148] G. F. Luo, W. H. Chen, Y. Liu, Q. Lei, R. X. Zhuo, and X. Z. Zhang, “Multifunctional enveloped mesoporous silica nanoparticles for subcellular co-delivery of drug and therapeutic peptide,” *Sci. Rep.*, vol. 4, pp. 1–10, 2014.
- [149] R. R. Castillo, M. Colilla, and M. Vallet-Regí, “Advances in mesoporous silica-based nanocarriers for co-delivery and combination therapy against cancer,” *Expert Opinion on Drug Delivery*, vol. 14, no. 2, pp. 229–243, 2017.
- [150] Y. Huang, S. Xu, and V. S. Y. Lin, “Bifunctionalized mesoporous materials with site-separated Brønsted acids and bases: Catalyst for a two-step reaction sequence,” *Angew. Chemie - Int. Ed.*, vol. 50, no. 3, pp. 661–664, 2011.
- [151] M. C. Llinàs, G. Martínez-Edo, A. Cascante, I. Porcar, S. Borrós, and D. Sánchez-García, “Preparation of a mesoporous silica-based nano-vehicle for dual DOX / CPT pH-triggered delivery,” *Drug Deliv.*, vol. 25, no. 1, pp. 1137–1146, 2018.
- [152] W. Wang, Y. Wen, L. Xu, H. Du, Y. Zhou, and X. Zhang, “A selective release system based on dual-drug-loaded mesoporous silica for nanoparticle-assisted combination therapy,” *Chemistry*, vol. 20, no. 25, pp. 7796–802, 2014.
- [153] S. El Sayed, C. Giménez, E. Aznar, R. Martínez-Mañez, F. Sancenón, and M. Licchelli, “Highly selective and sensitive detection of glutathione using mesoporous silica nanoparticles capped with disulfide-containing oligo(ethylene glycol) chains,” *Org. Biomol. Chem.*, vol. 13, no. 4, pp. 1017–1021, 2015.
- [154] E. Aznar *et al.*, “Delivery modulation in silica mesoporous supports via alkyl chain pore outlet decoration,” *Langmuir*, vol. 28, no. 5, pp. 2986–2996, 2012.
- [155] Y. C. Zhang, D. W. Zhang, H. Wang, Y. Zhou, and Z. T. Li, “Bipyridinium radical cation dimerization-driven polymeric pleated foldamers and a homoduplex that undergo ion-tuned interconversion,” *Polym. Chem.*, vol. 6, no. 24, pp. 4404–4408, 2015.
- [156] Z.-Y. Li *et al.*, “One-pot construction of functional mesoporous silica nanoparticles for the

- tumor-acidity-activated synergistic chemotherapy of glioblastoma.," *ACS Appl. Mater. Interfaces*, vol. 5, no. 16, pp. 7995–8001, 2013.
- [157] A. Agostini *et al.*, "Design of enzyme-mediated controlled release systems based on silica mesoporous supports capped with ester-glycol groups," *Langmuir*, vol. 28, no. 41, pp. 14766–14776, 2012.
- [158] A. Agostini *et al.*, "Dual enzyme-triggered controlled release on capped nanometric silica mesoporous supports.," *ChemistryOpen*, vol. 1, no. 1, pp. 17–20, 2012.
- [159] L. Xing, H. Zheng, Y. Cao, and S. Che, "Coordination polymer coated mesoporous silica nanoparticles for ph-responsive drug release," *Adv. Mater.*, vol. 24, no. 48, pp. 6433–6437, 2012.
- [160] J. E. Lee, D. J. Lee, N. Lee, B. H. Kim, S. H. Choi, and T. Hyeon, "Multifunctional mesoporous silica nanocomposite nanoparticles for pH controlled drug release and dual modal imaging," *J. Mater. Chem.*, vol. 21, no. 42, pp. 16869–16872, 2011.
- [161] J. Fan, G. Fang, X. Wang, F. Zeng, Y. Xiang, and S. Wu, "Targeted anticancer prodrug with mesoporous silica nanoparticles as vehicles.," *Nanotechnology*, vol. 22, no. 45, pp. 1–11, 2011.
- [162] G. F. Luo *et al.*, "Charge-reversal plug gate nanovalves on peptide-functionalized mesoporous silica nanoparticles for targeted drug delivery," *J. Mater. Chem. B*, vol. 1, no. 41, pp. 5723–5732, 2013.
- [163] L. F. Brittany, R. M. Jilian, and S. D. Emily, "Nanoshell-mediated photothermal therapy can enhance chemotherapy in inflammatory breast cancer cells," *Int. J. Na*, vol. 10, pp. 6934–6941, 2015.
- [164] G.-F. Luo, W.-H. Chen, Y. Liu, Q. Lei, R.-X. Zhuo, and X.-Z. Zhang, "Multifunctional enveloped mesoporous silica nanoparticles for subcellular co-delivery of drug and therapeutic peptide.," *Sci. Rep.*, vol. 4, p. 6064, 2014.
- [165] M. Costanzo *et al.*, "Fluorescence and electron microscopy to visualize the intracellular fate of nanoparticles for drug delivery," *Eur. J. Histochem.*, vol. 60, no. 2, pp. 107–115, 2016.
- [166] C. K. Huang, C. L. Lo, H. H. Chen, and G. H. Hsiue, "Multifunctional micelles for cancer cell targeting, distribution imaging, and anticancer drug delivery," *Adv. Funct. Mater.*, vol. 17, no. 14, pp. 2291–2297, 2007.
- [167] P. Botella *et al.*, "Surface-modified silica nanoparticles for tumor-targeted delivery of

- camptothecin and its biological evaluation," *J. Control. Release*, vol. 156, no. 2, pp. 246–257, 2011.
- [168] L. Wasim and M. Chopra, "Synergistic anticancer effect of panobinostat and topoisomerase inhibitors through ROS generation and intrinsic apoptotic pathway induction in cervical cancer cells," *Cell. Oncol.*, vol. 41, no. 2, pp. 201–212, 2018.
- [169] R. Grosjean *et al.*, "High pressures pathway toward boron-based nanostructured solids," *Dalt. Trans.*, vol. 47, no. 23, pp. 7634–7639, 2017.
- [170] J. Pan, K. Rostamizadeh, N. Filipczak, and V. P. Torchilin, "Polymeric co-delivery systems in cancer treatment: An overview on component drugs' dosage ratio effect," *Molecules*, vol. 24, no. 6, pp. 1–32, 2019.
- [171] S. Koplev *et al.*, "Dynamic Rearrangement of Cell States Detected by Systematic Screening of Sequential Anticancer Treatments," *Cell Rep.*, vol. 20, no. 12, pp. 2784–2791, 2017.
- [172] Q.-L. Li *et al.*, "pH and Glutathione Dual-Responsive Dynamic Cross-Linked Supramolecular Network on Mesoporous Silica Nanoparticles for Controlled Anticancer Drug Release.," *ACS Appl. Mater. Interfaces*, vol. 7, no. 51, pp. 28656–64, 2015.
- [173] F. Muhammad *et al.*, "Responsive delivery of drug cocktail via mesoporous silica nanolamps.," *J. Colloid Interface Sci.*, vol. 434, pp. 1–8, 2014.
- [174] M. Narvekar, H. Y. Xue, J. Y. Eoh, and H. L. Wong, "Nanocarrier for poorly water-soluble anticancer drugs - Barriers of translation and solutions," *AAPS PharmSciTech*, vol. 15, no. 4, pp. 822–833, 2014.
- [175] D. Christopher Vimalson, S. Parimalakrishnan, N. S. Jeganathan, and S. Anbazhagan, "Techniques to enhance solubility of hydrophobic drugs: An overview," *Asian J. Pharm.*, vol. 10, no. 2, pp. S67–S75, 2016.
- [176] F. Kratz, I. A. Müller, C. Ryppa, and A. Warnecke, "Prodrug Strategies in Anticancer Chemotherapy," *ChemMedChem*, vol. 3, no. 1, pp. 20–53, 2008.
- [177] R. Palmirotta *et al.*, "SNPs in predicting clinical efficacy and toxicity of chemotherapy: Walking through the quicksand," *Oncotarget*, vol. 9, no. 38, pp. 25355–25382, 2018.
- [178] E. J. Park, J. Choi, K. C. Lee, and D. H. Na, "Emerging PEGylated non-biologic drugs," *Expert Opin. Emerg. Drugs*, vol. 24, no. 2, pp. 107–119, 2019.
- [179] Z. Meng *et al.*, "Prodrug strategies for paclitaxel," *Int. J. Mol. Sci.*, vol. 17, no. 5, pp. 1–23, 2016.
- [180] Y. Noguchi *et al.*, "Early phase tumor accumulation of Macromolecules: A great

- difference in clearance rate between tumor and normal tissues," *Japanese J. Cancer Res.*, vol. 89, no. 3, pp. 307–314, 1998.
- [181] Z. Meng *et al.*, "Prodrug Strategies for Paclitaxel," *Int. J. Mol. Sci.*, vol. 17, no. 5, pp. 1–23, 2016.
- [182] H. Dong *et al.*, "Engineering of pegylated camptothecin into core-shell nanomicelles for improving solubility, stability and combination delivery," *Medchemcomm*, vol. 3, no. 12, pp. 1555–1561, 2012.
- [183] A. B. Fleming, K. Haverstick, and W. M. Saltzman, "In vitro cytotoxicity and in vivo distribution after direct delivery of PEG-camptothecin conjugates to the rat brain," *Bioconjug. Chem.*, vol. 15, no. 6, pp. 1364–1375, 2004.
- [184] M. Hu *et al.*, "Synergistic Combination Chemotherapy of Camptothecin and Floxuridine through Self-Assembly of Amphiphilic Drug-Drug Conjugate," *Bioconjug. Chem.*, vol. 26, no. 12, pp. 2497–2506, 2015.
- [185] W. J. Slichenmyer, E. K. Rowinsky, L. B. Grochow, S. H. Kaufmann, and R. C. Donehower, "Camptothecin analogues: studies from The Johns Hopkins Oncology Center," *Cancer Chemother. Pharmacol.*, vol. 34, no. 1 Supplement, pp. S53-7, 1994.
- [186] "Drug: Irinotecan - Cancerrxgene - Genomics of Drug Sensitivity in Cancer." [Online]. Available: <https://www.cancerrxgene.org/compound/Irinotecan/1088/overview/ic50>. [Accessed: 18-Feb-2020].
- [187] "Drug: Topotecan - Cancerrxgene - Genomics of Drug Sensitivity in Cancer." [Online]. Available: <https://www.cancerrxgene.org/compound/Topotecan/1808/overview/ic50>. [Accessed: 18-Feb-2020].
- [188] "Drug: Camptothecin - Cancerrxgene - Genomics of Drug Sensitivity in Cancer." [Online]. Available: <https://www.cancerrxgene.org/compound/Camptothecin/1003/overview/ic50>. [Accessed: 18-Feb-2020].
- [189] Z. Xu, D. Wang, S. Xu, X. Liu, X. Zhang, and H. Zhang, "Preparation of a camptothecin prodrug with glutathione-responsive disulfide linker for anticancer drug delivery," *Chem. - An Asian J.*, vol. 9, no. 1, pp. 199–205, 2014.
- [190] C. Muniesa *et al.*, "Glutathione-sensitive nanoplatfor for monitored intracellular delivery and controlled release of Camptothecin," *RSC Adv.*, vol. 3, no. 35, p. 15121, 2013.
- [191] Z. Xu, S. Liu, Y. Kang, and M. Wang, "Glutathione- and pH-responsive nonporous silica

- prodrug nanoparticles for controlled release and cancer therapy," *Nanoscale*, vol. 7, no. 13, pp. 5859–5868, 2015.
- [192] V. J. Venditto and E. E. Simanek, "Cancer therapies utilizing the camptothecins: A review of the in vivo literature," *Molecular Pharmaceutics*, vol. 7, no. 2, pp. 307–349, 2010.
- [193] O. Y. Zolotarskaya, A. F. Wagner, J. M. Beckta, K. Valerie, K. J. Wynne, and H. Yang, "Synthesis of water-soluble camptothecin-polyoxetane conjugates via click chemistry," *Mol. Pharm.*, vol. 9, no. 11, pp. 3403–3408, 2012.
- [194] Z. Li, H. Li, L. Liu, X. You, C. Zhang, and Y. Wang, "A pH-sensitive nanocarrier for co-delivery of doxorubicin and camptothecin to enhance chemotherapeutic efficacy and overcome multidrug resistance in vitro," *RSC Adv.*, vol. 5, no. 94, pp. 77097–77105, 2015.
- [195] J. Zhou, X. Yang, Y. Wang, and W. Chen, "An efficient oxidation of cyclohexane over Au@TiO₂/MCM-41 catalyst prepared by photocatalytic reduction method using molecular oxygen as oxidant," *Catal. Commun.*, vol. 46, pp. 228–233, 2014.
- [196] W. G. E. J. Schoonen, W. M. A. Westerink, J. A. D. M. De Roos, and E. Débiton, "Cytotoxic effects of 100 reference compounds on Hep G2 and HeLa cells and of 60 compounds on ECC-1 and CHO cells. I Mechanistic assays on ROS, glutathione depletion and calcein uptake," *Toxicol. Vitro.*, vol. 19, no. 4, pp. 505–516, 2005.
- [197] C.-J. Guo *et al.*, "Entry of Tiger Frog Virus (an Iridovirus) into HepG2 Cells via a pH-Dependent, Atypical, Caveola-Mediated Endocytosis Pathway," *J. Virol.*, vol. 85, no. 13, pp. 6416–6426, 2011.
- [198] M. Huber, M. Brabec, N. Bayer, D. Blaas, and R. Fuchs, "Elevated endosomal pH in HeLa cells overexpressing mutant dynamin can affect infection by pH-sensitive viruses," *Traffic*, vol. 2, no. 10, pp. 727–736, 2001.
- [199] N. Gabrielson and D. W. Pack, "Efficient polyethylenimine-mediated gene delivery proceeds via caveolae-mediated uptake in hela cells," *AIChE Annu. Meet. Conf. Proc.*, vol. 239, pp. 217–244, 2008.
- [200] N. Bertrand, J. Wu, X. Xu, N. Kamaly, and O. C. Farokhzad, "Cancer nanotechnology: The impact of passive and active targeting in the era of modern cancer biology," *Advanced Drug Delivery Reviews*, vol. 66, pp. 2–25, 2014.
- [201] A. Baeza, M. Colilla, and M. Vallet-Regí, "Advances in mesoporous silica nanoparticles for targeted stimuli-responsive drug delivery," *Expert Opin. Drug Deliv.*, vol. 12, no. 2, pp. 319–337, 2015.

- [202] P. Khosravian *et al.*, "Mesoporous silica nanoparticles functionalized with folic acid/methionine for active targeted delivery of docetaxel," *Onco. Targets. Ther.*, vol. 9, pp. 7315–7330, 2016.
- [203] S. Wagner *et al.*, "Enhanced drug targeting by attachment of an anti α v integrin antibody to doxorubicin loaded human serum albumin nanoparticles," *Biomaterials*, vol. 31, no. 8, pp. 2388–2398, 2010.
- [204] M. Ferrari, "Cancer nanotechnology: Opportunities and challenges," *Nature Reviews Cancer*, vol. 5, no. 3, pp. 161–171, 2005.
- [205] J. Zeromski, "Significance of tumor-cell receptors in human cancer," *Arch. Immunol. Ther. Exp. (Warsz.)*, vol. 50, no. 2, pp. 105–110, 2002.
- [206] N. M. Tunissiolli *et al.*, "Hepatocellular carcinoma: A comprehensive review of biomarkers, clinical aspects, and therapy," *Asian Pacific J. Cancer Prev.*, vol. 18, no. 4, pp. 863–872, 2017.
- [207] I. Fasolino *et al.*, "HepG2 and human healthy hepatocyte in vitro culture and co-culture in PCL electrospun platforms," *Biomed. Mater.*, vol. 13, no. 1, pp. 1–9, 2018.
- [208] J. Balogh, D. V. Iii, S. Gordon, X. Li, R. M. Ghobrial, and H. P. M. Jr, "Hepatocellular carcinoma: a review," *J. Hepatocell. Carcinoma*, vol. Volume 3, pp. 41–53, 2016.
- [209] R. Zhou *et al.*, "Anticancer Effects of Emodin on HepG2 Cell: Evidence from Bioinformatic Analysis," *Biomed Res. Int.*, vol. 2019, pp. 1–14, 2019.
- [210] X. Zeng *et al.*, "A Drug-Self-Gated Mesoporous Antitumor Nanoplatfrom Based on pH-Sensitive Dynamic Covalent Bond," *Adv. Funct. Mater.*, vol. 27, no. 11, pp. 1–9, 2017.
- [211] Y. Zhai *et al.*, "Design, synthesis, and characterization of Schiffbase bond-linked pH-responsive doxorubicin prodrug based on functionalized mPEG-PCL for targeted cancer therapy," *Polymers (Basel)*, vol. 10, no. 10, pp. 1–12, 2018.
- [212] L. Matesic, J. M. Locke, K. L. Vine, M. Ranson, J. B. Bremner, and D. Skropeta, "Synthesis and hydrolytic evaluation of acid-labile imine-linked cytotoxic isatin model systems," *Bioorganic Med. Chem.*, vol. 19, no. 5, pp. 1771–1778, 2011.
- [213] S. Li, W. Dai, Z. Z. Yin, J. Gao, D. Wu, and Y. Kong, "Synthesis of oxidized pullulan coated mesoporous silica for pH-sensitive drug delivery," *Eur. Polym. J.*, vol. 122, pp. 1–8, 2019.
- [214] X. Xu *et al.*, "Polymeric micelle-coated mesoporous silica nanoparticle for enhanced fluorescent imaging and pH-responsive drug delivery," *Chem. Eng. J.*, vol. 279, pp. 851–860, 2015.

- [215] Y. Yang *et al.*, "Fabrication of autofluorescent protein coated mesoporous silica nanoparticles for biological application," *Chem. Commun.*, vol. 47, no. 44, pp. 12167–12169, 2011.
- [216] C. Chen, W. Sun, X. Wang, Y. Wang, and P. Wang, "Rational design of curcumin loaded multifunctional mesoporous silica nanoparticles to enhance the cytotoxicity for targeted and controlled drug release," *Mater. Sci. Eng. C*, vol. 85, pp. 88–96, 2018.
- [217] S. Peng, X. Yuan, W. Lin, C. Cai, and L. Zhang, "pH-responsive controlled release of mesoporous silica nanoparticles capped with Schiff base copolymer gatekeepers: Experiment and molecular dynamics simulation," *Colloids Surfaces B Biointerfaces*, vol. 176, pp. 394–403, 2019.
- [218] Y. Gao, C. Yang, X. Liu, R. Ma, D. Kong, and L. Shi, "A Multifunctional Nanocarrier Based on Nanogated Mesoporous Silica for Enhanced Tumor-Specific Uptake and Intracellular Delivery," *Macromol. Biosci.*, vol. 12, no. 2, pp. 251–259, 2012.
- [219] S. Zhang and L. Echegoyen, "Non-covalent immobilization of C60 on gold surfaces by SAMs of porphyrin derivatives," *Tetrahedron*, vol. 62, no. 9, pp. 1947–1954, 2006.
- [220] X. Wang, X. Gu, H. Wang, Y. Sun, H. Wu, and S. Mao, "Synthesis, characterization and liver targeting evaluation of self-assembled hyaluronic acid nanoparticles functionalized with glycyrrhetic acid," *Eur. J. Pharm. Sci.*, vol. 96, pp. 255–262, 2017.
- [221] S. Banerji *et al.*, "Structures of the Cd44-hyaluronan complex provide insight into a fundamental carbohydrate-protein interaction," *Nat. Struct. Mol. Biol.*, vol. 14, no. 3, pp. 234–239, 2007.
- [222] Q. Tian, X. Wang, W. Wang, C. Zhang, Y. Liu, and Z. Yuan, "Insight into glycyrrhetic acid: The role of the hydroxyl group on liver targeting," *Int. J. Pharm.*, vol. 400, no. 1–2, pp. 153–157, 2010.
- [223] Q. Tian *et al.*, "Glycyrrhetic acid-modified chitosan/poly(ethylene glycol) nanoparticles for liver-targeted delivery," *Biomaterials*, vol. 31, no. 17, pp. 4748–4756, 2010.
- [224] R. Hrdina, C. E. Müller, and P. R. Schreiner, "Kinetic resolution of trans-cycloalkane-1,2-diols via Steglich esterification," *Chem. Commun.*, vol. 46, no. 15, pp. 2689–2690, 2010.
- [225] M. Prabakaran, J. J. Grailer, S. Pilla, D. A. Steeber, and S. Gong, "Amphiphilic multi-arm-block copolymer conjugated with doxorubicin via pH-sensitive hydrazone bond for tumor-targeted drug delivery," *Biomaterials*, vol. 30, no. 29, pp. 5757–5766, 2009.
- [226] I. Slowing, B. G. Trewyn, and V. S. Y. Lin, "Effect of surface functionalization of MCM-41-

- type mesoporous silica nanoparticles on the endocytosis by human cancer cells," *J. Am. Chem. Soc.*, vol. 128, no. 46, pp. 14792–14793, 2006.
- [227] Q. Wu, Z. Yang, Y. Nie, Y. Shi, and D. Fan, "Multi-drug resistance in cancer chemotherapeutics: Mechanisms and lab approaches," *Cancer Letters*, vol. 347, no. 2, pp. 159–166, 2014.
- [228] P. Babilas and R. M. Szeimies, "Photodynamic therapy," *Laser IPL Technol. Dermatology Aesthetic Med.*, vol. 90, no. 12, pp. 357–375, 2011.
- [229] K. T. De Oliveira *et al.*, "Synthesis of phthalocyanines-ALA conjugates: Water-soluble compounds with low aggregation," *J. Org. Chem.*, vol. 74, no. 20, pp. 7962–7965, 2009.
- [230] P. Agostinis *et al.*, "Photodynamic Therapy of cancer: an update," *CA Cancer J Clin*, vol. 61, no. 4, pp. 250–281, 2012.
- [231] M. R. Hamblin and H. Abrahamse, "Inorganic salts and antimicrobial photodynamic therapy: Mechanistic conundrums?," *Molecules*, vol. 23, no. 12, pp. 1–18, 2018.
- [232] G. M. F. Calixto, J. Bernegossi, L. M. De Freitas, C. R. Fontana, M. Chorilli, and A. M. Grumezescu, "Nanotechnology-based drug delivery systems for photodynamic therapy of cancer: A review," *Molecules*, vol. 21, no. 3, p. 342, 2016.
- [233] H. Abrahamse and M. R. Hamblin, "New photosensitizers for photodynamic therapy," *Biochem*, vol. 176, no. 10, pp. 139–148, 2016.
- [234] B. Ghazal, A. Husain, A. Ganesan, M. Durmuş, X. F. Zhang, and S. Makhseed, "Exceptionally effective generation of singlet oxygen in aqueous media via iodinated zinc-phthalocyanine," *Dye. Pigment.*, vol. 164, pp. 296–304, 2019.
- [235] L. Ricciardi *et al.*, "Plasmon-mediated cancer phototherapy: The combined effect of thermal and photodynamic processes," *Nanoscale*, vol. 9, no. 48, pp. 19279–19289, 2017.
- [236] R. C. H. Wong, D. K. P. Ng, W. P. Fong, and P. C. Lo, "Encapsulating pH-Responsive Doxorubicin-Phthalocyanine Conjugates in Mesoporous Silica Nanoparticles for Combined Photodynamic Therapy and Controlled Chemotherapy," *Chem. - A Eur. J.*, vol. 23, no. 65, pp. 16505–16515, 2017.
- [237] J.-J. Cid *et al.*, "Molecular Cosensitization for Efficient Panchromatic Dye-Sensitized Solar Cells," *Angew. Chemie Int. Ed.*, vol. 46, no. 44, pp. 8358–8362, 2007.
- [238] N. Mehraban, P. R. Musich, and H. S. Freeman, "Synthesis and encapsulation of a new zinc phthalocyanine photosensitizer into polymeric nanoparticles to enhance cell uptake

- and phototoxicity," *Appl. Sci.*, vol. 9, no. 3, pp. 1–14, 2019.
- [239] Z. Liu *et al.*, "An eximious and affordable GSH stimulus-responsive poly(α -lipoic acid) nanocarrier bonding combretastatin A4 for tumor therapy," *Biomater. Sci.*, vol. 7, no. 7, pp. 2803–2811, 2019.
- [240] W. A. Henne, S. A. Kularatne, J. Hakenjos, J. D. Carron, and K. L. Henne, "Synthesis and activity of a folate targeted monodisperse PEG camptothecin conjugate," *Bioorganic Med. Chem. Lett.*, vol. 23, no. 21, pp. 5810–5813, 2013.
- [241] F. Zhang *et al.*, "Transformative Nanomedicine of an Amphiphilic Camptothecin Prodrug for Long Circulation and High Tumor Uptake in Cancer Therapy," *ACS Nano*, vol. 11, no. 9, pp. 8838–8848, 2017.
- [242] X. Y. Zhao, W. A. Metz, F. Sieber, and K. D. Janda, "Expanding on the purification methodology of polyethylene glycol (PEG) bound molecules: The synthesis of 3,5-pyrazolidinediones," *Tetrahedron Lett.*, vol. 39, no. 46, pp. 8433–8436, 1998.
- [243] R. Maharani *et al.*, "Good coupling performance of PyBOP in the solid-phase synthesis of tetrapeptide, OH-Pro-Leu-Ala-Ileu-NH₂," in *MSCEIS*, 2017, vol. 1848, no. 1, p. 030006.
- [244] M. Moiola, M. G. Memeo, and P. Quadrelli, "Stapled peptides-a useful improvement for peptide-based drugs," *Molecules*, vol. 24, no. 20, 2019.
- [245] C. Muniesa *et al.*, "Glutathione-sensitive nanoplatfrom for monitored intracellular delivery and controlled release of Camptothecin," *RSC Adv.*, vol. 3, no. 35, pp. 15121–15131, 2013.
- [246] R. C. H. Wong, S. Y. S. Chow, S. Zhao, W. P. Fong, D. K. P. Ng, and P. C. Lo, "pH-Responsive Dimeric Zinc(II) Phthalocyanine in Mesoporous Silica Nanoparticles as an Activatable Nanophotosensitizing System for Photodynamic Therapy," *ACS Appl. Mater. Interfaces*, vol. 9, no. 28, pp. 23487–23496, 2017.
- [247] C. Dong *et al.*, "A Protein-Polymer Bioconjugate-Coated Upconversion Nanosystem for Simultaneous Tumor Cell Imaging, Photodynamic Therapy, and Chemotherapy," *ACS Appl. Mater. Interfaces*, vol. 8, no. 48, pp. 32688–32698, 2016.
- [248] C. Charnay, S. Bégu, C. Tourné-Péteilh, L. Nicole, D. a Lerner, and J. M. Devoisselle, "Inclusion of ibuprofen in mesoporous templated silica: drug loading and release property.," *Eur. J. Pharm. Biopharm.*, vol. 57, no. 3, pp. 533–40, 2004.
- [249] J. L. M. Gonçalves, C. I. C. Crucho, S. P. C. Alves, C. Baleizão, and J. P. S. Farinha, "Hybrid mesoporous nanoparticles for pH-actuated controlled release," *Nanomaterials*, vol. 9,

- no. 3, pp. 1–13, 2019.
- [250] R. C. H. Wong, D. K. P. Ng, W. P. Fong, and P. C. Lo, "Encapsulating pH-Responsive Doxorubicin–Phthalocyanine Conjugates in Mesoporous Silica Nanoparticles for Combined Photodynamic Therapy and Controlled Chemotherapy," *Chem. - A Eur. J.*, vol. 23, no. 65, pp. 16505–16515, 2017.
- [251] T. Yan, J. Cheng, Z. Liu, F. Cheng, X. Wei, and J. He, "pH-Sensitive mesoporous silica nanoparticles for chemo-photodynamic combination therapy," *Colloids Surfaces B Biointerfaces*, vol. 161, pp. 442–448, 2018.
- [252] V. Cauda, C. Argyo, and T. Bein, "Impact of different PEGylation patterns on the long-term bio-stability of colloidal mesoporous silica nanoparticles," *J. Mater. Chem.*, vol. 20, no. 39, pp. 8693–8699, 2010.
- [253] H. J. Kitto *et al.*, "Post-modification of helical dipeptido polyisocyanides using the 'click' reaction," *J. Mater. Chem.*, vol. 18, no. 46, pp. 5615–5624, 2008.
- [254] M. Wu, L. S. Chong, D. H. Perlman, A. C. Resnick, and D. Fiedler, "Inositol polyphosphates intersect with signaling and metabolic networks via two distinct mechanisms," *Proc. Natl. Acad. Sci. U. S. A.*, vol. 113, no. 44, pp. E6757–E6765, 2016.
- [255] C. A. Deforest and D. A. Tirrell, "A photoreversible protein-patterning approach for guiding stem cell fate in three-dimensional gels," *Nat. Mater.*, vol. 14, no. 5, pp. 523–531, 2015.
- [256] K. Brunner *et al.*, "Cell-penetrating and neurotargeting dendritic siRNA nanostructures," *Angew. Chemie - Int. Ed.*, vol. 54, no. 6, pp. 1946–1949, 2015.
- [257] E. J. L. Stéen *et al.*, "Convenient Entry to 18 F-Labeled Amines through the Staudinger Reduction," *European J. Org. Chem.*, vol. 2019, no. 8, pp. 1722–1725, 2019.
- [258] Y. QIAN *et al.*, "Compounds and methods for the targeted degradation of bromodomain-containing proteins," 030814 A1, 2017.
- [259] K. Brunner *et al.*, "Cell-penetrating and neurotargeting dendritic siRNA nanostructures," *Angew. Chemie - Int. Ed.*, vol. 54, no. 6, pp. 1946–1949, 2015.
- [260] N. Zenmyo *et al.*, "Optimized reaction pair of the CysHis tag and Ni(II)-Nta probe for highly selective chemical labeling of membrane proteins," *Bull. Chem. Soc. Jpn.*, vol. 92, no. 5, pp. 995–1000, 2019.
- [261] Y. L. Sun, Y. Zhou, Q. L. Li, and Y. W. Yang, "Enzyme-responsive supramolecular nanovalves crafted by mesoporous silica nanoparticles and choline-

- sulfonatocalix[4]arene [2]pseudorotaxanes for controlled cargo release,” *Chem. Commun.*, vol. 49, no. 79, pp. 9033–9035, 2013.
- [262] A. W. Snow and E. E. Foos, “Conversion of alcohols to thiols via tosylate intermediates,” *Synthesis (Stuttg.)*, no. 4, pp. 509–512, 2003.
- [263] C. Muniesa *et al.*, “Glutathione-sensitive nanoplatfom for monitored intracellular delivery and controlled release of Camptothecin,” *RSC Adv.*, vol. 3, no. 35, p. 15121, 2013.
- [264] M. Juríček *et al.*, “An ExBox [2]catenane,” *Chem. Sci.*, vol. 5, no. 7, pp. 2724–2731, 2014.